PHOTOABSORPTION INDUCED DISORDERING OF InGaAs-InGaAsP MULTIPLE QUANTUM WELL STRUCTURES FOR OPTOELECTRONIC INTEGRATION

by

Andrew McKee

May 1996

A thesis submitted to the Faculty of Engineering
of the University of Glasgow
for the degree of Doctor of Philosophy

Abstract

This thesis is concerned with the intermixing of indium phosphide based multiple quantum well structures using a high power continuous wave (CW) operated Nd:YAG laser which shall be referred to as Photoabsorption Induced Disordering (PAID).

A wide range of discrete devices have been fabricated from intermixed material such as low-loss single mode waveguides, broad area oxide stripe lasers, strip loaded ridge waveguide lasers and electroabsorption ridge waveguide modulators. These devices have been characterised which gives an indication as to how the optical and electrical properties of the multiple quantum well material changes as it is intermixed.

Single mode ridge waveguides have exhibited losses of around 5 $dBcm^{-1}$ at 1550 nm while losses as low as 1.6 $dBcm^{-1}$ have been observed at 1570 nm.

Broad area and ridge waveguide lasers have been fabricated from material which has been bandgap widened by up to 160 nm. There is little deterioration in the lasing performance as the material is intermixed with only a 20% increase in the threshold current density due to the alteration of the 2-D density of states towards bulk material.

Electroabsorption in disordered material is investigated using photocurrent spectroscopy and also by fabricating ridge waveguide modulators. The ON/OFF ratios are 20 dB in 500 μm long devices fabricated from material which has been bandgap shifted by 120 nm while material shifted by only 80 nm yielded devices with extinction ratios as high as 27 dB.

The thermodynamics of the PAID process have been modelled using a commercially available finite element package (ABAQUS). This modelling has yielded useful results which gives an insight into the resolution capabilities of the process, and the physical parameters (such as spot size and heat sink temperature) which affect it.

Extended cavity broad area oxide stripe lasers have been fabricated demonstrating that the process can be used to produce useful integrated devices. The fabrication of these devices is explained by the thermal modelling.

Acknowledgements

I wish to express my gratitude to Professor Peter Laybourn for the use of facilities and materials at the Department of Electronics and Electrical Engineering of the University of Glasgow.

I am extremely grateful to my joint supervisors Professor Richard M. De La Rue and Professor John Marsh for their guidance, encouragement and continual support given throughout the duration of this project.

Much of the work carried out in this thesis was aided by colleagues Dr. Chris McLean and Dr. Giuseppe Lullo to whom I am especially indebted. I also wish to thank Dr. Catrina Bryce, Dr. Steven Ayling, Dr. Ooi Boon Siew and Dr. Karen McIlvaney for helpful discussions and constant encouragement. Special thanks must go to the technical staff of the department particularly Jim Gray, the Dry Etch team and all members of the Cleanroom staff.

I would also like to acknowledge the practical assistance given by Dr. Chris Button at Sheffield University who supplied all of the epi-wafers used in this project.

I would finally like to thank all of my fellow Post-Graduate students and Research Assistants who helped to create a friendly and enjoyable atmosphere both within and outwith the department.

This project was supported by EPSRC and by a CASE studentship with the Defence Research Agency (Malvern) under the supervision of Dr. David Wight.

Table of Contents

Chapter 1	**Integrated Optoelectronic Circuits**	**1**
	1.1 Introduction	1
	1.2 Multiple growth epitaxy	1
	1.3 Selective area epitaxy	2
	1.4 Growth on non-planar substrates	3
	1.5 Laser assisted epitaxy	4
	1.6 Quantum well intermixing	4
	1.7 Conclusions	9
Chapter 2	**Properties of Quantum Well Structures**	**12**
	2.1 Introduction	12
	2.2 Quantum Well Modelling	12
	2.3 Band Structure of Indium Phosphide	21
	2.4 Density of States	23
	2.5 Optical Absorption	27
	2.6 The Effect of an E-Field on the Properties of Quantum Wells	29
Chapter 3	**Photo-Absorption-Induced-Disordering (PAID)**	**34**
	3.1 Introduction	34
	3.2 Experimental Arrangement	34
	3.3 PL Measurements	38
	3.4 Absorption of light in a Semiconductor	38
	3.5 Generation of heat in a Semiconductor	38
	3.6 Thermal Conduction in a Semiconductor	43
	3.7 Intermixing of Quantum Wells	48
	3.8 Calculation of Energy levels in a Disordered Quantum Well	51
	3.9 Advantages of PAID	51
	3.10 Conclusions	53
Chapter 4	**Low-Loss Optical Waveguides**	**55**
	4.1 Introduction	55
	4.2 General Theory of slab Waveguides	55
	4.3 Fabrication of Optical Waveguides	61
	4.4 Fabry-Perot Loss Measurements	68
	4.5 Results	74
	4.6 Conclusions	80

Chapter 5	**Broad Area Oxide Stripe Lasers**	**81**
	5.1 Introduction	81
	5.2 General Theory of a Fabry-Perot Laser Oscillator	81
	5.3 Application to Multiple Quantum Well Lasers	82
	5.4 Fabrication of Oxide Stripe Lasers	86
	5.5 Testing Lasers	88
	5.6 Results	93
	5.7 Conclusions	100
Chapter 6	**Bandgap Tuned Oxide Stripe Lasers**	**101**
	6.1 Introduction	101
	6.2 Fabrication	101
	6.3 Results	101
	6.4 Conclusions	106
Chapter 7	**Bandgap Tuned Ridge Waveguide Lasers**	**107**
	7.1 Introduction	107
	7.2 Fabrication	107
	7.3 Comparison between oxide stripe lasers and ridge waveguide lasers	113
	7.4 Results	113
	7.5 Comparison Between different amounts of disordering	115
	7.6 Temperature Dependence of threshold current	120
	7.7 CW measurements of ridge waveguide lasers	124
	7.8 Life-time measurements	132
	7.9 Spontaneous Emission of Lasers	135
	7.10 Conclusions	135
Chapter 8	**Electroabsorption in InGaAs(P) Quantum Wells**	**136**
	8.1 Introduction	136
	8.2 Photocurrent Spectroscopy	136
	8.3 Features in Photocurrent Spectroscopy of MQW Structures	136
	8.4 Device Fabrication	137
	8.5 Experimental Set-up	140
	8.6 Results	142
	8.7 Electroabsorption Modulators	147
	8.8 Measurement Set-up	148
	8.9 Results	148
	8.10 Conclusions	153

Chapter 9 **Broad Area Extended Cavity Oxide Stripe Lasers** **155**
9.1 Introduction 155
9.2 Fabrication 155
9.3 Results 160
9.4 Conclusions 166

Chapter 10 **Thermal Modelling** **167**
10.1 Introduction 167
10.2 Equations of Heat Flow 167
10.3 Model of the PAID process 171
10.4 Resolution of the PAID process 180
10.5 Conclusions 199

Chapter 11 **Conclusions and Future Work** **201**
11.1 Conclusions 201
11.2 Future Work 202

Appendix A **ABAQUS**

Chapter 1 Integrated Optoelectronic Circuits

1.1 Introduction

Monolithic integration of optoelectronic devices potentially offers similar advantages to those obtained from silicon based electronic integrated circuits. These advantages include the possibility of mass production, reduction in size leading to reduced cost and higher operating speeds (due to reduced parasitic capacitance and inductance), and increased reliability. There is a wide range of potential applications for optoelectronic integrated circuits, e.g. for optical generation and detection, optical waveguiding, switching, filtering, interferometry and signal processing.

Integrating optoelectronic devices, however, presents many problems that do not exist in standard silicon based processing. The fundamental problem with optoelectronic integration is the requirement to produce areas with significantly different optical and electrical properties on a single substrate. This is a far more complex problem than producing areas with only different electrical properties, which can easily be achieved by introducing the correct amount of electrically active dopants to the material.

Many different processes have been studied which allow areas of different optical properties to be produced on a single wafer. This discussion is confined to III-V semiconductor compounds, although optoelectronic circuits have also been fabricated in other materials such as lithium niobate and silica-on-silicon.

The different processes relevant to monolithic integration with III-V semiconductors include multiple growth steps, selective area epitaxy, laser assisted epitaxy, growth on non-planar substrates, and a range of quantum well intermixing techniques. These techniques differ substantially, but strive to achieve much the same result, namely, producing areas of different bandgap on a single epitaxial wafer or chip.

1.2 Multiple growth epitaxy

Multiple growth epitaxy is perhaps the simplest technique to understand. The first stage is an initial growth of a structure with a bandgap of say λ_1. This epitaxially grown structure usually consists of either bulk material, multiple quantum well layers, or a superlattice structure. Selected areas of the wafer are then etched away and material with a different bandgap is grown. During the second growth stage, the remaining initial structure is masked (typically with SiO_2) to prevent overgrowth. The bandgap of the material grown at the second growth stage is chosen for the

particular application required. For example, if the second growth is to serve as a passive waveguide region for a laser operating at wavelength λ_1, then it is desirable that the losses in the passive region are low and consequently $\lambda_2 < \lambda_1$ is chosen. The disadvantages of this process are the high costs incurred by the multiple growth stages, and the optical and electrical coupling problems between the areas of different bandgap. Another potential problem of such growth and regrowth processes in the indium phosphide system is intermixing of the quantum wells grown in the first growth run during the overgrowth stage. This can happen rather easily since intermixing occurs at temperatures similar to typical growth temperatures (of around 650°C).

A technique related to the one just described is to grow a coupled laser section and waveguide section on top of each other, with the upper laser section etched away in some regions. This process still, however, requires a regrowth stage to produce an upper cladding layer for the waveguide region. Wakita[1] *et al.* used this technique to fabricate an integrated Distributed Feedback (DFB) Laser and electroabsorption modulator. The active region of the laser consisted of four strained InGaAsP quantum wells with InGaAsP barriers grown on top of a multiple quantum well *pin* waveguiding layer. The modulator section had the upper quantum wells layers (i.e. the laser section) removed and an indium phosphide upper cladding layer regrown on top of the waveguide core. The device produced transform-limited 7 ps optical pulses at a repetition rate of 20 GHz, when the modulator was driven sinusoidally at 20 GHz with a 4.0 V peak-peak voltage.

A similar circuit was fabricated by Raybon[2] *et al.* where a Distributed Bragg Reflector (DBR) laser was integrated with an electroabsorption modulator. Again, a multiple quantum well active laser region consisting of strain compensated layers was grown on a waveguide layer which acted as the backbone of the device, with regrowth of p-doped indium phosphide forming the cladding layers of the modulator section. The DBR grating was etched into an InGaAsP layer situated between the active region and the waveguide core. The laser section was directly modulated at 2.5 $GBits^{-1}$ generating a non-return-to-zero (NRZ) signal while the modulator was sinusoidally driven giving a coded pulse stream at the output.

1.3 Selective Area Epitaxy

Selective area growth of a range of InGaAsP compounds by low pressure metal-organic chemical vapour deposition (MOCVD) has been carried out by Gibbon[3] *et al.* By growing on InP substrates patterned with silicon dioxide masks, they have achieved a 100 nm range in photoluminescence (PL) emission (and lasing) wavelengths in InGaAs(P) multiple quantum well structures. The technique relies on

the fact that the dielectric mask inhibits epitaxial growth of material. This means that some of the material which would have grown in the masked region will be deposited in the vicinity. This results in thicker layers being deposited around masked areas. So, in a multiple quantum well structure, the PL wavelength is increased due to the well thickness increasing.

Fabry-Perot lasers were fabricated from multiple quantum well material with lasing wavelengths ranging from 1507 nm to 1626 nm and with no degradation in the threshold current density or differential quantum efficiency.

By appropriate design of the SiO_2 mask pattern, areas of different bandgap can be grown with smooth transition regions between them. The transition region width is around 100 μm. This approach was used by Aoki[4] *et al.* to produce an InGaAs(P) multiple quantum well electroabsorption modulator integrated with a DFB laser in a circuit which operated at 10 $GBits^{-1}$ with only a 1 V peak-peak signal applied to the modulator. The laser section of the device was grown between two SiO_2 masks which were 15 μm wide and spaced by 10 μm. The PL emission wavelengths of the laser section and the modulator section were 1.57 μm and 1.49 μm respectively, with a transition region of approximately 70 μm between them.

1.4 Growth On Non-Planar Substrates

Growth on non-planar substrates is similar to selective area epitaxy in that the substrate has been altered in some way prior to growth, in order to alter the local growth rate of the material. In this case, areas of the substrate are etched away to reveal crystal planes other than the standard (100) plane. Since these crystal sidewalls have lower growth rates than the (100) plane, the atoms tend to migrate onto the top of the ridge, thereby increasing the growth rate. Regions which are designed to have a long PL wavelength (i.e. thick quantum wells) are grown on top of narrow ridges, while areas which are required to have a short PL wavelength are grown on unetched planar regions of the substrate.

Work by Brovelli[5] *et al.* focused on growing strained quantum wells of InGaAs with AlGaAs barriers on non-planar GaAs substrates, with PL shifts of up to 70 nm attained using this technique. They fabricated a mode-locked InGaAs-AlGaAs quantum well laser with integrated passive waveguide cavity and quantum well modulator[6] capable of generating transform-limited pulses of 4.4 ps duration. The lasing section was grown on a 16 μm wide ridge while the modulator section was grown on a 19 μm wide ridge. The passive waveguide section was grown on a planar region. The different ridge widths gave a shift in bandgap energy of about 10 nm between the laser and modulator section while there was an approximately 35 nm difference between the lasing and waveguide sections.

1.5 Laser Assisted Epitaxy

Work by Iga *et al.* involved using a laser to alter the composition of InGaAsP compounds grown by metal-organic molecular beam epitaxy (MOMBE). The laser was a continuous-wave (CW) operated argon ion (multi-lines) with a power density of 40 Wmm^{-2}, which was scanned over selected areas of the wafer using a galvanometer controlled mirror.

The substrate temperature at growth was fixed at 510°C, which was increased to 535°C in the areas exposed to the laser. This increase in temperature caused the gallium content in the layers to reduce by 90% and the growth rate to drop by 30%. Layers of different composition (and therefore bandgap) were grown simultaneously on different areas of the wafer defined by laser exposure. It should be noted that since the gallium content of the film changed so much in areas exposed to the laser, the layers did not remain lattice matched to indium phosphide. The transition width between areas of different composition was around 30 μm, which was due to the diffusion of heat from areas of high temperature to lower temperature.

Using this technique, the authors fabricated an InAsP-InGaAsP superlattice structure[7] simply by turning the laser on and off, on a time scale of seconds. They also demonstrated an integrated laser array operating at two different frequencies[8] and an integrated detector[9,10] operating at both 1.3 μm and 1.55 μm.

1.6 Quantum Well Intermixing

Although the work in this thesis is confined to the InP based system (with compounds of InGaAsP lattice matched to InP), it is also worthwhile reviewing the work carried out on the (Al)GaAs system, since the basic concepts of well-barrier intermixing are essentially the same. The main difference between the two systems is the greater thermal stability of the GaAs system.

1.6.1 Impurity Induced Disordering

The first experiment carried out using Impurity Induced Disordering (IID) was by Laidig[11] *et al.* in 1980 in an attempt to intermix undoped AlAs-GaAs superlattice (SL) structures. They diffused zinc into the SL and found that the layers intermixed at temperatures much less than those necessary for ordinary thermal interdiffusion in the undoped SL, yielding bulk material with a composition of $Al_{1-x}Ga_xAs$. Using silicon nitride masks, they produced regions of disordered and undisordered material with a spatial resolution of around 1-2 μm.

Zinc has proved to be one of the most widely studied diffusants in the (Al)GaAs system with a wide range of work reported. Kamizato[12] *et al.* used Zn diffusion to intermix (Al)GaInP layers on GaAs substrates. They used intermixed regions to fabricate non-absorbing mirrors (NAMs) at the cleaved facets of conventional Fabry-Perot lasers to prevent catastrophic optical damage (COD). The reduced absorption at the facets increases the output power achievable before facet damage occurs. However, the Zn diffusion increases the free-carrier absorption coefficient in the intermixed regions, which leads to increased laser threshold and reduced ex-facet efficiency.

Zn-diffusion enhanced intermixing has also been investigated in long wavelength material. Van Gurp[13] *et al.* demonstrated that Zn enhances the group III diffusion rate in InGaAsP-InP structures at temperatures as low as 420°C compared to 750°C for unimplanted material. Increased diffusion on the group III site causes the bandgap of the well to reduce and also induces strain. Reducing the bandgap of the quantum well is opposite to most intermixing mechanisms.

Another electrically active diffusant used to promote intermixing in the (Al)GaAs system is silicon. The silicon is incorporated into the structures from a layer deposited on the material surface. Deppe[14] *et al.* used silicon-enhanced interdiffusion of (Al)GaAs multiple quantum well structures to fabricate buried heterostructure laser diodes. During the diffusion process, the active region of the device was masked with a 5 μm wide stripe of silicon nitride. Outside the active region, the increase in bandgap due to intermixing reduces the refractive index, thus forming a lateral refractive index step which leads to optical confinement. The Si doping also provides current confinement, as Si acts as an n-type dopant in (Al)GaAs.

Thornton[15] *et al.* used Si-enhanced intermixing to produce an extended cavity laser in which the passive waveguide section was bandgap shifted to higher energies.

Silicon has also been used to enhance the diffusion rate of long wavelength materials. Tell[16] *et al.* used material consisting of 50 periods of InGaAs-InP (wells-barriers) capped with 0.1 μm of InP. Photoresist was used to mask areas of the material during the Si-ion implantation at a dose of 5.10^{14} cm^{-2} with an energy of 200 keV. The material was then annealed in a furnace for 2 hrs at 650°C resulting in the PL wavelength shifting from 1.45 μm to 1.2 μm. TEM micrographs showed selective intermixing at the edges of the masks, although they also showed significant residual damage in the implanted regions.

1.6.2 Neutral Impurity Induced Disordering (IID)

In optoelectronic integrated circuits (OEICs) it is important that the absorption losses of passive components are low (≤10 $dBcm^{-1}$). Electrically active dopants,

however, introduce higher losses due to free-carrier absorption. Another requirement of OEICs is good electrical isolation[17] (≥100 kΩ) between components in the circuit to avoid crosstalk. In a typical waveguide structure (3 μm x 1 μm x 5 mm), this would require a doping level of under 10^{17} cm^{-3}, which is below the threshold level required for enhanced interdiffusion to take place. These are the two main reasons which led to work using electrically neutral impurities to increase the intermixing rate.

Work carried out by Marsh and co-workers at Glasgow involved studying boron and fluorine; both of which are electrically neutral dopants at room temperature in GaAs and AlGaAs. Double quantum well and multiple quantum well (Al)GaAs structures were implanted with doses ranging from 3.10^{16} to 3.10^{19} cm^{-3}. Fluorine caused the PL to shift by twice as much as boron under identical annealing conditions, although Secondary-Ion Mass Spectrometry (SIMS) studies showed that fluorine diffused during the anneal while boron did not. This means that boron would be more suited to applications requiring high spatial resolution.

Propagation losses in passive waveguides were lower for F-disordered material than B-disordered material[18]. Using the sequential cleave technique, losses as low as 4.7 $dBcm^{-1}$ were measured at a wavelength of 875 nm in material blue-shifted by 60 meV using fluorine.

Using F-disordering, a double quantum well (Al)GaAs extended cavity single mode ridge waveguide laser was fabricated[19]. The waveguide region was implanted with F at a doping level of 10^{14} cm^{-2} with an implantation energy of 1 MeV during which, the active region was masked with a 3 μm layer of SiO_2. The material was then annealed in a furnace at 890°C for 90 mins, giving a blue shift in the PL peak of the waveguide section of 40 meV. The threshold current for a 600 μm laser with no passive section was 55 mA, while a laser with the combination of a 600 μm active section and a 600 μm passive section had a threshold current of 60 mA. The losses were calculated to be about 19 $dBcm^{-1}$ in the passive section. This loss is substantially higher than that for the passive waveguides (4.7 $dBcm^{-1}$), simply due to the free-carrier absorption in the n and p-cladding layers.

Neutral IID has also been investigated in long wavelength material by Bradshaw[20] and co-workers at Glasgow. Multiple quantum well structures containing InGaAs wells and barriers of AlGaInAs or InGaAsP were annealed as-grown, implanted with boron, and implanted with fluorine. Unimplanted InGaAs(P) material was found to intermix at temperatures above 500°C for a 30 min. furnace anneal. The PL shift was always to higher energies, attributed to P diffusing into and As diffusing out of the wells. The (Al)GaInAs material was more stable, with no shifts observed up to 650°C. Above that temperature, small red shifts were observed due to the interdiffusion of In and Ga.

Phosphorus-quaternary material implanted with boron showed red-shifts for temperatures over 650°C, which can be explained by enhanced group III interdiffusion. Zn has already been shown to increase only the group III diffusion rate, which introduces strain into the structures. Boron-implanted aluminium-quaternary showed small blue shifts at temperatures below 650°C, independent of dose, which suggests that the implantation damage caused the intermixing. Above 650°C, the material showed a red shift similar to that for as-grown material.

Fluorine implantation induced large blue shifts (of > 60 meV) in P-quaternary structures at temperatures of 650°C, but this shift was only 20 meV larger than for the as-grown material, implying that the thermal instability of the material was the dominant intermixing mechanism. Passive waveguides were fabricated from fluorine-intermixed InGaAs(P) material with losses as low as 8.5 $dBcm^{-1}$. In Al-quaternary, fluorine produced significant blue shifts at all temperatures above 600°C indicating that fluorine plays an active part in the intermixing process.

1.6.3 Impurity-Free Vacancy Disordering

Impurity-free vacancy disordering (IFVD) has also been used to selectively disorder both GaAs and InP based materials. This process does not require impurities to be introduced by either ion implantation or diffusion, but relies on atoms diffusing out selectively from the material into dielectric caps at high temperatures, causing vacancies to be generated at the surface which diffuse rapidly through the material and cause intermixing. Certain dielectric caps, such as silicon dioxide and silicon nitride (Si_3N_4) have been found to enhance intermixing, while strontium fluoride[21,22] (SrF_2) inhibits it.

IFVD was used to fabricate an extended cavity laser from InGaAs-InP multiple quantum well material[23]. Silicon nitride films were used to enhance the intermixing rate in the waveguide regions, while the lasing regions were uncapped during the anneal. Although both regions intermixed, producing blue shifts, there was a 55 nm difference in PL wavelength between the lasing section and waveguide section. The poor thermal stability of this material system presents problems in inhibiting intermixing. By fabricating lasers with different lengths of waveguide section, the loss in these regions was calculated to be 7.8 cm^{-1} (34 $dBcm^{-1}$).

Rao[24] *et al.* have investigated a process which worked well in the InP system. $(InGaAsP)_1$-$(InGaAsP)_2$ multiple quantum well samples were annealed in either a Rapid Thermal Annealer (RTA) or a conventional diffusion furnace, partially coated with silicon dioxide doped with phosphorus. The uncapped regions were protected during the high temperature anneal with an InP proximity cap. The capped regions

demonstrated blue shifts of over 50 meV due to group V diffusion, with no shift in the uncapped regions. This process, however, is restricted to near-surface layers which means that, in a standard laser structure, the upper cladding layers and cap layer have to be overgrown after the active region has been disordered.

1.6.4 Plasma Damage Induced Disordering

Plasma damage induced disordering relies on generating point defects at the material surface due to reactive ion bombardment. These point defects can enhance the group III interdiffusion of the quantum well region during a subsequent high temperature anneal as they diffuse through the structure. This process was used by Ooi[25] *et al.* to produce broad area oxide stripe lasers with different operating wavelengths from a single GaAs-AlGaAs quantum well laser structure. A range of 25 nm in lasing wavelength was achieved. Extended cavity lasers were also fabricated using this technique with the passive waveguide section blue shifted using plasma damage induced disordering. Losses as low as 18 $dBcm^{-1}$ were measured in a laser with an active region of 450 μm and a passive length of 500 μm.

1.6.5 Laser Assisted Disordering

Lasers have been used to intermix quantum well structures in the (Al)GaAs system in the past. Epler[26] *et al.* fabricated buried heterostructure (BH) lasers from a single quantum well (Al)GaAs structure by direct-write laser-assisted intermixing. These devices were similar to those previously described[27], but with the areas of intermixing defined by a scanning laser instead of a dielectric mask.

The laser used in the process was a focused argon ion laser with a beam size of ~1 μm, power of 200 mW and a scan speed of 100 μms^{-1}. To fabricate single stripe BH lasers, the scan pattern was a pair of lines separated by 8 μm. The laser beam caused melting of the crystal on a micron scale due to the high power densities involved (~250 $kWmm^{-2}$). During this melt phase, the constituents intermixed rapidly and large amounts of silicon were incorporated from the surface layers of Si-Si_3N_4, yielding a homogeneous AlGaAs alloy heavily doped with Si to a concentration of ~10^{20} cm^{-3}. A subsequent thermal anneal of 850°C for 0.7 hrs caused the Si to diffuse through the structure causing the intermixed region to increase in size. The increase in bandgap due to intermixing caused the refractive index to decrease, thus giving lateral optical confinement. Lasers were fabricated

from the material which operated CW for several minutes with no degradation although no meaningful lifetest data were obtained.

Brunner[28] *et al.* have used a similar process, but on a much smaller scale, to fabricate quantum wires from (Al)GaAs quantum wells. They used a CW operated argon ion Gaussian profiled laser beam (514 nm) focused to a spot with a FWHM of 500 nm and a power of 6.6 mW (~30 $kWmm^{-2}$). This power density caused the material to heat up to around 1000°C where rapid interdiffusion of atoms between the wells and barriers occurred. The interdiffused region was found to be narrower than the laser beam, with a lateral distance of 200 nm.

Intermixing multiple layer structures is not confined to using CW operated lasers. Ralston[29] *et al.* intermixed (Al)GaAs superlattices using pulsed irradiation from a KrF excimer laser at a wavelength of 248 nm, with a pulse duration of 22 ns. The energy density was controlled by varying the laser power and the spot size (of around 2.5 mm^2). It was found that energy densities of ~400 $mJcm^{-2}$ caused visible damage on the material surface, while 220 $mJcm^{-2}$ caused no damage.

Sputter-Auger profiles of the 20 period superlattice indicated that, after one pulse of 220 $mJcm^{-2}$, the first 11 periods were completely intermixed while the remaining 9 remained unaltered. The intermixing mechanism was assumed to be purely thermal i.e. the large energy densities caused the material to melt where the laser was absorbed. In the molten state, the Al atoms from the barriers diffused rapidly, followed by epitaxial recrystallization to a homogeneous AlGaAs alloy. The authors proposed a simple 1-dimensional heat flow model to explain the temperature distribution as a function of time and depth within the material. For large incident energies, the temperature of the material rises above the melting point of GaAs (1507 K) at depths greater than $1/\alpha$, where α is the absorption coefficient of the material. This model explained why there was such an abrupt transition region between intermixed material and unaffected material. Such a process is obviously restricted to near-surface layers unless the laser radiation used has a long absorption length.

1.7 Conclusions

This chapter has given a brief introduction into the wide range of processes which have been used to integrate optoelectronic components on both gallium arsenide and indium phosphide substrates. Each different process has both advantages and drawbacks and none has yet been universally accepted.

1 K. Wakita, K. Sato, I. Kotaka, M. Yamamoto, and M. Asobe, IEEE Photonics Tech. Lett., **5** (8), pp 899-901, 1993

2 G.Raybon et al., IEEE Photonics Tech. Lett., **6** (11), pp 1330-1331, 1994

3 M. Gibbon, J.P. Stagg, C.G. Cureton, E.J. Thrush, C.J. Jones, R.E. Mallard, R.E. Pritchard, N. Collis, A. Chew, Semicond. Sci. Technol., **8**, pp 998-1010, 1993

4 M. Aoki, M. Suzuki, H. Sano, T. Kawano, T. Ido, T. Taniwatari, K. Uomi, A. Takai, IEEE Journal of Quantum Electronics, **29** (6), pp 2088-2096, 1993

5 L.R. Brovelli, D.J. Arent, H. Jäckel, H.P. Meier, IEEE Journal of Quantum Electronics, **27**, p 1470, 1991

6 L.R. Brovelli, R. Germann, J.P. Reithmaier, H. Jäckel, H.P. Meier, H. Melchior, IEEE Photonics Tech. Lett., **5** (8), pp 896-899

7 R. Iga, T. Tamada, H. Sugiura, Journal of Crystal Growth, **136**, pp 273-277, 1994

8 R. Iga, T. Tamada, H. Sugiura, Appl. Phys. Lett., **61**, p 1423, 1992

9 H. Sugiura, K. Wakita, R. Iga, T. Yamada, Journal of Crystal Growth, **136**, pp 64-68, 1994

10 H. Sugiura, IEEE Proc. of LEOS, **1**, pp 46-47, 1994

11 W.D. Laidig, N. Holonyak, Jr., M.D. Camras, K. Hess, J.J. Coleman, P.D. Dapkus, J. Bardeen, Appl. Phys. Lett., **38**, p 776, 1981

12 T. Kamizato, S. Arimoto, H. Watanabe, K. Kadoiwa, E. Omura, S. Kakimoto, K. Ikeda, 13th IEEE International Semi. Laser conf., Takamatsu, Japan, **D-30**, pp 94-95, 1992

13 G.J. van Gurp, W.M van ve Wijgert, G.M. Fontijn, P.J.A. Thijs, J. Appl. Phys., **67** (6), pp 2919-2926, 1990

14 D.G. Deppe, K.C. Hsieh, N. Holonyak, Jr., R.D. Burnham, R.L. Thornton, J. Appl. Phys., **58**, p 4515, 1985

15 R.L. Thornton, W.J. Mosby, T.L. Paoli, IEEE Journal Lightwave tech., **LT-6**, pp 786-792, 1987

16 B. Tell, B.C. Johnson, J.L. Zyskind, J.M. Brown, J.W. Sulhoff, K.F. Brown-Goebeler, B.I. Miller, U. Koren, Appl. Phys. Lett., **52** (17), pp 1428-1430, 1988

17 M. Suzuki, H. Tanaka, S. Akiba, Y. Kushiro, Journ. Lightwave Tech., **6**, p 779, 1988

18 M. O'Neill, J.H. Marsh, R.M. De La Rue, J.S. Roberts, C. Button, R. Gwilliam, Electron. Lett., **26**, pp 1613-1615, 1990

19 S.R. Andrew, J.H. Marsh, M.C. Holland, A.H. Kean, Photonics Tech. Lett., **4** pp 426-428, 1992

20 J.H. Marsh, S.A. Bradshaw, A.C. Bryce, R. Gwilliam, R.W. Glew, J. Electron. Mat., **20** (12), pp 973-978, 1991

21 J. Beauvais, J.H. Marsh, A.H. Kean, A.C. Bryce, C.Button, Electron Lett., **28**, pp 1670-1672, 1992

22 J. Beauvais, S.G. Ayling, J.H. Marsh, IEEE Photonics Tech. Lett. **5** (4), p 372, 1993

23 T. Miyazawa, H. Iwamura, M Naganuma, IEEE Photonics Lett., **3** (5), pp 421-423, 1991

24 E.V.K. Rao, A. Hamoudi, Ph. Krauz, M. Juhel, H. Thibierge, Appl. Phys. Lett., **66** (4), pp 472-474, 1995

25 B.S. Ooi, A.C. Bryce, J.H. Marsh, Electron Lett., **31** (6), pp 449-451, 1995

26 J.E. Epler, R.D. Burnham, R.L. Thornton, T.L. Paoli, Appl. Phys. Lett., **50** (23), pp 1637-1639, 1987

27 D.G. Deppe, K.C. Hsieh, N. Holonyak, Jr., R.D. Burnham, R.L. Thornton, J. Appl. Phys., **58**, p 4515, 1985

28 K. Brunner, G. Abstreiter, M. Walther, G. Böhm, G. Tränkle, Surface Science, **267**, pp 218-222, 1992

29 J. Ralston, A.L. Moretti, R.K. Jain, F.A. Chambers, Appl. Phys. Lett., **50** (25), pp 1817-1819, 1987

Chapter 2 Multiple Quantum Well Structures

2.1 Introduction

This thesis deals with quantum well intermixing of structures containing InGaAs wells and InGaAsP barriers. In order to understand the disordering process and the range of optoelectronic devices fabricated, it is necessary to understand the basic optical and electrical properties of quantum wells and multiple quantum well structures.

2.2 Quantum Well Modelling

2.2.1 The Schrödinger Equation

The classical expression for the energy of a particle is given as:

kinetic energy + potential energy = total energy
(K.E. + P.E. = T.E.).

This expression can be written as:

$$W = H(r,p) = \frac{1}{2m}p^2 + U(r) \tag{2.1}$$

where W is the total energy,
H is the Hamiltonian,
m is the mass,
p is the momentum,
r is the position of the particle, and
U(r) is some time independent potential

In quantum-mechanical theory, however, the position and momentum of a particle are defined by a complex scalar wavefunction $\Psi(r,t)$. The quantity $\Psi(r,t)\Psi^*(r,t)dxdydz$ gives the probability that at a time t, the particle will be found in the elementary volume $dxdydz$. Since the particle must be found somewhere in space, this leads to the normalising condition:

$$\int\int\int_{-\infty}^{\infty} |\Psi|^2 dxdydz = 1 \tag{2.2}$$

The function $\Psi(r,t)$ and its derivative $\nabla\Psi = \left(\frac{\partial\Psi}{\partial x}, \frac{\partial\Psi}{\partial y}, \frac{\partial\Psi}{\partial z}\right)$ are assumed to be continuous.

Quantities such as average position and momentum must be derived from the wavefunction, Ψ, rather than directly from classical equations of motion.

In quantum mechanics, classical variables such as position and momentum are replaced with operators (which operate on the wavefunction) and are given in Table 1.

	Classical variable	Quantum mechanical operator
Position	$\mathbf{r} = (x,y,z)$	$\mathbf{r}$
Momentum	$\mathbf{p} = (p_x,p_y,p_z)$	$\frac{\hbar}{i}\nabla = \frac{\hbar}{i}\left(\frac{\partial}{\partial x}, \frac{\partial}{\partial y}, \frac{\partial}{\partial z}\right)$
Energy	W	$-\frac{\hbar}{i}\frac{\partial}{\partial t}$

Table 1 Classical and quantum mechanical definitions of particle properties

It is now possible to write the Hamiltonian in the quantum mechanical form given by the partial differential equation:

$$-\frac{\hbar^2}{2m}\left(\frac{\partial^2\Psi}{\partial x^2}, \frac{\partial^2\Psi}{\partial y^2}, \frac{\partial^2\Psi}{\partial z^2}\right) + U(r)\Psi = -\frac{\hbar}{i}\frac{\partial\Psi}{\partial t} \tag{2.3}$$

Equation (2.3) is called the time-dependent Schrödinger Equation. Solutions to this equation given by $\Psi(r,t)$ completely describe the motion of a particle in the quantum mechanical sense.

A useful simplification is to seek separable solutions where $\psi(r)$ and $T(t)$ are independent such that:

$$\Psi(r,t) = \psi(r)T(t) \tag{2.4}$$

Substituting equation (2.4) into the time-dependent Schrödinger equation and dividing by ψT gives:

$$-\frac{1}{\psi}\frac{\hbar^2}{2m}\left(\frac{\partial^2\psi(r)}{\partial x^2}, \frac{\partial^2\psi(r)}{\partial y^2}, \frac{\partial^2\psi(r)}{\partial z^2}\right) + U(r) = -\frac{\hbar}{i}\frac{1}{T}\frac{\partial}{\partial t}T(t) \tag{2.5}$$

The left hand side of equation (2.5) is a function of r only and the right hand side is a function of t, so the separation has been shown to be valid. If the constant of separation is equal to W then:

$$-\frac{\hbar}{i}\frac{\partial}{\partial t}T(t) = WT \tag{2.6}$$

which has a solution of the form:

$$T = \exp(-iWt/\hbar) \tag{2.7}$$

The wavefunction can now be written as:

$$\Psi(r,t) = \psi(r)\exp(-iWt/\hbar) \tag{2.8}$$

It has already been stated in equation (2.3) that the time derivative of the wavefunction represents the total energy of the particle. Therefore:

$$\begin{aligned} -\frac{\hbar}{i}\frac{\partial}{\partial t}(\Psi(r,t)) &= W\psi(r)\exp(-iWt/\hbar) \\ &= W\Psi(r,t) \end{aligned} \tag{2.9}$$

implying that W is the total energy of the particle.
The position dependent part of equation (2.8) substituted into equation (2.3) yields the time-independent Schrödinger equation:

$$-\frac{\hbar^2}{2m}\left(\frac{\partial^2\psi}{\partial x^2},\frac{\partial^2\psi}{\partial y^2},\frac{\partial^2\psi}{\partial z^2}\right) + U(r)\psi = W\psi \tag{2.10}$$

where W is an eigenvalue of the equation and Ψ is an eigenfunction of the equation.

2.2.2 The One-Dimensional Square Potential Well

A thin layer of low bandgap material (such as InGaAs) sandwiched between two identical layers of high bandgap material (such as InGaAsP) results in a conduction band profile similar to that shown in Fig. 1.

The potential profile for the conduction band of such a quantum well can be described by:

$$U(x) = \begin{cases} 0 & for \quad |x| < a \\ U_0 & for \quad |x| > a \end{cases} \tag{2.11}$$

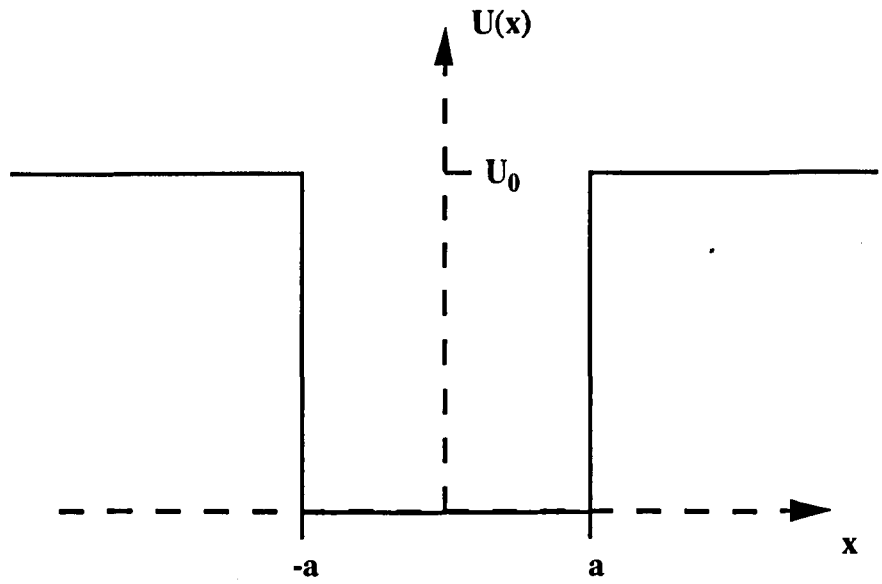

Fig. 1 Conduction band potential profile for a quantum well of finite depth

Schrödinger's Equation then reduces to:

$$\begin{aligned} -\frac{\hbar^2}{2m_e(x)}\frac{\partial^2\psi}{\partial x^2} &= W\psi \quad for \ |x| < a \\ -\frac{\hbar^2}{2m_e(x)}\frac{\partial^2\psi}{\partial x^2} &= (W - U_0)\psi \quad for \ |x| > a \end{aligned} \tag{2.12}$$

where $m_e(x)$ is the effective mass of the electron in the conduction band which is composition dependent (i.e. the mass of an electron is different in the well and the barrier).

For $0 < W < U_0$ this equation has the general solution:

$$\begin{aligned} \psi(x) &= A\sin\alpha x + B\cos\alpha x \quad for \ |x| < a \\ \psi(x) &= C\exp(-\beta x) + D\exp(\beta x) \quad for \ |x| > a \end{aligned} \tag{2.13}$$

$$\alpha = +\sqrt{2m_e(x)W/\hbar^2} \ , \ \beta = +\sqrt{2m_e(x)(U_0 - W)/\hbar^2} \tag{2.14}$$

The solutions of the Schrödinger equation for a potential well are analogous to finding the guided modes in an optical waveguide (see Chapter 4). The only solutions

of interest are normalizable wavefunctions, implying that D = 0 for $x > a$ and C = 0 for $x < -a$. The requirement that $\psi(x)$ and $\frac{1}{m_e(x)}\frac{\partial \psi}{\partial x}$ are both continuous imposes further conditions at the boundaries $x = \pm a$. Working through some simple maths leads to:

$$\beta a = \alpha a \tan \alpha a \qquad or \quad \beta a = -\alpha a \cot \alpha a \tag{2.15}$$

Solutions to equation (2.13) are then given by the intersection points (in the αa-βa plane) of equations (2.15) and the circular arc given by equation (2.14) such that:

$$(\alpha a)^2 + (\beta a)^2 = 2m_e(x)U_0 a^2 / \hbar^2 \tag{2.16}$$

Solutions of the wavefunction which fit the boundary conditions therefore only occur for discrete eigenvalues and are called bound states. For $W > U_0$ there is a continuous spectrum of wavefunctions whose magnitudes do not decay to zero as $|x| \to \infty$. For $W \leq 0$ there is no normalizable function which is a solution.

In the valence band, the wavefunction must be solved for both light and heavy holes since they have different effective masses (both in the well and in the barrier). This typically leads to twice as many bound levels in the valence band compared to the conduction band. Fig. 2 shows a schematic representation of the bound states (or eigen-energies) for electrons, light holes and heavy holes, in a quantum well of finite depth.

2.2.3 The Potential Well of Infinite Depth

A simpler model to analyse is the square well of infinite depth (i.e. where the potential barriers are infinitely high). The potential profile can be described as:

$$U(x) = \begin{cases} 0 & for \quad |x| < a \\ \infty & for \quad |x| > a \end{cases} \tag{2.17}$$

with boundary conditions at $x = \pm a$ simplifying to:

$$\begin{aligned} A\sin \alpha a + B\cos \alpha a = 0 \\ -A\sin \alpha a + B\cos \alpha a = 0 \end{aligned} \tag{2.18}$$

which gives:

$$A\sin \alpha a = 0 \ , \ B\cos \alpha a = 0 \tag{2.19}$$

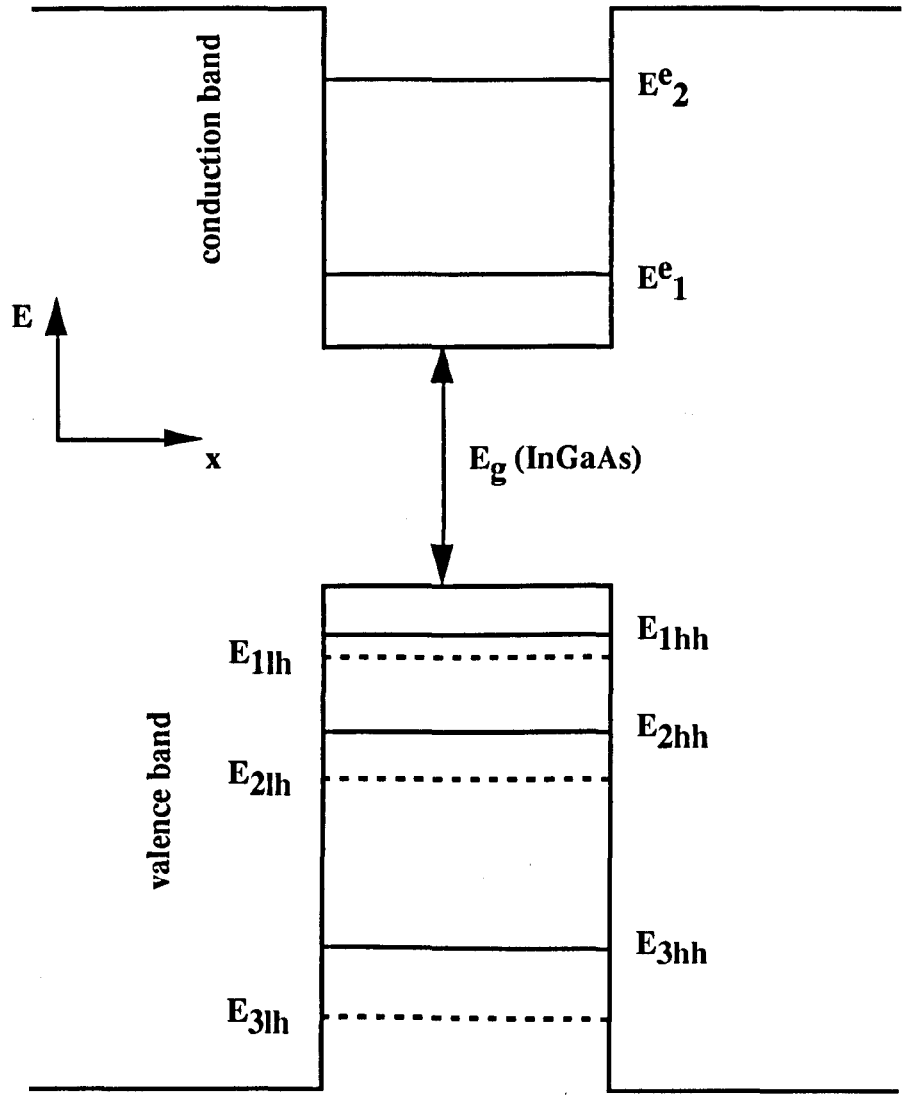

Fig.2 Schematic diagram of bound states in a quantum well of finite depth

For symmetric solutions:

$$A = 0 \text{ and } \cos \alpha a = 0 \tag{2.20}$$

while for asymmetric solutions:

$$B = 0 \text{ and } \sin \alpha a = 0 \tag{2.21}$$

This requires that $\alpha a = m\pi/2$, which gives (from equations (2.20) & (2.21)):

$$W_m = \frac{\pi^2 \hbar^2 m^2}{8 m_e a^2} \quad , m = 1,2,3... \tag{2.22}$$

The wavefunctions can then be described by:

$$\psi(x) = B \cos \frac{(2m-1)\pi x}{2a} \tag{2.23}$$

and,

$$\psi(x) = A \sin \frac{2m\pi x}{2a} \tag{2.24}$$

with A and B given by the normalising condition in equation (2.1).

Fig. 3 shows the first three wavefunctions in a square well of infinite depth which correspond to

$$\psi(x) = B \cos \frac{\pi x}{2a} \ , \ \psi(x) = A \sin \frac{\pi x}{a} \ , \ \psi(x) = B \cos \frac{3\pi x}{2a} \tag{2.25}$$

The square well of infinite depth can be used as a quick way of calculating approximately the lowest energy eigenvalue in a square well of finite depth.

It has been assumed in the above that the barriers are infinitely thick and that no interaction takes place between wells (i.e. the wavefunctions do not overlap). This is not always the case, especially when dealing with superlattice structures which are specifically designed to utilise the effects of overlapping wavefunctions. The material used in this thesis, however, can be assumed to have no overlap of the wavefunctions between adjacent quantum wells.

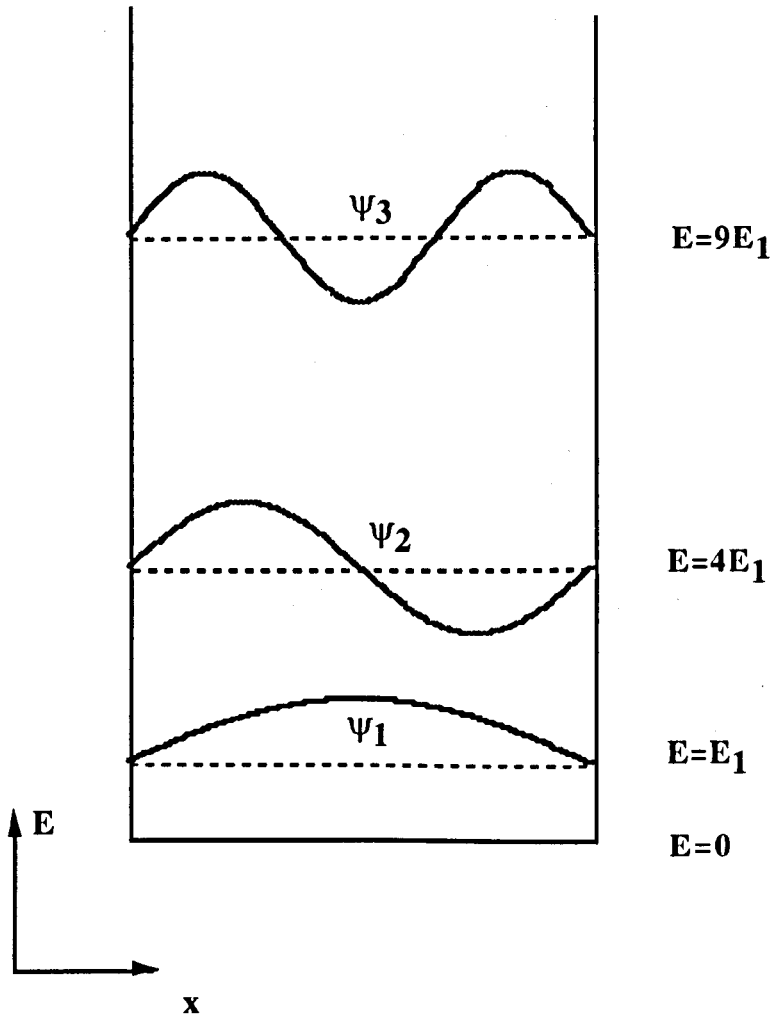

Fig.3 First three wavefunctions in conduction band
of quantum well of infinite depth

2.2.4 The free electron

It is possible to regard an electron in the conduction band of a semiconductor as a free electron on which no forces are acting. If the potential U(r) is arbitrarily set to zero, then the time-independent Schrödinger equation can be written as:

$$-\frac{\hbar^2}{2m_e}\left(\frac{\partial^2\psi}{\partial x^2},\frac{\partial^2\psi}{\partial y^2},\frac{\partial^2\psi}{\partial z^2}\right)=W\psi \tag{2.26}$$

Solutions to equation (2.25) are plane waves of the form:

$$\psi(x,y,z)=const.\exp\{i\boldsymbol{k}\cdot\boldsymbol{r}\} \tag{2.27}$$

where:

$$k^2=k_x^2+k_y^2+k_z^2=2m_eW/\hbar^2 \tag{2.28}$$

There are energy states for all values of $W>0$, thus forming a continuous spectrum. The parabolic relationship between the wave number, k, and the energy, W, is shown in Fig. 4.

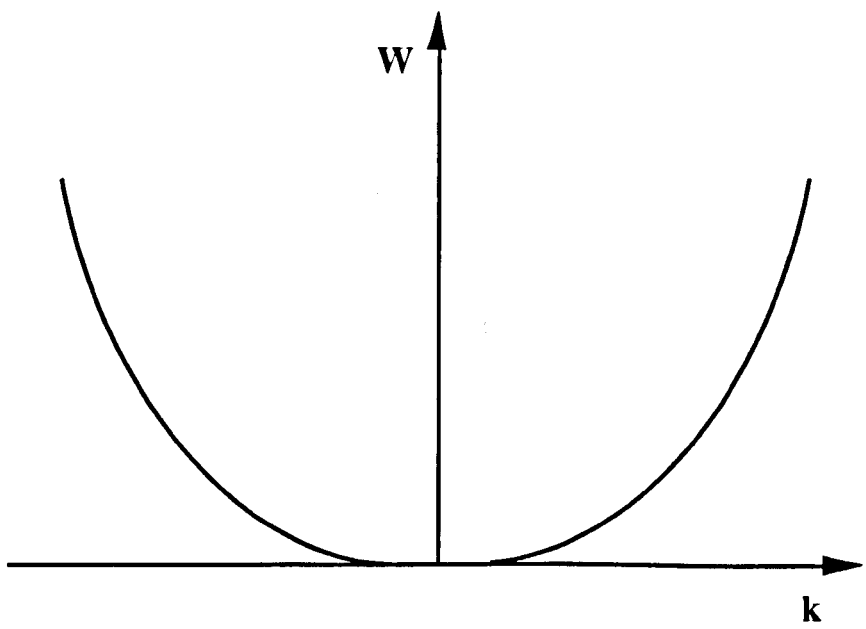

Fig. 4 Parabolic relationship between the wavenumber and energy of a free-electron

2.3 Band structure of indium phosphide

The band structure of InP[1] is shown schematically in Fig. 5. The profiles of various bands are shown in two different crystal directions starting from the centre of the first Brillouin zone at $\Gamma = \frac{2\pi}{\hat{a}}(0,0,0)$. The point L corresponds to the limit of the first Brillouin zone along the Λ axis < 111 > and the co-ordinates are given by $L = \frac{2\pi}{\hat{a}}\left(\frac{1}{2},\frac{1}{2},\frac{1}{2}\right)$. The point X corresponds to the limit of the first Brillouin zone along the Δ axis < 100 > and the co-ordinates are given by $X = \frac{2\pi}{\hat{a}}(0,0,1)$. $\hat{a}$ is the relevant lattice parameter of the unit cell under consideration.

The conduction and valence bands both consist of sub-bands which play important roles in determining the properties of the semiconductor. For example, in the valence band there is a heavy-hole (hh) band and a light-hole (lh) band which have the same energy at **k**=0 (Γ) and are said to be degenerate. The hh band is less strongly bent away from this point and lies at higher energies than the lh band. The split-off band (sb) lies at lower energies than the lh and hh bands with a separation at **k**=0 of 0.11 eV. In the conduction band, higher bands exist which electrons can reach if they obtain enough kinetic energy. This effect is used in microwave devices such as the Gunn diode.

The conduction band minima and valence band maxima are both situated at **k**=0, which is indicative of a direct bandgap semiconductor. The energy gap at room temperature is 1.35 eV. The band structure of InGaAsP compounds lattice matched to InP is also direct[2] and is similar to Fig. 5.

The most important part of Fig. 5 is around the minima of the conduction band and the maxima of the valence band. This is where electrons will be found in the conduction band, and holes in the valence band. In the neighbourhood of the conduction band minima, the band profile can be approximated by the parabolic relation

$$W(\mathbf{k}) = W_g + \frac{\hbar^2 k^2}{2m_e} \tag{2.29}$$

where the top of the valence band has been chosen as the point of zero energy,

W_g is the energy of the bandgap,

k is the wave number, and

m_e is the effective mass of the electron.

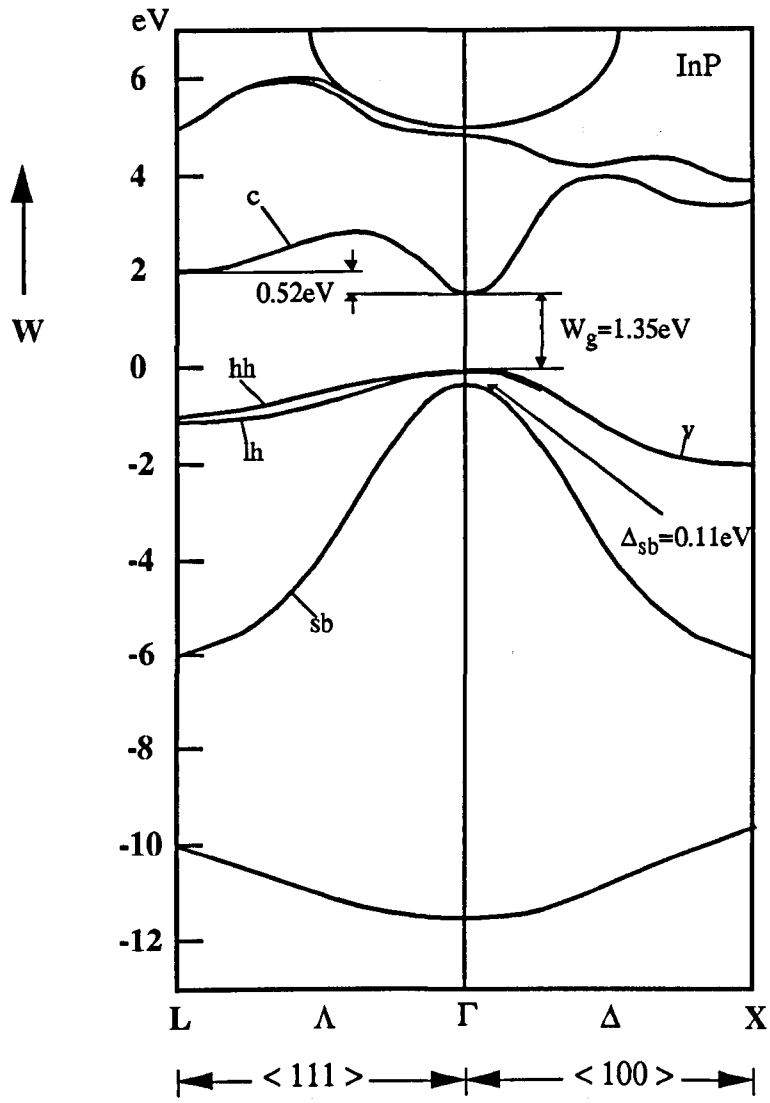

Fig. 5 Band structure of indium phosphide

The effective mass of the electron at **k**=0 is then given by:

$$m_e = \hbar^2 \left(\frac{\partial^2 W}{\partial k^2} \right)^{-1} \tag{2.30}$$

Similarly, the effective masses of the heavy-hole and the light-hole can be obtained by using a parabolic approximation for the different valence sub-bands:

$$W(\mathbf{k}) = -\frac{\hbar^2 k^2}{2m_{hh}} \tag{2.31}$$

for heavy-holes,

$$W(\mathbf{k}) = -\frac{\hbar^2 k^2}{2m_{lh}} \tag{2.32}$$

for light-holes, and

$$W(\mathbf{k}) = -\Delta_{sb} - \frac{\hbar^2 k^2}{2m_{sb}} \tag{2.33}$$

for the split-off band.

2.4 Density of States

2.4.1 Density of states for a parabolic band

In section 2.2.4 it was assumed that electrons close to the band edge behave like particles which are described by the wavefunction $\psi(x,y,z) = const.\exp\{i\boldsymbol{k}\cdot\boldsymbol{r}\}$. In a cube of material length L, the allowed **k** vectors are given by:

$$k_x, k_y, k_z = 0 \ , \ \pm 2\pi / L \ , \ \pm 4\pi / L \ , ... \tag{2.34}$$

as shown in Fig. 6. This means that each allowed **k**-value occupies a volume of $(2\pi/L)^3$ in **k**-space and the number of states per unit volume (in **k**-space) is given as $(L/2\pi)^3$. Dividing by the volume of the cube gives the density of states as:

$$D(\mathbf{k})d\mathbf{k} = \frac{2}{(2\pi)^3} d\mathbf{k} \tag{2.35}$$

where the factor of 2 has been introduced to account for the 2 spin orientations possible for each state. $D(\mathbf{k})d\mathbf{k}$ represents the total number of states in the region from **k** to **k** + d**k**.

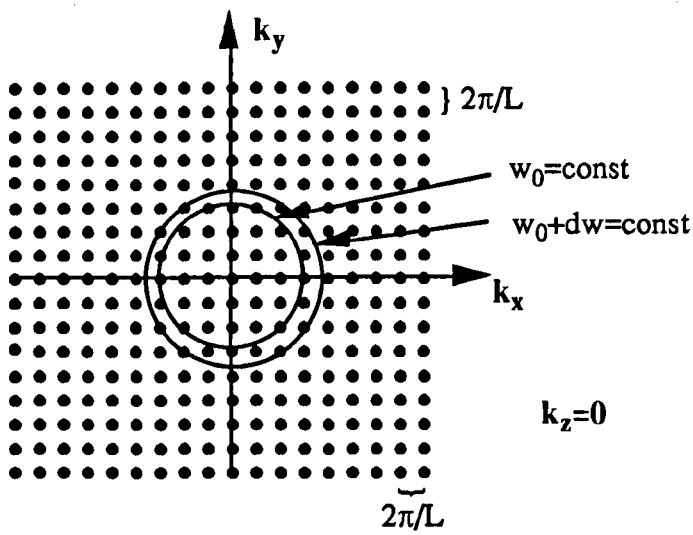

Fig. 6 Density of states in k-space

The number of states in the energy interval W_0 to W_0+dW is given by the volume of **k**-space bounded by these energies, multiplied by the density of states in **k**-space. From Fig. 6 it can be seen that regions of constant energy form concentric spheres in k-space with the volume, V, between two concentric spheres given as:

$$V = 4\pi \mathbf{k}^2 d\mathbf{k} \tag{2.36}$$

where **k** is the radius of the inner sphere, and
d**k** is the distance between them.

Combining equations (2.35) and (2.36), the total number of states in the energy interval W_0 to W_0+dW is then given by:

$$D(W_0)dW = 2/(2\pi)^3 * 4\pi \mathbf{k}^2 d\mathbf{k} \tag{2.37}$$

Substituting W for **k** using equation (2.31) gives:

$$D(W_0)dW = \sqrt{2}\pi^{-2}\hbar^{-3} m_e^{3/2} (W - W_g)^{1/2} dW \tag{2.38}$$

and

$$D(W_0) = \sqrt{2}\pi^{-2}\hbar^{-3}m_e^{3/2}(W - W_g)^{1/2} \tag{2.39}$$

where $D(W_0)$ is called the density of states i.e. the density of allowed energy states per unit volume.

2.4.2 Density of states for a quantum well

In a quantum well, the motion of the electrons and holes (in the direction perpendicular to the plane of the well) is described by discrete values of the wavevector component $k_{x\gamma}$, $\gamma = 1,2,3,....$ In the plane of the quantum well, the carriers are free to move, thus forming a 2-dimensional gas.

For each value of γ, the energy of the electrons is given as:

$$W_{c\gamma}(\mathbf{k}) = W_{c\gamma} + \frac{\hbar^2}{2m_e}\left(k_y^2 + k_z^2\right) \tag{2.40}$$

where the wavevector **k** is written as $\mathbf{k} = \left(k_{x\gamma}, k_y, k_z\right)$ with fixed x-components and arbitrary y and z components.

The components $k_{x\gamma}$ can be found by solving the Schrödinger equation for the particular well and finding the energy levels, $W_{c\gamma}$, and using the equation:

$$k_{x\gamma}^2 = \frac{2m_e W_{c\gamma}}{\hbar^2} \tag{2.41}$$

k_y and k_z are identical to the parabolic case

$$k_y, k_z = 0 \ , \ \pm 2\pi / L \ , \ \pm 4\pi / L \ , ... \tag{2.42}$$

The density of states is then given by:

$$D_{c\gamma}(\mathbf{k})d\mathbf{k} = \frac{2\delta(k_x - k_{x\gamma})d\mathbf{k}}{a_x(2\pi)^2} \tag{2.43}$$

where δ is the Dirac delta function, and

a_x is the width of the quantum well.

From equation (2.39), surfaces of constant energy in k-space will form circular cylinders with their axis being the k_x axis. The energy dependent density of states is then given by:

$$D_{c\gamma}(W)dW = \frac{m_e}{\pi a_x \hbar^2} dW \quad \text{for } W \geq W_{c\gamma} \tag{2.44}$$

i.e. the function $D_{c\gamma}(W)$ is constant. For each sub-band, the density of states is therefore constant so that the density of states consists of a series of steps given by

$$D_c(W) = \sum_{\gamma} D_{c\gamma}(W) = \frac{m_e}{\pi a_x \hbar^2} \sum_{\gamma} H(W - W_{c\gamma}) \tag{2.45}$$

where H is the step function

$$H(W - W_{c\gamma}) = \int_{-\infty}^{W} \delta(W' - W)dW' = \begin{cases} 1 & \text{for } W \geq W_{c\gamma} \\ 0 & \text{otherwise} \end{cases} \tag{2.46}$$

In reality the density of states does not follow a sharp step but is smeared out due to the finite width of the energy levels within the quantum wells. This leads to the step like function shown in Fig. 7 with the density of states for bulk material (3-D) and the true 2-D density of states shown for reference.

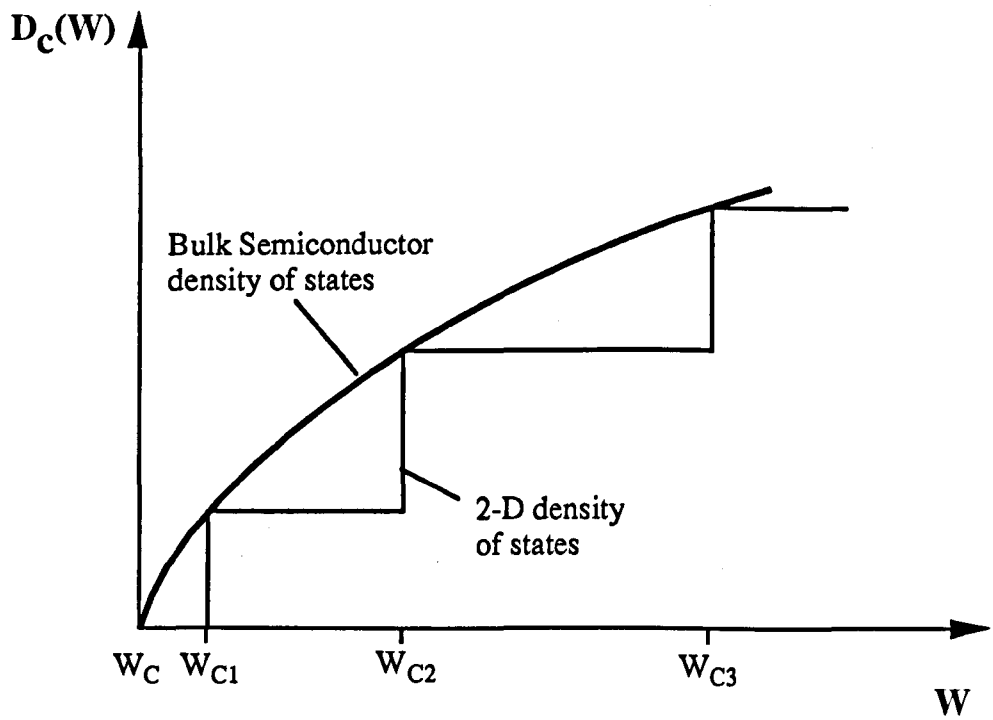

Fig. 7 Density of states for bulk material and quantum-well material

2.5 Optical Absorption

In multiple quantum well structures, interband optical absorption results when a photon excites an electron from a confined state in the valence band to a confined state in the conduction band. It is for this reason that the absorption spectrum follows the density of states function, since the electron must move from one allowed energy level to another. In addition to this condition, the transition probability must be non-zero which means that there must be a finite overlap of the wavefunctions of the initial and final states. For a quantum well which has equal confinement factors of the carriers in the conduction and valence bands (i.e. the barrier heights and the effective masses are equal) then this imposes the condition $\Delta n=0$ for an allowed transition.

2.5.1 Effect of Material Structure

The multiple quantum well structures studied in this thesis consist of InGaAs wells (≈5 nm thick) sandwiched between wider bandgap InGaAsP barriers (≈12 nm thick). The difference in bandgap between the two layers results in potential wells in both the valence band and conduction band. There is some uncertainty as to the ratio of the well depths[3], but it is of the order of 60 : 40, valence band : conduction band (i.e. the potential well in the valence band is deeper than the conduction band). Carriers in the valence band and conduction band also have different effective masses which affect the eigen-energies within the well. The carriers also have different effective masses in the wells and barriers which leads to a modification of the boundary conditions when solving the Schrödinger equation; $\frac{1}{m(x)}\left(\frac{\partial\psi}{\partial x}\right)$ must be continuous at the well/barrier interface, rather than $\left(\frac{\partial\psi}{\partial x}\right)$.

The well strength parameter (which is a measure of the confinement factor of the carrier in the potential well) is dependent on the depth of the potential well and the effective mass of the confined carriers and as a result leads to different well strengths for the electrons, light holes and heavy holes. It is the different well strengths of the hh and lh bands that leads to the degeneracy at $\mathbf{k}=0$ being lifted, since the $1/m^*$ factor in the kinetic energy term in the Hamiltonian results in the hh eigen-energies being smaller than the lh eigen-energies.

The points raised in this section lead to slight modifications of the selection rules which control the interband transitions and thus the absorption spectrum. The different well strengths mean that while eigen-functions in one well remain orthogonal, eigen-functions of different bands with $\Delta n\neq 0$ may not necessarily be

orthogonal. As a consequence, transitions of Δn=even integer are observed as weak peaks in the absorption spectrum of MQW material.

2.5.2 Excitonic Effects in MQWs

Interband optical absorption always involves the creation of an electron-hole pair which are attracted due to Coulombic forces. Since the electron and hole interact, they cannot be regarded as single particle states and therefore the concept of the exciton must be introduced. An exciton is defined as an electron-hole pair which is bound together like a hydrogen atom but free to move through the lattice. In bulk semiconductors, peaks are observed in the absorption spectra due to excitons but only at low temperatures since the weakly bound e-h pair is easily ionised by phonon interactions.

The confinement of an exciton in a quantum well modifies the spherically symmetric orbit by squashing it into the quantum well plane. The reduced average separation of the electron and hole increases the Coulombic force between them and leads to an increase in the binding energy. This increase in binding energy means the thermal energy required to ionise them increases which means that excitons can exist at room-temperature in MQW structures and thus have an important effect on the absorption spectrum of an MQW structure.

There are excitonic states associated with each step in the optical absorption spectrum with two peaks observed at the n=1 transition. The low energy peak is associated with an exciton created from an electron and a heavy-hole while the high energy peak is associated with a light-hole exciton. In general, excitons are in the 1s hydrogenic ground state and lie at an energy just below the step in the density of states function.

The binding energy for an exciton in 3-dimensions is given by:

$$B_{3D} = -\frac{e^2\mu^*}{2\varepsilon^2 h^2} \tag{2.47}$$

where μ^* is the reduced effective mass of the exciton, and

ε is the dielectric constant of the material.

In a purely 2-dimensional case, the binding energy is increased by a factor of 4 giving[4]:

$$B_{2D} = -\frac{2e^2\mu^*}{\varepsilon^2 h^2} \tag{2.48}$$

In reality, both the finite width of the quantum wells and the penetration of the electron and hole wavefunctions into the barriers results in a quasi 2D exciton with a binding energy lying somewhere between B_{2D} and B_{3D}. It is this increase in the binding energy that allows excitons to be observable at room temperature in MQW structures.

2.5.3 Polarisation Dependence Of Absorption Spectra

The absorption spectrum of an MQW structure is polarisation dependent. For light which is polarised in the plane of the wells (TE), two excitonic peaks are observed; one associated with the heavy-hole band $|3/2,\pm3/2\rangle$ and a second associated with the light-hole band $|3/2,\pm1/2\rangle$. The relative absorption strengths of the peaks are 3:1 for the heavy and light holes respectively. For light polarised perpendicular to the plane of the wells (TM), there is only one peak observed, corresponding to the light hole exciton which gives relative absorption strengths of 0:1 for the heavy and light hole transitions. These selection rules are related to crystal symmetry and can be explained in terms of the transition matrix elements.

2.6 The Effect Of An Electric Field On The Properties Of Quantum Wells

The previous sections in this chapter have dealt with analysis of the properties of quantum wells with no applied electric field. By applying an electric field, the properties of quantum wells can be radically changed, which can be utilised in different optoelectronic components. The electric field can be applied either parallel to the plane of the wells or, more usefully, perpendicularly. Before analysing the effect an electric field has on an MQW structure it is worth examining the effect on bulk semiconductor.

2.6.1 The Franz-Keldysh Effect In Bulk Semiconductors

When a large DC electric field ($\approx 10^5$ Vcm^{-1}) is applied to a semiconductor, the optical absorption edge broadens, causing a tail in the absorption spectrum at energies below the band edge and oscillations in the absorption spectrum at energies above the band edge[5]. This effect is known as the Franz-Keldysh effect[6].

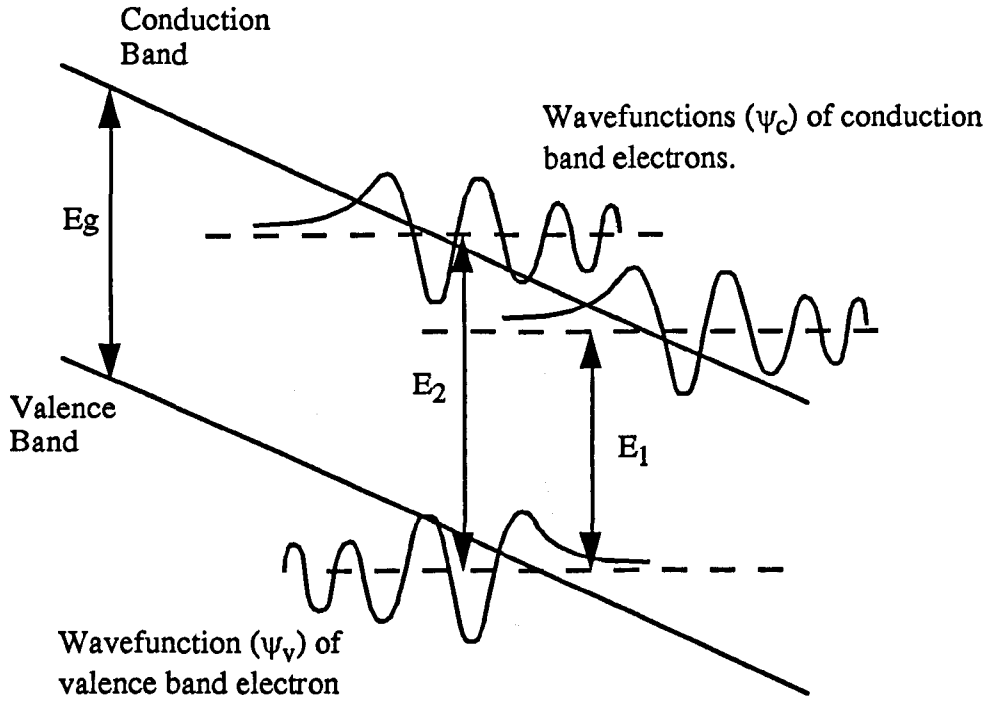

Fig. 8 Wavefunctions of electrons in valence and conduction bands under an applied electric field

The effective decrease in the band gap can be explained in terms of photon assisted tunnelling of electrons from the valence band to the conduction band. In the presence of an electric field, the bands tilt but remain parallel and with the same vertical bandgap as shown in Fig. 8. The wavefunction of the carriers in the conduction and valence bands are now asymmetric, decaying into the band gap and oscillating into the bands. It is apparent from the wavefunctions that an electron can be excited from the valence band to the conduction band by a photon whose energy, E_1, is less than the vertical band gap, E_g. The electron can also be excited from a region where the wavefunction is oscillatory by a photon with energy, E_2, greater than the band gap, giving rise to the oscillations observed in the absorption spectrum.

2.6.2 Electric Field Perpendicular to the Plane of the Quantum Wells

When an electric field is applied perpendicular to the plane of the quantum wells, the change in absorption is radically different to changes observed when the field is parallel to the plane of the quantum wells or to that for bulk semiconductors. The effect which is observed is called the Quantum Confined Stark Effect (QCSE) and is shown schematically in Fig. 9.

In section (2.2.2) it was shown that carriers in a finite potential well exist at discrete energies given by the solution to the time-independent Schrödinger equation

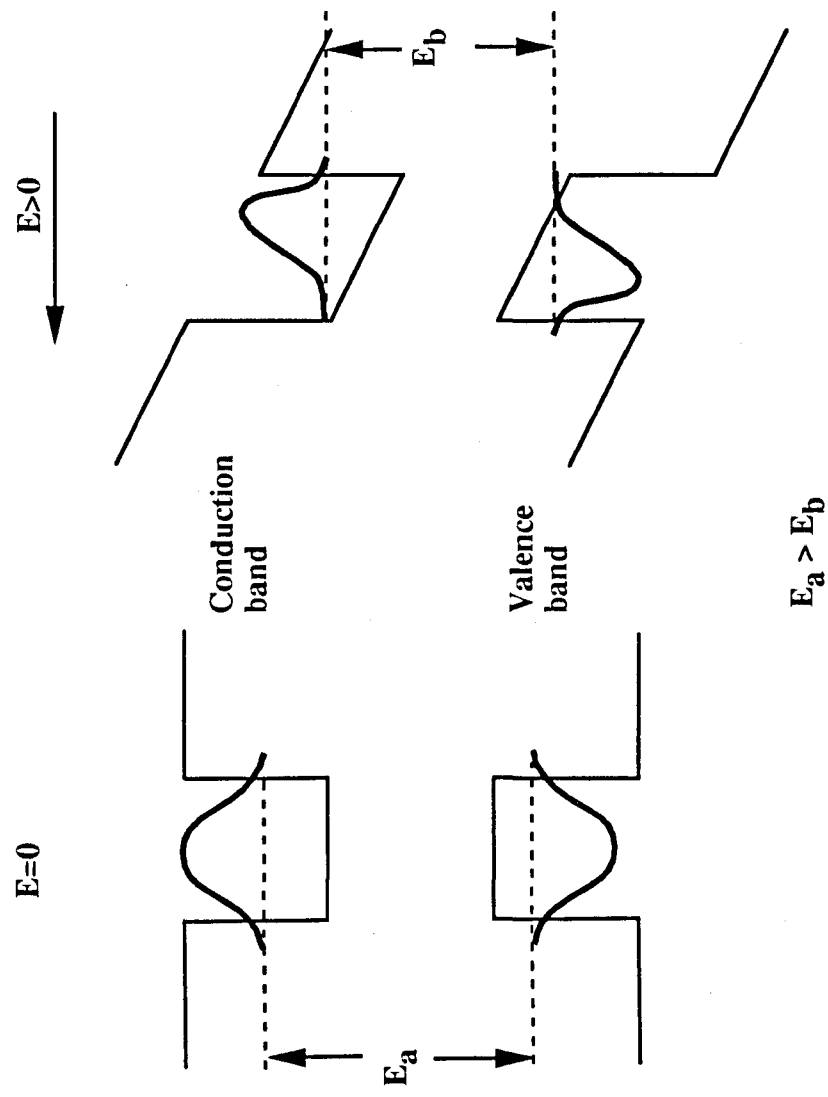

Fig. 9 Quantum Confined Stark Effect

(2.10). When an electric field is applied normal to the plane of the quantum wells, the bands slope (as shown in Fig. 9) with Eq. (2.12) now redefined as:

$$\begin{aligned} -\frac{\hbar^2}{2m_e(x)}\frac{\partial^2\psi}{\partial x^2} &= eF_x x + W\psi \quad \text{for } |x| < a \\ -\frac{\hbar^2}{2m_e(x)}\frac{\partial^2\psi}{\partial x^2} &= eF_x x + (W - U_0)\psi \quad \text{for } |x| > a \end{aligned} \tag{2.49}$$

where e is the electronic charge, and

F_x is the electric field.

Solving equations (2.49) yields wavefunctions which have been displaced to the lower energy sides of the well (i.e. the electron wavefunction has moved in the direction of the field and the hole wavefunction has moved in the opposite direction). Another important consequence of the electric field is that the eigen-energies in the wells have changed, with the effective bandgap being reduced. This change in bandgap moves the absorption edge to lower energies, with the shift being proportional to the square of the applied electric field. This is the effect known as the Quantum Confined Stark Effect (QCSE).

The main features of the QCSE are that the exciton associated with the n=1 transition moves to lower energies[7] and that the exciton resonances remain resolvable for electric field strengths of up to 50 times the classical exciton ionisation field[8].

The asymmetry of the wavefunctions introduced by the field causes a reduction in the overlap and thus reduces the oscillator strength of the absorption. By the same argument, the overlap (and oscillator strength) for transitions with $\Delta n \neq 0$ increases with field, thus increasing the absorption. The asymmetry in the wavefunctions will cause the absorption edge to broaden in a manner similar to that for bulk semiconductor. This effect is called the Quantum Confined Franz-Keldysh effect (QCFKE).

---

1 Integrated Optoelectronics, K.J. Ebeling, Springer-Verlag

2 GaInAsP Alloy Semiconductors, T.P. Pearsall, Wiley & Sons, New York, 1982, p 295

3 Properties of Lattice matched and strained InGaAs, INSPEC EMIS Data Review Series, No. 8,

4 D.S. Chemla, D.A.B. Miller, P.W. Smith, A.C. Gossard, W. Wiegman, IEEE J. Quantum Electron., **20**, p265, 1984

5 J.D. Dow, D. Renfield, Phys. Rev. B, **1**, p3358, 1970

6 L.V. Keldysh, Sov. Phys., JETP, **34**(7), p788, 1958

7 M. Whitehead, G. Parry, K. Woodbridge, P.J. Dobson, G. Duggan, Appl. Phys. Lett., **52**, p345, 1988

8 D.A.B. Miller, D.S. Chemla, T.C. Damen, A.C. Gossard, W. Weigmann, T.H. Wood, C.A. Burrus, Appl. Phys. Lett., **45**, p13, 1984

Chapter 3 Photoabsorption Induced Disordering

3.1 Introduction

Laser induced disordering processes are unlike any other quantum well intermixing process in that they rely entirely on using the temperature dependence alone of the diffusion coefficient to produce preferential intermixing across a wafer. All other intermixing processes rely on changing the diffusion coefficient in some way, and using a constant temperature to produce areas of different bandgap on a wafer. Photoabsorption Induced Disordering (PAID), however, is unique amongst laser induced intermixing processes in that it is aimed at processing large areas of material.

For this reason, there are several important considerations in understanding the PAID process. For example: what are the mechanisms which produce heat in the material when being irradiated with a laser and, perhaps more importantly, what does that heat do after it is generated?

This chapter will describe the experimental procedure used to intermix multiple quantum well structures by PAID. The processes involved in heating semiconductor material using a laser will be discussed, along with the thermal properties of semiconductors.

The potential profile of the quantum wells is also investigated with a brief explanation given as to how changes in the photoluminescence emission wavelength of multiple quantum well material can be related to the amount of intermixing.

3.2 Experimental Arrangement

The experimental set-up for intermixing material using PAID is shown in Fig. 1. The laser used in PAID was a CW operated Spectron Nd:YAG solid state laser shown schematically in Fig. 2. The laser can operate at either 1064 nm or 1320 nm depending on the mirror set used but was used exclusively at 1064 nm in this work.

The YAG rod of the Spectron laser is flashlamp pumped and water cooled. The rear mirror (which is dielectric coated) is approximately 99 % reflecting while the output coupler is approximately 95 % reflecting. Inside the optical cavity, there is a mount which allows various diameters of aperture to be placed, which controls the transverse mode profile of the beam. All work carried out in this thesis involved using the largest possible aperture (to maximise the power), with the resultant beam being multimoded in the transverse direction. There is also a mount which holds an

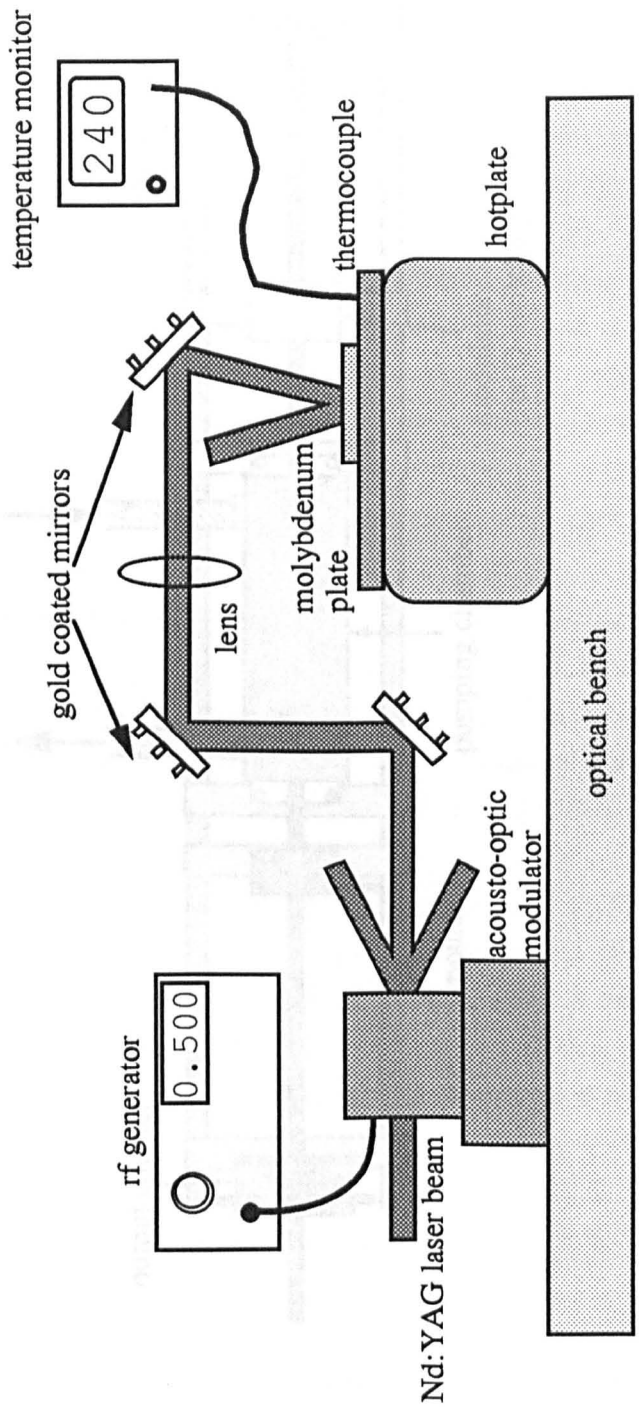

Fig. 1 Experimental set-up used in the PAID process

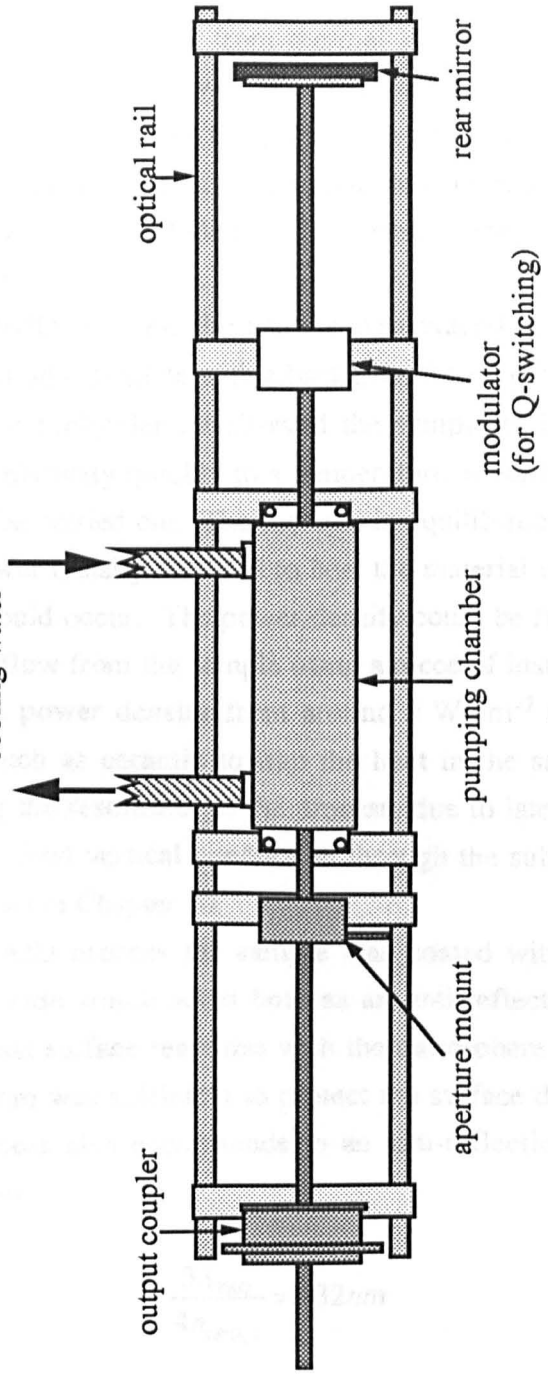

Fig. 2 Schematic diagram of Spectron Nd:YAG laser

intra-cavity acousto-optic modulator which allows the laser to be Q-switched, although the modulator was not used during this work.

Since Nd:YAG lasers suffer from thermal lensing (which causes the beam divergence to increase at higher powers), an external acousto-optic modulator was used to control the beam power. The beam direction was controlled using gold coated mirrors on kinematic mounts which allowed accurate control of the beam position on the sample. A lens was also included in the system, depending on the beam size required at the sample.

During the PAID process, the sample was placed on a piece of polished molybdenum and then on a hotplate with a background temperature of around 240°C. The use of a piece of molybdenum allowed the sample to be removed from the hotplate and cooled relatively quickly to a temperature at which photoluminescence measurements could be carried out. The increase in equilibrium temperature reduced the incident laser power density required to heat the material up to a temperature at which intermixing would occur. The power density could be further reduced simply by reducing the heat flow from the sample using a piece of insulating ceramic. This reduced the required power density from around 5 Wmm^{-2} to around 1 Wmm^{-2}. Using an insulator such as ceramic to trap the heat in the sample has the effect, however, of reducing the resolution of the process, due to lateral conduction of the heat instead of the desired vertical conduction through the substrate. This effect is discussed in more detail in Chapter 10.

During the PAID process the sample was coated with a layer of plasma-deposited silicon dioxide which acted both as an anti-reflection coating and as a protective layer against surface reactions with the atmosphere. It was found that a layer of around 500 nm was sufficient to protect the surface during the disordering process. This thickness also corresponds to an anti-reflection coating since it is approximately equal to:

$$\frac{3\lambda_{YAG}}{4n_{(SiO_2)}} = 532nm$$

If the layer was thinner, then it tended to crack open at high temperatures, exposing the material to the air and causing surface reactions. The reason for it cracking open was due to the fact that the thermal expansion coefficient of the epitaxial material is an order of magnitude greater than that of the silicon dioxide which meant that, at high temperatures, the silicon dioxide could not withstand the strain caused by the expanding material.

3.3 Photoluminescence Measurements

Photoluminescence measurements were carried out relatively simply using the same Nd:YAG laser as that used to intermix the material. The set-up is shown schematically in Fig. 3. The laser beam used was the first diffracted order from the acousto-optic modulator, at a power level of approximately 50 mW coupled into a multimode fibre using a X10 microscope objective lens. By gluing the sample to the multimode fibre, the photoluminescence spectra could be measured at both room temperature and at 77 K (by immersing the sample in liquid nitrogen). The spectrum was measured by an Advantest Optical Spectrum Analyser.

3.4 Absorption of light in a semiconductor

The absorption of light by semiconductor material is substantially dependent on the bandgap of the different epi-layers within the structure. This means that, for any appreciable absorption to take place, the material must not be transparent to the laser irradiation.

Fig. 4 shows the bandgap of different layers within a typical InGaAs(P) multiple quantum well laser structure. Also indicated is the photon energy of the incident laser radiation from a Nd:YAG laser (λ = 1064 nm). From this diagram it is obvious that absorption should only take place within the active region, with the indium phosphide substrate and cladding layers being effectively transparent.

Absorption in the active region will cause electrons to be promoted from the valence band to empty states in the conduction band.

3.5 Generation of heat inside a Semiconductor

3.5.1 Debye Temperature

An important quantity when dealing with thermal conduction is the Debye temperature of the material. This temperature, θ_D, is defined as:

$$\theta_D = \frac{\hbar \omega_{max}}{k_B} \tag{3.1}$$

where $\hbar$ is Planck's constant,

ω_{max} is the maximum frequency of atomic vibrations in the crystal lattice, and

k_B is Boltzmann's constant.

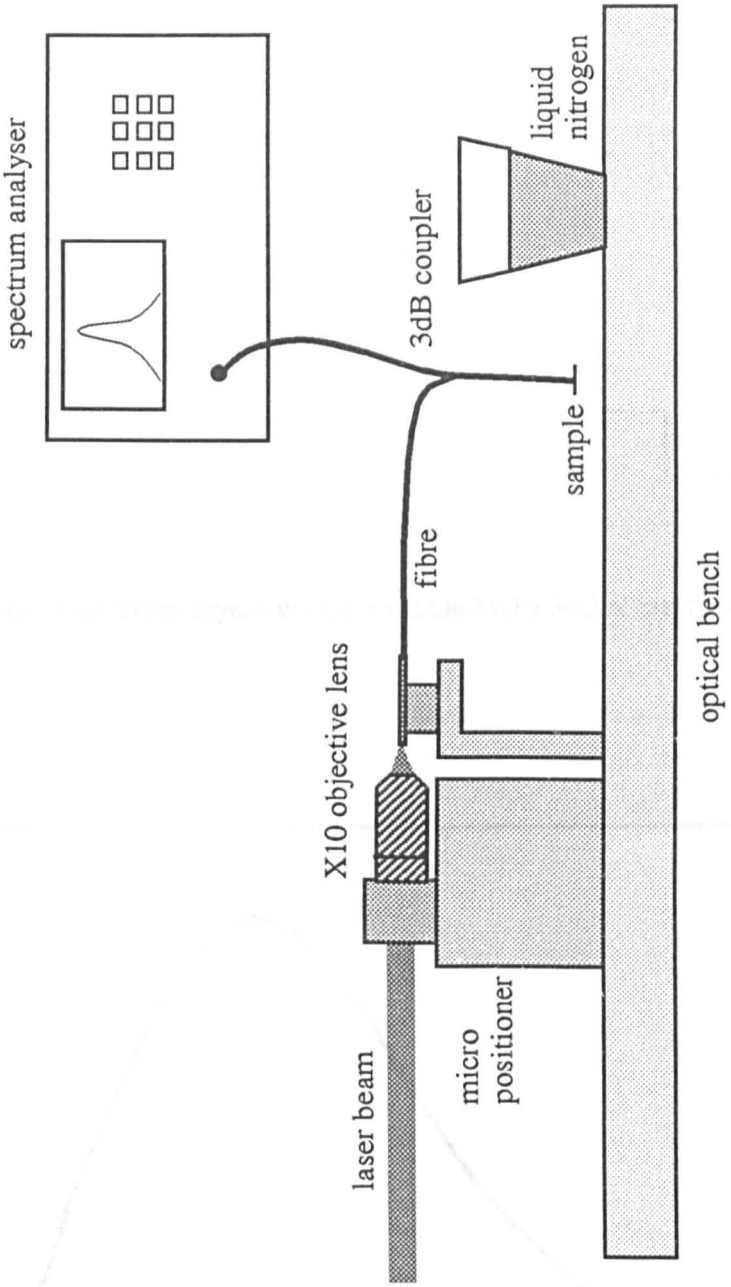

Fig. 3 Experimental set-up for measuring PL spectra

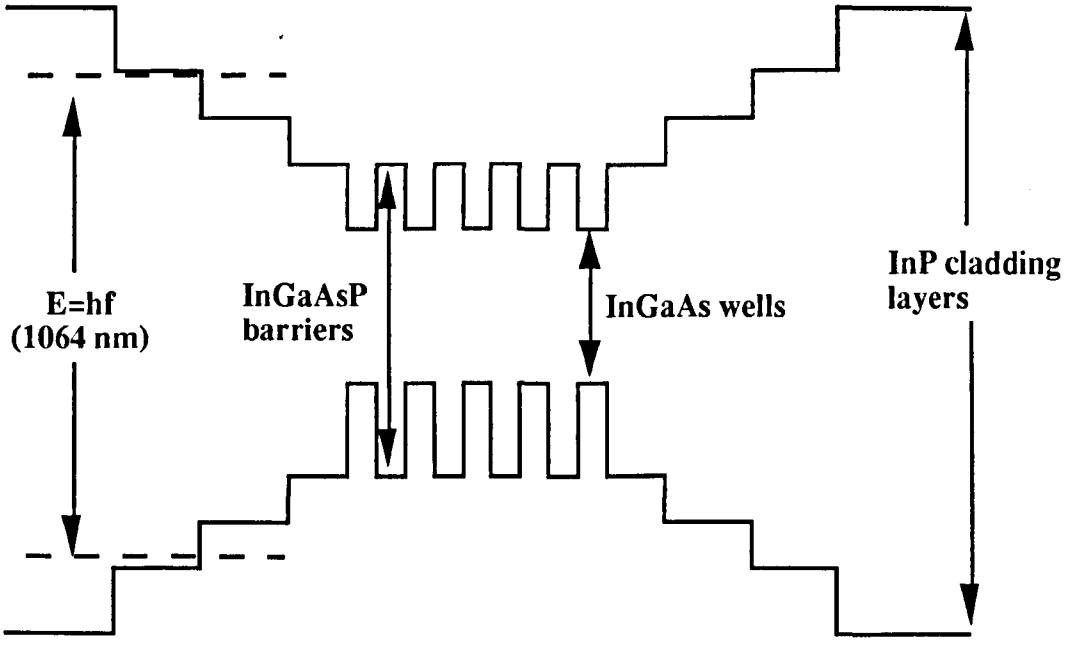

Fig.4 Bandgap of different layers within an InGaAs(P) MQW laser structure

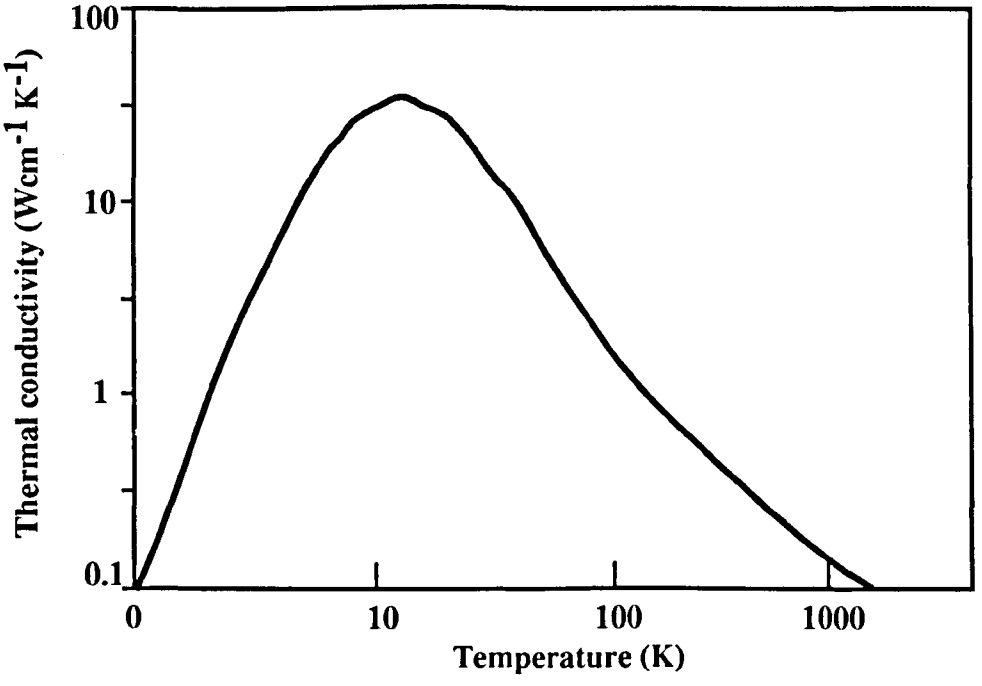

Fig.5 Thermal conductivity as a function of temperature of InP

The Debye temperature can be regarded as a measure of the maximum frequency of atomic vibrations[1] within a crystal lattice For a material with a high θ_D there is a large ratio of interatomic force to the atomic mass. Of course, there will be a temperature dependent spectral range of vibrational frequencies in the crystal lattice. For temperatures which are well above the Debye temperature, most of the oscillators in the system will vibrate with frequency equal or close to ω_{max}.

Typical values of θ_D for semiconductors are of the order of a few hundred Kelvin. In indium phosphide[2], the Debye temperature is 460 K which means that the maximum frequency of oscillation in the system is approximately 10^{13} Hz, calculated from Eq. (3.1).

3.5.2 Carrier Cooling

The electrons which are promoted to the conduction band by the laser radiation will cool rapidly, giving up their energy to the crystal lattice through electron-phonon collisions[3].

Due to the large difference between electron and phonon energies, the energy exchange typically requires several collisions between the electrons and phonons and occurs on a time scale of the order of a few picoseconds. For example, an electron which absorbs a photon with wavelength, λ = 1064 nm, will gain energy given by:

$$E = \frac{hc}{\lambda} \tag{3.2}$$

where h is Planck's constant,
c is the speed of light in a vacuum, and
λ is the wavelength in free-space.

which is equal to 1.165 eV.

This means that an electron at the top of the valence band will be promoted high into the conduction band, since the bandgap of the multiple quantum well active region is only 800 meV (1550 nm) at room temperature. Now the energy of a phonon is simply given by:

$$E = hf \tag{3.3}$$

where h is Planck's constant, and
f is the frequency of the phonon vibration

This means that in indium phosphide at temperatures of around 700°C to 800°C (i.e. $T \gg \theta_D$) the typical energy of a phonon is 41 meV (since most phonons will have a frequency approaching 10^{13} Hz). This means that an electron will require to interact with approximately 9 phonons to give up energy before reaching the bottom of the conduction band.

The process is obviously more complicated than this for several reasons. Firstly, as electrons are raised into the conduction band there will be a reduction in the number of filled states at the top of the valence band. This means that electrons will be promoted from energies deeper in the valence band to lower levels in the conduction band, implying that they have less free energy to give to the lattice. There is also the possibility that free electrons in the conduction band will absorb the laser radiation thus removing the need to overcome the bandgap. Another consideration is that, as the temperature is increased, the bandgap of the multiple quantum well active region will become smaller as the width of the quantum wells increases due to thermal expansion. This effective bandgap decrease will have the effect of promoting electrons to higher states in the conduction band and also increasing the thermal energy that they pass to the lattice.

After the electron has "cooled" and occupies a state at the bottom of the conduction band, it will recombine with a hole in the valence band and either emit a photon or not. The probability of a photon being emitted is defined as the internal quantum efficiency of the material and is typically around 80 % in the InP based material system. For the 20 % of occasions in which there is no photon emitted, the electron and hole are said to recombine non-radiatively. This can be due to imperfections in the material or different non-radiative processes such as Auger recombination or intra-valence band absorption. Since energy and momentum must be conserved, these recombinations also contribute to heating the crystal lattice.

Of course, the photons emitted by the e-h recombination may themselves be re-absorbed and contribute to lattice heating. This process is known as photon recycling and has been observed in InP[4]. The typical recombination time for an electron in an InGaAs(P) multiple quantum well structure is of the order of nanoseconds which means that an electron on average has "plenty of time" to transfer its energy to the lattice before recombining. If this is considered with the value of 80 % for the internal efficiency of the material, then it can be assumed that carrier cooling is the dominant heat generation process in laser-irradiated material.

This energy exchange between the electrons and the lattice causes the material to heat up, with a steady-state temperature reached in the order of a second.

3.6 Thermal Conduction in Semiconductors

In semiconductors, various carriers can contribute to the thermal conductivity[5] including phonons, electrons, and holes.

Phonons are the main contributor to the thermal conductivity in most semiconductors and it useful to describe them briefly. A phonon is a quantized mode of vibration in a crystal lattice and involves collective vibrations from the entire atomic system. These vibrations take the form of displacement waves in the volume of the crystal which produce coupled simple harmonic motion of the individual atoms. The thermal conductivity can be thought of as the propagation of these displacement waves through the lattice.

Due to the periodicity of the crystal lattice, phonons have a similar band structure to electrons although it is somewhat more complicated since phonons are polarised. In crystals with more than one type of atom per unit cell (as in the case of most semiconductors) the dispersion relationship for phonons is quite complicated. Different branches of the dispersion relation exist as a result of atoms of different mass being present in the lattice and this leads to the definition of acoustic and optic phonons.

For a given direction in a crystal lattice (e.g. [100]) the acoustic and optic phonons can both propagate in three modes, one being longitudinal and the other two being transverse. The longitudinal mode is similar to a sound wave with the atoms moving backward and forward in the direction of propagation, giving alternating areas of compression and expansion. For the transverse modes, the atoms vibrate in a plane normal to the direction of propagation and are orthogonal, as in the case of electromagnetic waves.

In a perfect crystal with completely elastic binding forces between atoms, free from defects, and boundless in size, the thermal conductivity would be infinite. In real crystals however, the atoms are not in perfect harmonic motion due to anharmonic mechanisms which determine the maximum value of thermal conductivity and how it varies with temperature. Fig. 5 shows a curve of thermal conductivity vs. temperature which is typical of virtually all semiconductors.

A simple expression for the thermal conductivity can be given as:

$$k = \frac{1}{3} C v l \tag{3.4}$$

where k is the thermal conductivity in units of $Wm^{-1}K^{-1}$,

C is the specific heat capacity of the material in units of $JKg^{-1}K^{-1}$,

v is the propagation velocity, and

l is the mean free path of the excitation.

The effective mean free path, l, is defined as the average distance an excitation (phonon, photon, or electron) will travel before being scattered and can be expressed as:

$$\frac{1}{l} = \sum_j \frac{1}{l_j} \tag{3.5}$$

where l_j is the average distance travelled between collisions due to the j_{th} scattering process. Examples of these scattering processes are impurity scattering, isotopic scattering, defect scattering, and phonon scattering. If there are several types of excitation contributing to the conductivity, then k is simply the sum of each. Reference 3 contains much more detailed maths regarding Eq. (3.4) and (3.5), and supplies values for the relaxation times for different scattering mechanisms

The thermal conductivity is zero at 0 K and rises approximately exponentially to a maximum at around 20 K due to the increase in specific heat capacity[6]. The maximum value of thermal conductivity depends on the imperfections and impurities within the material. Above 20 K the thermal conductivity drops due to other scattering mechanisms which have the effect of reducing the scattering length of the excitations. As the temperature increases, the phonons begin to scatter each other to a significant extent, thereby further reducing the mean free path length and, consequently, the conductivity. At high temperatures, the conductivity decreases approximately as 1/T, due to three phonon scattering.

Contributions to the thermal conductivity from electrons (and holes) in semiconductors[7] becomes important only at temperatures well above the Debye temperature. At these temperatures and above, the conductivity due to electrons and holes in the lattice will be of the same order of magnitude as the conductivity due to phonons.

3.6.1 Effect of Doping

Highly doped semiconductors with carrier concentrations around 10^{18} cm^{-3} to 10^{19} cm^{-3} have a lower thermal conductivity than undoped semiconductors[8]. While the extra carriers might be expected to contribute to the thermal conductivity, they actually have the effect of increasing both impurity scattering and electron-phonon scattering, with the overall effect of reducing the conductivity by as much as 30 % in

heavily doped material. A simple approximation is that the conductivity drops by a factor of 8 % for every decade of doping above 3.10^{15} cm^{-3}.

3.6.2 Thermal Conductivity of Indium Phosphide

The temperature dependence of the thermal conductivity of indium phosphide is similar to that shown in Fig. 5, with a maximum occurring between 10 K and 20 K. Above 60 K the conductivity is well described by:

$$k=AT^{-n} \tag{3.6}$$

with values of A=2890 and n=1.45 given in the literature[9]. Eq. (3.6) gives a room temperature thermal conductivity of 0.74 $Wcm^{-1}K^{-1}$ for undoped indium phosphide. Fig. 6 shows the thermal conductivity for temperatures up to 1000 K which indicates that there is a massive reduction in thermal conductivity at elevated temperatures. The Debye temperature for InP is about 460 K, which means that electrons and holes will contribute significantly to the thermal conductivity only at these temperatures and above.

Experimentally measured values[10,11,12] for the thermal conductivity give a mean of 0.74 ± 0.1 $Wcm^{-1}K^{-1}$ with the reason for such a range in measured values being attributed to material purity and stoichiometry. Adachi[13] gives a room temperature calculated value of 0.68 $Wcm^{-1}K^{-1}$.

3.6.3 Thermal Conductivity of Ternary and Quaternary Alloys of InGaAsP

It is also useful to know how the thermal conductivity of the different layers within the epitaxial structure vary with respect to their atomic composition. It was stated in section (3.6.1) that introducing large numbers of foreign atoms to the host lattice (such as doping) has the effect of reducing the thermal conductivity. The formation of ternary and quaternary alloys can also be regarded as introducing foreign atoms to a simple compound at a high level. For example, indium phosphide is a simple binary compound which has a relatively high thermal conductivity (approximately 60 % higher than gallium arsenide[14]). However, when this compound forms an alloy with gallium and arsenic atoms to form InGaAs(P), the thermal conductivity drops dramatically. This drop is due to an increase in anharmonicity between the atoms in the lattice as a result of atoms of different masses being present in the crystal. Another reason for the conductivity to drop is the random position of the atoms in the lattice, especially when considering quaternary compounds.

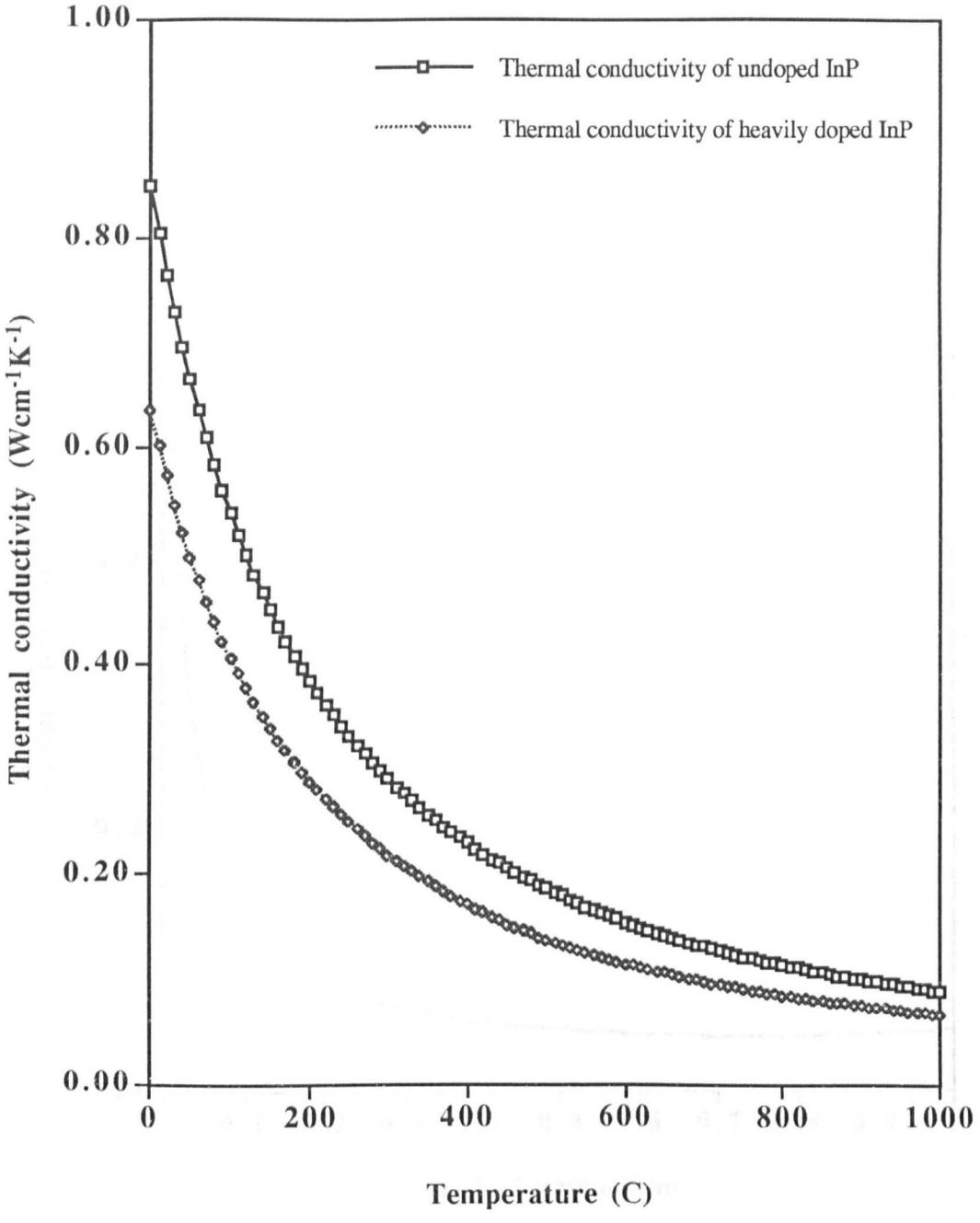

Fig.6 Thermal conductivity of doped and undoped InP
as a function of temperature

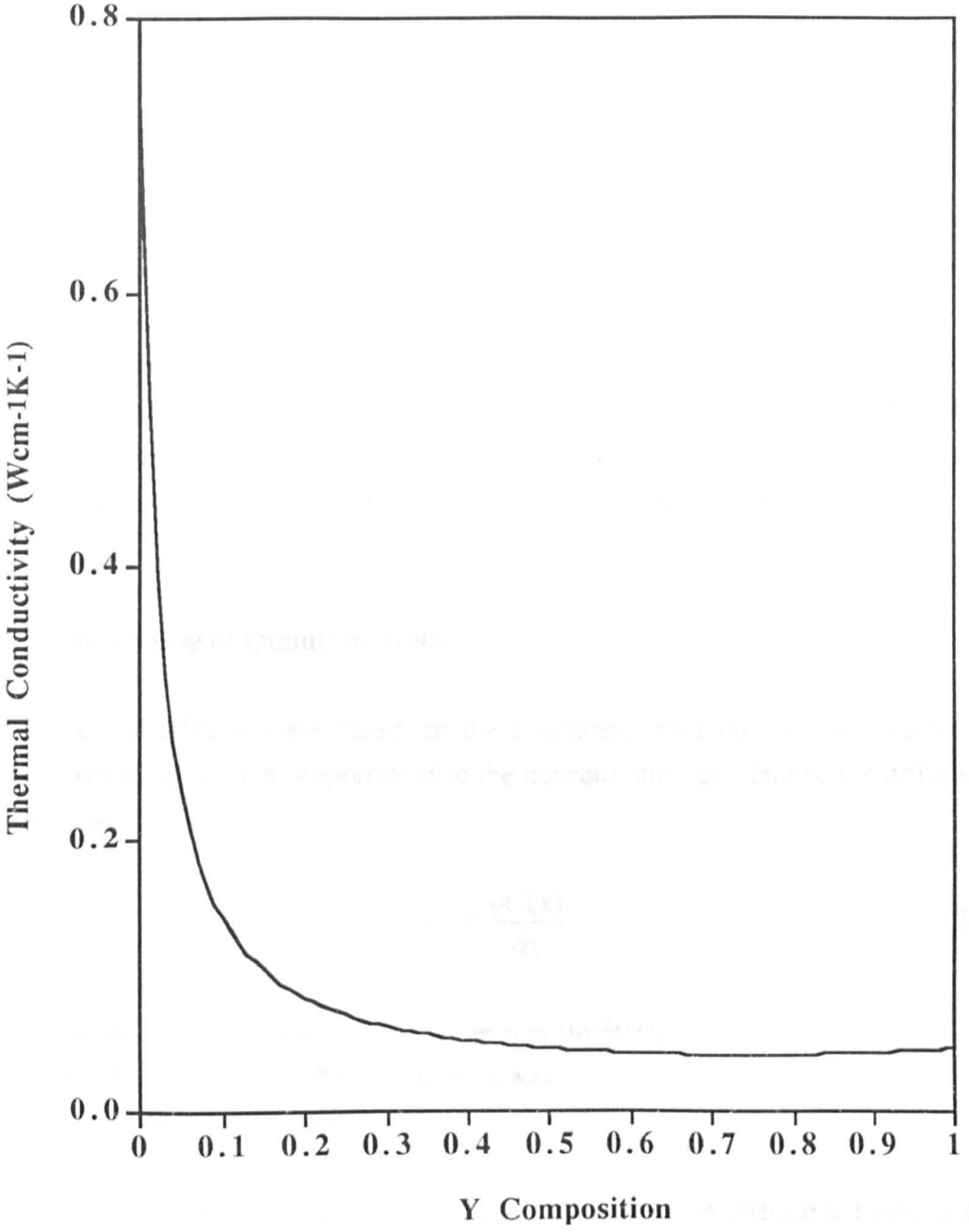

Fig. 7 Thermal conductivity of $In_{1-x}Ga_xAs_yP_{1-y}$ lattice matched to InP

Fig. 7 shows the change in thermal conductivity as a function of y for $In_{1-x}Ga_xAs_yP_{1-y}$ alloys lattice matched to InP and shows that the minimum conductivity occurs at approximately y = 0.75. At y = 0 the composition is InP, while at y=1 the composition is $In_{0.53}Ga_{0.47}As$. This is a theoretical curve predicted by Adachi[15].

Although there is a large difference between the thermal conductivity of the different compositions, this will only affect heat transfer problems which are either on a very small scale (such as focused laser beam writing) or problems which are transient in nature (such as pulsed laser irradiation). This is because the layers with ternary or quaternary compositions in the MQW structures under investigation here are very thin compared to the substrate. This structural factor means that such layers then have negligible thermal resistance and will not greatly affect the heat flow.

3.7 Intermixing of Quantum Wells

Fick's laws of diffusion are based on the hypothesis that the rate of transfer of diffusant across an area is proportional to the concentration gradient of the diffusant. This leads to:

$$F = -D\frac{\partial C(x)}{\partial x} \tag{3.7}$$

where F is the rate of diffusant crossing the area ($m^{-2}s^{-1}$),
D is the diffusion coefficient (m^2s^{-1}), and
C(x) is the concentration (m^{-3})

The negative sign arises from the convention that the diffusants move in the direction of negative gradient. This is Fick's first law of diffusion in 1-dimension.

By considering diffusion through a unit volume and using equation (3.7), Fick's second law can be written as:

$$\frac{\partial C}{\partial t} = D\frac{\partial^2 C(x)}{\partial x^2} \tag{3.8}$$

Since we are dealing with quantum wells, it is possible to disregard diffusion in the y and z directions where the composition is constant, so the 1-dimensional equations are adequate. A solution to Eq. (3.8) is:

$$C(x) = \frac{A}{\sqrt{t}} \exp\left(\frac{-x^2}{4Dt}\right) \tag{3.9}$$

where A is a constant. Eq. (3.9) represents the diffusion from an infinite source at x=0 with the diffusion profile being symmetric about $x = 0$. The total amount of diffusant per unit area is then given by:

$$\begin{aligned} M &= \int_{-\infty}^{\infty} C(x)dx \\ &= 2A\sqrt{\pi D} \end{aligned} \tag{3.10}$$

where M is the total amount of diffusant present at $x = 0$ and $t = 0$.
Substituting Eq. (3.10) into Eq. (3.9) then gives:

$$C(x) = \frac{M}{2\sqrt{\pi Dt}} \exp\left(\frac{-x^2}{4Dt}\right) \tag{3.11}$$

which represents the solution to the diffusion equation for a total amount of substance M deposited at a surface at $x = 0$ and $t = 0$. In the case of quantum wells the source is also finite in width (in the x-direction), but this can be modelled by using an infinite number of line sources, as shown in Fig. 8. The total amount of diffusant per unit area for each strip is given by $C_0\delta\zeta$. The concentration of diffusant at a point P due to the highlighted strip is then given by:

$$C = \frac{C_0\delta\zeta}{2\sqrt{\pi Dt}} \exp\left(\frac{-\zeta^2}{4Dt}\right) \tag{3.12}$$

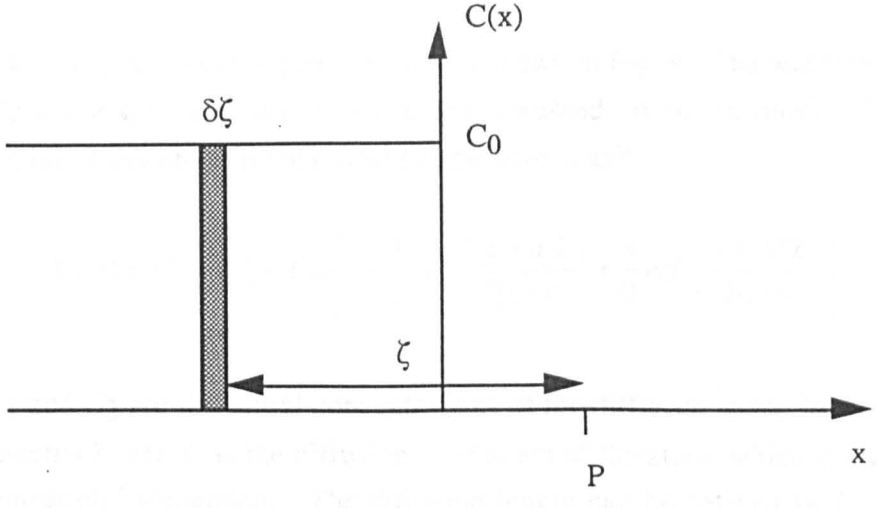

Fig. 8 Diffusion model used to find the concentration profile for an intermixed quantum well

The total concentration at point P is found by integrating over all the line sources in the region $-\infty < x < 0$. The result of the integration can be expressed in terms of the complementary error function, (erfc):

$$C(x,t) = \frac{C_0}{2}\mathrm{erfc}\frac{x}{2\sqrt{Dt}} \tag{3.13}$$

where

$$\mathrm{erfc}(x) \equiv 1 - \frac{2}{\sqrt{\pi}}\int_0^x \exp(-y^2)dy \tag{3.14}$$

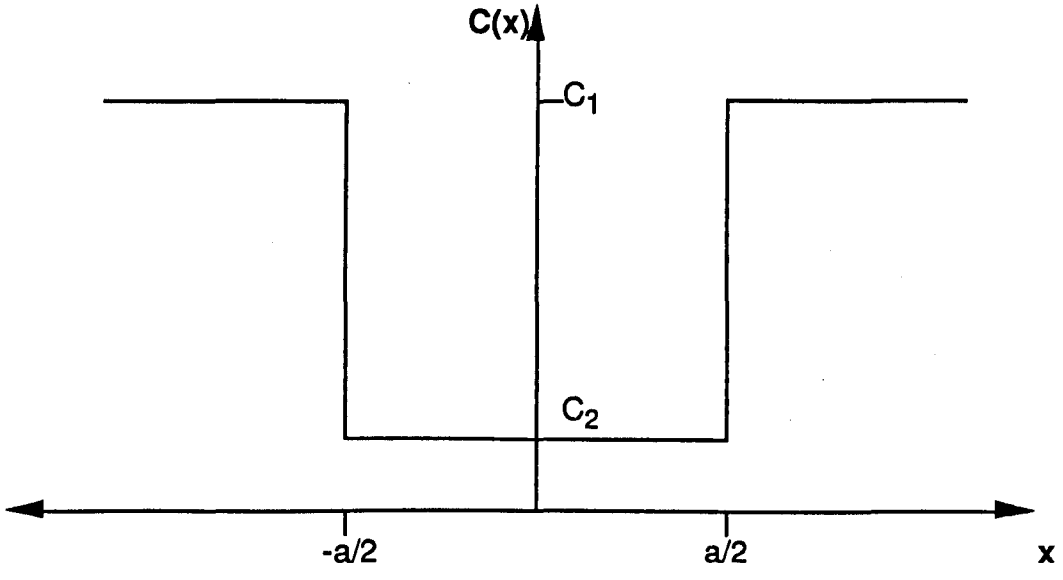

Fig. 9 Concentration profile of diffusing atom in quantum well and surrounding barrier before intermixing

The simplest way to model a quantum well is shown in Fig. 9. The width of the well is a ($-a/2 < x < a/2$) and the barriers are assumed to be infinite. The final concentration of any atom in the model can be written as[16]:

$$C(x,t) = C_2 + (C_1 - C_2)\left[1 - \frac{1}{2}erfc\left(\frac{x + a/2}{2\sqrt{Dt}}\right) + \frac{1}{2}erfc\left(\frac{x - a/2}{2\sqrt{Dt}}\right)\right] \tag{3.15}$$

where C_1 and C_2 are the initial concentrations of the diffusant in the barrier and the well, respectively and D is the diffusion coefficient of the atom, which is assumed to be concentration independent. The diffusion length can be defined as $L_D = 2\sqrt{Dt}$. Eq. (3.15) holds provided that the width of the well (a) is large compared to the

diffusion length, so that no diffusing species can migrate from one barrier through the well to the other barrier. Fig. 10 shows an 80 Å quantum well at different stages of intermixing corresponding to three different diffusion lengths of 20Å, 40Å, and 60 Å. The limit of this model is around 40 Å, at which point the diffusing species reach the opposite barrier with a concentration of around 5 %. Above this limit, the problem becomes more complex and requires a more complicated, Green's function[17,18] approach.

3.8 Calculation Of Energy Levels In A Disordered Quantum Well

The simplest way to model the PAID process in a quantum well of $In_{0.53}Ga_{0.47}As$ with barriers of InGaAsP is to look at the diffusion of the phosphorus from the barriers to the well. For a given diffusion length ($=2\sqrt{Dt}$), the final phosphorus concentration can be found using Eq. (3.15). If the material is assumed to remain lattice-matched throughout the intermixing process i.e. the diffusion coefficients of the two sublattices are equal ($D_{III} \approx D_V$), then it is simple to calculate the quaternary composition ($In_{1-x}Ga_xAs_yP_{1-y}$) as a function of position using Vergard's Law[19]. Using this composition profile, the bandgap of the quantum well can be deduced from Ref. 20. The conduction and valence band discontinuities are then used to determine the energy profile for the respective bands. The energy levels can now be found for the conduction and valence bands using the time independent Schrödinger Equation (described in Chapter 2), taking care to define the effective mass of the carriers as a function of material composition.

3.9 Advantages of PAID

Photo Absorption Induced Disordering has several advantages over other forms of intermixing processes.

1) The process is not restricted to near surface layers. This is because the laser is only absorbed in the active region of the multiple quantum well material as discussed in section (3.4), with the cladding layers being transparent. Impurity Induced Disordering (IID)[21] which relies on ion implantation is limited by the stopping range of the ions in the material while Impurity Free Vacancy Disordering (IFVD) is limited by the diffusion length of the vacancies generated in the cap layers.

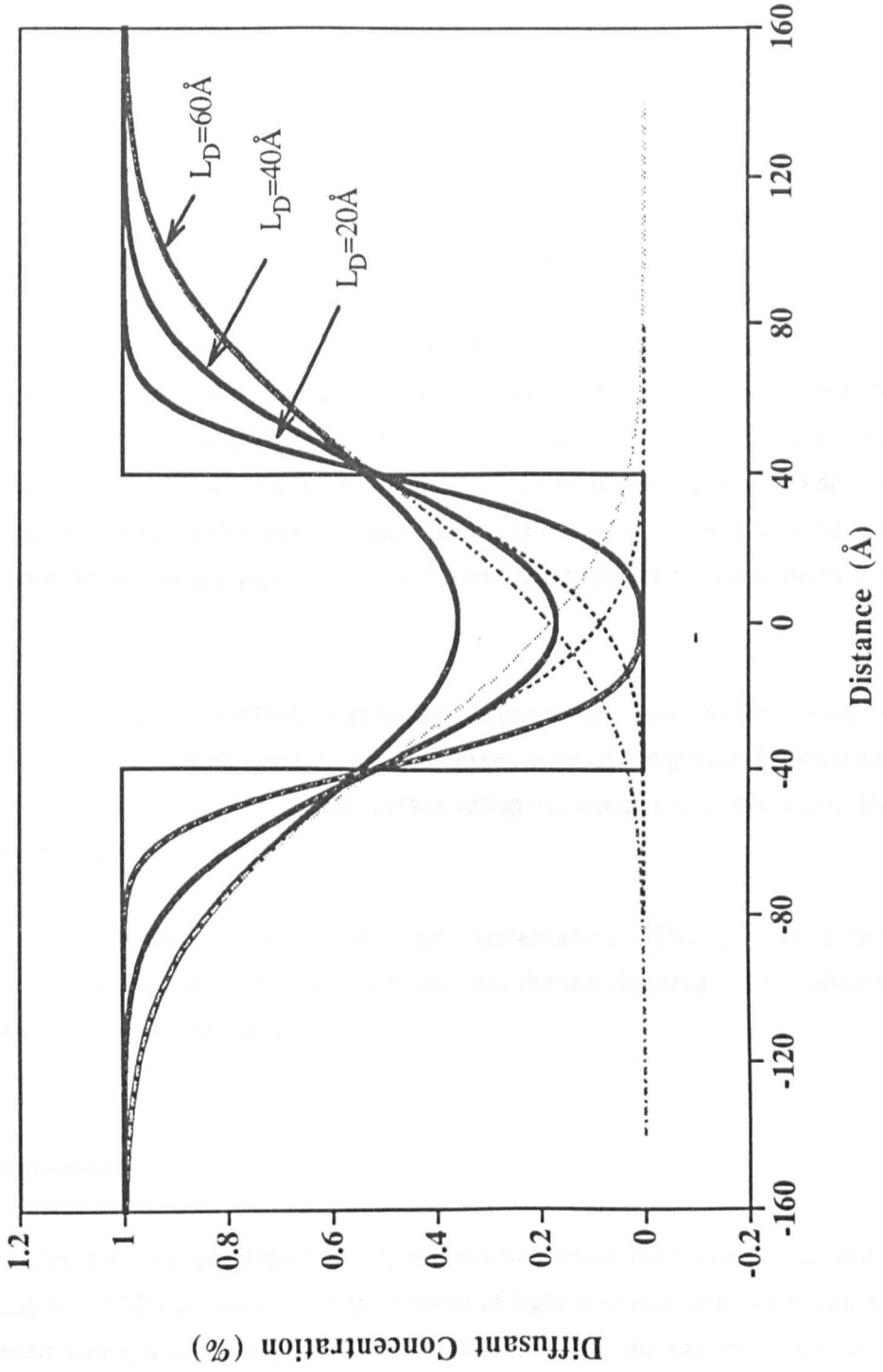

Fig.10 80Å quantum well at three different stages of intermixing

2) The power density required to intermix the material is much less than other laser intermixing processes which use focused laser beams. The typical power density used in PAID is $\approx$1 Wmm^{-2} while direct write processes have used power densities of 30 $kWmm^{-2}$ in the (Al)GaAs system.

3) Since PAID is essentially a free-space process, it is possible to carry out photoreflectance[22] measurements on the material as it is intermixed. This in-situ high temperature photoreflectance monitoring could allow very accurate one-step processing to achieve a precise wavelength shift in the as-grown material.

4) The process is potentially self-limiting. It may be possible to design a laser structure such that as the active region is intermixed and the bandgap widens, then the entire structure becomes transparent to the irradiating laser. This could happen, for example, in the InGaAs(P) system using a Nd:YAG laser operating at 1320 nm. A problem which may arise is that the bandgap shrinks at elevated temperatures but this could be overcome by using a repetitive heating-cooling cycle on a time scale of tens of seconds.

5) After processing, the surface morphology remains very good which is vital for subsequent processing. Other intermixing processes such as strontium fluoride cap annealing have not always yielded good surface integrity, which can prove a problem when making devices.

6) The process does not require any ion implantation. This is both a time consuming and an expensive process which also has the disadvantage of introducing foreign atoms into the crystal lattice.

3.10 Conclusions

This chapter has described the experimental procedure used to intermix material using the PAID process. The absorption of light within a semiconductor has been discussed along with heat generation mechanisms and the thermal conduction properties of semiconductors.

A simple model has been described which allows the measured photoluminescence shifts to be related to the rate of intermixing between the wells and barriers within the multiple quantum well structure. Finally, some advantages of PAID over other intermixing processes have been described.

1 H.M. Rosenberg, The Solid State, 3rd Edition, Oxford Science Press, 1989
2 U. Piesbergen, Semiconductors and Semimetals, Academic, New York, 1967, Vol. **2**
3 T.Q. Qiu, C.L. Tien, International Journal of Heat and Mass Transfer, Vol35 (3),1992, pp719-726
4 W.P. Dumke, Physics Review, Vol. **105**, 1957, p 139
5 M.G. Holland, Semiconductors and Semimetals, Academic, New York, 1967, Vol. **2**
6 U. Piesbergen, Semiconductors and Semimetals, Academic, New York, 1967, Vol. **2**
7 M.G. Holland, Semiconductors and Semimetals, Academic, New York, 1967, Vol. **2**
8 S. Adachi, Journal of Applied Physics, Vol. **54** (4), April 1983, pp 1844-1848
9 Properties of Indium Phosphide, INSPEC EMIS Datareviews Series No. 6
10 I. Kudman, E.F. Steigmeier, Physics Rev. vol.**133** (1964) p. A 1665
11 P.D. Maycock, Solid State Electronics, vol **10**, 1967, p 161
12 S.A. Aliev, A.Ya.Nashel'skii, S.S. Shalyt, Sov. Phys.-Solid State, vol. 7 (1965), p. 127
13 S. Adachi, Journal of Applied Physics, Vol. **54** (4), April 1983, pp 1844-1848
14 P.D. Maycock, Solid State Electronics, vol **10**, 1967, p 161
15 S. Adachi, Journal of Applied Physics, Vol. **54** (4), April 1983, pp 1844-1848
16 H. Peyre, F. Alsina, J. Camassel, J. Pascual, R.W. Glew, Journal of Applied Physics, **73** (8), April 1993 pp 3760-3768
17 B.I. Boltaks in *Diffusion in Semiconductors*, Infosearch Ltd., London, 1963
18 K.P. Homewood, D.J. Dunstan, Journal Appl. Phys., **69**, p7581, 1991
19 T.P. Pearsall, GaInAsP Alloy Semiconductors, Wiley & Sons, New York, 1982, p 295
20 S. Adachi, Journal of Applied Physics, Vol. **54** (4), April 1983, pp 1844-1848
21 J.H. Marsh, S.A. Bradshaw, A.C. Bryce, R. Gwilliam, R.W. Glew, J. Electron. Mat., 20 (12), pp 973-978, 1991
22 I. Gontijo, Y.S. Tang, R.M. De La Rue, C.M.S. Torres, J.S. Roberts, J.H. Marsh, J. Appl. Phys. **76** (9), pp.5434-5438, 1994

Chapter 4 Low Loss Optical Waveguides

4.1 Introduction

Low-loss single-mode optical waveguides[1] are required in optoelectronic circuits to transport the light around the chip from one device to another, in a similar way to the use of wires in an electrical circuit.

This chapter deals with the theory behind these waveguides and the fabrication processes involved in making them. The testing of these waveguides is then described in detail with loss measurements and other results presented at the end.

4.2 General Theory of Slab Waveguides

4.2.1 Three layer slab waveguide

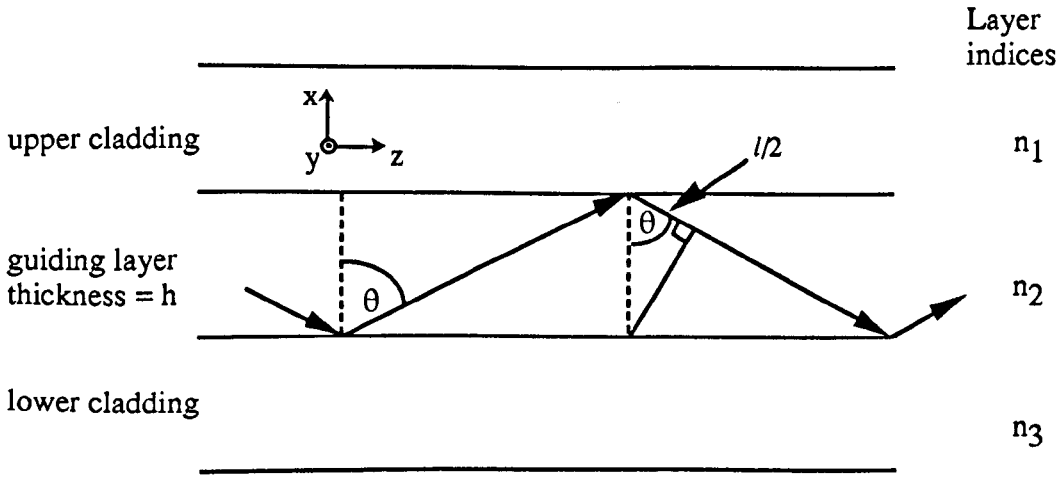

Fig. 1 Schematic diagram of three-layer waveguide

In a three-layer slab waveguide[2], the composition of the layers is chosen such that $n_1 < n_2 > n_3$ as shown in Fig. 1. The effect of sandwiching a high refractive index layer between two low index layers is that light is confined or "guided" due to the principle of total internal reflection.

To avoid decay of optical power as the plane waves travel along the guide, the wavefronts of successive reflections (normal to the zig-zag rays) must interfere constructively. This means that the total phase change of a point on such a wavefront which travels from the n_1-n_2 interface to the n_3-n_2 interface and back again must be a multiple of 2π. This condition can be expressed as:

$$2n_2kh\cos\theta - 2\phi_1 - 2\phi_3 = 2m\pi \qquad (m = 0,1,2....) \qquad (4.1)$$

where h is the thickness of the guide layer, $k = 2\pi/\lambda_0$ where λ_0 is the free-space wavelength of the guided light, θ is the angle of reflection with respect to the x-direction, m is the mode number, and ϕ_1 and ϕ_3 are the phase shifts incurred at the interfaces due to total internal reflection. These phase shifts can be interpreted as penetration of the zig-zag ray into the confining layers, 1 and 3, before being reflected and are defined as:

$$\phi_1 = \tan^{-1} \frac{+\sqrt{n_2^2 \sin^2 \theta_i - n_1^2}}{n_2 \cos \theta_i} \tag{4.2}$$

$$\phi_3 = \tan^{-1} \frac{+\sqrt{n_2^2 \sin^2 \theta_i - n_3^2}}{n_2 \cos \theta_i} \tag{4.3}$$

for TE polarised fields and:

$$\phi_1 = \tan^{-1} \frac{+n_2^2\sqrt{n_2^2 \sin^2 \theta_i - n_1^2}}{n_1^2 n_2 \cos \theta_i} \tag{4.4}$$

$$\phi_3 = \tan^{-1} \frac{+n_2^2\sqrt{n_2^2 \sin^2 \theta_i - n_3^2}}{n_3^2 n_2 \cos \theta_i} \tag{4.5}$$

for TM polarised fields.

For a given mode and the parameters n_1, n_2, n_3, and h, the angle θ_m can be calculated. This produces a set of discreet angles corresponding to the various modes.

Equation (4.1) can be solved graphically by plotting $n_2 kh\cos\theta - m\pi$ and $\phi_1 + \phi_3$ as a function of θ. Intersections of the two curves represent the solutions to the equation with characteristic angles θ_m, where m is the order of the mode. For each mode there is a corresponding propagation constant given by:

$$\beta_m = n_2 k \sin \theta_m \tag{4.6}$$

and one can define an effective index for that particular mode as:

$$n_{eff} = \beta_m / k = n_2 \sin \theta_m \tag{4.7}$$

Fig. 2 shows a typical graphical representation of this equation for a symmetrical waveguide (i.e. $n_1 = n_3$) which is sufficiently thick to support 2 modes.

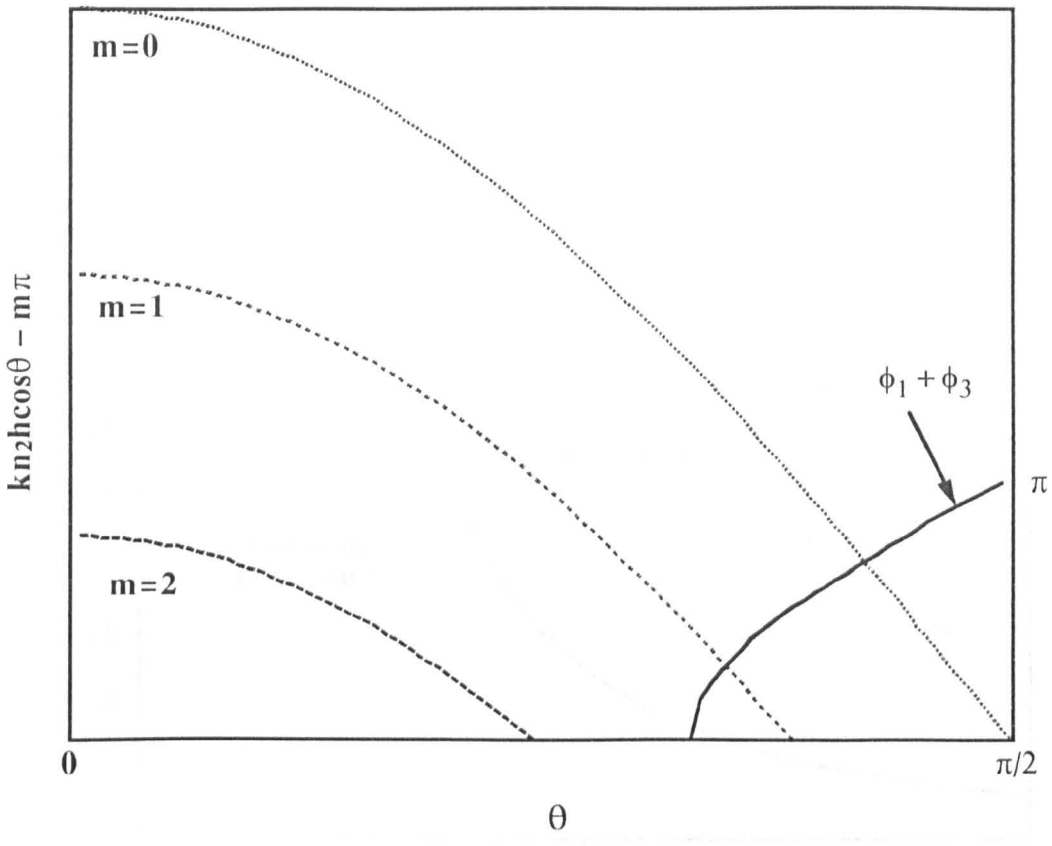

Fig. 2 Graphical solution to Eq. (4.1) showing the allowed modes

As guiding layer thicknesses and refractive index steps are reduced, the number of modes which a waveguide can support gets smaller. When a mode just ceases to propagate it is said to be "cut-off". For a symmetrical three-layer waveguide, the cut-off condition for TE polarised light is given by:

$$k\sqrt{(n_2^2 - n_1^2)}h = m\pi \qquad (m = 0,1,2....) \tag{4.8}$$

or,

$$\Delta n = (n_2 - n_1) > \frac{m^2\lambda_0^2}{4h^2(n_2 + n_1)} \qquad (m = 0,1,2....) \tag{4.9}$$

Fig. 3 shows this relationship graphically with the minimum $\Delta\varepsilon = n_2^2 - n_1^2$ plotted as a function of guide layer thickness and wavelength. This condition is very important in semiconductor waveguide devices as choosing m=1 defines the maximum thickness of

active region which will ensure single mode propagation in the direction perpendicular to the plane of the quantum wells.

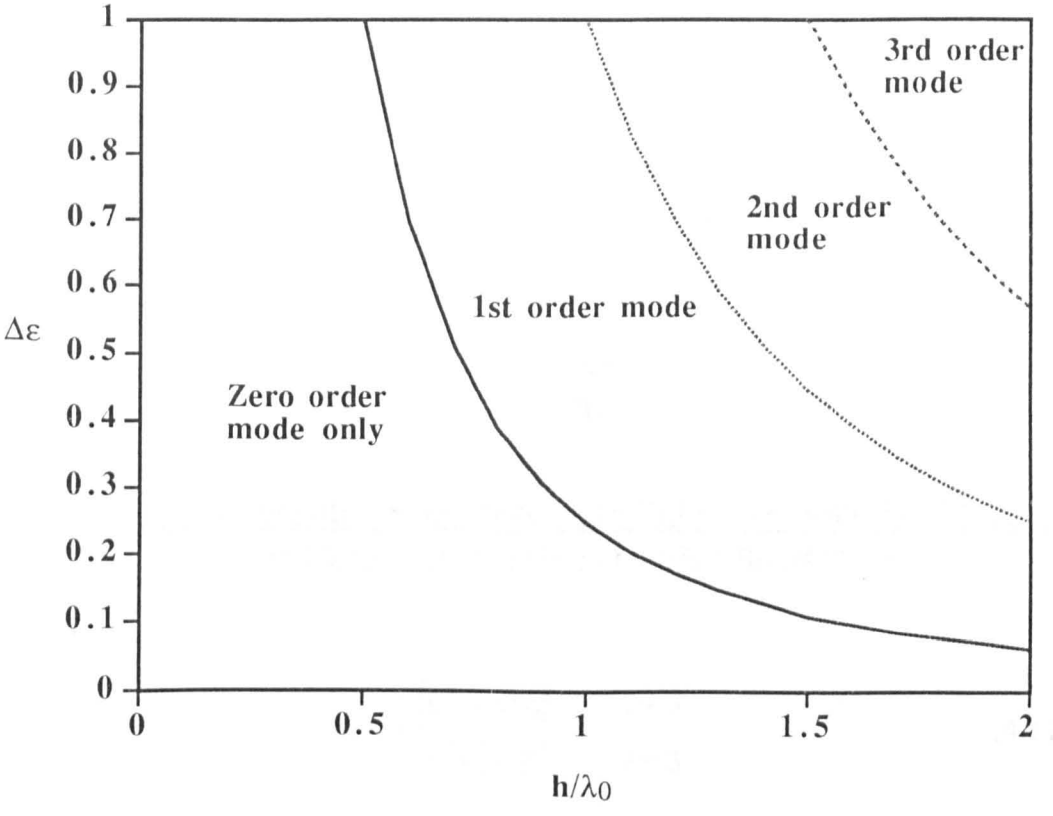

Fig. 3 Mode cut-off conditions for a symmetrical three layer waveguide

Due to the large refractive index changes introduced by heterojunctions, it is necessary for the active region to be quite thin to ensure single mode operation. For example, a double heterostructure InP-InGaAsP-InP laser operating at 1.3 μm would require an active region to be less than 0.5 μm for single mode operation.

It is interesting to note that in a symmetrical waveguide, the lowest order mode (m=0) does not exhibit a cut-off as all others do. This implies that any wavelength of light is guided in this mode no matter how small the refractive index change, or guide layer thickness is. Of course under these conditions (with small Δn or h) the confinement will be poor, with large evanescent fields extending into the substrate and upper cladding layers.

4.2.2 Four layer slab waveguide

The three layer model takes no account of the thickness of the cladding layers and therefore assumes that the optical field decays to zero in these regions. Obviously this is not always the case especially when the upper cladding layer is thin, or if certain areas of it have been etched away.

A more accurate and useful model is the four-layer slab waveguide which takes account of the thickness of the upper cladding layer and how that affects the effective index of a given mode within the guide layer. The characteristic equation for a four layer slab is given by[3]:

$$k_3 h_3 = \tan^{-1}\left[\frac{\eta_4 k_4}{\eta_3 k_3}\right]$$

$$+\tan^{-1}\left[\frac{\eta_2 k_2(\eta_2 k_2 + \eta_1 k_1)\exp(k_2 h_2) - (\eta_2 k_2 - \eta_1 k_1)\exp(-k_2 h_2)}{\eta_3 k_3(\eta_2 k_2 + \eta_1 k_1)\exp(k_2 h_2) + (\eta_2 k_2 - \eta_1 k_1)\exp(-k_2 h_2)}\right] \quad (4.10)$$

where

$$k_i^2 = \begin{cases} \beta^2 - n_i^2 k_0^2 & i \neq 3 \\ n_i^2 k_0^2 - \beta^2 & i = 3 \end{cases} \quad (4.11)$$

The terms η_i have been included to account for the two different sets of boundary conditions which are required for TE and TM polarised light and are defined as:

$$\eta_i = \begin{cases} 1 & TE\ fields \\ \dfrac{1}{n_i^2} & TM\ fields \end{cases} \quad (4.12)$$

4.2.3 The Effective Index Method

Fig. 4 shows a strip loaded waveguide which can be modelled relatively simply using the four-layer model and the effective index method (EIM)[4].

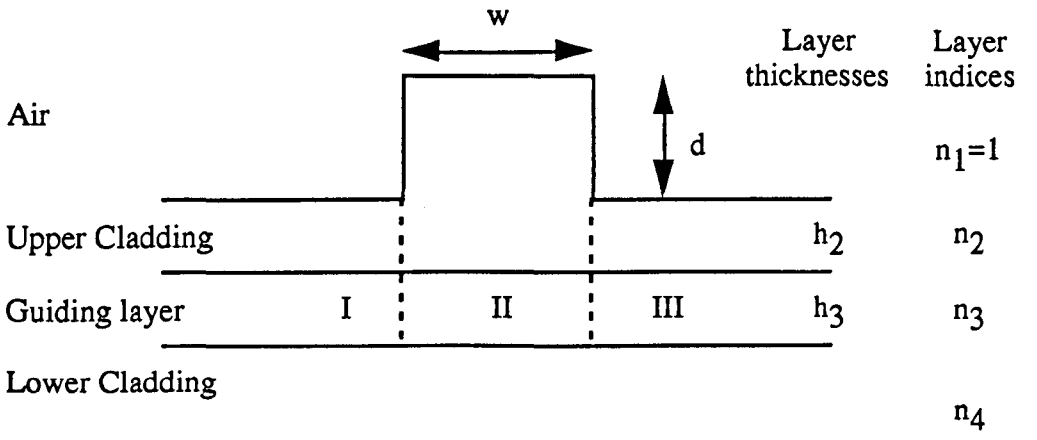

Fig. 4 The cross-section of a strip-loaded waveguide.

The first step in analysing this structure using the EIM is to separate the three regions (see fig. 5(a)) and solve the characteristic four-layer slab equation (4.10) for each one. This yields the effective index for the fundamental (m=0) mode for each of the sections.

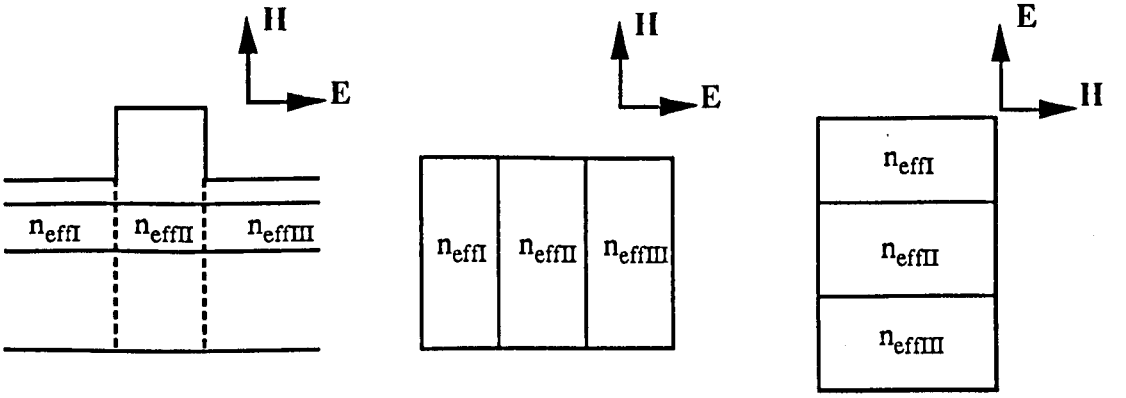

Fig. 5(a) 5(b) 5(c)

It is obvious that regions I and III will be more strongly influenced by the air and so subsequently the effective index in these regions will be lower than in region II where the upper cladding layer is much thicker.

The original 2-D model can now be simplified to a 1-D case (see fig. 5(b)) in which the refractive indices are n_{effI}, n_{effII}, and n_{effIII}. Rotating this model by 90° yields a situation similar to a three-layer vertical slab guide (see fig. 5(c)). This model can be solved using equations (4.1), (4.2) and (4.3), remembering to solve for TM polarised light.

To solve the original problem for TM modes, the four-layer slab equation (4.10) should be solved for TM polarised light yielding different effective indices, and the three-layer vertical slab should be solved for TE polarised light. The EIM makes the

assumption that the three regions are independent and infinite in size which is not strictly the case. In fact, the electric field distribution is influenced by the guiding structure of the neighbouring region with the effect that the accuracy deteriorates as these "edge effects" increase.

The four-layer slab method is usually sufficient for most waveguide structures, however, the structures used in this thesis are more complicated with graded index layers between the waveguide core and the outer cladding layers. A more suitable method for analysing a multi-quantum well graded index ridge waveguide is to use a multi-layer matrix solver which allows the effective indices of the three regions (I, II, and III) within the EIM, to be calculated more accurately. Section 4.5.1 in this chapter presents some calculations on the waveguides fabricated.

4.3 Fabrication of Optical Waveguides

4.3.1 Material Structure

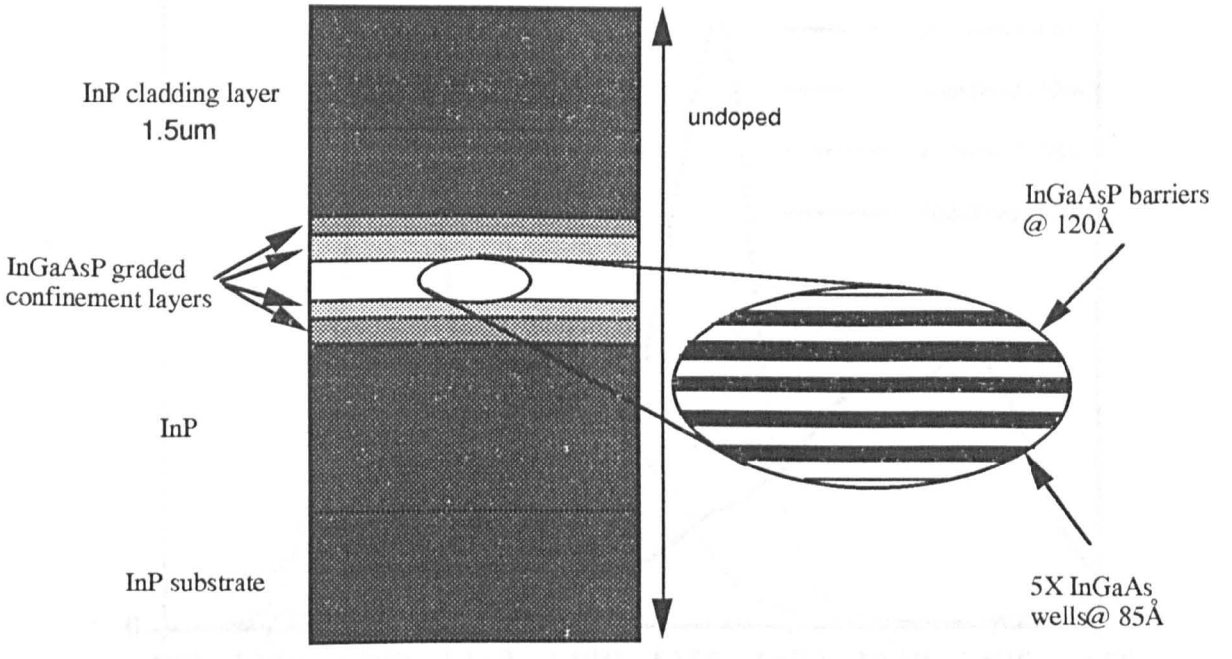

Fig. 6 Structure of waveguide material

The epitaxial structure used to fabricate the waveguides is shown in Fig. 6. It is a standard multiple quantum well structure with a core region containing five 85 Å InGaAs wells and 6 120 Å InGaAsP (λg = 1.26 μm, where λg is the bandgap of the material expressed as wavelength) barriers. The core region was surrounded by a stepped graded index (GRIN) waveguide core consisting of two InGaAsP confining

layers. The thicknesses and compositions of these layers (working out from the QWs) were 500 Å of $\lambda g = 1.18$ μm and 800 Å of $\lambda g = 1.05$ μm. The structure, which was lattice matched to InP throughout and nominally undoped, was completed with an InP upper cladding layer of thickness 1.5 μm

This structure is based on a standard 1.55 μm multiple quantum well laser design except that there is no doping in the structure and there is no InGaAs contact layer on the surface. These modifications mean that the fabrication of the waveguides is simpler and the resulting losses will be lower due to the absence of dopants.

4.3.2 Disordering of quantum well waveguides

The material was disordered using the procedure described in Chapter 3 with the result that the material was shifted from a starting photoluminescence wavelength of 1585 nm to a final photoluminescence wavelength of 1385 nm which is approaching total intermixing between the wells and barriers.

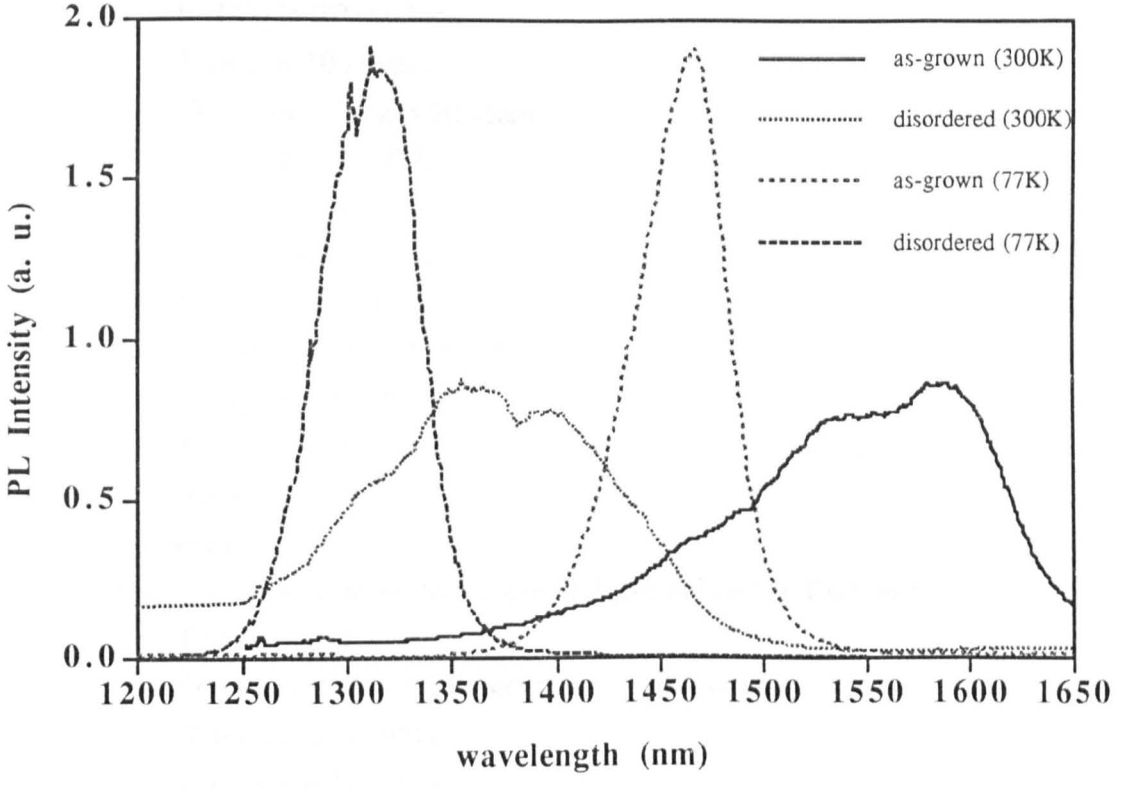

Fig. 7 Room temperature and 77K photoluminescence measurements of the material before and after disordering.

4.3.3 Fabrication of waveguides

After the material had been disordered, ridge waveguides were fabricated in the following manner.

1. Remove 500 nm SiO_2 cap layer with buffered HF for 5 mins.
2. Plasma-Enhanced Chemical-Vapour-Deposition (PECVD) of 200 nm SiO_2
   - Power = 10 watts
   - Gas flow : SiH_4 = 9 sccm, N_2O = 710 sccm, N_2 = 171 sccm
   - Temperature = 300°C
   - Pressure = 1 torr
3. Spin on primer: Hexadimethylsylane
4. Spin on resist : S1400-31 @ 6000 rpm for 30 secs
5. Post bake for 30 mins. @ 90°C
6. Expose with alignment in β direction to ensure vertical sidewalls
7. Develop pattern for 60 secs.
8. Dry etch SiO_2 in BP machine
   - Power = 100 watts
   - Gas flow : C_2F_6 = 20 sccm
   - Temperature = 30°C
   - Bias = 400 V
9. Oxygen clean in BP machine
   - Power = 50 watts
   - Gas flow : O_2 = 30 sccm
   - Temperature = 30°C
   - Pressure = 50 mtorr
   - Time = 5 mins.
10. Remove resist
11. Dry etch InP for 12 mins. to a depth of 1 μm in Electro-Tech 340
    - Power = 100 watts
    - Gas flow : CH_4 = 3.6 sccm, H_2 = 26.4 sccm
    - Temperature = 300°C
    - Pressure = 14 mtorr
    - Bias = 850 V
12. Oxygen clean to remove polymer build-up
13. Wet etch with HCl : H_3PO_4 (in ratio 1:3) for 90 secs. to etch stop layer
14. Remove SiO_2 with buffered HF
15. Thin sample to 150 μm using 9 μm alumina grit
16. Scribe and cleave sample to a length of 3.3 mm

The mask used in the fabrication process contained lines which ranged in size from 2 μm to 10 μm. This ensured that the photolithography process was not critical in terms of the final ridge widths and gave a range of single and multi-moded waveguides.

4.3.4 Wet etching of InP

The ridge direction is very important in the InP system as ridges can be fabricated with either vertical or sloping sidewalls using a selective wet etch[5]. This wet etch, hydrochloric acid mixed with orthophosphoric acid, is also very controllable in that it will stop on any layers containing arsenic leaving good surface quality. Fig. 8 and 10 show the different etching characteristics for ridges aligned in the α and β directions with Fig. 9 and 11 showing the crystal planes revealed after etching. For ridges aligned in the α-direction, the etch stops on (211) planes of In atoms which have a much lower etch rate than the (100) plane. This plane forms an angle of 35° with the substrate. For ridges aligned in the β-direction, a reverse mesa is produced as the mask is undercut with (111) planes of In revealed, producing an angle of 55° to the substrate.

However, in order to achieve good lateral confinement in the waveguides, a step in the effective refractive index is required between the different regions I, II, and III as shown in Fig. 5. This means that it is vital to have vertical sidewalls on our waveguides in order to achieve such an index step. It is obvious that purely wet etching will not give the desired waveguide profile. For this reason, a combined dry-etch wet-etch process was used which yielded vertical sidewalls (in the β-direction), together with reasonable surface quality. Fig. 12 shows a waveguide fabricated in this manner which was used for the loss measurements described later in this chapter. Although the etched surface is of reasonable quality, it is evident that the sidewalls are appreciably more ragged which will increase the scattering losses of the waveguide. This is most likely caused by non-uniform dry-etching of the material surface after it has been disordered or poor lithography.

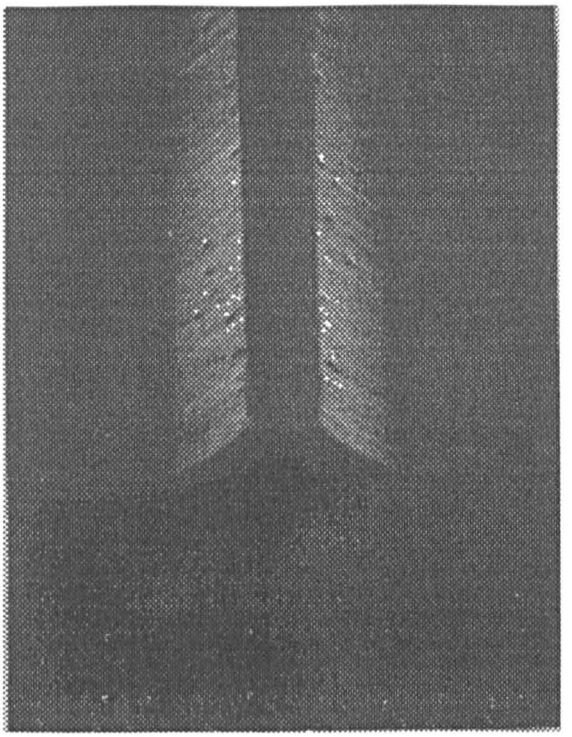

Fig. 8 Waveguide fabricated in the α-direction ($01\bar{1}$)

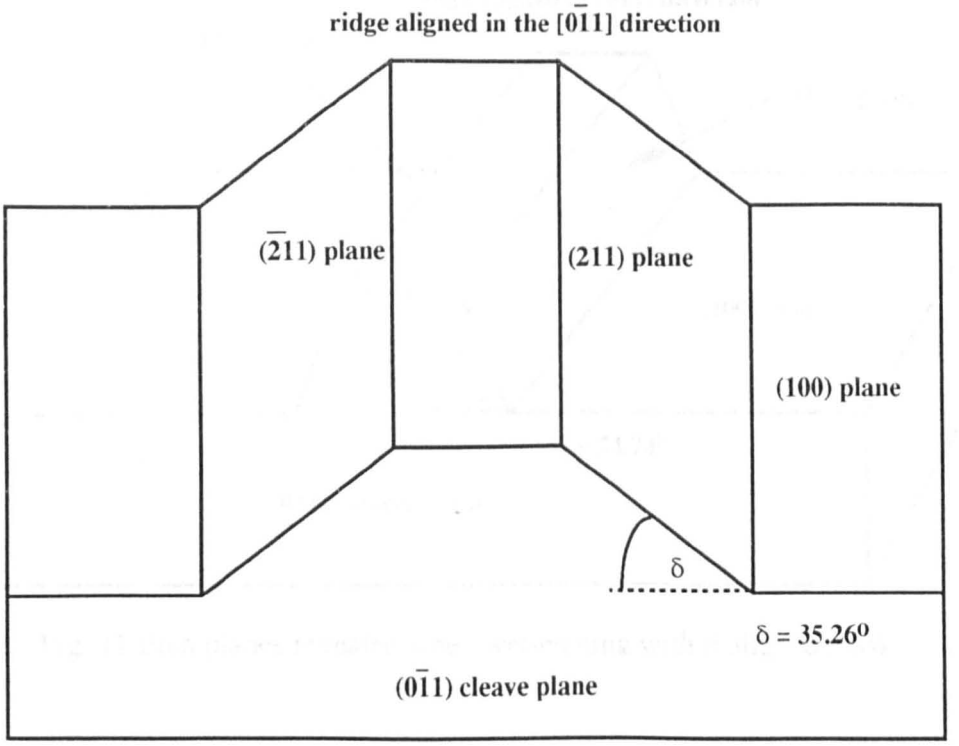

Fig. 9 Etch planes revealed when wet-etching with α aligned mask

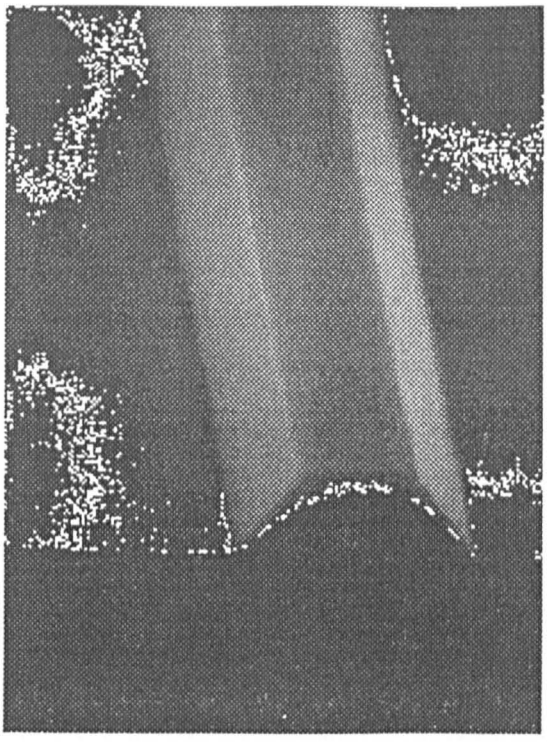

Fig. 10 Wet-etched waveguide fabricated in the β-direction (011)

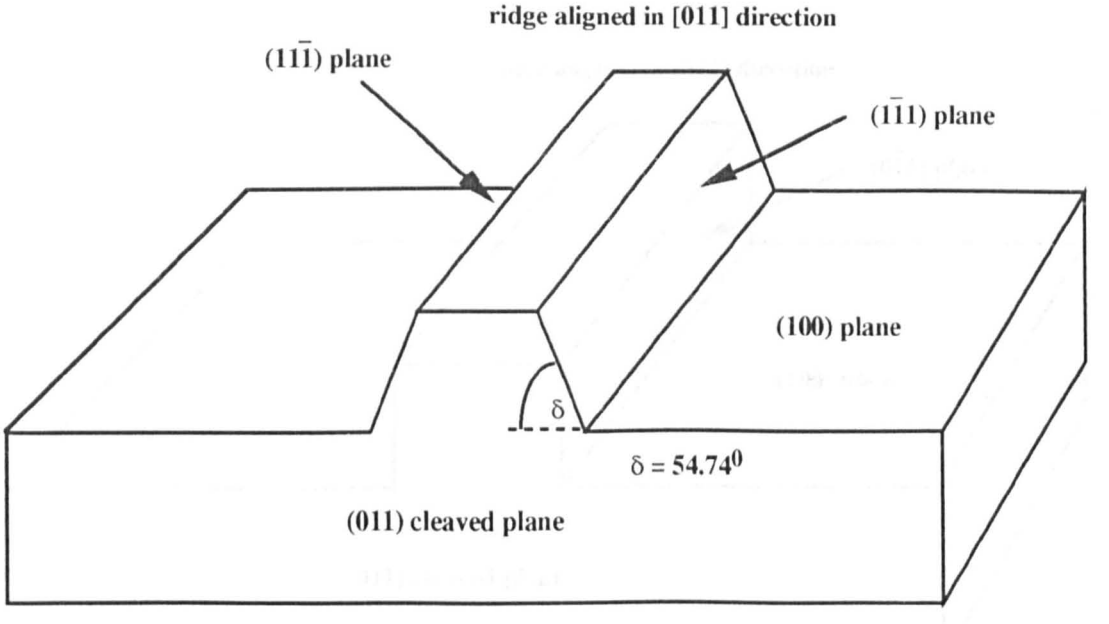

Fig. 11 Etch planes revealed when wet-etching with β aligned masks

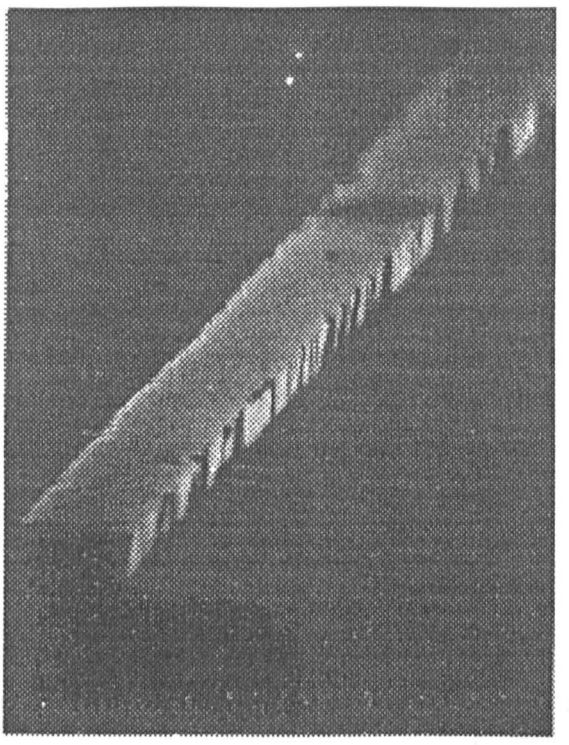

Fig. 12 Waveguide fabricated in β-direction by dry-etching and wet-etching

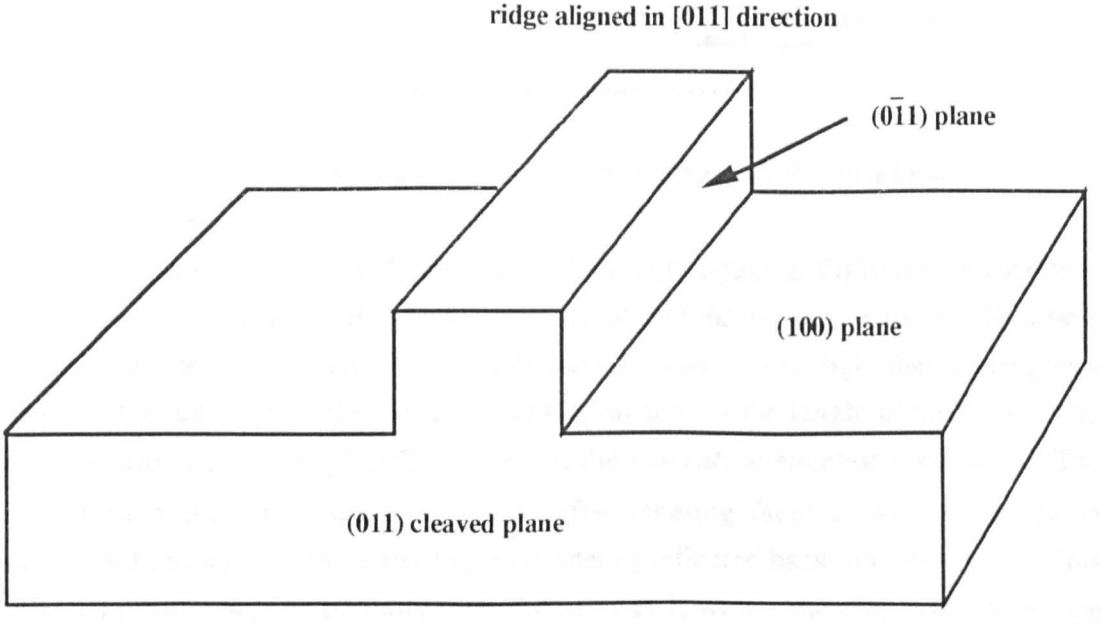

Fig. 13 Etch planes revealed when dry-etching then wet-etching with β aligned masks

4.4 Fabry-Perot Loss Measurements

4.4.1 Fabry-Perot theory

The Fabry-Perot technique[6] is a simple non-destructive way of measuring waveguide losses. The technique relies on cleaved facets to form a Fabry-Perot waveguide resonator, the finesse of which is measured by varying the optical length of the cavity using thermal tuning. Fig. 14 shows the transmission characteristics of such a waveguide resonator[7]. It is worth noting that throughout this thesis, the loss, α, of any given device (waveguide or laser) will be defined as the *Intensity Attenuation Coefficient* (i.e. $I=I_o\exp(-\alpha l)$.)

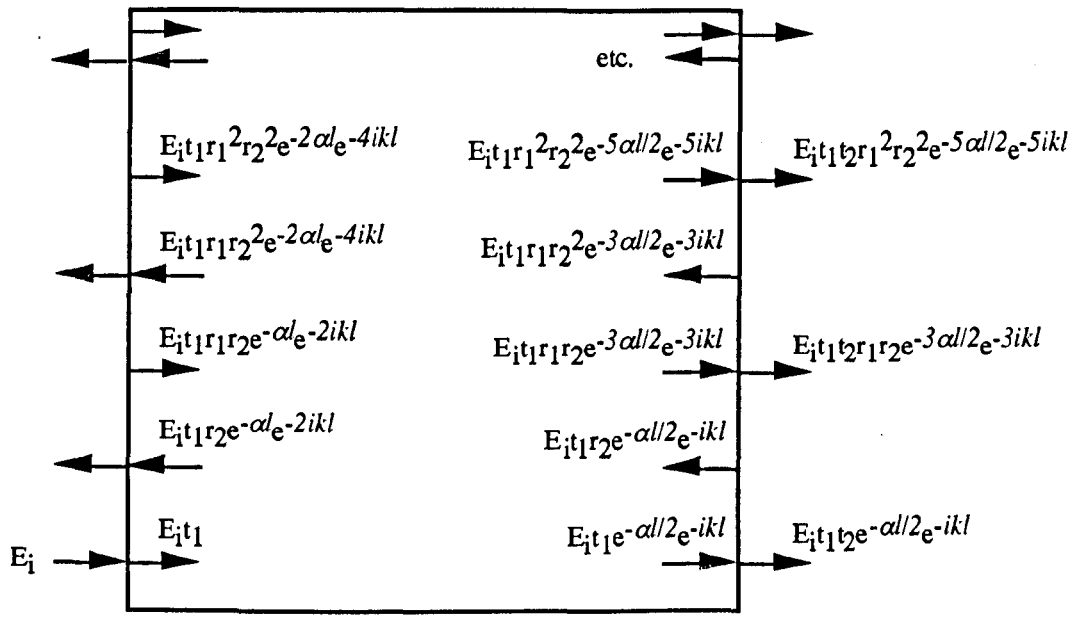

Fig. 14 Optical waveguide resonator with partially reflecting facets

The incident light (with electric field strength equal to E_i) to this resonator is partially reflected such that the portion transmitted into the cavity is equal to t_1E_i, where t_1 represents the e-field transmission coefficient of facet 1. This light then undergoes a phase shift equal to $\exp(-ikl)$, where $k=2\pi n_{eff}/\lambda_0$ and l is the length of the cavity, and an attenuation equal to $\exp(-\alpha l/2)$ where α is the *intensity* attenuation coefficient. The light is then split into two components after meeting facet 2, with a portion t_2 transmitted through the facet and the remainder r_2 reflected back into the cavity. This reflected portion will be partially reflected at facet 1, with a standing wave being the result of these multiple reflections.

From the diagram it can be seen that the transmission at facet 2 can be expressed as:

$$E_t = E_i t_1 t_2 e^{-ikl} e^{-\alpha l/2}\left[1 + r_1 r_2 e^{-2ikl} e^{-\alpha l} + r_1^2 r_2^2 e^{-4ikl} e^{-2\alpha l} + ...\right] \qquad (4.13)$$

This equation can be simplified by substituting $T=t_1t_2$ and $R=r_1r_2$, and noting that the term in the bracket is a geometrical expansion giving:

$$\frac{E_t}{E_i} = \left[\frac{Te^{-ikl}e^{-\alpha l/2}}{1 - Re^{-2ikl}e^{-\alpha l}}\right] \qquad (4.14)$$

The ratio of transmitted to incident intensities is then given as:

$$\left[\frac{E_t}{E_i}\right]^2 = \frac{E_t E_t^*}{E_i E_i^*} = \frac{T^2 e^{-\alpha l}}{\left[\left(1 - Re^{-\alpha l}\cos(2kl)\right) - iRe^{-\alpha l}\sin(2kl)\right]\left[\left(1 - \mathrm{Re}^{-\alpha l}\cos(2kl)\right) + iRe^{-\alpha l}\sin(2kl)\right]} \qquad (4.15)$$

where E_x^* is the complex conjugate of E_x. This can be simplified to:

$$\left[\frac{E_t}{E_i}\right]^2 = \frac{T^2 e^{-\alpha l}}{1 - 2Re^{-\alpha l}\cos(2kl) + R^2 e^{-2\alpha l}} \qquad (4.16)$$

Substituting $\gamma=e^{-\alpha l}$ and $T=(1-R)$ gives:

$$\left[\frac{E_t}{E_i}\right]^2 = \frac{(1-R)^2\gamma}{1 - 2R\gamma\cos(2kl) + R^2\gamma^2} \qquad (4.17)$$

where γ is the single pass loss of the waveguide.

This equation yields values for the transmission at resonant (T_R) and anti-resonant (T_A) conditions and these are given by:

$$T_R = \left[\frac{(1-R)\sqrt{\gamma}}{1 - R\gamma}\right]^2 \qquad T_A = \left[\frac{(1-R)\sqrt{\gamma}}{1 + R\gamma}\right]^2 \qquad (4.18)$$

Using these two equations, we can find the loss of the waveguide, γ, by measuring the Fabry-Perot fringe contrast which is given by:

$$K = \frac{I_i T_R}{I_i T_A} = \frac{T_R}{T_A} \qquad (4.19)$$

giving:

$$\gamma = \frac{\sqrt{K} - 1}{R(\sqrt{K} + 1)} \tag{4.20}$$

which yields a single pass loss in dB of:

$$\Gamma = -10\log_{10}\gamma = -10\log_{10}\left[\frac{\sqrt{K} - 1}{R(\sqrt{K} + 1)}\right] \tag{4.21}$$

where the reflection coefficient, R, is given by:

$$R = \left(\frac{n_{dielec.} - n_{air}}{n_{dielec.} + n_{air}}\right)^2 \tag{4.22}$$

where $n_{dielec.}$ is the refractive index of the waveguide and n_{air} is the refractive index of air (=1). Dividing this loss by the length of the waveguide yields the loss in units of $dBcm^{-1}$.

The Fabry-Perot fringes are produced by varying αl in equation (4.17) which produces the resonant and anti-resonant transmission conditions. The variation is achieved by applying gentle heat to the sample, which has the effect of increasing both the length and the refractive index of the waveguide which increases the optical length of the cavity.

Fig. 15 shows typical Fabry-Perot fringes from a low loss single mode waveguide indicated by the high contrast between the resonant and anti-resonant conditions.

In order that the contrast fringes can be resolved, it is important that the linewidth of the probe source be much less than the free-spectral range of the cavity (i.e. the spacing between longitudinal modes of the cavity) which is given by:

$$\Delta\nu = \frac{c}{2n_{eff}l} \tag{4.23}$$

where c is the speed of light in a vacuum,
l is the length of the waveguide, and
n_{eff} is the effective index of the waveguide.

This value is typically around 15 GHz (or $\approx$ 1.3 Å) for a 3 mm long waveguide compared with a linewidth of around 1 MHz for an extended cavity ridge

waveguide laser[8]. Any errors introduced by using a broad linewidth source would result in an over-estimation of the losses.

Another limitation of the Fabry-Perot technique is its restriction to single mode waveguide propagation. The response of a multimode waveguide is the superposition of the resonance fringes for each different phase velocity which will oscillate at different rates due to the change in effective index for each mode.

4.4.2 Experimental Technique

Fig. 16 shows the experimental arrangement used to determine the waveguide losses by the Fabry-Perot technique. The source used was a CW operated ridge waveguide laser with one facet anti-reflection coated. The output from this facet was collimated onto a grating with the reflection coupled back into the laser. This arrangement ensured that only one longitudinal mode oscillated in the cavity. Tuning was achieved simply by rotating the grating with a resulting tuning range of 1510 nm to 1570 nm. The laser was powered by a battery pack via a variable power supply unit to eliminate power spikes which may damage the laser, and temperature controlled using a Peltier cooler.

A collimating lens coupled the light from the laser facet to the end-fire arrangement where the light was coupled into and out of the waveguide using a X40 (NA=0.65) microscope objective lenses. The output from the waveguide was monitored by an infra-red camera and the intensity measured by an optical spectrum analyser (OSA). Heat was supplied to the sample in the form of a fine tipped soldering iron with the resulting Fabry-Perot oscillations observed on the OSA.

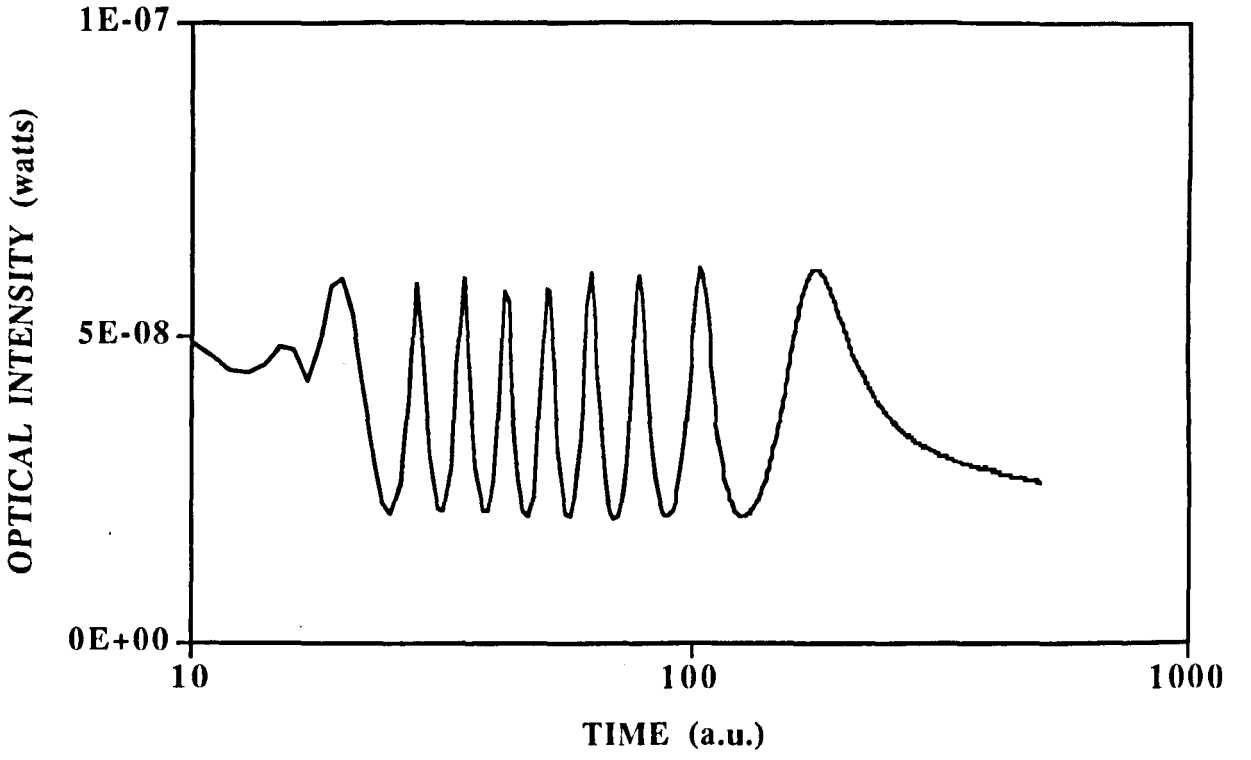

Fig. 15 Typical Fabry-Perot oscillations observed from a single mode waveguide.

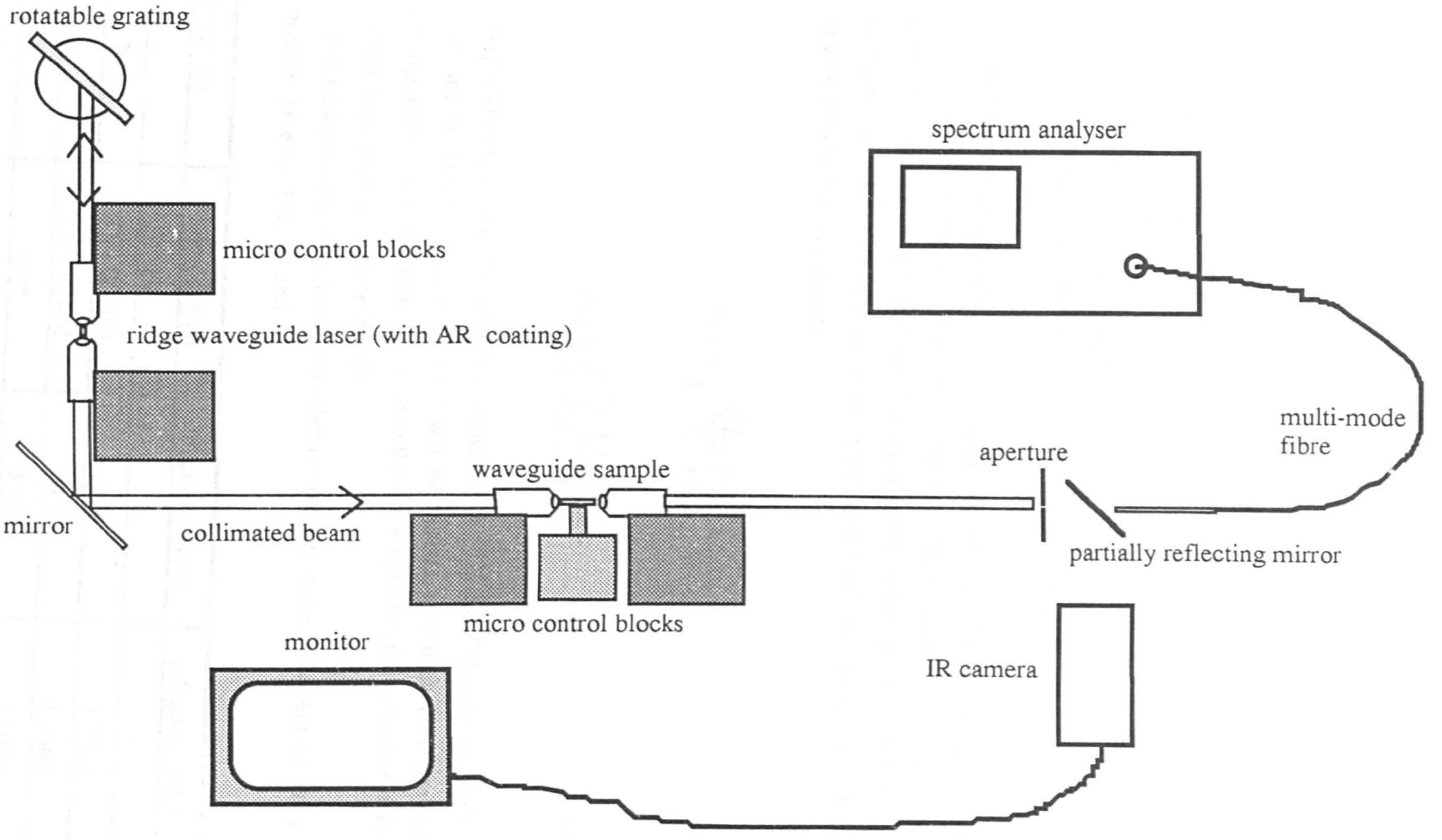

Fig. 16 Experimental set-up for measuring waveguide losses

4.5 Results

4.5.1 Modelling of Waveguides using the Effective Index Method

The EIM described earlier in this chapter (see section 4.2.3) has been used to evaluate the characteristics of the fabricated waveguides. Some approximations have been used to simplify the model, for example the refractive indices of the different quaternary layer compositions has been linearly extrapolated from the refractive indices of InP (n=3.16886) and InGaAs (n=3.6)[9]. This is a common technique for determining material properties of alloy semiconductors and should not introduce large errors[10].

Another simplification is that the core region (of wells and barriers) has been regarded as a single layer. To evaluate the refractive index of this core region, a weighted root-mean-square method[11] is used which takes into account the relative thicknesses and refractive indices of the wells and barriers. Equations (4.24) and (4.25) give these refractive indices:

$$n_{TE} = \sqrt{\frac{n_w^2 L_w + n_b^2 L_b}{L_w + L_b}} \tag{4.24}$$

$$n_{TM} = \sqrt{\frac{(L_b + L_w) n_w^2 n_b^2}{n_w^2 L_w + n_b^2 L_b}} \tag{4.25}$$

where n_{TE} and n_{TM} denote the refractive indices of the TE and TM polarised light. L_w and L_b are the total thicknesses of the wells and the barriers, with their refractive indices given by n_w and n_b. For the structure used in these waveguides, the refractive index of the core has been calculated to be 3.4084.

It is now possible to evaluate the effective indices in the three regions using the layer profiles given in Fig. 17 and 18.

layer no.	composition	thickness (μm)	refractive index
1	air	5	1
2	Q(1.05μm)	0.08	3.2212
3	Q(1.18μm)	0.05	3.2664
4	core	0.1145	3.4084
5	Q(1.18μm)	0.05	3.2664
6	Q(1.05μm)	0.08	3.2212
7	InP	5	3.16886

Fig. 17 Layer parameters for regions I and III in waveguide structure

layer no.	composition	thickness (μm)	refractive index
1	air	5	1
2	InP	1.5	3.16886
3	Q(1.05μm)	0.08	3.2212
4	Q(1.18μm)	0.05	3.2664
5	core	0.1145	3.4084
6	Q(1.18μm)	0.05	3.2664
7	Q(1.05μm)	0.08	3.2212
8	InP	5	3.16886

Fig. 18 Layer parameters for region II in waveguide structure

Fig. 19 shows a schematic diagram of the variation in refractive index within the layers of region II in the waveguide model and gives an indication of how the core region has been simplified to a single layer.

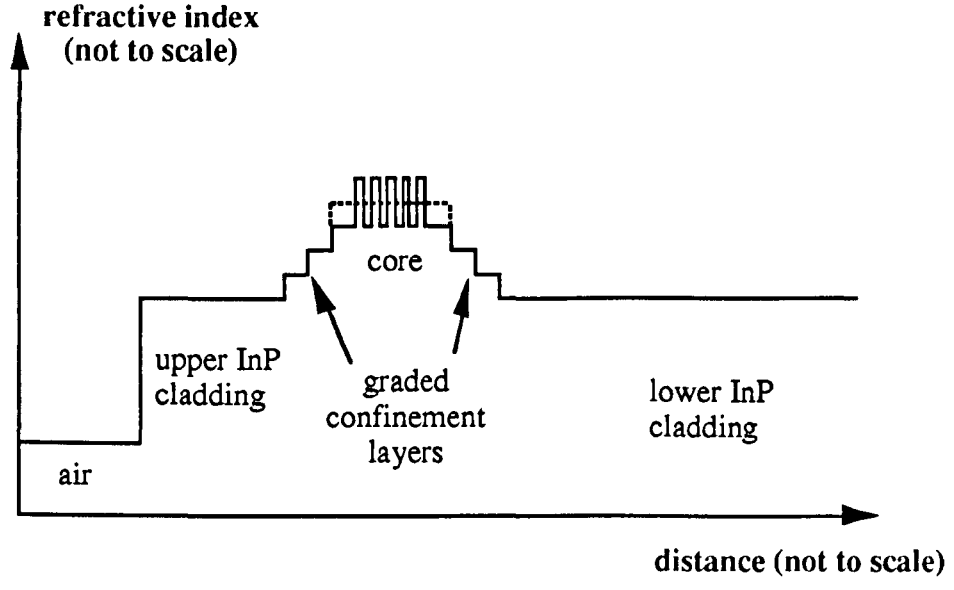

Fig. 19 Schematic diagram of refractive index of the different layers within the waveguide structure

Using these two different models, the effective indices calculated for the three regions were 3.1705, 3.209, and 3.1705 for TE polarised light. The effective index in regions I and III is much lower than region II because the upper cladding has been entirely etched away, resulting in a greater portion of the guided mode extending to the air. The original 2-D model has been greatly simplified to a 3-layer 1-D case as described previously. This problem can be solved simply using a program called FOURLAY[12].

Calculations carried out using this program indicate that the waveguides remain single-moded in the transverse direction for widths up to 1.8 μm. These results are not entirely consistent with experimental observations, with waveguides of wider dimensions exhibiting single-mode behaviour. The second order modes which will propagate in the waveguides which are wider than 1.8 μm will be quite leaky, which means that they will not contribute to the Fabry-Perot oscillations. It should be noted that waveguides were determined to be single moded from both their near-field pattern and the shape of the Fabry-Perot oscillations.

4.5.2 Experimental Results

Guiding was in fact observed in all the waveguides (15 in total) with the larger guides being multi-mode in the transverse direction, as predicted by the calculations in section 4.5.1. Figs. 20 and 21 show the different near-field patterns for single and multi-mode waveguides

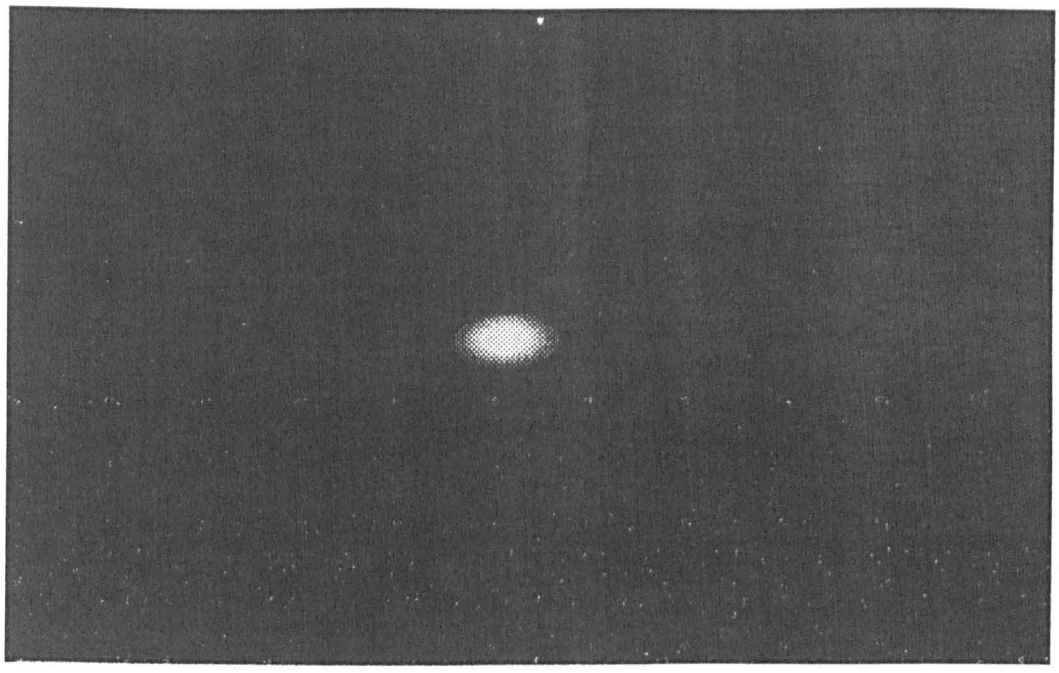

Fig. 20 Near field pattern of single mode waveguide showing the TE_{00} mode propagating.

Fig. 21 Near field pattern of double mode waveguide showing the TE_{01} mode propagating.

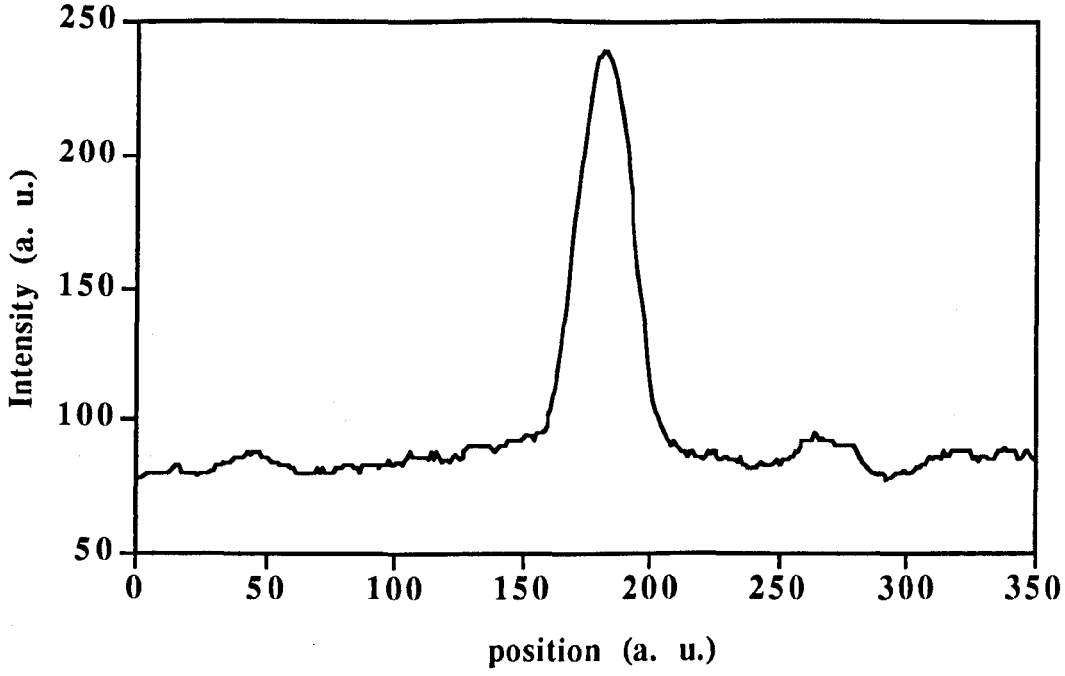

Fig. 22 Intensity profile of TE_{00} mode

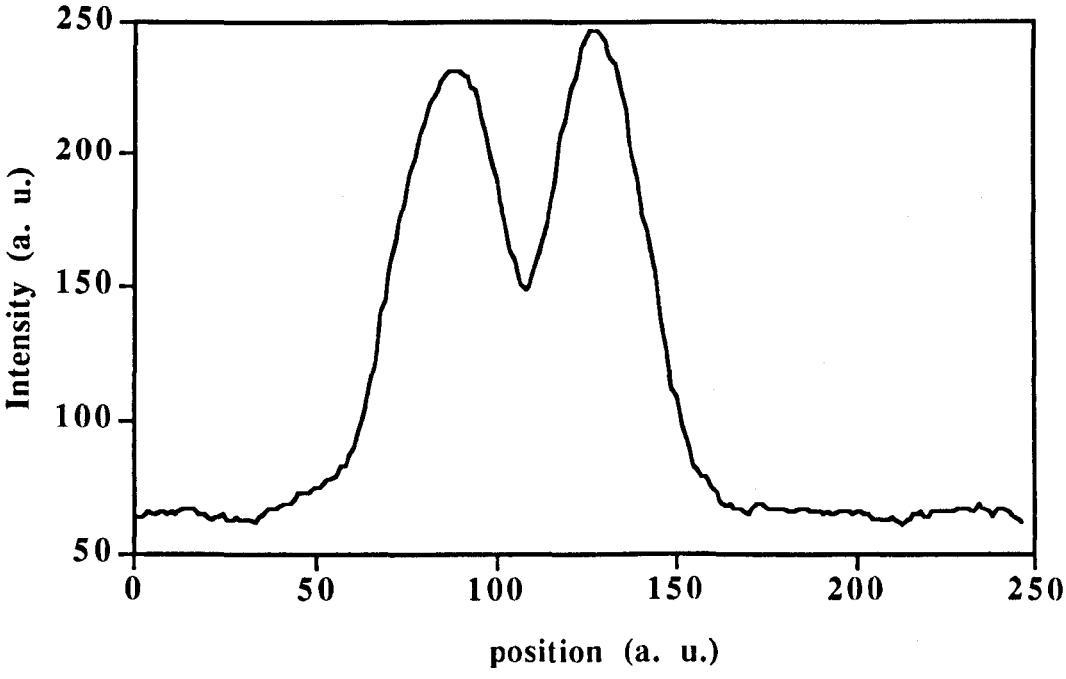

Fig. 23 Intensity profile of the TE_{01} mode

Loss measurements were carried out on the largest waveguide which exhibited apparently single mode behaviour (about 2 μm measured on the SEM.) Fig. 24 shows the loss measured as a function of wavelength in the range 1510 nm to 1570 nm.

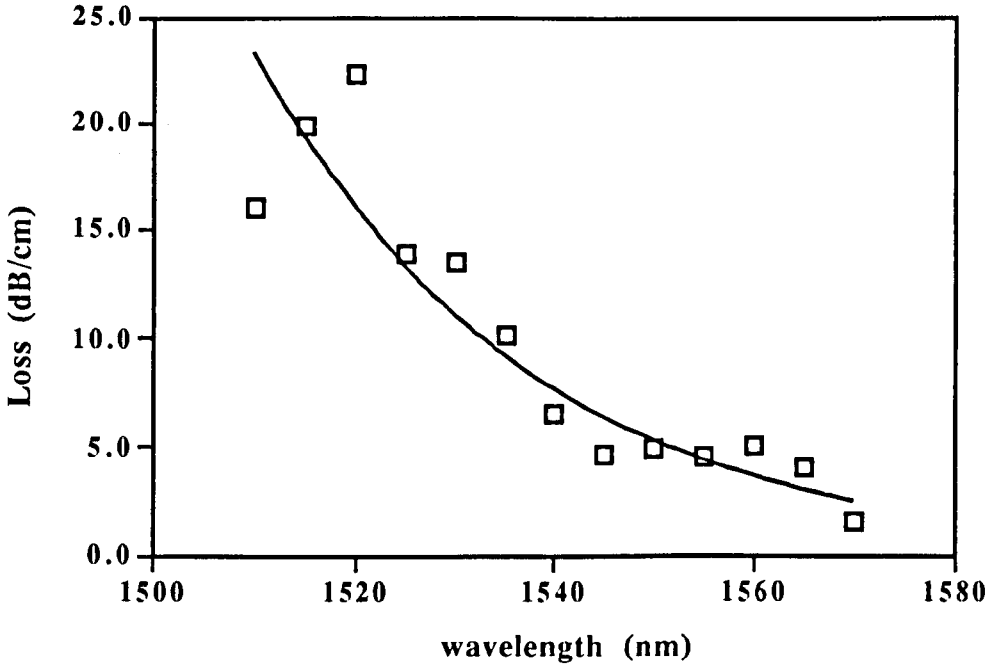

Fig. 24 Single mode waveguide loss as a function of wavelength

The loss calculated from the peak to trough ratio of the Fabry-Perot transmission oscillations indicates the absolute single pass loss in decibels. Dividing this loss by the length of the waveguide gives the loss in $dBcm^{-1}$.

Losses in this material should be quite low as the band-edge of the material has been shifted by a substantial amount. At higher wavelengths (lower energy) the losses will be mainly due to scattering from rough interfaces[13] (both epilayer boundaries and etched waveguide sidewalls) and absorption losses from impurities in the material. At shorter wavelengths the losses will rise as the tail of the band-edge is encountered and the absorption increases. Free-carrier absorption should not contribute greatly to the losses as the cladding layers are undoped. Such doping, as would be found in a typical laser structure, would contribute approximately a further 5-10 $dBcm^{-1}$ to the values observed here. It is evident from this graph that the losses are very low, with a value of 5 $dBcm^{-1}$ at a wavelength of 1550 nm, the wavelength at which integrated devices in the InP system will operate. The loss is actually as low as 1.6 $dBcm^{-1}$ at a wavelength of 1570 nm, which is close to the original PL peak wavelength of the material. These results compare favourably with Impurity Induced Disordering[14] (fluorine) where

typical losses were around 8.4 $dBcm^{-1}$ at 1550 nm. This superiority is to be expected, however, as no impurities are introduced at any stage during the PAID process which could cause damage in the crystal structure and increase the scattering losses.

4.6 Conclusions

These results (propagation losses of below 10 $dBcm^{-1}$) demonstrate that PAID is an effective way of producing low loss interconnecting waveguides for use in photonic integrated circuits.

---

1 R.J. Deri, E. Kapon, IEEE Journal of Quantum Electronics, **27**(3), pp 626-640, 1991

2 Integrated Optics : Theory and Technology, R.G. Hunsperger, Springer Series in Optical Sciences, Vol. 33, Springer-Verlag

3 D.W. Hewark, J.W.Y. Lit., Applied Optics, **26**(5), pp 833-841, 1984

4 Electromagnetic Principles of Integrated Optics, D.L. Lee, J. Wiley and Sons, New York, 1986

5 Properties of Indium Phosphide, INSPEC EMIS Datareviews Series No. 6

6 R.G. Walker, Electronics Letters, **21**, p 581, 1985

7 Integrated Optoelectronics, K.J. Ebeling, Springer-Verlag

8 M.W. Fleming, A. Mooradian, IEEE Journal Quantum Electron., **QE-17**, pp 44-59, 1981

9 Properties of Indium Phosphide, INSPEC EMIS Datareviews Series No. 6

10 S. Adachi, Journal of Applied Physics, **53**(12), p 8775, 1982

11 S. Ohke, T. Umeda, Y. Cho, Optics Communications, **56**(4), pp 235-239, 1985

12 Program written by Bindi Bhumbra (former Research Student in Dept.)

13 R.J. Deri, E. Kapon, Applied Physics Letters, **54**(18), pp 1737-1739, 1989

14 S.A. Bradshaw, J.H. Marsh, R.W. Glew, IEEE Proceedings Fourth International Conference on Indium Phosphide and Related Materials, Newport, April 1992

Chapter 5 Broad Area Oxide Stripe Lasers

5.1 Introduction

This chapter deals with the fabrication and testing of Broad Area Oxide Stripe Lasers using as-grown multiple quantum well (MQW) laser material. By fabricating devices such as these it is possible to determine different material characteristics (e.g. threshold current density, internal quantum efficiency and propagation losses) and how they vary when the material is intermixed.

5.2 General Theory of a Fabry-Perot Laser Oscillator

The equation of a simple model of a Fabry-Perot cavity. was given in Chapter 4 as:

$$\frac{E_t}{E_i} = \left| \frac{Te^{-ikl}e^{-\alpha l/2}}{1 - Re^{-2ikl}e^{-\alpha l}} \right| \tag{5.1}$$

From the above equation relating the transmitted and incident electric field intensities, it can be seen that if the denominator becomes zero then, for an incident wave with finite amplitude, the transmitted wave will have infinite amplitude. The condition for laser oscillation requires a round trip net gain equal to one and is the threshold required for amplification to take place within the cavity. To introduce gain to the model, we modify the losses α in such a way that they are the difference of the intrinsic losses and the gain of the cavity. This can be written as:

$$\alpha = \alpha_i - g \tag{5.2}$$

where α, α_i and g are defined for intensity.
We can now write the threshold condition as:

$$r_1 r_2 \exp\{(g - \alpha_i)l\} \exp\{-2ikl\} = 1 \tag{5.3}$$

where r_1 and r_2 are the electric field reflection coefficients. Solving the real part of this equation yields the threshold gain, g_{th}, required for lasing to occur.

$$r_1 r_2 \exp\{(g_{th} - \alpha_i)l\} = 1 \tag{5.4}$$

$$\Rightarrow g_{th} = \alpha_i + \frac{1}{l}\ln\left(\frac{1}{R}\right) \tag{5.5}$$

where $R = r_1 r_2$.

This gain, g_{th}, is the gain required to overcome the intrinsic losses of the cavity (both absorption and scattering) and the losses (due to transmission) at the cleaved mirror facets, in order that amplification and laser oscillation can occur.

Solving the imaginary part of equation (5.3) gives:

$$\exp(-2ikl) = 0 \tag{5.6}$$

$$\Rightarrow 2kl = 2m\pi \quad (m = 1,2,3,....) \tag{5.7}$$

where

$$k = \frac{2\pi n_{eff}}{\lambda}$$

$$\Rightarrow \lambda_m = \frac{2n_{eff}l}{m} \quad (m = 1,2,3,....) \tag{5.8}$$

These values of λ are the Fabry-Perot (or longitudinal) modes of the cavity and indicate the wavelengths at which lasing will take place. The spacing of these modes is given by:

$$\Delta\lambda = \frac{\lambda^2}{2nl(1 - \frac{\lambda}{n}(\frac{d\lambda}{dn}))} \tag{5.9}$$

and is typically 0.9 nm for a 400 μm InGaAs(P) multiple quantum well laser operating at 1.55 μm. This value is much less than the width of a gain curve of a typical semiconductor laser and it is for this reason that more than one Fabry-Perot (longitudinal) mode may be supported in the cavity.

5.3 Application to Multiple Quantum Well Lasers

5.3.1 Loss in an MQW laser

The loss in an MQW laser is due to a combination of free-carrier absorption in the cladding layers, bulk absorption within the active region and scattering losses.

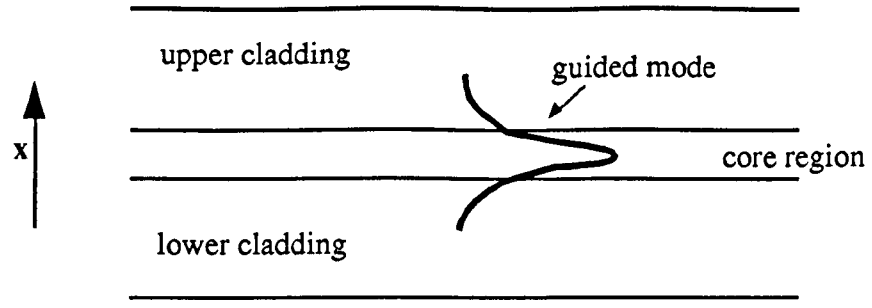

Fig. 1 Schematic diagram of optical overlap of guided mode with cladding layers

The free-carrier absorption arises from the optical overlap of the guided mode with the doped p and n cladding layers. Equations (5.10) give the expression which relates the total power in a mode to the power in the cladding layers, which is an important consideration when calculating the free-carrier absorption loss in an MQW laser.

$$\Gamma_n = \frac{\int_{-\infty}^{-d/2} P(x).dx}{\int_{-\infty}^{\infty} P(x).dx} \qquad ,\Gamma_p = \frac{\int_{d/2}^{\infty} P(x).dx}{\int_{-\infty}^{\infty} P(x).dx} \tag{5.10}$$

where the x-direction is defined as perpendicular to the plane of the quantum wells and the active region extends from -d/2<x<d/2. P(x) is the power and the denominator in both equations is equal to the total power in the laser.

These equations give the fraction of the total power which is present in the n and p-type cladding layers which must be multiplied by the absorption coefficient (for both the p-type cladding and the n-type) to determine the actual loss within the laser cavity. This absorption coefficient for a free electron is given in Eq. (5.11) which would suggest that the n-type cladding will contribute more absorption due to the different effective masses. This, however, is not the case because of the different band structure in the conduction and valence bands which leads to more absorption in the p cladding layers[1].

$$\alpha_{fc} = \frac{Ne^3\lambda_0^2}{4\pi^2 n(m^*)^2 \mu\varepsilon_0 c^3} \tag{5.11}$$

where, N is the doping level in the cladding layer (either n-type or p-type),
e is the charge of an electron,
λ_0 is the free-space wavelength of the guided light,
n is the refractive index of the cladding layers,
m^* is the effective mass of the free carriers (for n-type and p-type)
μ is the mobility,

ε_0 is the dielectric constant of air, and
c is the speed of light in a vacuum.

The bulk absorption in the active region is due to interband absorption between the conduction and valence bands due to the wavelength of the light being close to the bandgap of the quantum wells. Again, the confinement must be taken into account as only a certain fraction of the power will overlap with the quantum wells. Equation (5.10) can be simply modified to calculate this confinement factor.

Another important loss mechanism in InP based lasers is interband Auger recombination[2]. This arises when an electron in the conduction band relaxes into the valence band with the energy (and momentum) being conserved by promoting an electron from within the valence or within the conduction band to a higher energy. Since no photon is emitted in this process, it is said to be non-radiative.

5.3.2 Gain in an MQW Laser

The effective gain of an MQW laser up to threshold can be expressed as[34]:

$$g(J) = n\Gamma_w g_0 \ln\left(\frac{\eta_i J}{nJ_T}\right) \tag{5.12}$$

where J is the total injected current density in units of Acm^{-2},
n is the number of wells,
J_T is the transparency current for one well in units of Acm^{-2},
Γ_w is the optical overlap of the mode profile with one well,
η_i is the internal quantum efficiency of the material, and
g_0 is the maximum gain coefficient for one well

Fig. 2 shows a typical gain curve for a MQW laser with n=5, Γ=0.02, g_o=600 cm^1, J_T=30 Acm^{-2}, and η_i =80 %.

The transparency current, J_T, is defined as the injected current density required to overcome the intrinsic losses in a well and produce net gain for that well, assuming an internal quantum efficiency equal to 1 (i.e. there is a 100 % conversion factor from injected carriers to created photons). A factor of η_i must be introduced which allows for material imperfections and has the effect of increasing the injected current density required to achieve this transparency.

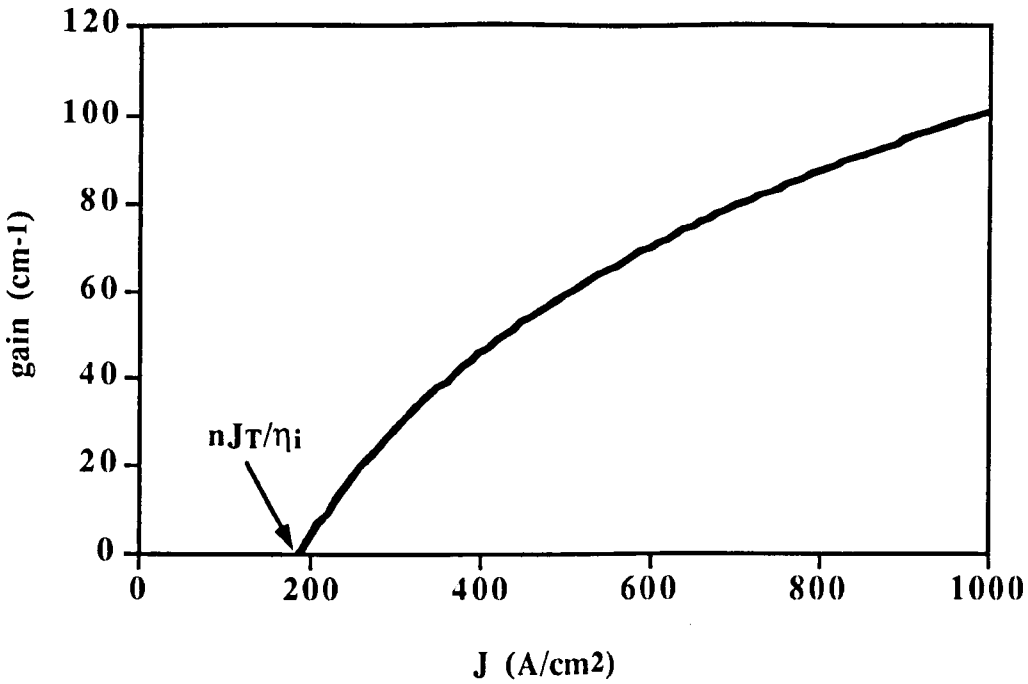

Fig. 2 Gain curve for a typical MQW laser

If the current density is increased above the lasing threshold current density then the gain does not increase but remains constant (just below g_{th} due to spontaneous emission where g_{th} is the gain at threshold) The extra injected electrical power is converted into optical power with a conversion factor given by:

$$\eta_{ex} = \eta_i\left(1-\frac{\alpha}{g_{th}}\right) \tag{5.13}$$

where η_{ex} is defined as the differential external quantum efficiency.

Combining equations (5.5) and (5.13) gives:

$$\frac{1}{\eta_{ex}} = \frac{1}{\eta_i}\left(1-\frac{\alpha l}{\ln(R)}\right) \tag{5.14}$$

Using equation (5.14), it is possible to calculate the intrinsic loss, α, and the internal quantum efficiency, η_i, of the laser by plotting $1/\eta_{ex}$ against the cavity length, l. It is now possible to modify equation (5.5) to incorporate the gain in a quantum well structure.

$$g_{th} = \alpha_i + \frac{1}{l}\ln\left(\frac{1}{R}\right) \tag{5.15}$$

If we incorporate the threshold gain given in equation (5.12) then:

$$n\Gamma_w g_0 \ln\left(\frac{\eta_i J_{th}}{nJ_T}\right) = \alpha_i + \frac{1}{l}\ln\left(\frac{1}{R}\right) \tag{5.16}$$

$$\Rightarrow J_{th} = \frac{nJ_T}{\eta_i}\exp\left(\frac{\alpha_i + \frac{1}{l}\ln\left(\frac{1}{R}\right)}{n\Gamma_w g_0}\right) \tag{5.17}$$

where J_{th} is the injected threshold current density. If we take the natural log of both sides, we obtain:

$$\ln(J_{th}) = \ln\left(\frac{nJ_T}{\eta_i}\right) + \frac{\alpha}{n\Gamma_w g_0} + \frac{1}{L}.\frac{\ln(1/R)}{n\Gamma_w g_0} \tag{5.18}$$

The threshold current density, J_{th}, can be determined as a function of cavity length which makes it possible to calculate J_{th} for an infinitely long laser and also the gain factor, $n\Gamma_w g_0$, of the lasers.

5.4 Fabrication of Oxide Stripe Lasers

5.4.1 Laser Structure

The laser structure as shown in Fig. 3 was grown by metal organic vapour phase epitaxy (MOVPE) on an n+ doped (Si) InP substrate and consisted of five 85 Å InGaAs wells with 120 Å InGaAsP (λ_g = 1.26 μm) barriers. The active region was surrounded by a stepped graded index (GRIN) waveguide core consisting of InGaAsP confining layers. The thicknesses and compositions of these layers (working out from the QWs) were 500 Å of InGaAsP (λ_g = 1.18 μm) and 800 Å of InGaAsP (λ_g = 1.05 μm). The structure, which was lattice matched to InP throughout, was completed with an InP upper cladding layer and a InGaAs contact layer. The first 0.2 μm of the upper cladding layer was doped with Zn to a concentration of 5 x 10^{17} cm^{-3} and the remaining 1.2 μm to 2 x 10^{18} cm^{-3}. The lower cladding layer was Si doped to a concentration of 1 x 10^{18} cm^{-3}. The waveguide core was undoped, so forming a *pin* structure with the intrinsic region restricted to the QWs and the GRIN region.

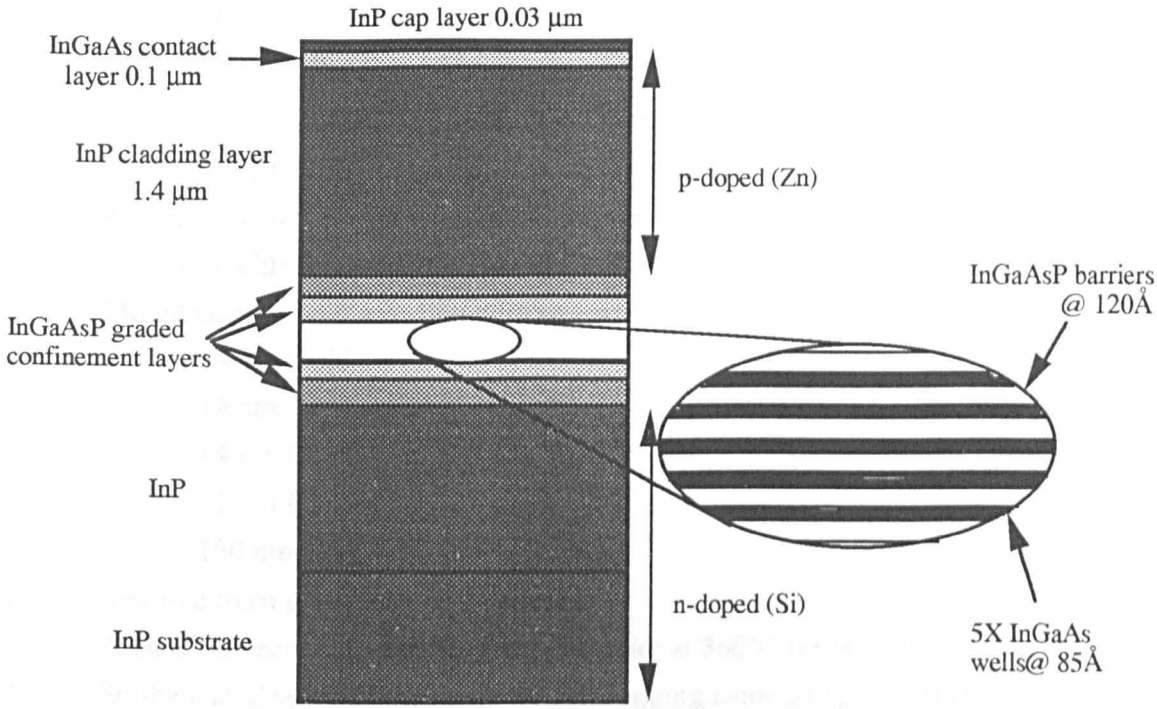

Fig. 3 Laser Structure

5.4.2 Fabrication Process

The fabrication process is described in detail below:

1. Clean sample in ultrasonic bath: 3 mins. methanol,
   3 mins. acetone,
   rinse in RO water
2. Etch off InP cap layer with HCl : H_3PO_4 (in ratio 1:3) for 20 secs.
3. Plasma-Enhanced Chemical-Vapour-Deposition (PECVD) of 200 nm SiO_2
   Power = 10 watts
   Gas flow : SiH_4 = 9 sccm, N_2O = 710 sccm, N_2 = 171 sccm
   Temperature=300°C
   Pressure=1 torr
3. Spin on primer : dihexamethylsylane
4. Spin on resist : S1400-31 @ 6000 rpm for 30 secs
5. Post bake for 30 mins. @ 90°C
6. Expose with pattern of 75 μm windows spaced by 300 μm
7. Develop pattern for 60 secs.
8. Wet-etch SiO_2 in buffered HF for 15 secs.
9. Remove resist with Acetone
10. Mount sample in holder for p-contact evaporation

70 nm Titanium

150 nm Gold

11. Mount sample on small glass slide with resist for thinning
12. Thin sample to 200 μm using 9 μm alumina grit
13. Thin sample to 150 μm using 3 μm alumina grit
14. Wet-etch with HCl : H_3PO_4 (in ratio 1:3) for 10 mins. to remove any damage
15. Mount sample on glass slide with resist for n-contact evaporation

    14 nm Gold

    14 nm Germanium

    14 nm Gold

    11 nm Nickel

    150 nm Gold
16. Remove from glass slide with acetone
17. Anneal contacts in Rapid Thermal Annealer at 360°C for 90 secs.
18. Scribe and cleave samples with lengths ranging from 200 μm to 1000 μm

Fig. 4 shows a schematic diagram of the lasers which are now ready for testing.

5.5 Testing Lasers

5.5.1 Test Procedure for L-I-V characteristics

Fig. 5 shows the experimental set-up used to test lasers. The rig is fully automated and is controlled from an Apple Mac computer using LabView (a commercial software package from National Instruments) which allows accurate measurements to be taken very quickly.

The devices are held in a spring-loaded, gold-plated laser clip p-side down in such a way that the output of only one facet was monitored by the detector. Because of the lasing wavelengths under investigation, the detector used was a Germanium photodetector which was reverse biased at 4.5 V.

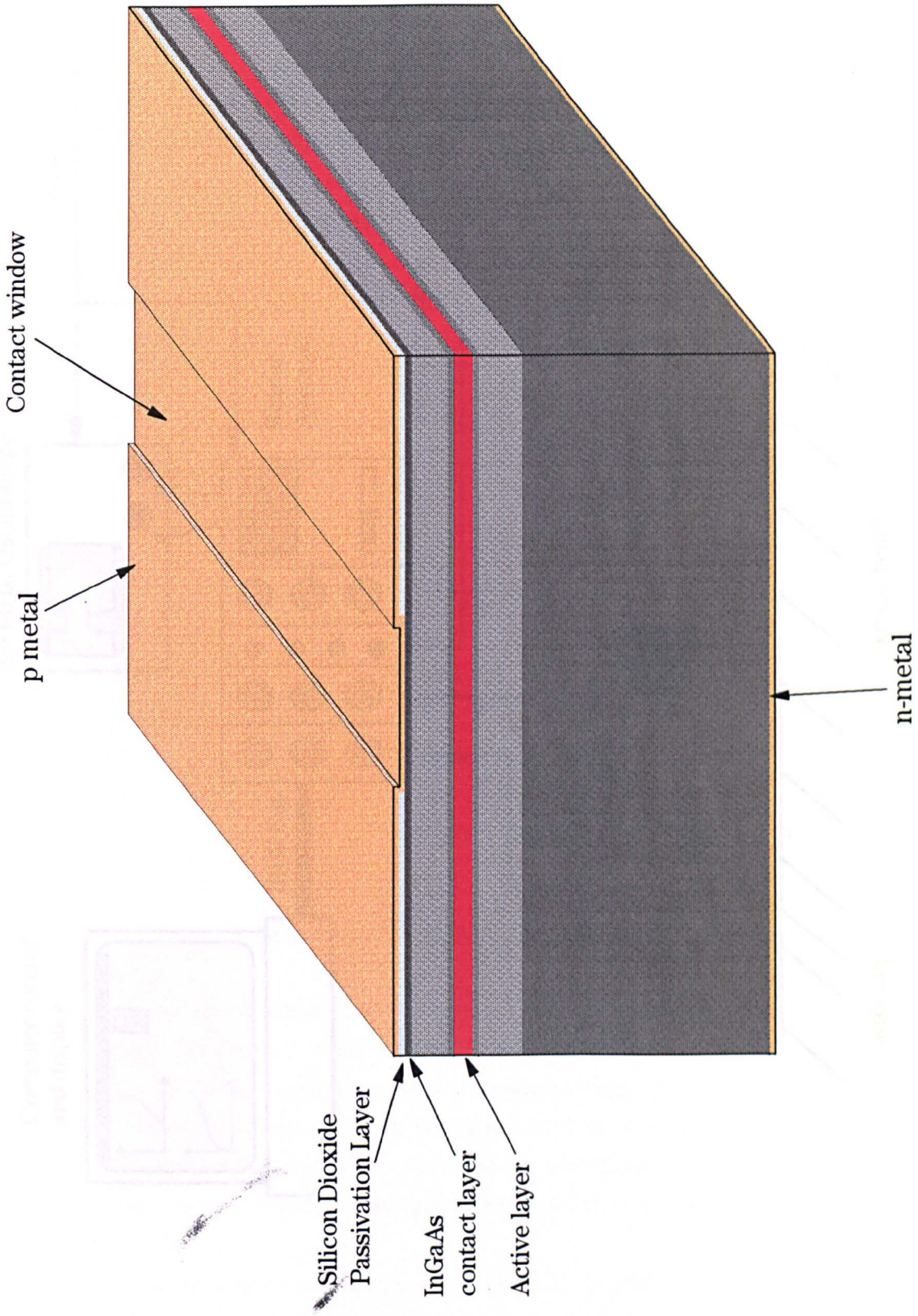

Fig. 4 Schematic diagram of oxide stripe laser

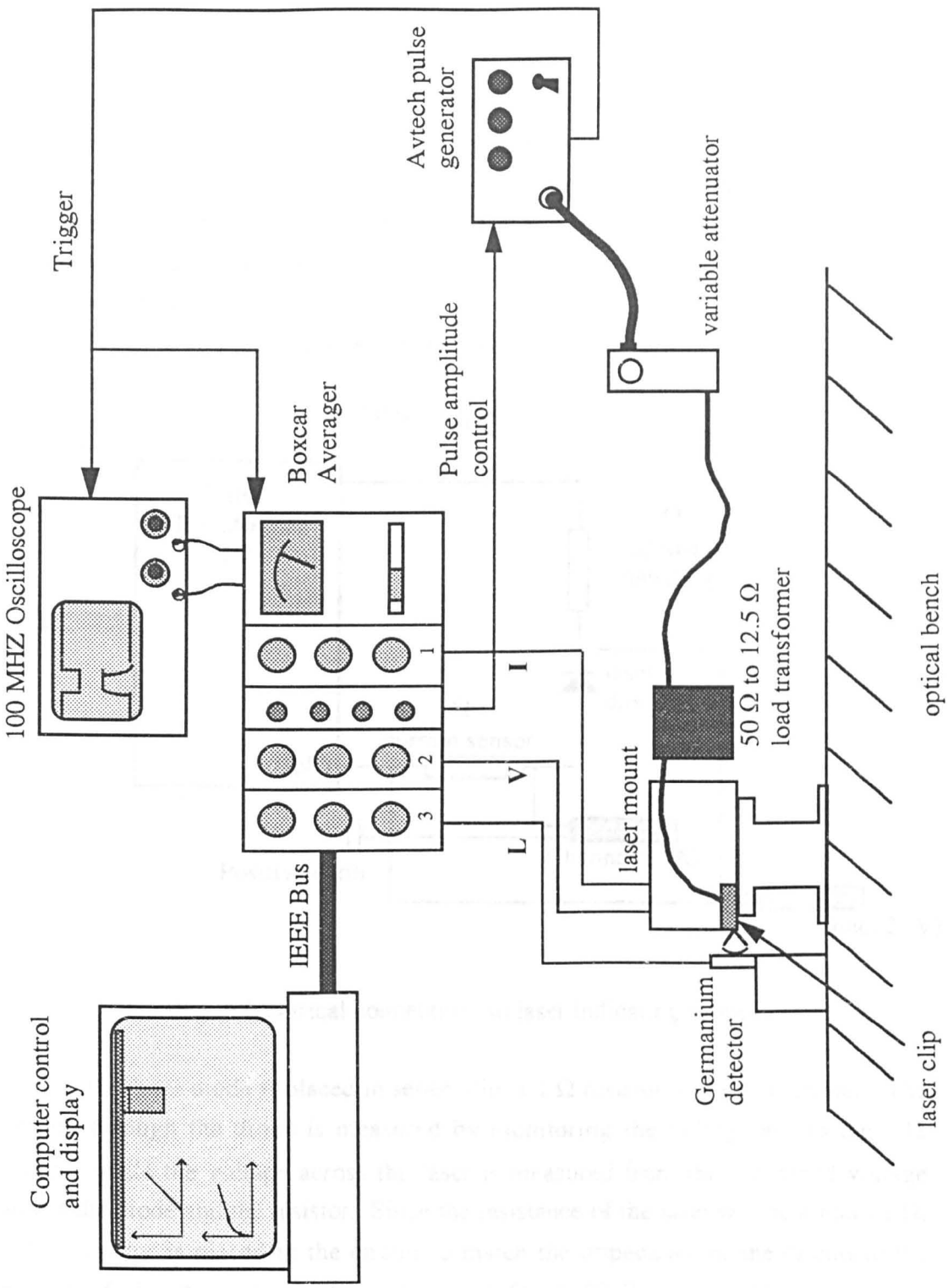

Fig. 5 Experimental set-up for measuring laser characteristics

The current supply is an Avtech pulse generator which has an adjustable pulse width and repetition rate. All pulsed measurements in this thesis were carried out using a 400 ns pulse at a 1 kHz repetition rate (i.e. a duty cycle of 0.04 %). The pulse generator can be controlled manually or automatically, which allows the lasers to be tested very quickly manually (to see if they work) before taking any accurate measurements. Between the signal generator and the laser there is a variable attenuator and a transformer which allows a wide range of currents to be supplied to the devices (0 to ≈ 4 A).

Fig. 6 shows the circuit which the laser is driven from.

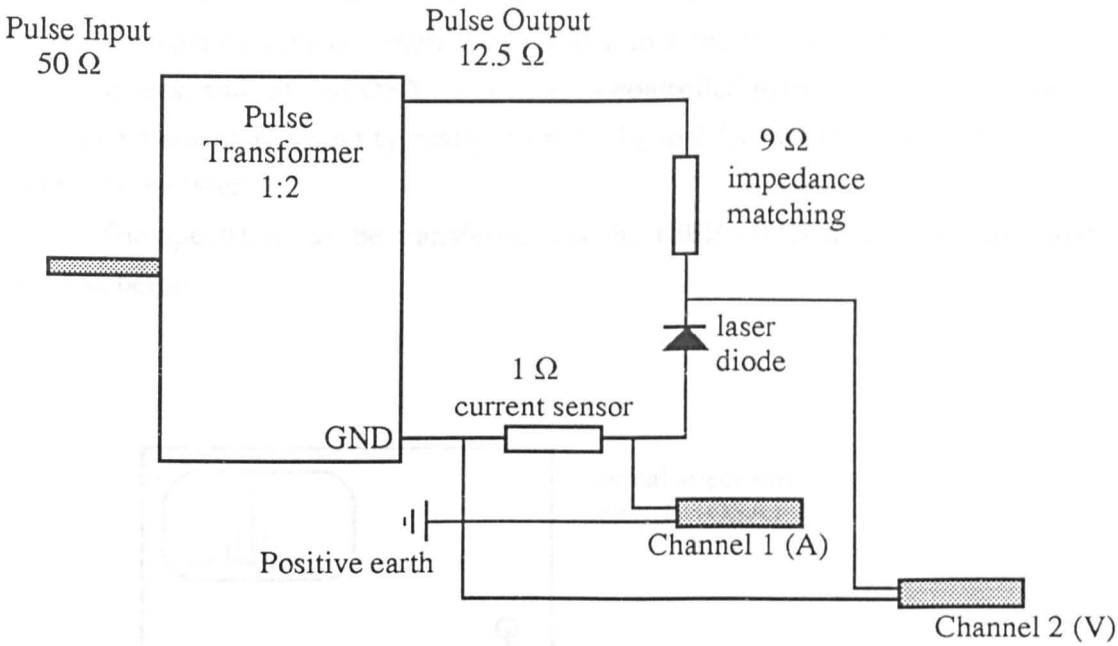

Fig. 6 Electrical connections to laser indicating probes

The laser diode is placed in series with a 1 Ω resistor and a 9 Ω resistor. The current through the diode is measured by monitoring the voltage across the 1 Ω resistor while the voltage across the laser is measured from the combined voltage across the diode and the resistor. Since the resistance of the laser will be around 2 Ω, a 9 Ω resistor is placed in the circuit to match the impedance of the circuit to the output of the Avtech which is designed for a 50 Ω load (allowing for the transformer).

A Boxcar Averager monitors these voltages and also the voltage generated by the Germanium photodetector. It averages the measurements over a number of cycles which reduces the noise from the signals. This data is then transferred to the computer via an IEEE GPIB which then calculates the current through the laser, the

voltage across the laser and the output power from the laser. The data is also displayed on the screen and saved in memory.

The output of the Boxcar Averager is also monitored by an oscilloscope which looks at the current through the laser and the output from the detector and is the main indicator to the operator that the laser is working.

5.5.2 Test Procedure for Spectrum Analysis

It is possible to analyse the spectrum of the lasers, simply by rotating the laser mount by 180° on the optical bench where it is aligned with a collimating lens as seen in Fig. 7. This collimated beam is focused into a multi-mode fibre using a X10 objective lens, and into an OSA. The laser is controlled manually from the Avtech pulse generator at a current typically from 1.5 I_{th} to 2 I_{th}, where I_{th} is the threshold current of the laser.

The spectrum can be transferred via the IEEE GPIB to the computer and saved as before.

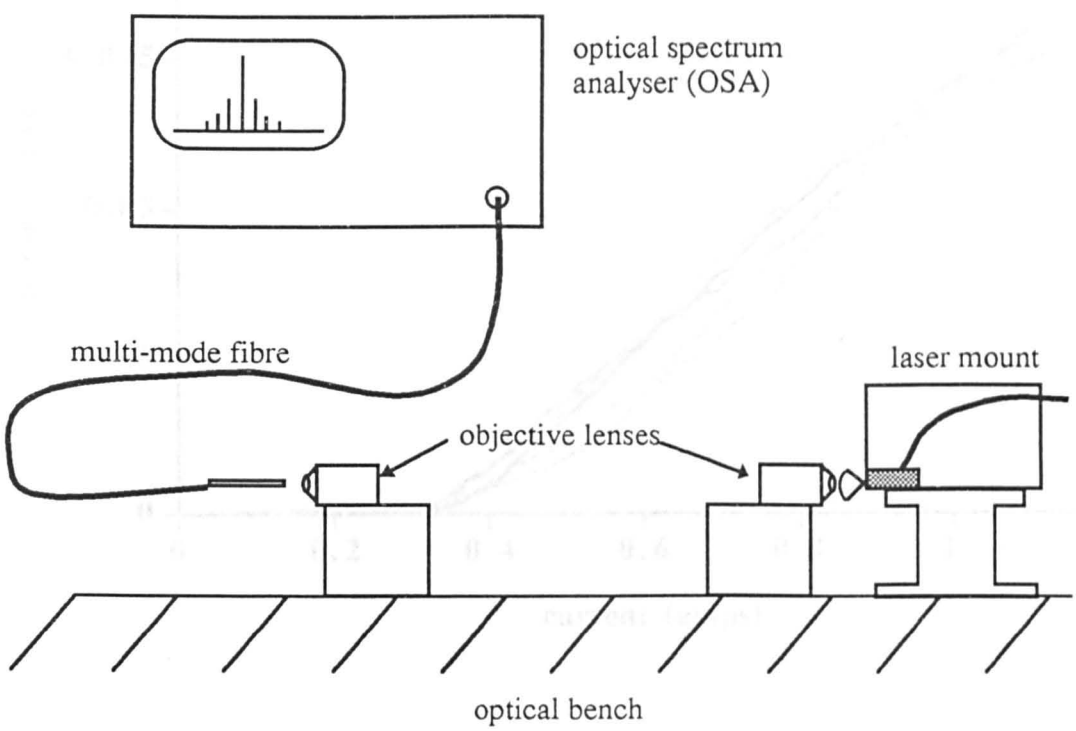

Fig. 7 Experimental set-up for measuring laser spectra

5.6 Results

5.6.1 L-I Characteristics of lasers

The material was tested, with L-I-V measurements taken from lasers with cavity lengths ranging from 200 μm to 1000 μm. Because of imperfections in the material and processing non-uniformities, all lasers do not have similar characteristics. Fig. 8 shows a spread in Light-Current (L-I) performance for a bar of 400 μm long lasers which is typical for all lengths of devices. Also shown in Fig. 9 is the spread in current-voltage (IV) characteristics for the same bar of lasers.

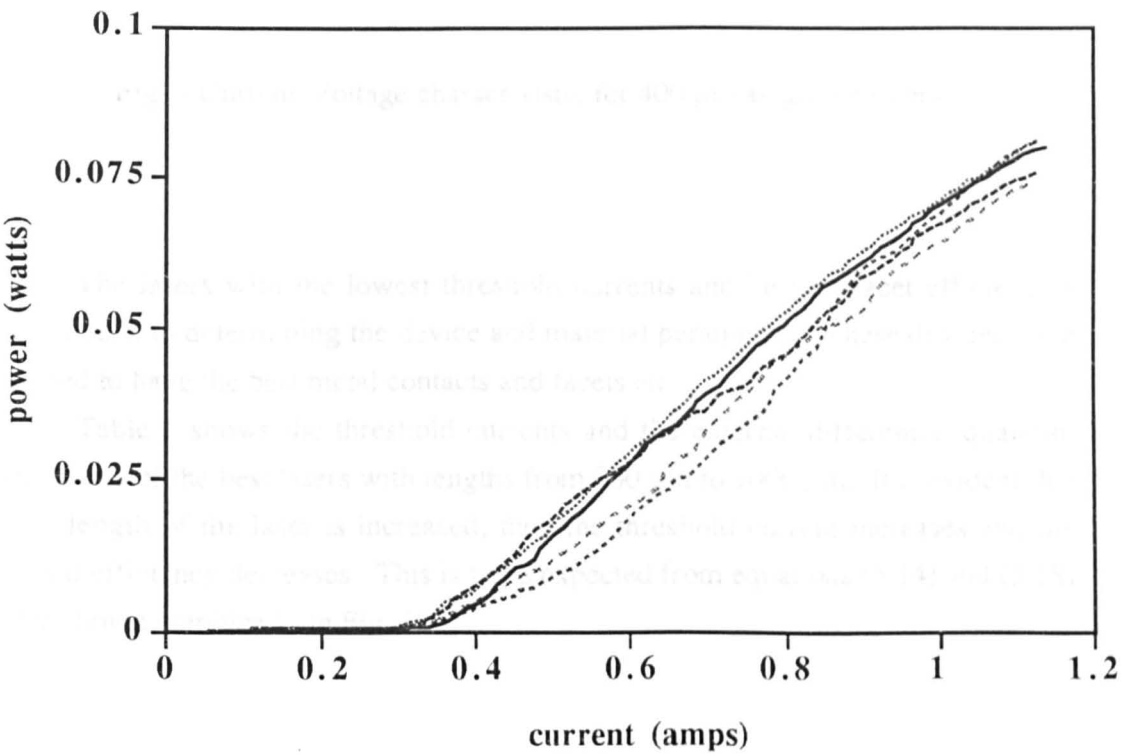

Fig. 8 Light-Current characteristic for 400 μm as-grown lasers

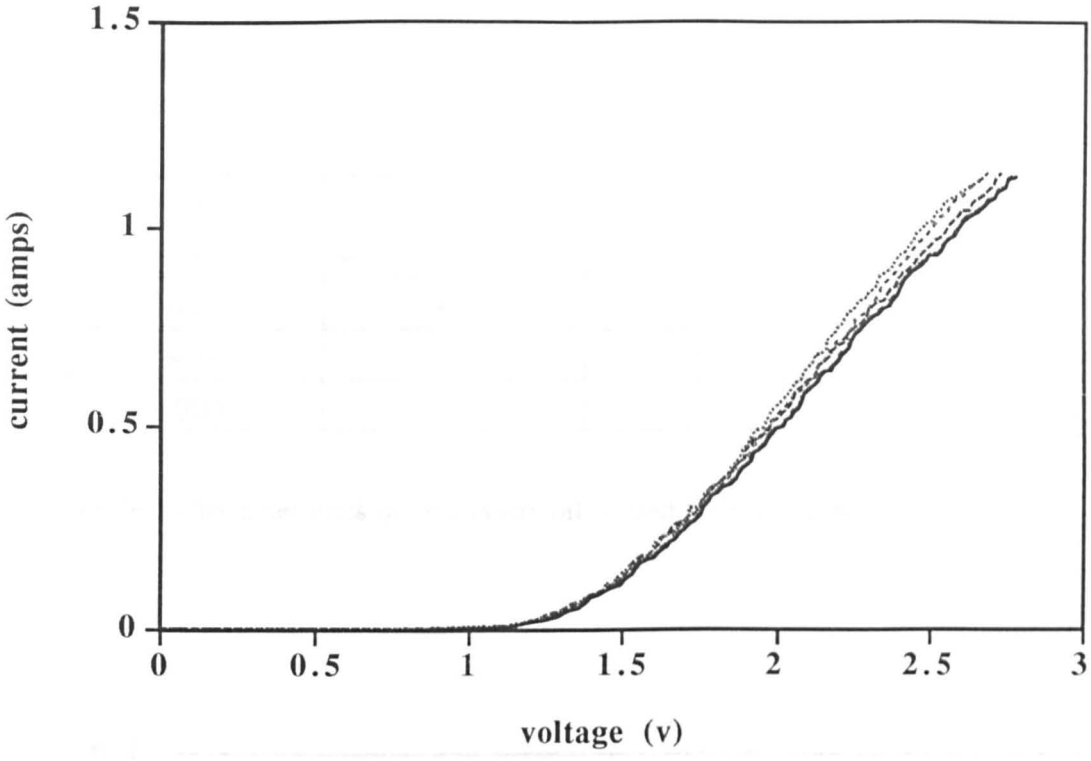

Fig. 9 Current-Voltage characteristic for 400 μm as-grown lasers

The lasers with the lowest threshold currents and best ex-facet efficiencies were chosen in determining the device and material parameters. These devices were assumed to have the best metal contacts and facets etc.

Table 1 shows the threshold currents and the external differential quantum efficiencies of the best lasers with lengths from 200 μm to 1000 μm. It is evident that as the length of the laser is increased, then the threshold current increases and the external efficiency decreases. This is to be expected from equations (5.14) and (5.18) and is shown graphically in Fig. 10.

length (μm)	Threshold current (mA)	External quantum efficiency (mW/mA)
200	330	0.151
400	333	0.106
600	370	0.0952
800	450	0.08
1000	500	0.061

Table 1 Characteristics of best lasers fabricated from as-grown material

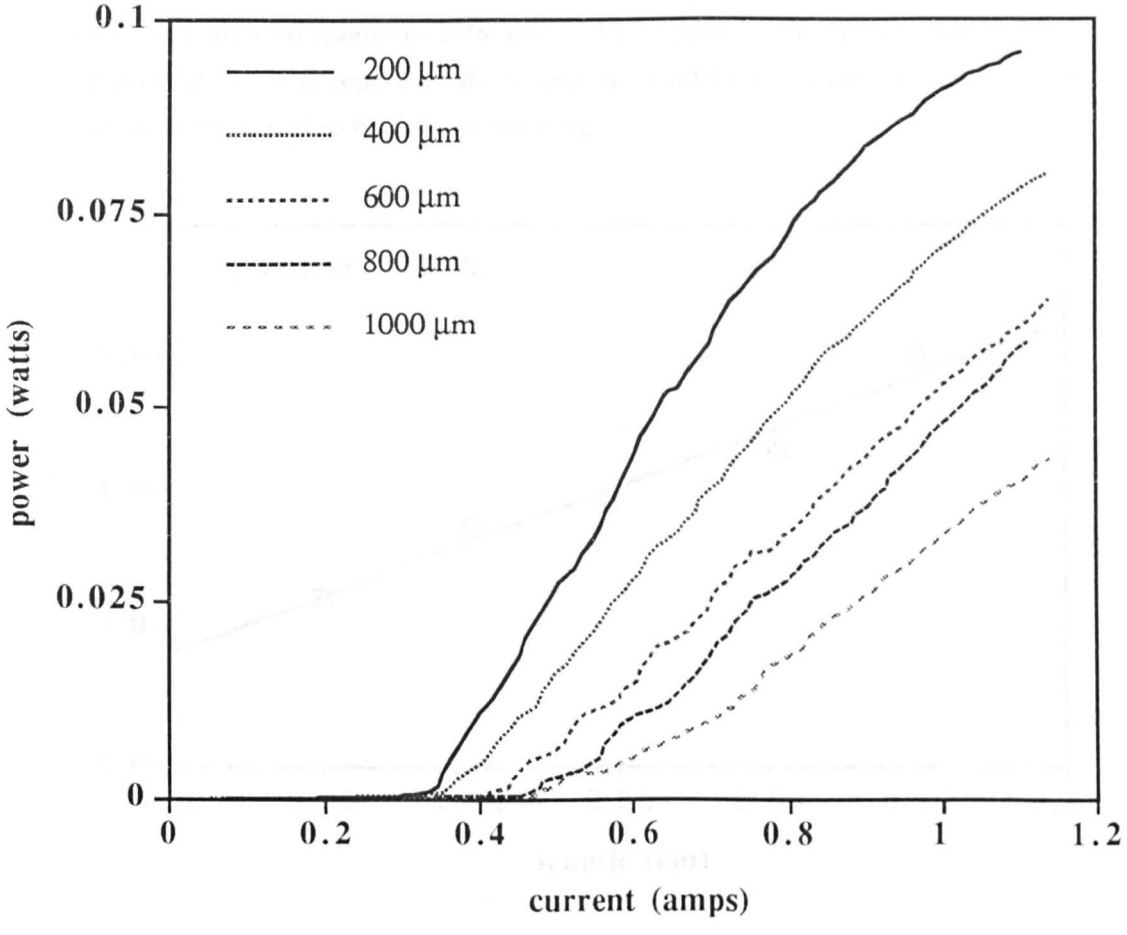

Fig. 10 Light-Current characteristics for different cavity length lasers

Using these results, it is now possible to calculate the threshold current density for an infinitely long cavity, the internal quantum efficiency and the propagation loss of the material using the equations described previously.

The external efficiency measured by the Germanium photodetector is in units of milliwatts per milliamp. However, the photodetector has a non-uniform response at these wavelengths and requires to be calibrated as a function of the emission wavelength of the laser. Calibration is relatively simple if the spectral response of the detector is known which can usually be found in data sheets. After calibrating these results, the efficiency can then be expressed in units of emitted photons per injected electrons by multiplying by a factor of $\frac{e\lambda}{hc}$ which is equal to $\frac{\lambda}{1.242}$ where λ is expressed in μm. This gives the external quantum efficiency per facet (as the detector only monitors the output from one facet) which must be multiplied by 2 to give the correct external efficiency. It is assumed here that the output power from both facets is equal which should be the case for a symmetrical Fabry-Perot laser. Fig. 11 is a plot of the inverse of the external efficiency as a function of cavity length from which the internal quantum efficiency can be found. From equation (5.14) it can be seen that the intercept with the y-axis is equal to the inverse of the internal efficiency which is equal to 62.2 % in this case.

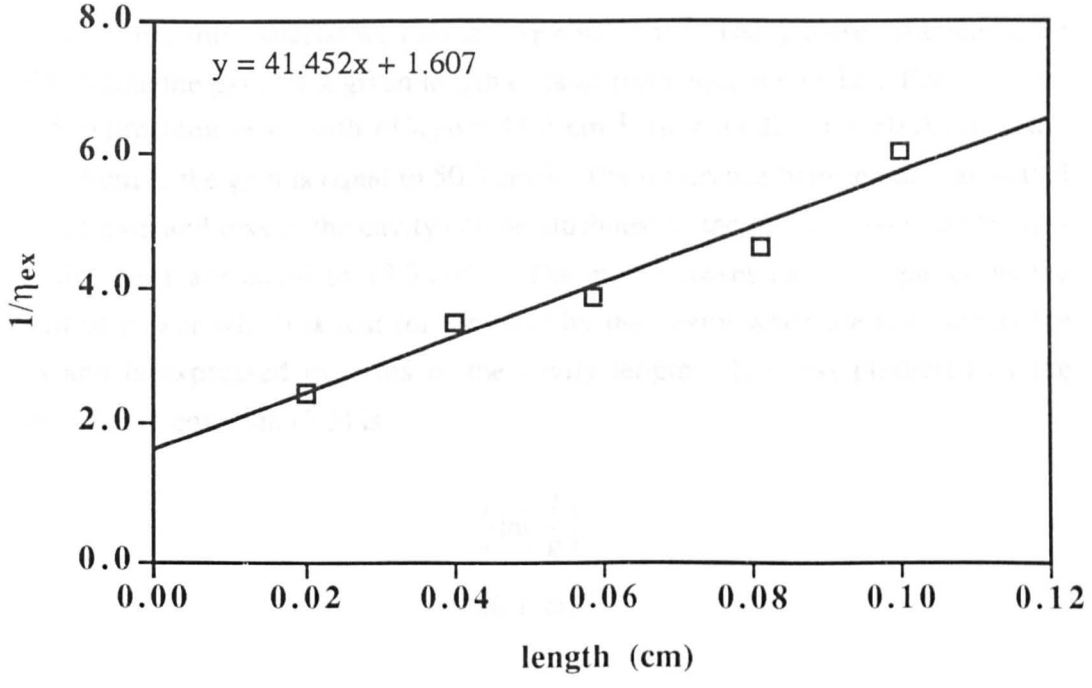

Fig. 11 Graph of inverse of external efficiency as a function of length

Equation (5.14) also states that the gradient of the graph is equal to $-\alpha/\eta_i \ln(R)$ from which the loss of the material at the lasing wavelength, α, can be easily found. Assuming R=0.3 and η_i=0.622, α for this material is equal to 31 cm^{-1}.

The threshold current density for each laser is simply given by:

$$J_{th} = \frac{I_{th}}{lw} \tag{5.19}$$

where l is the length of the laser and w is the width of the oxide stripe. Fig. 12 shows a plot of $\ln(J_{th})$ against 1/L from which the threshold density for an infinitely long laser can be inferred. The intercept on the y-axis (where L=∞) yields a value of 491 Acm^{-2} which indicates that the material is of good quality. The gain factor, $n\Gamma_w g_0$, can be found from the gradient of this graph assuming a power reflection coefficient of R=0.3. For these devices the gain factor is equal to 41.5 cm^{-1}. If we return to equation (5.16), it is apparent that the threshold current density of 491 Acm^{-2} is equal to:

$$\ln\left(\frac{nJ_T}{\eta_i}\right) + \frac{\alpha}{n\Gamma_w g_0} \tag{5.20}$$

Since we have calculated η_i, α and $n\Gamma_w g_0$, it is possible to evaluate the transparency current, J_T. For this material we find that J_T =30 Acm^{-2}. Using these parameters, we can determine the gain for a given length of laser from equation (5.12). For example, for a 600 μm long laser with $n\Gamma_w g_0$ = 41.5 cm^{-1}, η_i = 0.622, J_T = 30 Acm^{-2}, and J = 810 Acm^{-2}, the gain is equal to 50.3 cm^{-1}. The difference between the calculated values of gain and loss in the cavity can be attributed to the mirror losses and for this particular laser are equal to 19.3 cm^{-1}. The mirror losses can be regarded as the amount of power which is lost (or emitted) by the cavity when the light meets the facets and is expressed in terms of the cavity length. The loss predicted by the second term in equation (5.5) is :

$$\frac{1}{l}\ln\left(\frac{1}{R}\right)$$
$$= 20.1 \ cm^{-1}$$

and therefore shows close agreement with the measured value.

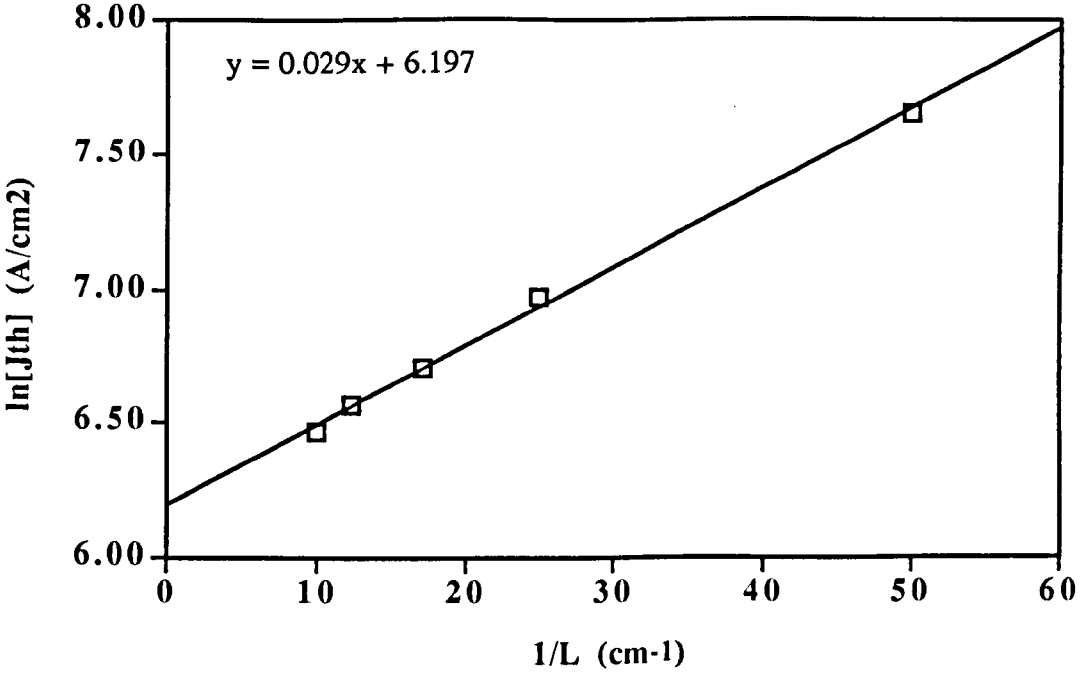

Fig. 12 Graph of $\ln(J_{th})$ against 1/L of as-grown material

5.6.2 Lasing Spectra of Lasers

Because shorter lasers require a higher threshold current density to achieve lasing, their lasing wavelength alters. A higher threshold current will cause band-filling in such a way as to increase the energy of the emitted photons and reduce the lasing wavelength of the device.

Fig. 13 shows the output spectrum of lasers with three different lengths, 200 μm, 600 μm, and 1000 μm, with a bias current of around 1.5 I_{th}. It is obvious that, as the length of the laser increases (and the current density decreases), the lasing wavelength increases. This wavelength variation (which is of the order of 20 nm in this case) leads to small errors in the calculated quantum efficiencies due to the wavelength dependence of photon energy. However, these errors have been ignored for simplification purposes and each length of laser is assumed to emit at the same wavelength.

It is also worth noting that the spacing of the Fabry-Perot (longitudinal) modes decreases from about 1.73 nm for a 200 μm long laser to 0.36 nm for a 1000 μm laser. These are in good agreement with results predicted by equation (5.9).

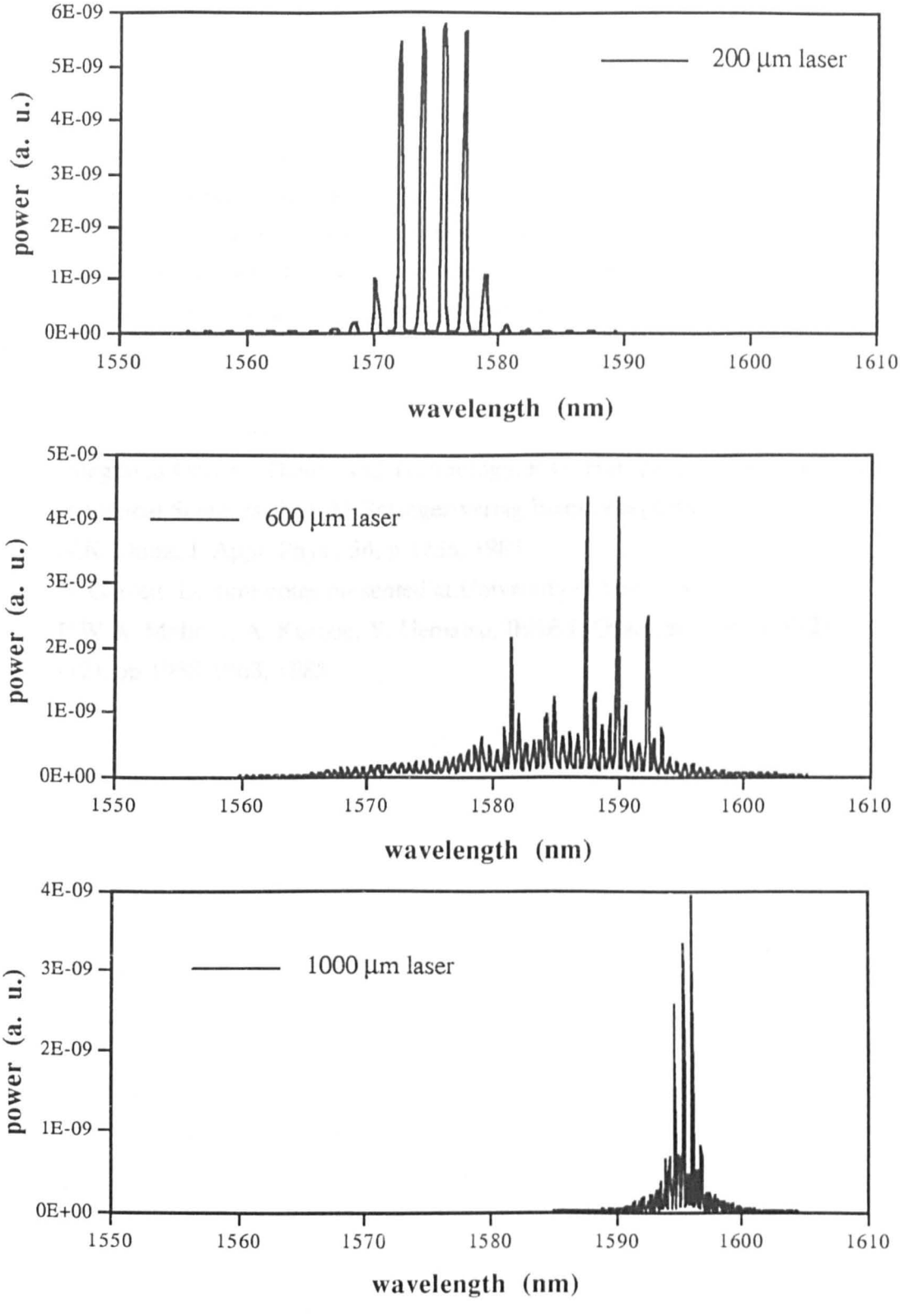

Fig. 13 Spectra of different length lasers under similar bias conditions

5.7 Conclusions

By fabricating broad area oxide stripe lasers of different lengths, the electrical and optical properties of the as-grown material have been thoroughly examined. The threshold current density, internal quantum efficiency, transparency current, gain, and loss have been determined and the lasing spectra of different length lasers have been examined. The same parameters will allow monitoring of the electrical and optical properties of material which has been intermixed to determine if any significant degradation in material quality or device performance occurs and this is found in Chapter 6.

---

1 Integrated Optics : Theory and Technology, R.G. Hunsperger, Springer Series in Optical Sciences, Vol. 33 Springer-verlag Electromagnetic

2 N.K. Dutta, J. Appl. Phys., 54, p 1236, 1983

3 B. Garrett, Lecture notes presented at University of Glasgow

4 P.W.A. McIlroy, A. Kurobe, Y. Uematsu, IEEE J. Quantum Elec., **QE-21** (12), pp 1958-1963, 1985

Chapter 6 Bandgap Tuned Broad Area Oxide Stripe Lasers

6.1 Introduction

Intermixing MQW structures can also be used to shift the gain envelope of as-grown material to allow lasers with a range of tuned wavelengths to be fabricated from a single wafer. Integrated arrays of lasers with different wavelengths have many applications, e.g. in wavelength division multiplexing (WDM) and instrumentation.

By fabricating Oxide Stripe Lasers from material which has been intermixed by different amounts it is possible to determine how the intermixing affects the optical and electrical properties of the material.

6.2 Fabrication

The material used to fabricate the lasers was identical to that used in Chapter 5 with the samples being 5 mm x 5 mm in size. The material was disordered using a ceramic heat sink as described in Chapter 3, with a relatively large laser spot size of FWHM = 2.9 mm. The use of a ceramic heat sink meant that the temperature profile of the sample was much more uniform (see Chapter 10) than simply placing the sample on the polished molybdenum. Material was intermixed by varying degrees with room temperature photoluminescence (PL) peak shifts of approximately 40 nm, 100 nm, and 140 nm.

As the samples were heated using a Gaussian profiled laser beam, the sample was not uniformly heated over its entire area, despite the use of the ceramic insulator. This meant that slightly less disordering occurred around the edges of the samples, where the temperature was lower compared with the more uniform central region. For this reason there was a range of lasing wavelengths obtained from each sample, typically a spread of about 30 nm, so only lasers from the centre of the samples (with a wavelength spread of around 10 nm) were used for assessment.

6.3 Results

Fig. 1 shows the spectra of 600 μm long oxide stripe lasers fabricated from the samples intermixed by 40 nm, 100 nm, and 140 nm respectively. From the graphs, it is clear that the gain envelope of the material has not broadened measurably as the wells and barriers have intermixed. This result indicates that wells are disordering by the same amount, irrespective of depth within the epitaxial structure,

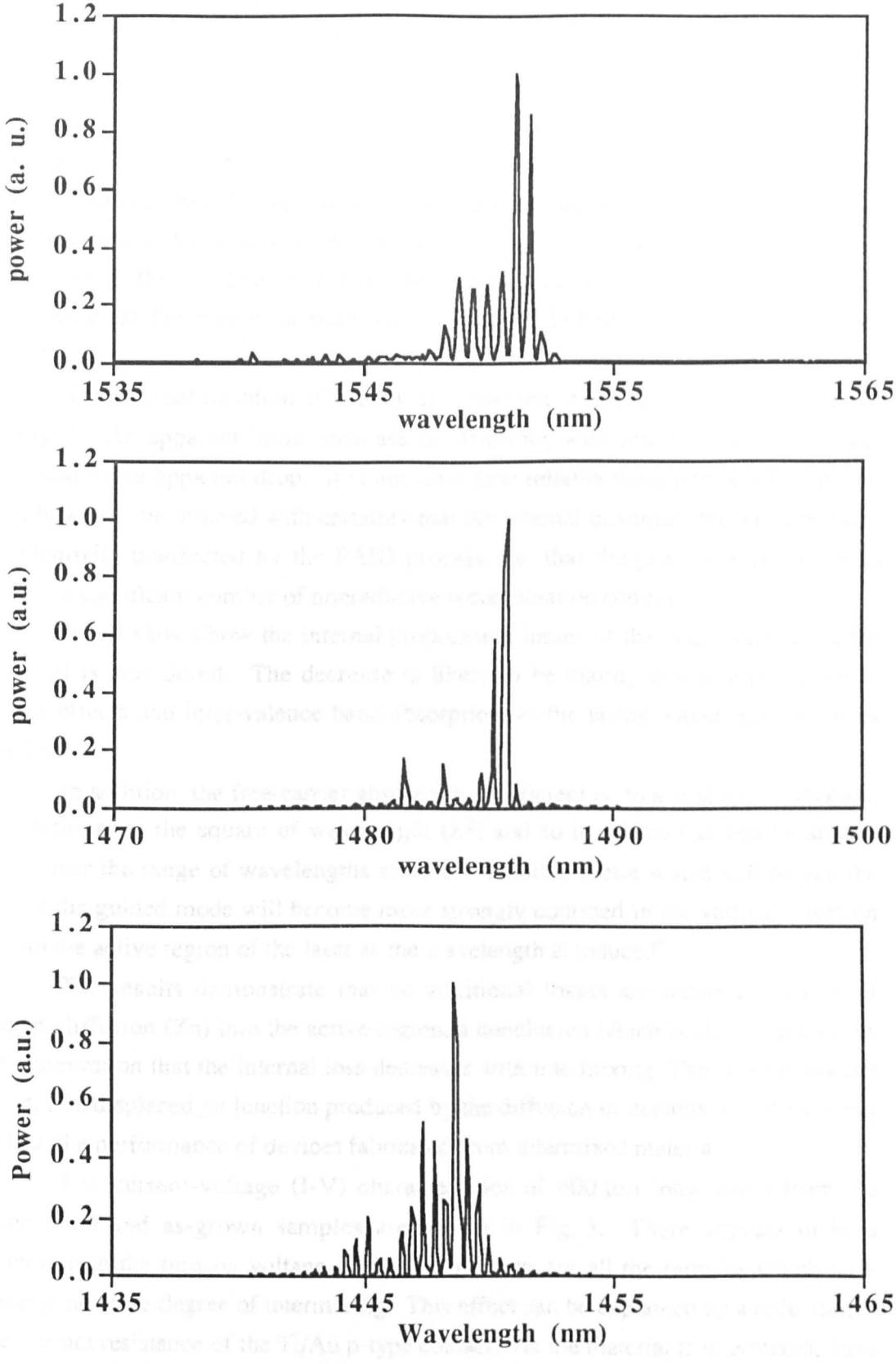

Fig. 1 Lasing spectra of 600 μm long lasers from samples intermixed by 40 nm, 100 nm and 140 nm

which is to be expected because of the thermal nature of the disordering process and the close spacing of the wells. The material parameters were then calculated for the three samples using the methods described in Chapter 5.

The threshold current density for infinite cavity length as a function of lasing wavelength is plotted in Fig. 2. As the material is intermixed and the lasing wavelength becomes shorter, the threshold current density increases from a value of 490 Acm^{-2} for the as-grown material to 600 Acm^{-2} for material which has been shifted by 150 nm. This is due to the current required to achieve transparency increasing[1] as the density of states changes from 2-D like to bulk like (see section (2.4.2)).

The internal quantum efficiency as a function of lasing wavelength is plotted in Fig. 3. An apparent initial increase in efficiency with intermixing is observed, followed by an apparent drop. It is not clear how reliable these trends really are. It can, however, be inferred with certainty that the internal quantum efficiency remains substantially unaffected by the PAID process, i.e. that the process appears not to induce a significant number of nonradiative recombination centres.

Fig. 4 shows how the internal propagation losses of the laser decrease as the material is disordered. The decrease is likely to be mainly due to a reduction in Auger effects and inter-valence band absorption, as the lasing wavelength becomes shorter[2].

In addition, the free-carrier absorption coefficient is, to a first approximation, proportional to the square of wavelength (λ^2) and so it will be reduced by around 20 % over the range of wavelengths studied[3]. Another factor which will reduce the loss is the guided mode will become more strongly confined in the vertical direction within the active region of the laser as the wavelength is reduced[4].

The results demonstrate that no additional losses are incurred because of dopant diffusion (Zn) into the active region, a conclusion which is also supported by the observation that the internal loss decreases with intermixing. This is an important point, as a displaced *pn* junction produced by the diffusion of dopants would seriously reduce the performance of devices fabricated from intermixed material.

The current-voltage (I-V) characteristics of 600 μm long lasers from the intermixed and as-grown samples are shown in Fig. 5. There appears to be a reduction in the turn-on voltage of around 0.2 volts for all the samples which have undergone some degree of intermixing. This effect can be explained by a reduction in the contact resistance of the Ti/Au p-type contact. As the material is intermixed, there will be Gallium outdiffusion from the InGaAs contact layer into the cap layer of SiO_2. This will cause the composition at the material surface to be a lower bandgap $In_{1-z}Ga_zAs$ ($z < 0.47$) compound[5] which has been reported elsewhere to reduce the

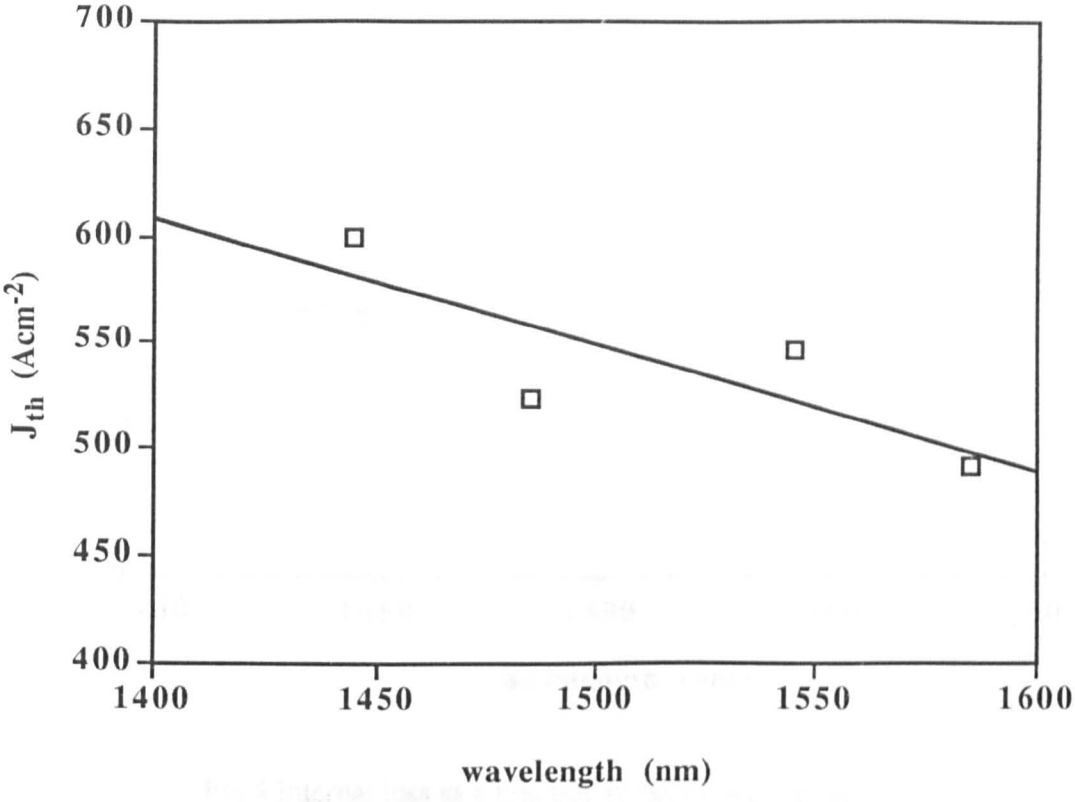

Fig. 2 Threshold current density as a function of lasing wavelength

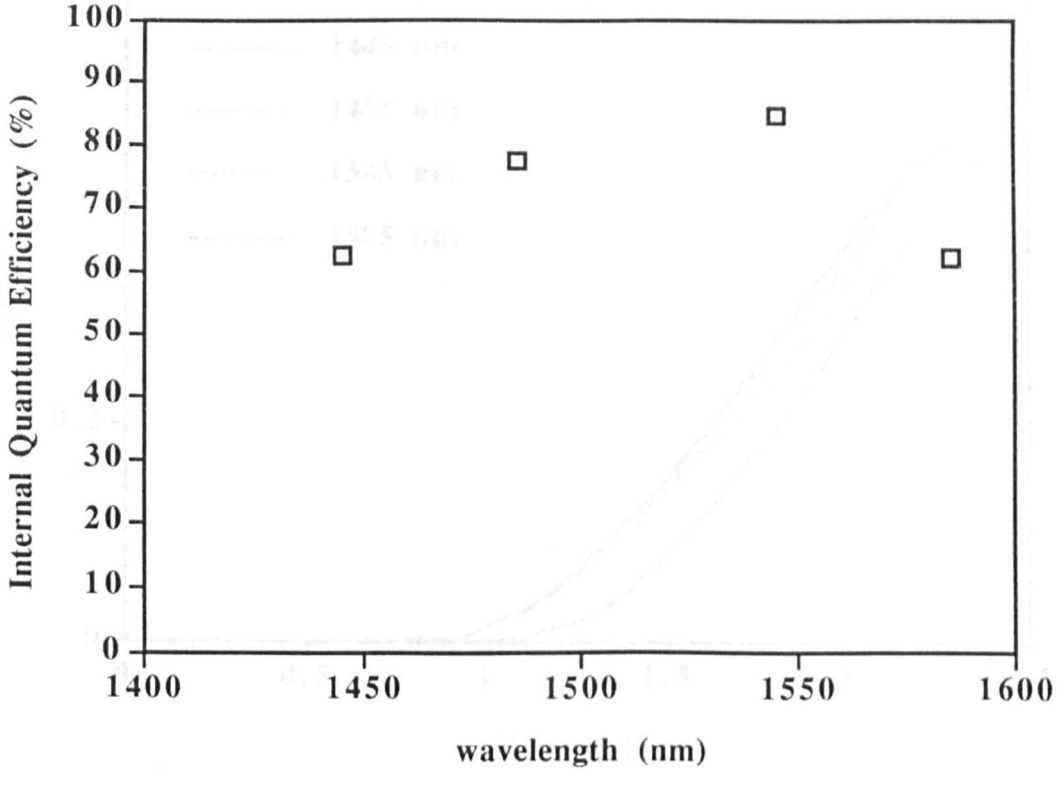

Fig.3 Internal quantum efficiency as a function of lasing wavelength

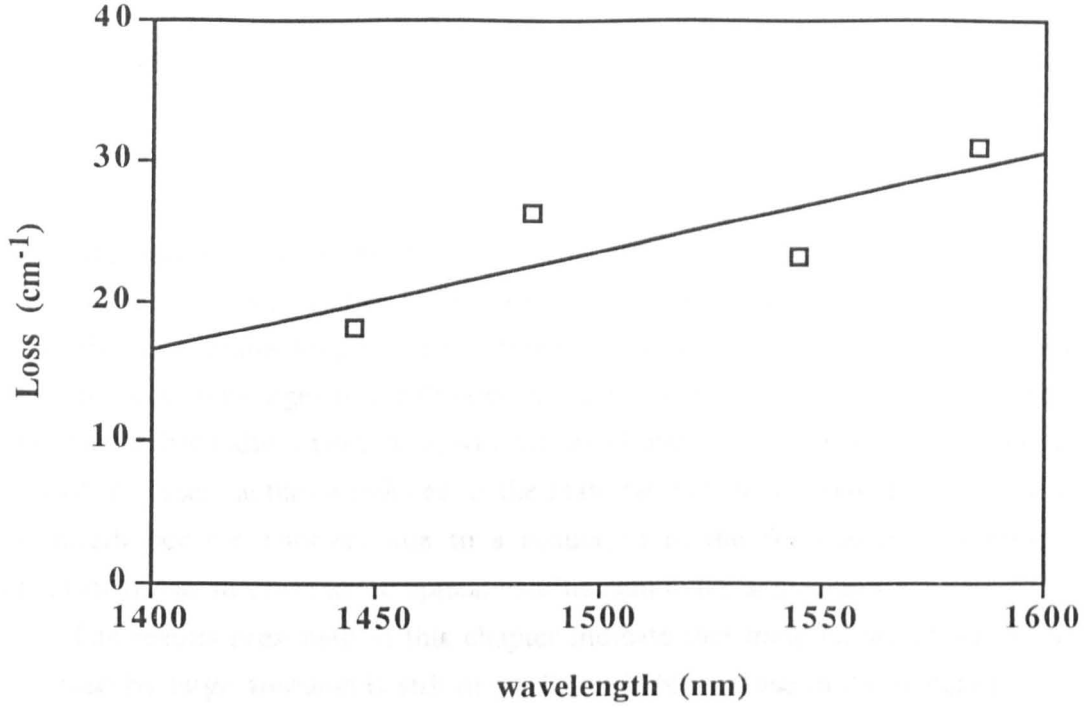

Fig.4 Internal loss as a function of lasing wavelength

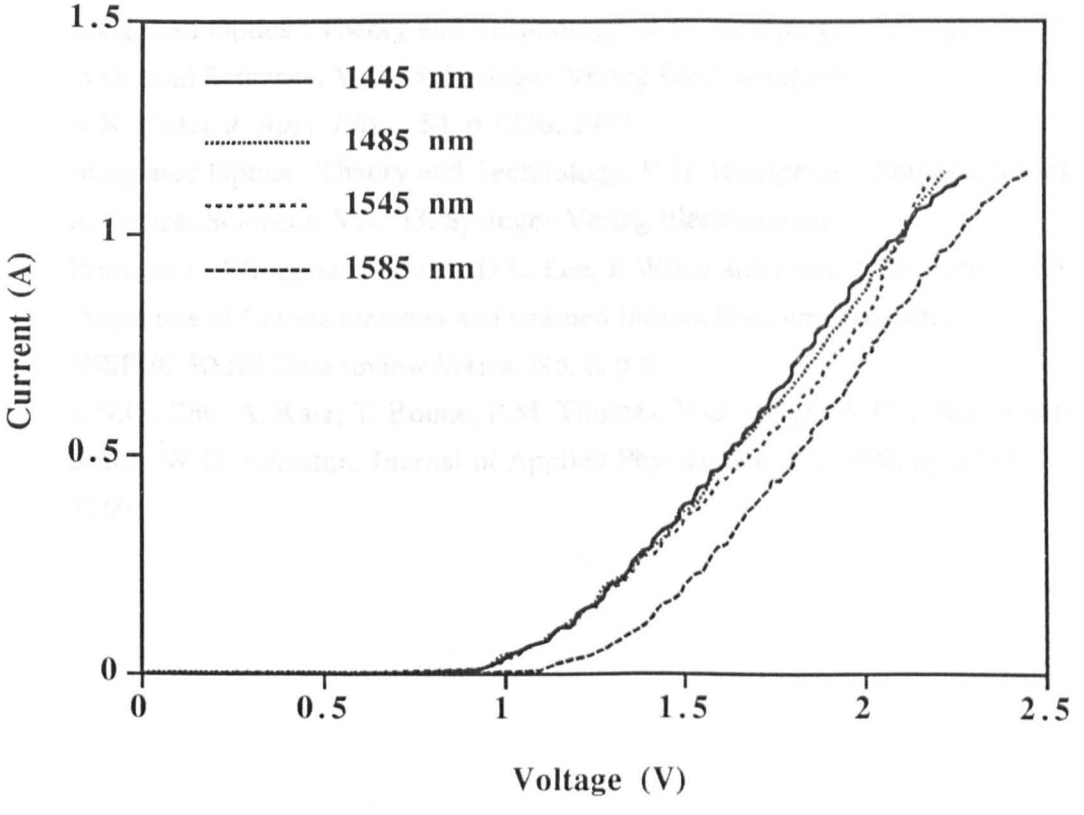

Fig. 5 I-V curves for different lasing wavelengths

contact resistance[6] of Ti/Au contacts by forming a favourable interfacial microstructure.

6.4 Conclusions

Broad area oxide stripe lasers have been fabricated from intermixed material which has been bandgap shifted by up to 140 nm. The threshold current density for lasers with an infinite length cavity increased by only 20% from 490 Acm^{-2} to 600 Acm^{-2} due to changes in the density of states. The internal quantum efficiency also remained high after intermixing with values of over 60% measured. The internal losses of the lasers actually reduced as the material was intermixed (and the lasing wavelength became shorter) due to a reduction in the free-carrier absorption coefficient and an increase in the optical confinement in the active region.

The results presented in this chapter indicate that material which has been intermixed by large amounts is still of quality suitable for use in the integration of devices.

---

1 Integrated Optics : Theory and Technology, R.G. Hunsperger, Springer Series in Optical Sciences, Vol. 33, Springer-Verlag Electromagnetic

2 N.K. Dutta, *J. Appl. Phys.*, **54**, p 1236, 1983

3 Integrated Optics : Theory and Technology, R.G. Hunsperger, Springer Series in Optical Sciences, Vol. 33, Springer-Verlag Electromagnetic

4 Principles of Integrated Optics, D.L. Lee, J. Wiley and Sons, New York, 1986

5 Properties of Lattice matched and strained Indium Gallium Arsenide, INSPEC EMIS Data review Series, No. 6, p 6

6 S.N.G. Chu, A. Katz, T. Boone, P.M. Thomas, V.G. Riggs, W.C. Dautremont-Smith, W.D. Johnston, Journal of Applied Physics, vol. **67**, 1990, pp 3754-3760

Chapter 7 Bandgap Tuned Ridge Waveguide Lasers

7.1 Introduction

The oxide stripe lasers described in Chapter 5 are ideal for checking the quality and various parameters of epitaxially grown laser material. They are also useful practical devices for high power applications, such as pumping solid state lasers, where the mode structure and lasing spectra are not critical. However, when a high degree of phase coherence or minimal dispersion is required, such as in long distance fibre communications, single mode operation becomes a necessity.

In a laser structure, single transverse mode operation can be achieved in a number of ways such as proton bombardment, diffusion of dopants to define current injection, and epitaxially grown buried-heterostructures (BH). Another simple way to achieve single transverse mode operation is to fabricate strip-loaded waveguides in the laser structure, utilising the change in effective index described in detail in Chapter 4. Single longitudinal mode operation is more difficult to achieve (especially in long wavelength lasers where the gain spectrum is quite broad) and typically requires a grating of some sort to be fabricated.

7.2 Fabrication

The material used to fabricate the Ridge Waveguide Lasers (RWLs) was identical to that used in Chapter 5. Fig. 1 shows a schematic diagram of the RWLs fabricated in this chapter. The areas which have been etched away do not extend between consecutive ridges but are only 8 μm wide, thus forming a double trench pattern. Because the mode is quite strongly confined in the transverse direction by the large change in effective index, this should not affect the guiding properties of the ridges and also means that the ridges are effectively protected during subsequent processing and testing. The fabrication process is listed below:

1. Clean sample in ultrasonic bath: 3 mins. methanol,
   3 mins. acetone,
   rinse in RO water
2. Etch off InP cap layer with HCl : H_3PO_4 (in ratio 1:3) for 20 secs.
3. Plasma-Enhanced Chemical-Vapour-Deposition (PECVD) of 500 nm SiO_2
   Power = 10 watts
   Gas flow : SiH_4 = 9 sccm, N_2O = 710 sccm, N_2 = 171 sccm
   Temperature = 300°C

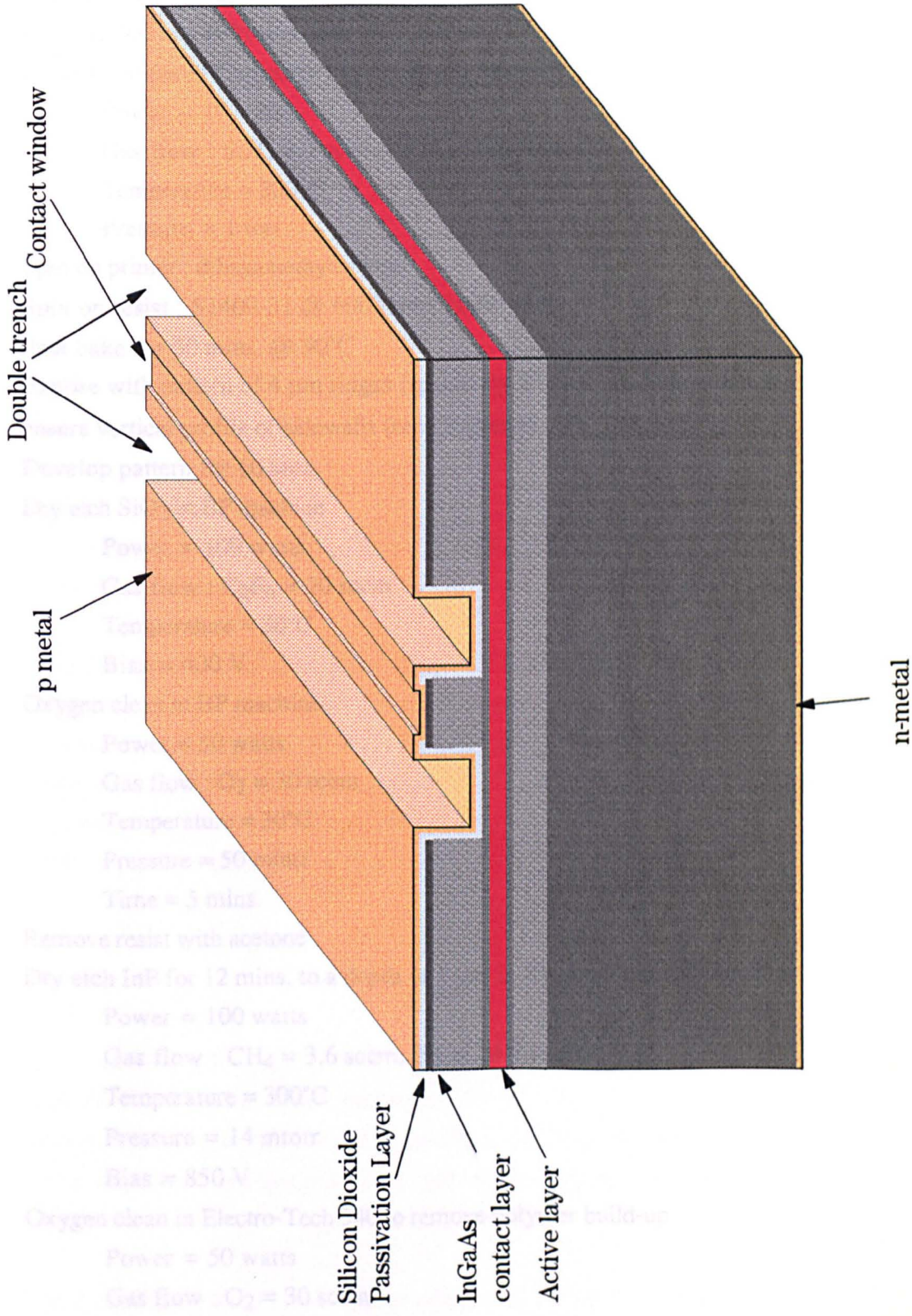

Fig. 1 Schematic diagram of ridge waveguide laser

Pressure = 1 torr

4. Disorder samples as described in Chapter 3
5. Remove 500 nm SiO_2 cap layer with buffered HF for 5 mins.
6. Plasma-Enhanced Chemical-Vapour-Deposition (PECVD) of 200 nm of SiO_2
   Power = 10 watts
   Gas flow : SiH_4 = 9 sccm, N_2O = 710 sccm, N_2 = 171 sccm
   Temperature = 300°C
   Pressure = 1 torr
7. Spin on primer : dihexamethylsylane
8. Spin on resist : S1400-31 @ 6000 rpm for 30 secs
9. Post bake for 30 mins. @ 90°C
10. Expose with pattern of 4 μm ridges (spaced by 300 μm) in β-direction to ensure vertical profile of sidewalls (see Chapter 4)
11. Develop pattern for 60 secs.
12. Dry etch SiO_2 in BP machine
    Power = 100 watts
    Gas flow : C_2F_6 = 20 sccm
    Temperature = 30°C
    Bias = 400 V
13. Oxygen clean in BP machine
    Power = 50 watts
    Gas flow : O_2 = 30 sccm
    Temperature = 30°C
    Pressure = 50 mtorr
    Time = 5 mins.
14. Remove resist with acetone
15. Dry etch InP for 12 mins. to a depth of 1 μm in Electro-Tech 340 machine
    Power = 100 watts
    Gas flow : CH_4 = 3.6 sccm, H_2 = 26.4 sccm
    Temperature = 300°C
    Pressure = 14 mtorr
    Bias = 850 V
16. Oxygen clean in Electro-Tech 340 to remove polymer build-up
    Power = 50 watts
    Gas flow : O_2 = 30 sccm
    Temperature = 30°C
    Pressure = 50 mtorr
    Time = 5 mins.

17. Wet etch remainder of InP cladding layer with HCl : H_3PO_4 (in ratio 1:3) for 90 secs. to etch stop layer
18. Remove SiO_2 with buffered HF
19. Plasma-Enhanced Chemical-Vapour-Deposition (PECVD) of 200 nm of SiO_2
    Power = 10 watts
    Gas flow : SiH_4 = 9 sccm, N_2O = 710 sccm, N_2= 171 sccm
    Temperature = 300°C
    Pressure = 1 torr
20. Spin on primer : dihexamethylsylane
21. Spin on resist : S1400-31 @ 6000 rpm for 30 secs
22. Post bake for 30 mins. @ 90°C
23. Expose with pattern of 3 μm contact windows spaced by 300 μm
24. Develop pattern for 60 secs.
25. Etch SiO_2 with buffered HF for 12 seconds
26. Remove resist with acetone
27. Mount sample in holder for p-contact evaporation
    70 nm titanium
    150 nm gold
28. Mount sample on small glass slide with resist for thinning
29. Thin sample to 200 μm using 9 μm alumina grit
30. Thin sample to 150 μm using 3 μm alumina grit
31. Wet-etch with HCl : H_3PO_4 (in ratio 1:3) for 10 mins. to remove any damage
32. Demount from glass slide with acetone
33. Mount sample on glass slide with resist for n-contact evaporation
    14 nm gold
    14 nm germanium
    14 nm gold
    11 nm nickel
    150 nm gold
34. Remove from glass slide with acetone
35. Anneal contacts in Rapid Thermal Annealer at 360°C for 90 secs.
36. Scribe and cleave samples into chips with lengths ranging from 300 μm to 1000 μm

Fig. 2 to Fig. 5 show SEM photographs of lasers fabricated from four individual samples, one as-grown and three with different amounts of intermixing. It is obvious that the processing required to fabricate ridge waveguide lasers is far more complicated than that required to fabricate oxide stripe lasers (OSLs). In particular, no alignment is required when fabricating OSLs whereas, when fabricating RWLs,

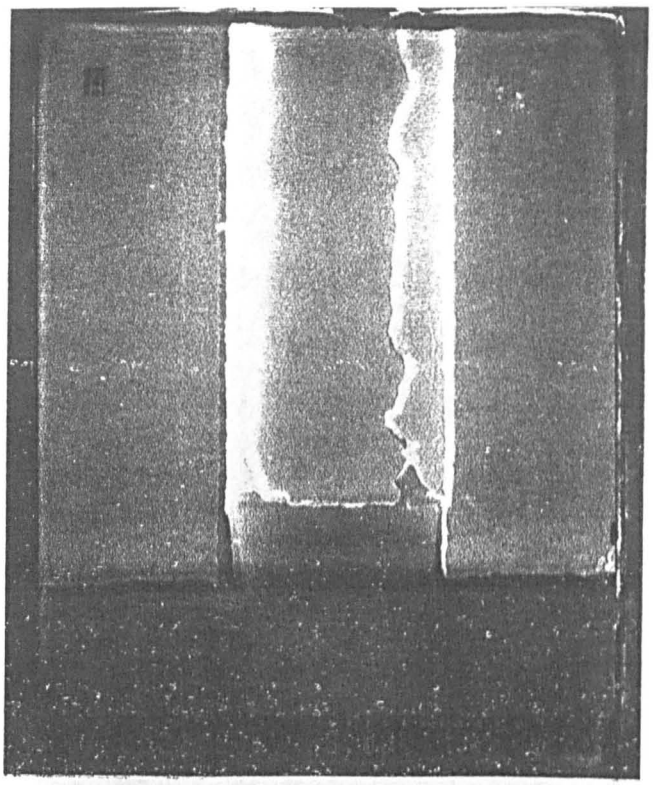

Fig. 2 SEM micrograph of laser fabricated from sample A

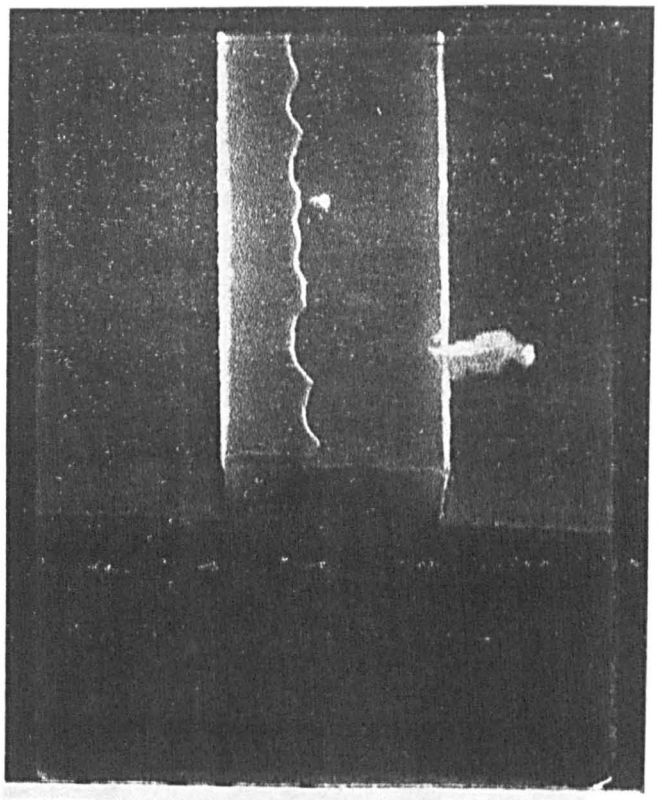

Fig. 3 SEM micrograph of laser fabricated from sample B

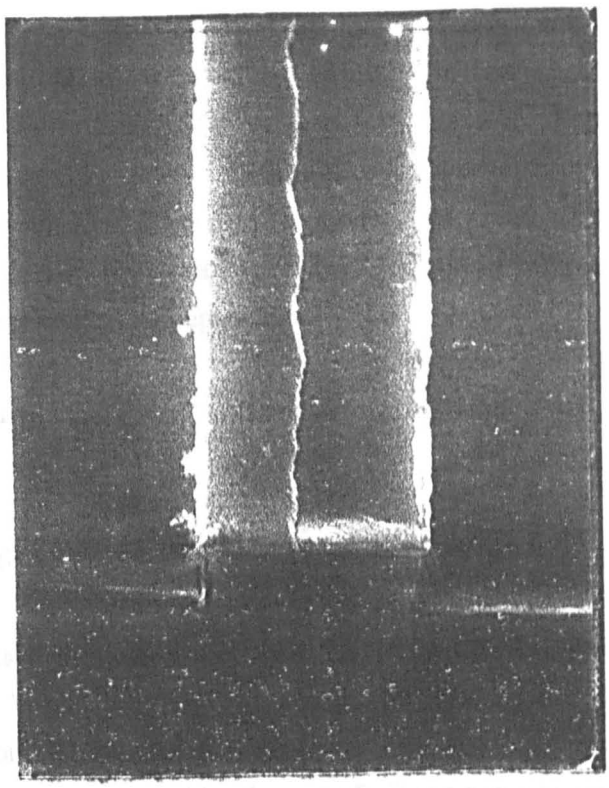

Fig. 4 SEM micrograph of laser fabricated from sample C

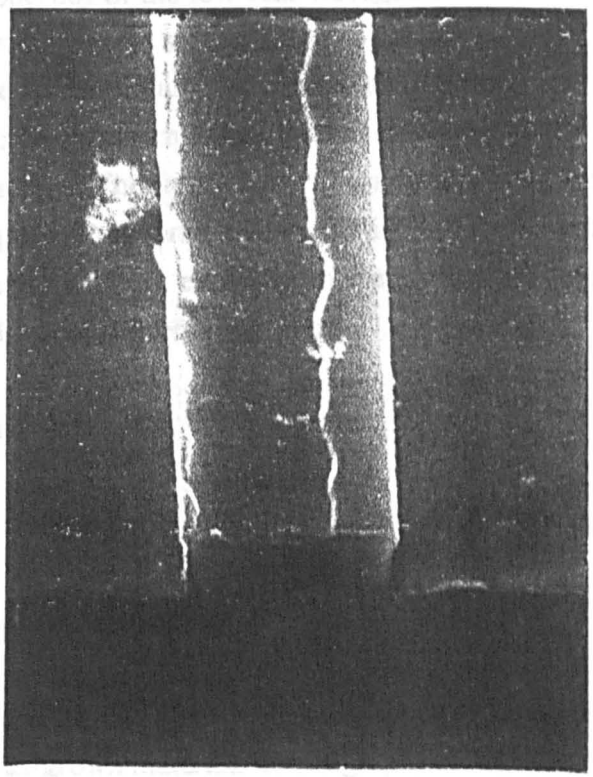

Fig. 5 SEM micrograph of laser fabricated from sample D

accurate alignment is required between the contact windows and the tops of the etched ridges. Consequently there is usually a variation in performance between devices fabricated from different samples. A slight variation in ridge width is observed between samples and this variation will affect the device properties. There is also misalignment between the ridges and the contact windows. For these reasons it is difficult to compare material parameters from sample to sample with any accuracy, unlike the OSLs fabricated in Chapter 5.

7.3 Comparison between oxide stripe lasers and ridge waveguide lasers

7.3.1 Waveguiding

An important difference between the OSLs fabricated in Chapter 5 and the RWLs fabricated here is the way in which the light is confined or guided in the transverse direction. The broad area lasers achieve guiding simply by restricting the areas to which current is injected by the use of silicon dioxide passivation layers. The ridge waveguide devices described here, however, use a change in the effective index to produce waveguiding and confine the light.

The waveguiding properties of the RWLs will be very similar to the waveguiding properties of the low-loss waveguides fabricated in Chapter 4 since the basic material structure is the same.

The ridge width required to achieve single mode operation was calculated in section (4.5.1) to be approximately 2 μm but it was decided that this was too small to fabricate successfully. The ridges fabricated in this chapter were approximately 4 μm wide and consequently supported two modes in the transverse direction. However, the second order mode was not expected to feature strongly due to the lower optical confinement and, hence, lower modal gain.

7.4 Results

Devices were tested in a similar manner to that described in Chapter 5.

7.4.1 L-I Characteristics

Fig. 6 shows the L-I characteristics obtained for a bar of 600 μm long lasers fabricated from as-grown material. If this graph is compared to Fig.8 in Chapter 5 it is obvious that the L-I curve, above threshold, is much more linear for the ridge lasers than for the oxide stripe lasers. This is due to the number of transverse modes being

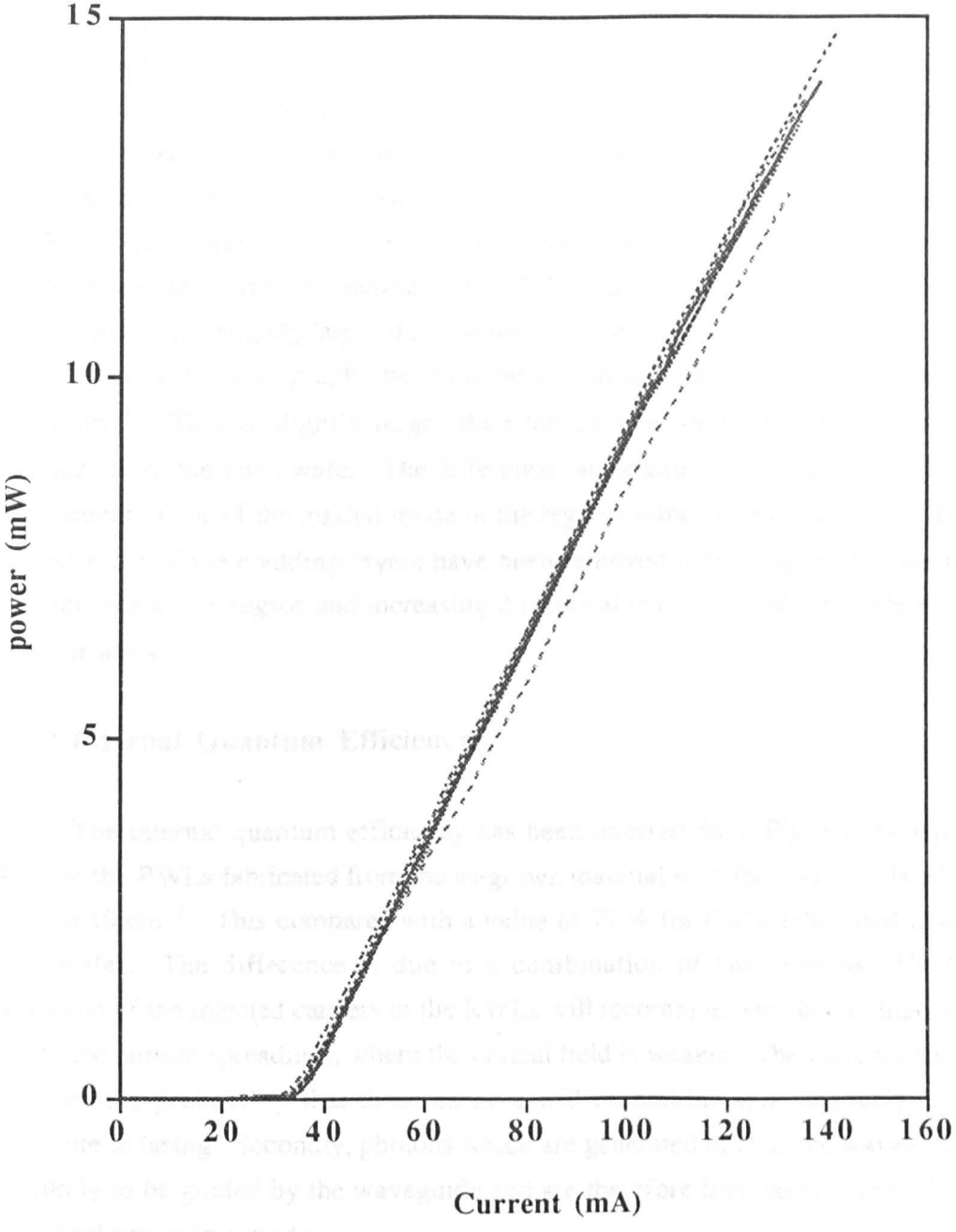

Fig. 6 L-I curves for a bar of 600 μm long ridge waveguide lasers

less in the RWLs, meaning that there is less mode hopping (the transfer of power between the different transverse modes) causing kinks in the L-I curve.

For the as-grown material, the threshold current varies from 25 mA for a 300 μm long device to 41.5 mA for a 1 mm long device. Fig. 7 is a plot of the natural log of the threshold current density as a function of inverse cavity length, from which the threshold current density for an infinitely long device has been calculated to be 800 Acm^{-2}. This value is substantially larger than the threshold current density of 560 Acm^{-2} for oxide stripe lasers fabricated from the same wafer. The difference is due to the injected current spreading in the MQW region, which results in the effective area pumped being slightly larger than the width of the ridge.

From the same graph the gain factor, $n\Gamma g_0$, has been calculated to be $=44.4\ cm^{-1}$. This is slightly larger than the gain factor of 37.5 cm^{-1} for OSLs fabricated from the same wafer. The difference can be explained by an increase in the confinement factor of the guided mode in the regions either side of the ridge. This is because most of the cladding layers have been removed thus *compressing* the mode more into the active region and increasing the optical overlap, Γ, of the mode with the quantum wells.

7.4.2 Internal Quantum Efficiency

The internal quantum efficiency has been inferred from Fig. 8 to be equal to 54 % for the RWLs fabricated from the as-grown material with the loss calculated to be equal to 10 cm^{-1}. This compares with a value of 72 % for OSLs fabricated from the same wafer. The difference is due to a combination of two reasons. Firstly, a proportion of the injected carriers in the RWLs will recombine outside the ridge region (due to the current spreading), where the optical field is weaker. The current spreading increases the probability that these carriers will recombine spontaneously and not contribute to lasing. Secondly, photons which are generated outside the waveguide are less likely to be guided by the waveguide and are therefore less likely to contribute to the optical power in a mode.

These effects will of course occur in OSLs but, because the gain section is so wide, can be neglected.

7.5 Comparison between different amounts of disordering

Figs. 9, 10, 11 & 12 show the lasing spectra of 600 μm long ridge waveguide lasers fabricated from the four samples. As mentioned previously, these devices are not ideal for studying material parameters, due to their strict fabrication requirements,

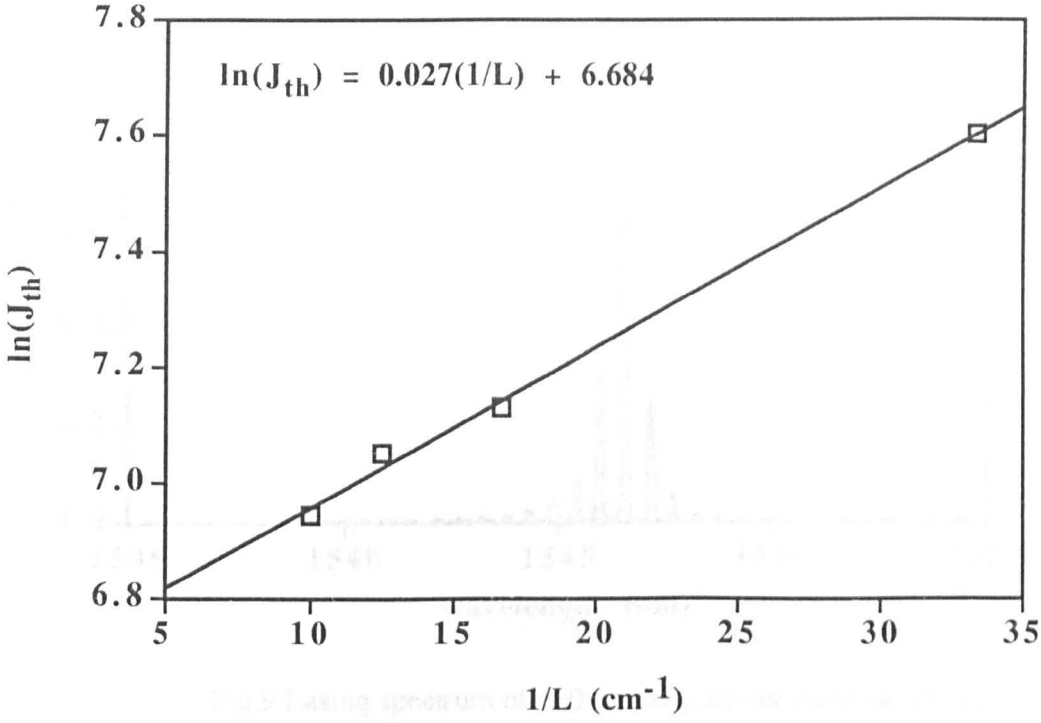

Fig.7 Graph of $\ln(J_{th})$ as a function of inverse cavity length

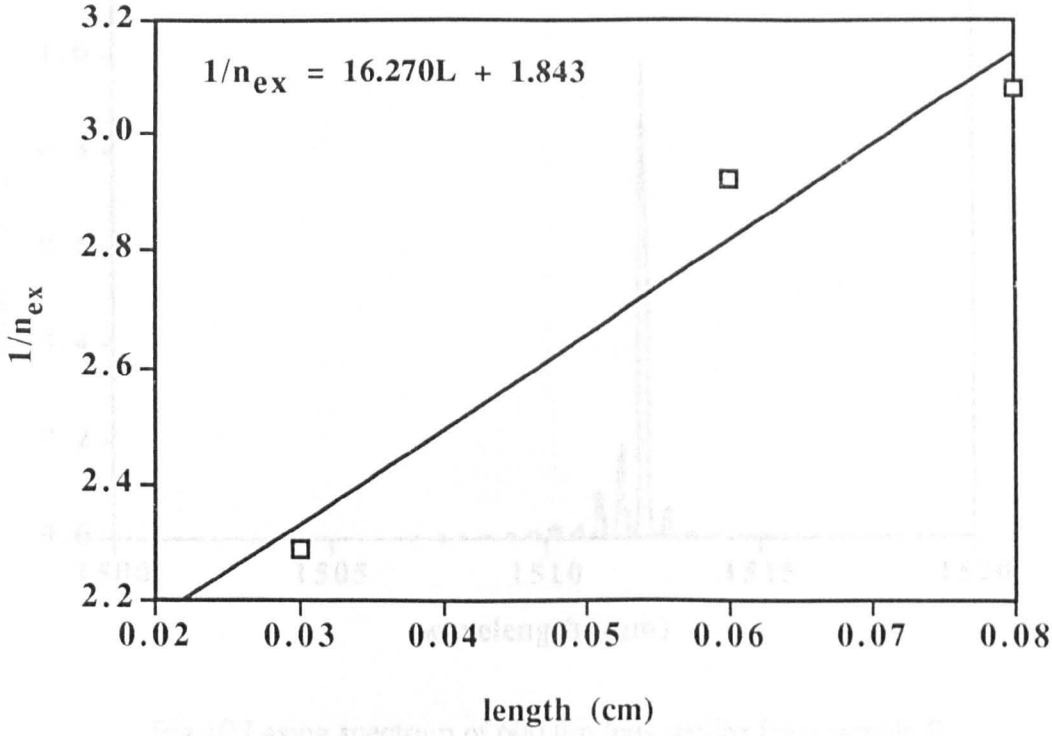

Fig.8 Graph of inverse of external efficiency as a function of cavity length

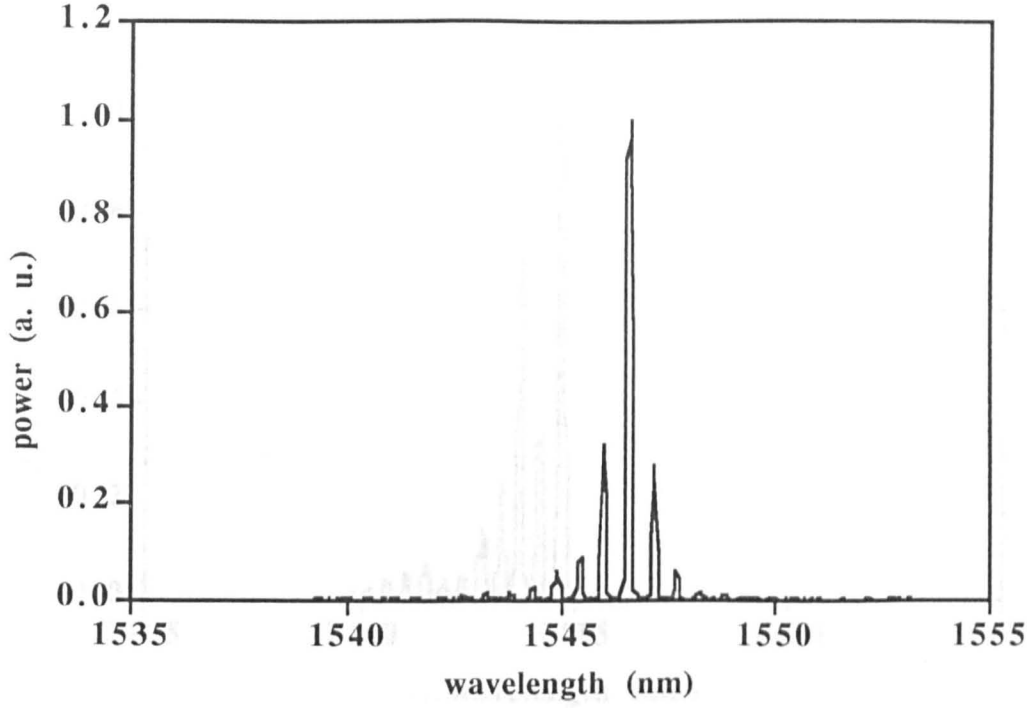

Fig.9 Lasing spectrum of 600 μm long device from sample A

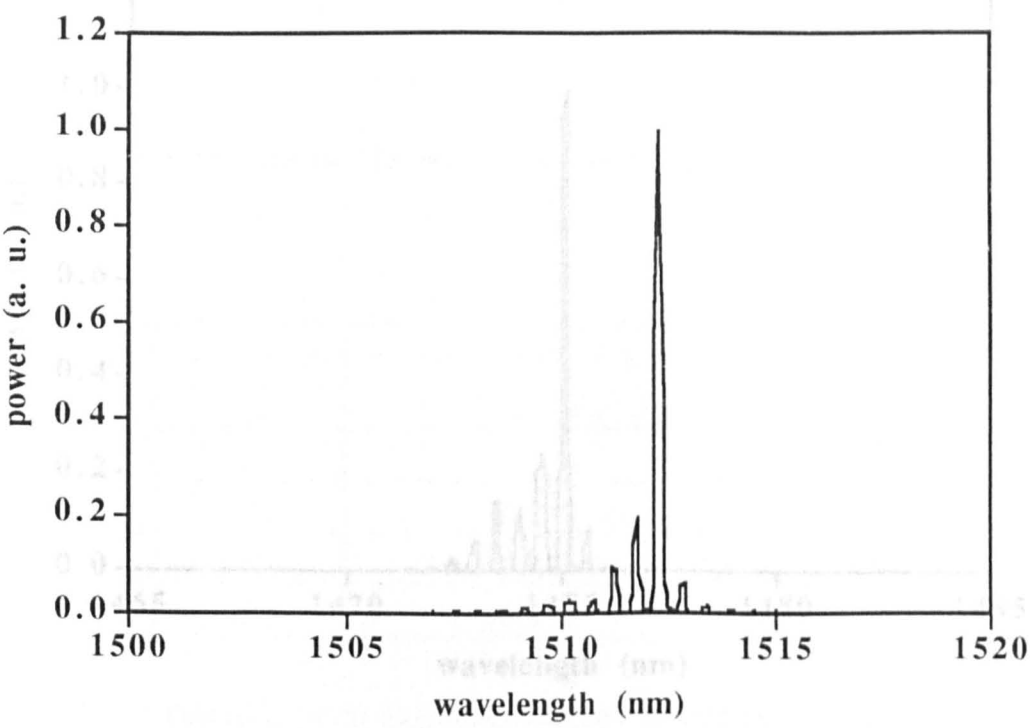

Fig.10 Lasing spectrum of 600 μm long device from sample B

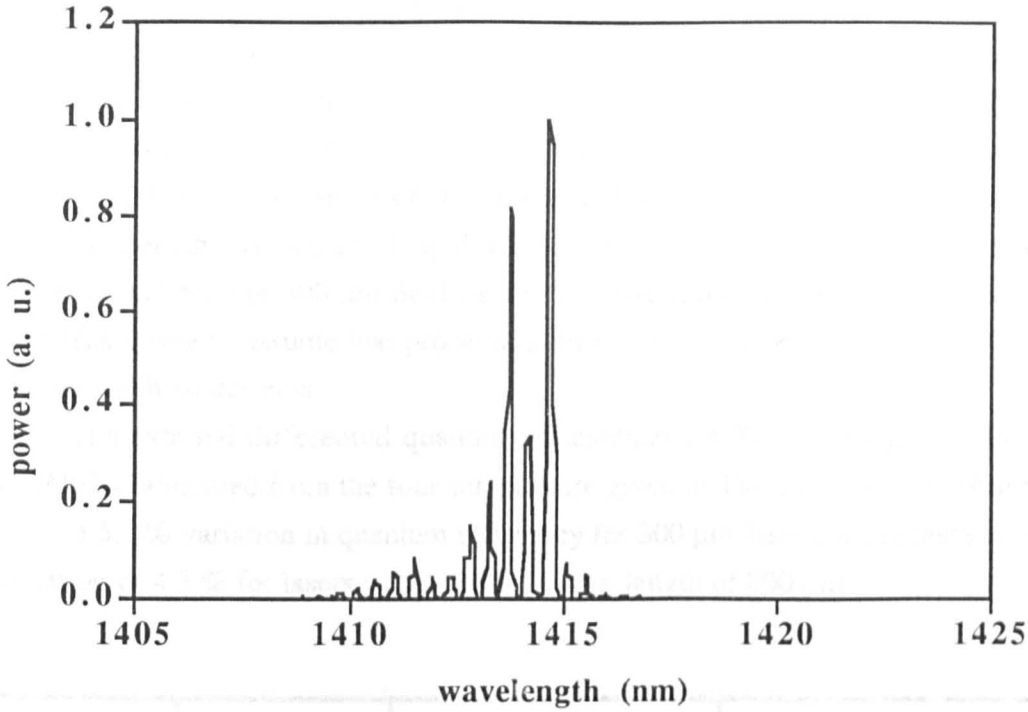

Fig.11 Lasing spectrum of 600 μm long device from sample C

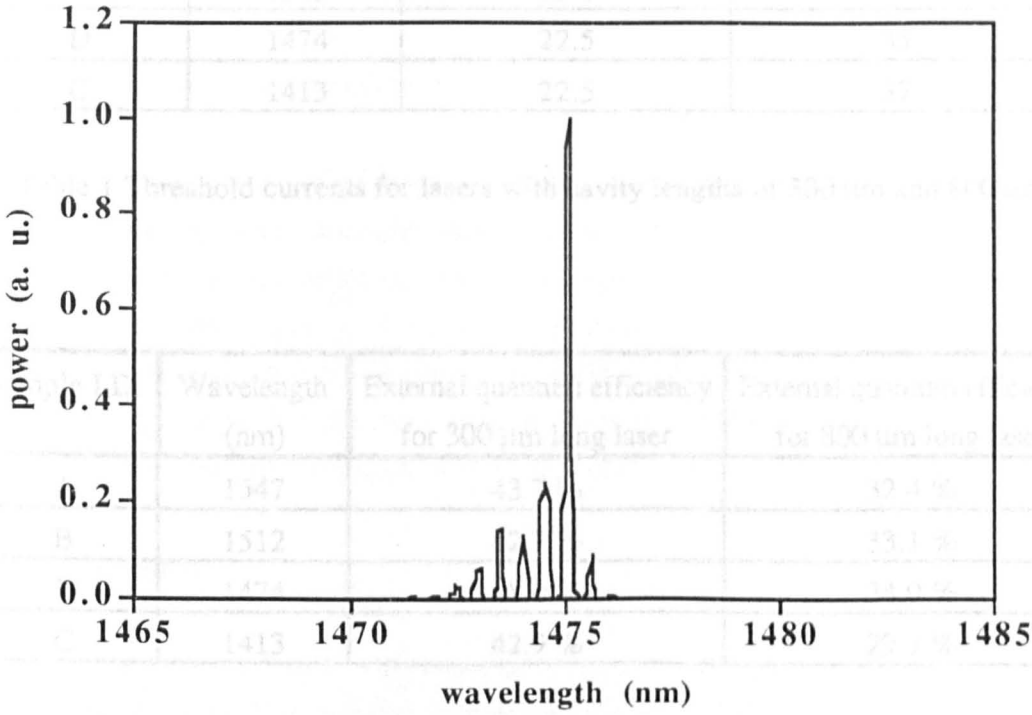

Fig.12 Lasing spectrum of 600 μm long device from sample D

particularly alignment of contact windows on the ridges, and consequently this study has not been carried out.

It is, however, sensible to compare actual device parameters for the different chips. For example, in Table 1, the threshold currents are presented for 300 μm and 800 μm long RWLs fabricated from the four samples. The wavelengths quoted are the lasing wavelengths for 600 μm long devices. The table indicates that there is only a 2.5 mA spread for the 300 μm devices and a 7 mA spread for 800 μm devices. It seems reasonable to assume that processing differences will be a major cause for the range in threshold currents.

The external differential quantum efficiencies for 300 μm long and 800 μm long RWLs fabricated from the four samples are given in Table 2. It can be seen that there is a 5.1 % variation in quantum efficiency for 300 μm lasers, while there is only a variation of 4.3 % for lasers which have a cavity length of 800 μm.

Sample I.D.	Wavelength (nm)	Threshold current (mA) for 300 μm long laser	Threshold current (mA) for 800 μm long laser
A	1547	25.0	37
B	1512	25.0	42
D	1474	22.5	35
C	1413	22.5	37

Table 1 Threshold currents for lasers with cavity lengths of 300 μm and 800 μm

Sample I.D.	Wavelength (nm)	External quantum efficiency for 300 μm long laser	External quantum efficiency for 800 μm long laser
A	1547	43.7 %	32.4 %
B	1512	42.7 %	33.1 %
D	1474	48.0 %	34.0 %
C	1413	42.9 %	29.7 %

Table 2 External differential quantum efficiencies of lasers with cavity lengths of 300 μm and 800 μm

7.6 Temperature Dependence of Threshold Current

The temperature dependence of the threshold current can be expressed as:

$$I_{th} = I_{th0} \exp\left(\frac{T}{T_0}\right) \tag{7.1}$$

where I_{th} is the threshold current (A),
I_{th0} is the threshold current at 0 K, and
T_0 is the characteristic temperature (K).

The characteristic temperature, T_0, of a laser is a measure of the degree of temperature sensitivity of the threshold current. A typical value of T_0 for a conventional (Al)GaAs double heterostructure laser is 150 K, with a higher value of around 220 K for (Al)GaAs quantum well lasers. In InGaAs(P) double heterostructure lasers however, the characteristic temperature is much lower[1], at around 70 K, and is due to the strong Auger recombination in this material system. Furthermore, no improvement (i.e. an increase in T_0) has been observed in InGaAs(P) quantum well lasers.

7.6.1 Experimental Procedure

The temperature of the lasers under test was varied using a Peltier cooler placed just below the laser clip. A simple control box with temperature feedback controlled the temperature of the Peltier device by altering the magnitude and polarity of the bias applied to it, meaning a range of temperatures could be obtained.

Light-current pulsed measurements (400 ns @ a 1 kHz rep. rate) were carried out on 800 μm long devices from each of the four samples, A, B, C, & D. Fig. 13 shows the L-I graph for sample A over a range of temperatures from 10°C to 40°C.

7.6.2 Results

It is obvious that, as the temperature is increased, the threshold current of the laser also increases. The external differential efficiency of the lasers however, remains virtually constant. The threshold current for each temperature is given in Table 3, from which it can be seen that there is a strong dependence with temperature. For example, there is an increase of 56 % in the threshold current for a modest 30°C increase in the temperature, which is indicative of a low characteristic temperature. By plotting ln(Ith)

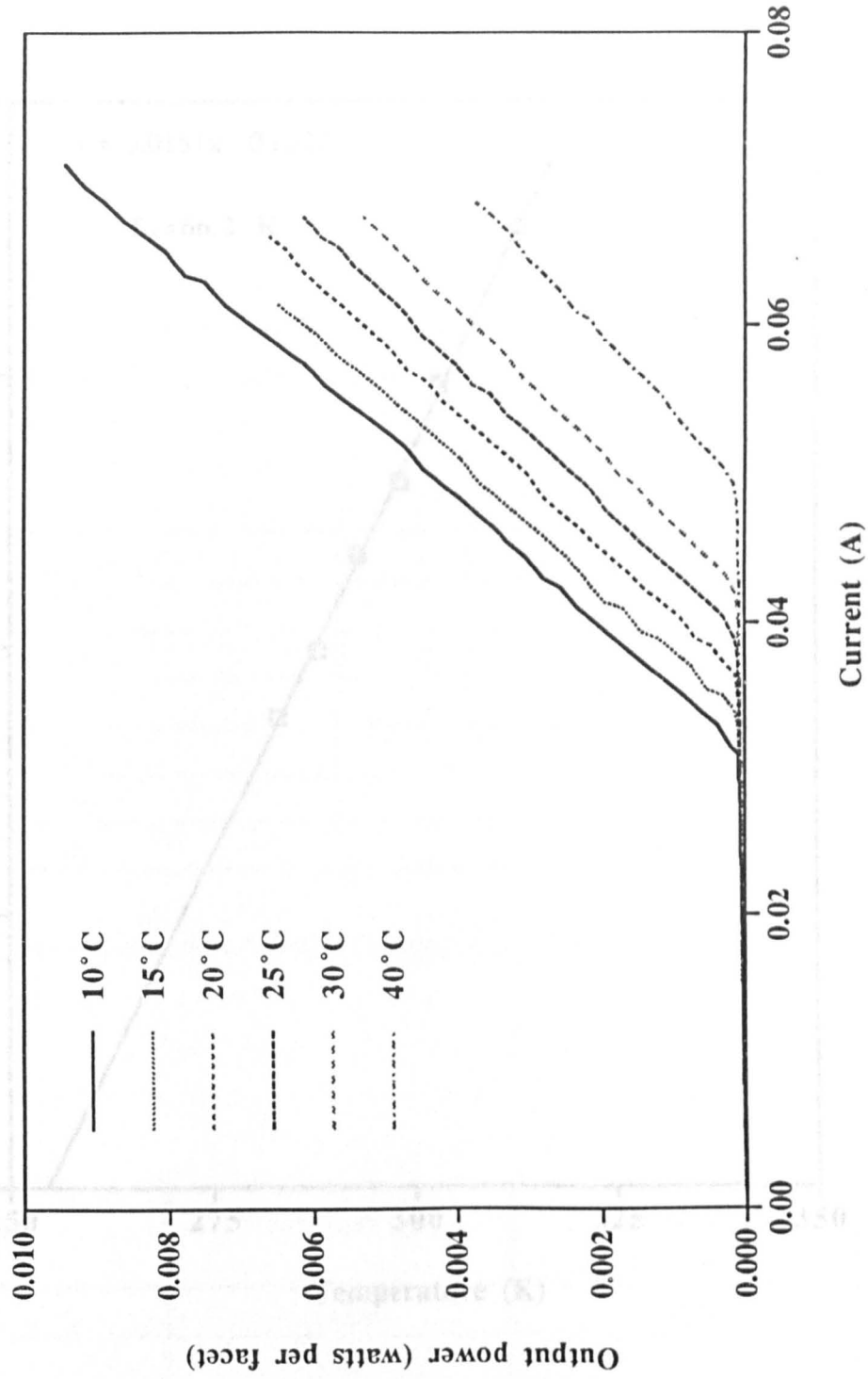

Fig. 13 Light-Current Curve for 800 μm as-grown laser as a function of temperature

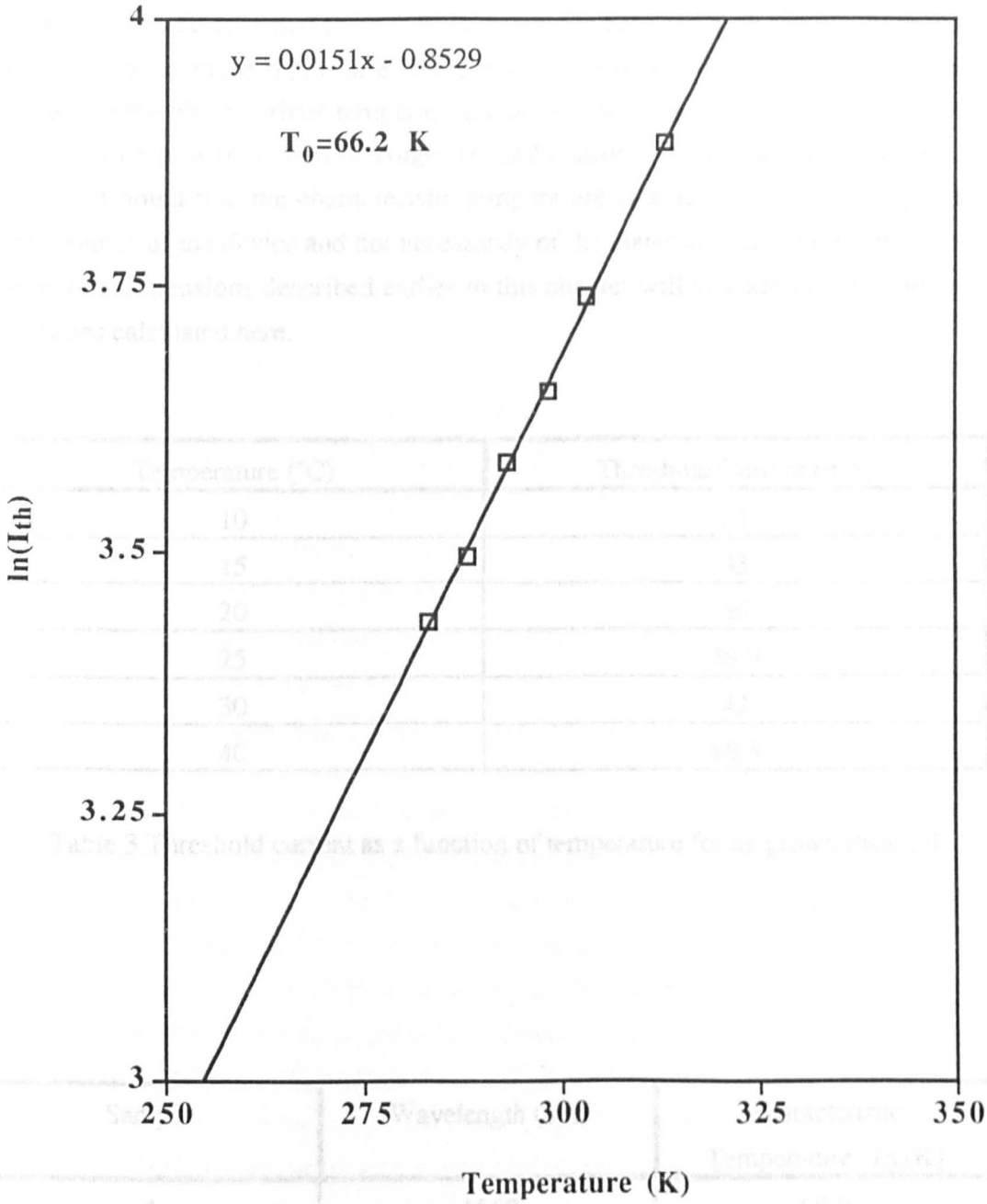

Fig. 14 Threshold current as a function of temperature

against temperature, a straight line is obtained with the gradient equal to the reciprocal of the characteristic temperature. Results are shown in Fig. 14, from which T_0 has been calculated to be 66.2 K.

Measurements were repeated for each sample, with the calculated T_0s given in Table 4. It can be seen that there is little difference between each sample, with values of T_0 similar to those reported elsewhere[2,3,4]. It might have been expected that an increase in the characteristic temperature would be seen as the lasing wavelength was reduced, due to a reduction in Auger recombination, but this was not the case. It should be noted that the characteristic temperature is a measure of the temperature performance of the *device* and not necessarily of the material. Therefore, variations in the device dimensions described earlier in this chapter will also affect the accuracy of the values calculated here.

Temperature (°C)	Threshold Current (mA)
10	31
15	33
20	36
25	38.5
30	42
40	48.5

Table 3 Threshold current as a function of temperature for as-grown material

Sample	Wavelength (nm)	Characteristic Temperature, T_0 (K)
A	1550	66.2
B	1500	67.6
D	1470	57
C	1420	76

Table 4 Characteristic temperature (T_0) as a function of wavelength

7.7 CW Measurements of Ridge Waveguide Lasers

The lasers described in Chapters 6 and 7 have been fabricated from material which has been intermixed by large amounts. Although there is no significant degradation in lasing properties, no tests have been carried out to determine device reliability.

7.7.1 Bonded Devices

To carry out Continuous Wave (CW) measurements, it is important to heat-sink the devices so that the active region does not overheat during operation. Devices were soldered to a copper block using small balls of indium and deoxidising flux (shown in Fig. 15). The flux is necessary to make the indium "flow" on the copper block. The devices were bonded p-side down which meant that the active region was as close as possible to the heat-sink. A bond pad was glued onto the end of the block, from which a Gold wire connection was made (using an ultrasonic bonder). This block was then placed in a mount which contained a Peltier cooler, with the current supplied through a probe to the bond pad. The current source consisted of a battery pack and a variable power supply unit which allowed currents of up to 110 mA to be supplied to the lasers. The output from one facet was collimated by a X40 objective lens (NA=0.65) and measured by an Anritsu optical power meter.

Fig. 16 shows the Light-Current characteristics for 600 μm long devices from samples A-D. Although the devices worked, there was a large variation in the threshold currents and external differential quantum efficiencies which was not predicted by the pulsed measurements on the same lasers. The reason for the variation (and general deterioration) in the threshold current and external efficiency was thought to be the combination of two problems; solder induced stress around the ridges, and the flux used in the soldering. When the lasers are bonded p-side down, the solder will flow in the double trench structure of the devices. The solder will then contract as it cools down, leading to stress around the ridge and the nearby active region. This problem has been observed in p-side down ridge lasers before, although it is not a problem in buried heterostructure lasers which have a planar p-side. The flux is extremely difficult to remove and often forms a tough layer on the laser facets. This layer will have the effect of altering the reflection coefficient of the facets, thereby altering the threshold current and external efficiency of the laser. To verify these assumptions, the lasers were tested again in pulsed operation and the L-I curves were found to be similar to those for CW operation. This similarity indicates that the degradation in the performance of the lasers, is due to the bonding process and not due to the heating of the active region caused by CW operation.

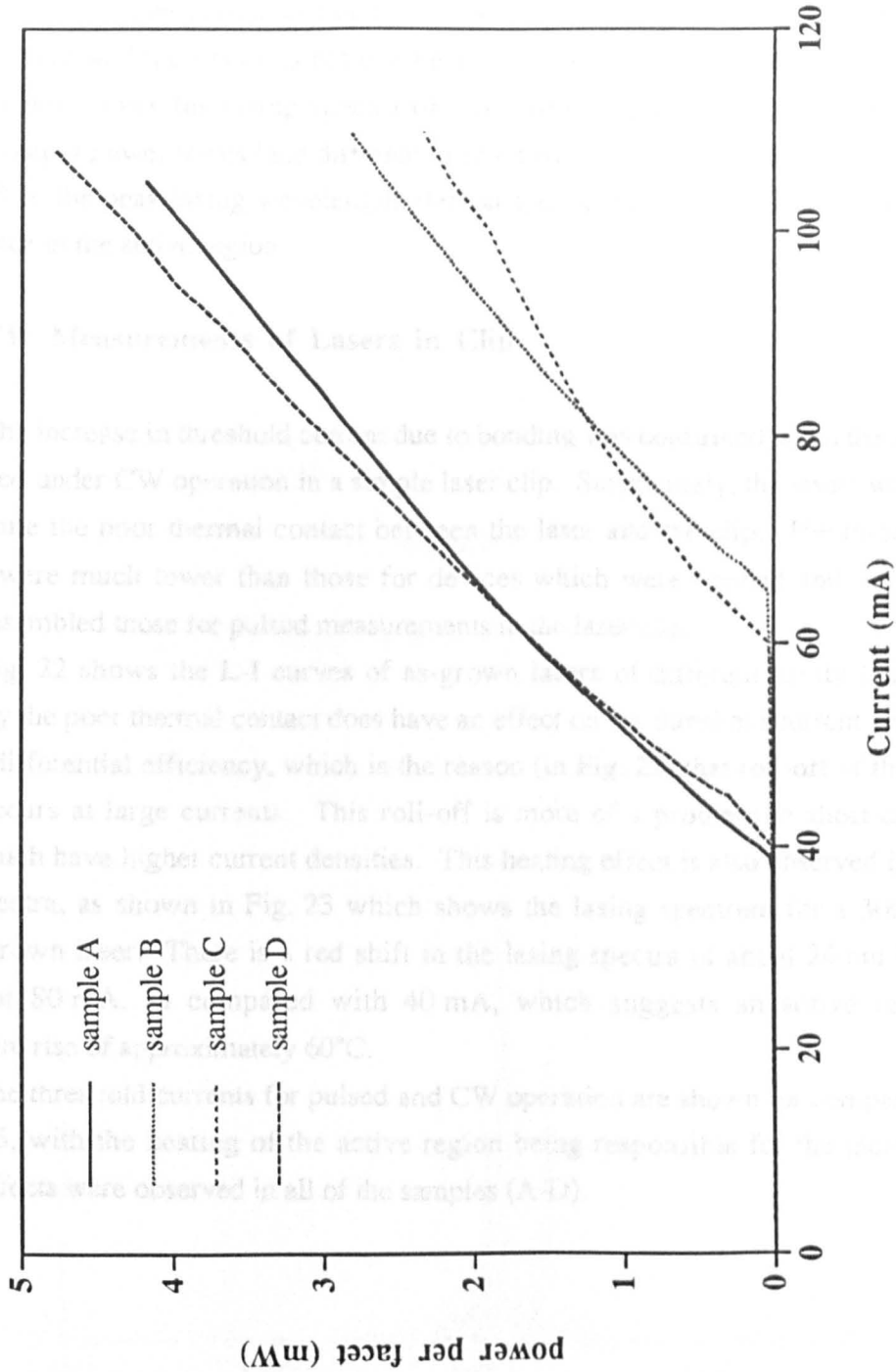

Fig.16 CW L-I curves for 600 μm long lasers from samples A, B, C, and D.

The lasing spectra of the devices are shown in Figs. 17, 18, 19 & 20 at a power output of 1 mW (per facet) for each laser.

The peak wavelength of each spectrum is at an identical position to the spectrum of the laser taken under pulsed operation, indicating that the active region temperature is well controlled and the device is not overheating. There is further evidence of this in Fig. 21 which shows the lasing spectra of a 600 μm long laser from sample B for different output power levels (and different injected current levels). Again there is very little shift in the peak lasing wavelength, demonstrating that no significant heating is taking place in the active region.

7.7.2 CW Measurements of Lasers in Clip

The increase in threshold current due to bonding was confirmed when the lasers were tested under CW operation in a simple laser clip. Surprisingly, the lasers worked well despite the poor thermal contact between the laser and the clip. The threshold currents were much lower than those for devices which were bonded and, instead, closely resembled those for pulsed measurements in the laser clip.

Fig. 22 shows the L-I curves of as-grown lasers of different cavity lengths. Obviously the poor thermal contact does have an effect on the threshold current and the external differential efficiency, which is the reason (in Fig. 22) that roll-off of the L-I curves occurs at large currents. This roll-off is more of a problem in short cavity lasers, which have higher current densities. This heating effect is also observed in the lasing spectra, as shown in Fig. 23 which shows the lasing spectrum for a 300 μm long as-grown laser. There is a red shift in the lasing spectra of about 24 nm for a current of 80 mA, as compared with 40 mA, which suggests an active region temperature rise of approximately 60°C.

The threshold currents for pulsed and CW operation are shown for comparison in Table 5, with the heating of the active region being responsible for the increase. Similar effects were observed in all of the samples (A-D).

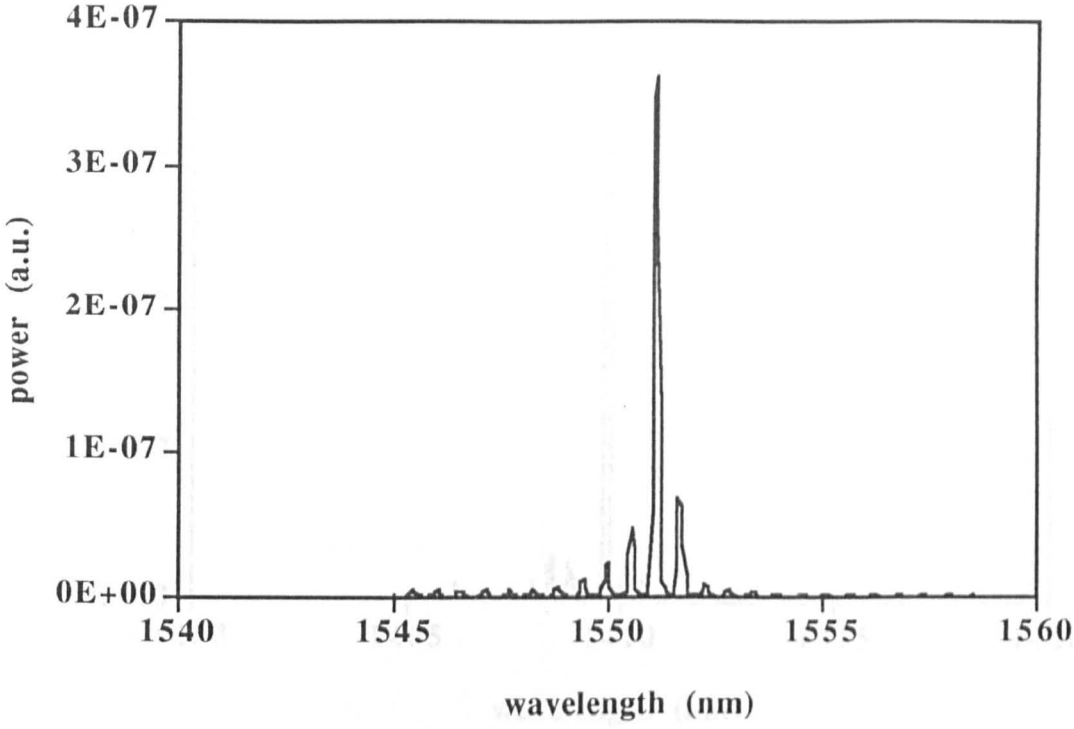

Fig.17 CW lasing spectrum of 600 μm device from sample A

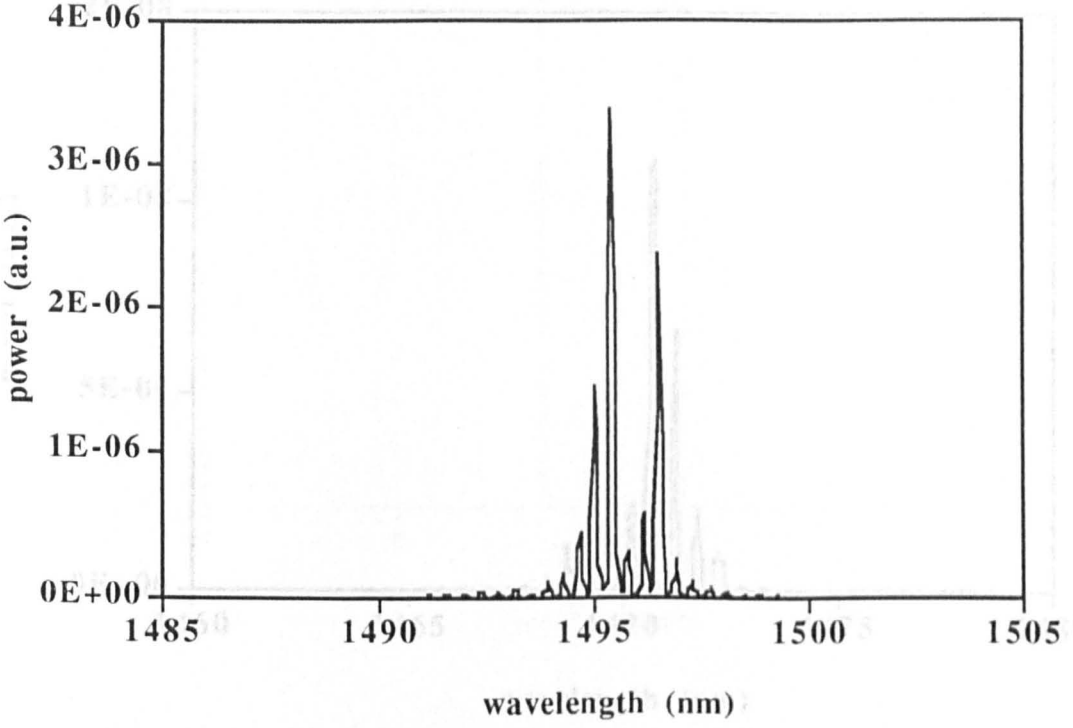

Fig.18 CW lasing spectrum of 600 μm device from sample B

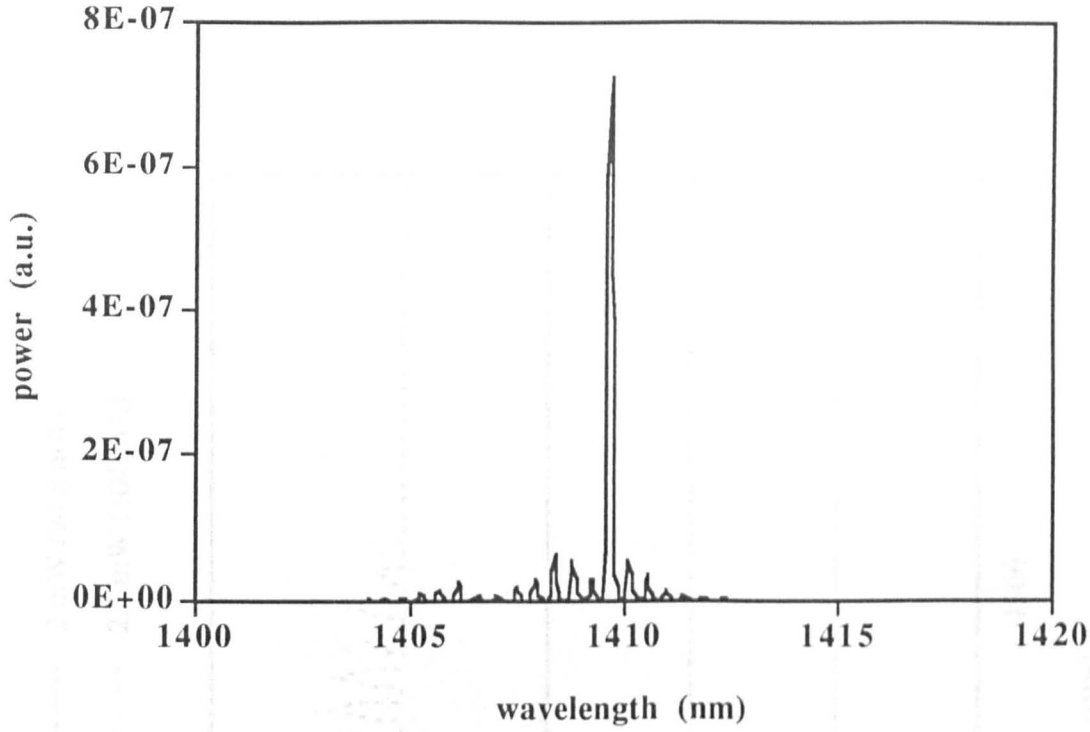

Fig.19 CW lasing spectrum of 600 μm device from sample C

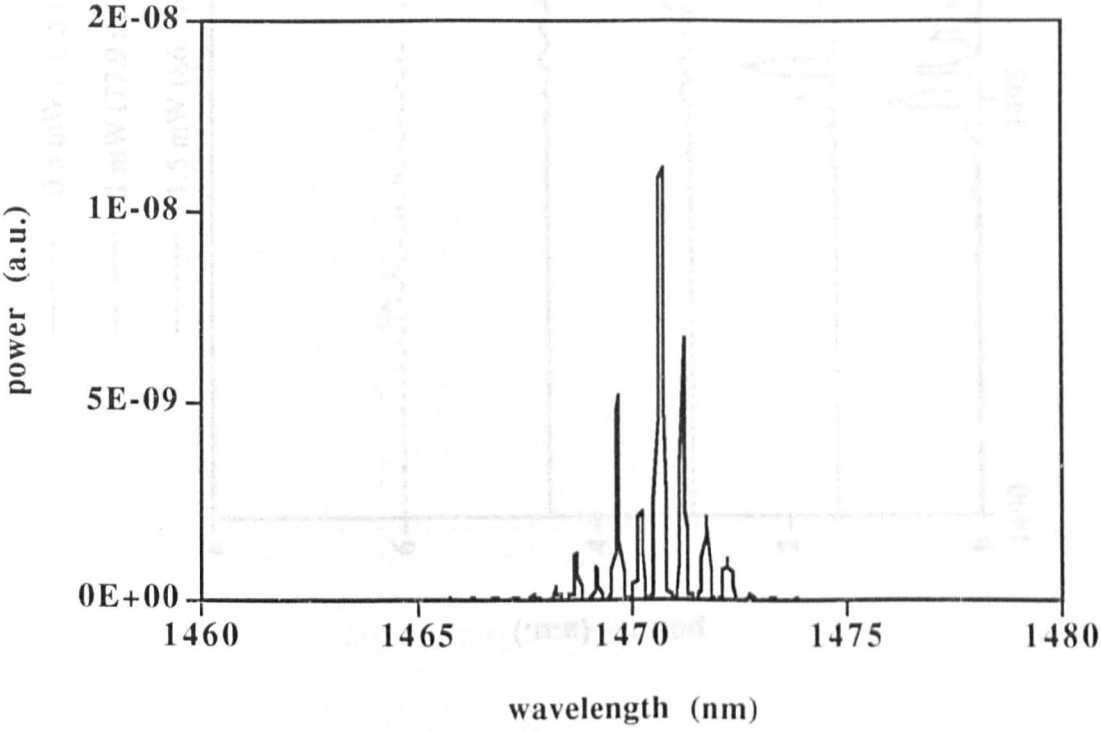

Fig. 20 CW lasing spectrum of 600 μm device from sample D

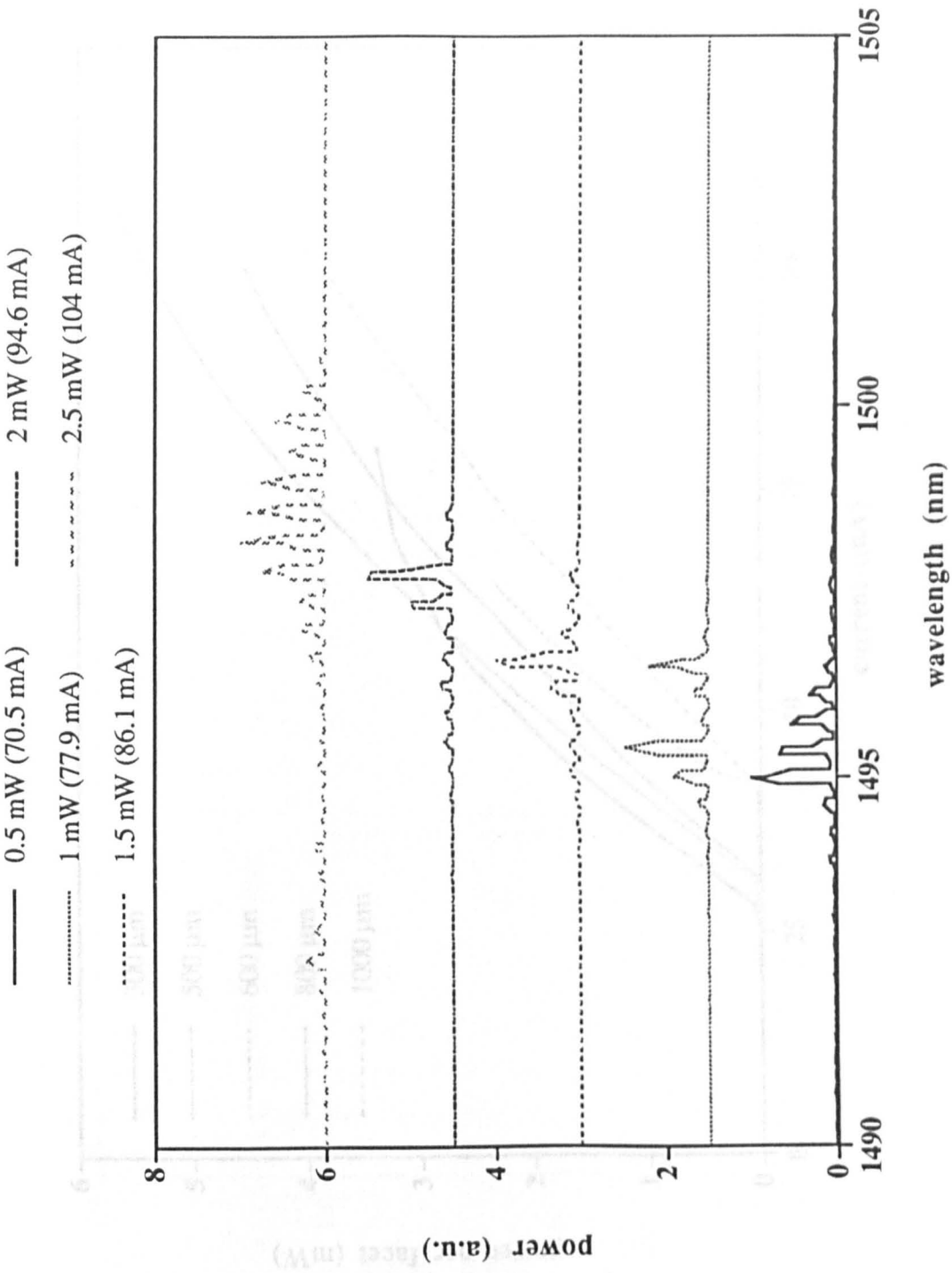

Fig. 21 Lasing spectra of 600 μm long device
at different output powers

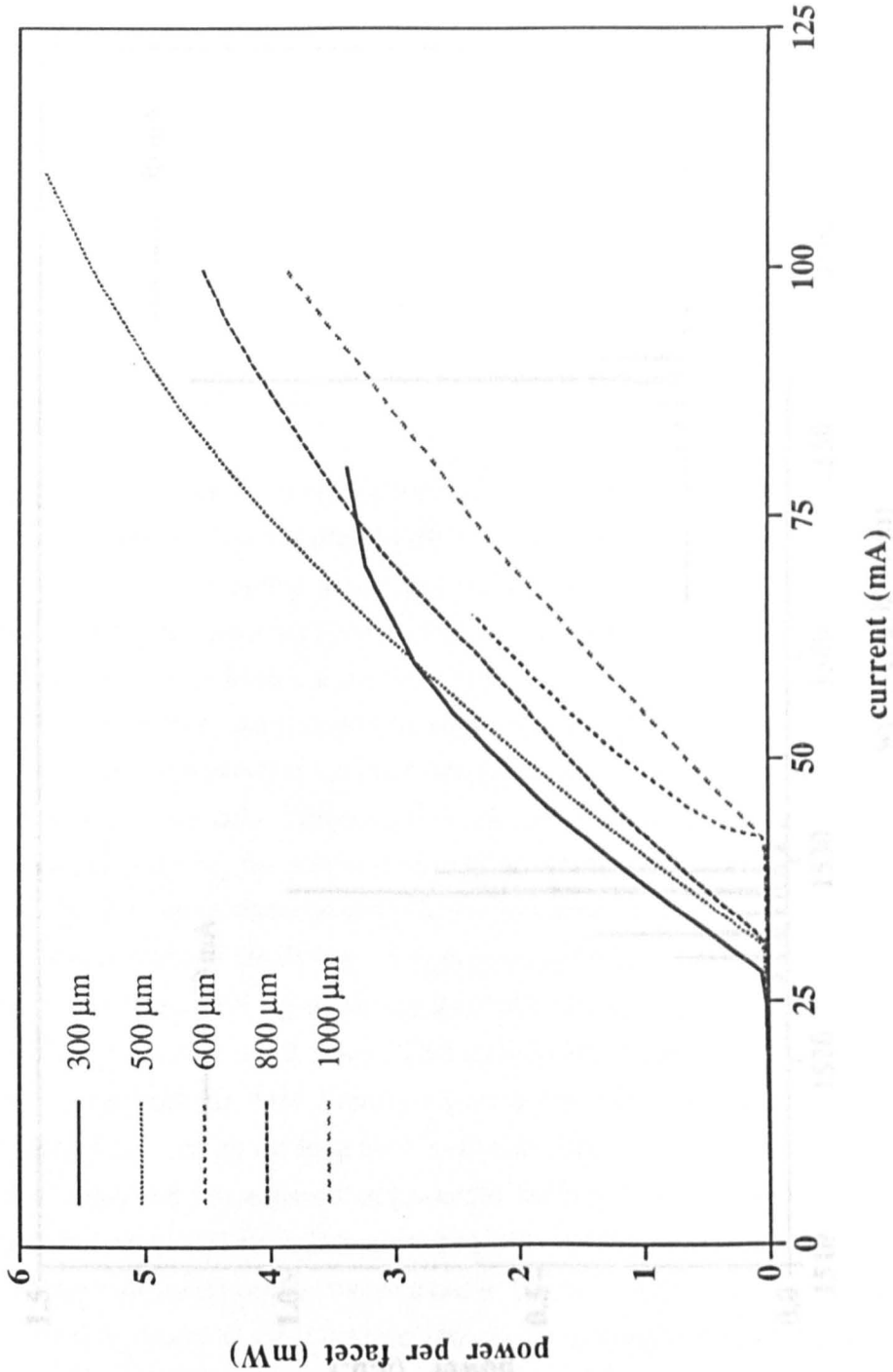

Fig. 22 L-I curves of devices operated CW in a laser clip

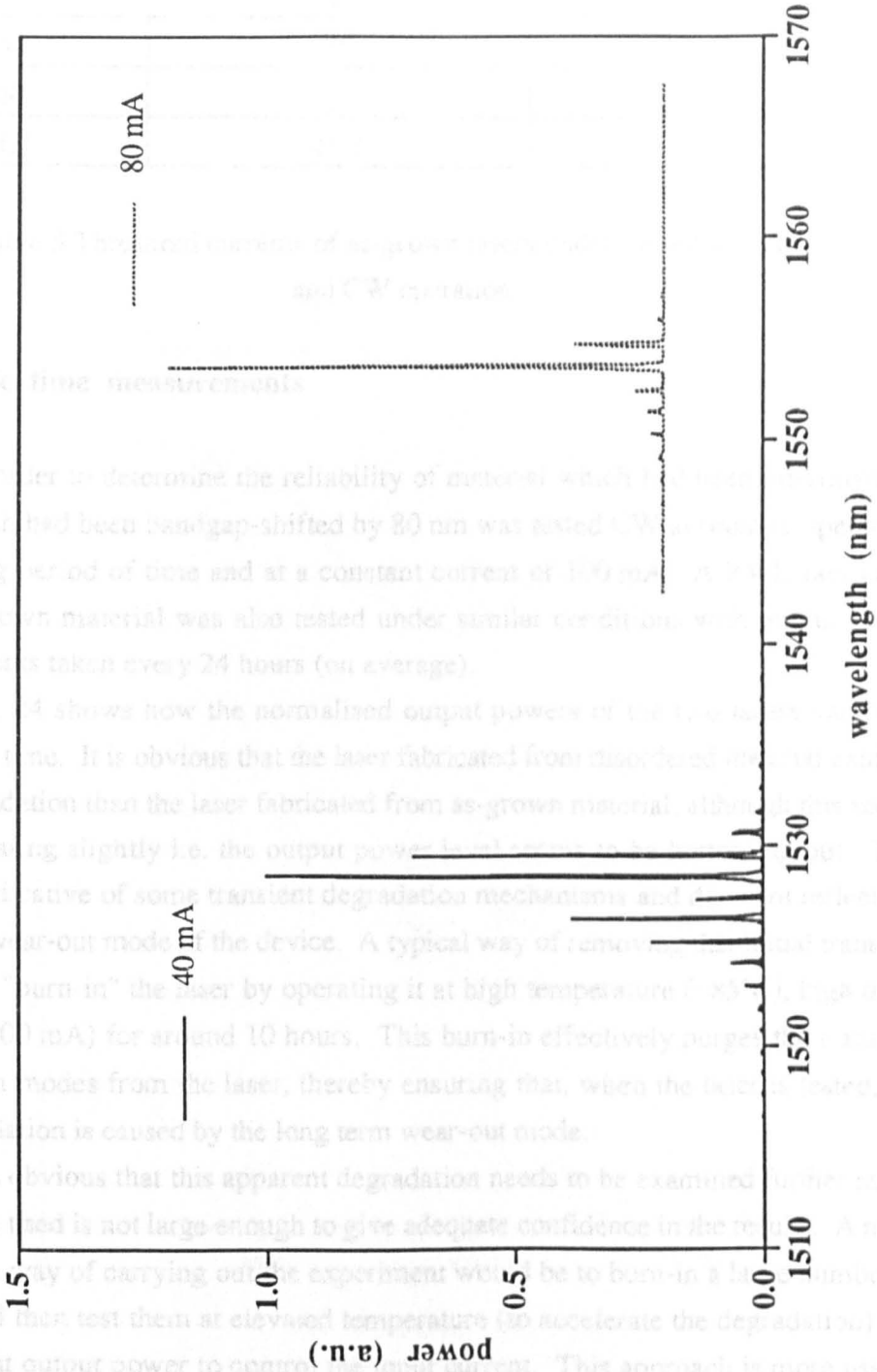

Fig. 23 Lasing spectra of 300 μm long device in laser clip at drive currents of 40 mA and 80 mA

Cavity Length (μm)	Threshold Current under pulsed operation (mA)	Threshold Current under CW operation in laser clip (mA)
300	25	27.5
600	30	31
800	37	39
1000	41.5	42

Table 5 Threshold currents of as-grown lasers under pulsed operation and CW operation

7.8 Life time measurements

In order to determine the reliability of material which had been intermixed, a RWL which had been bandgap-shifted by 80 nm was tested CW at room temperature, over a long period of time and at a constant current of 100 mA. A RWL fabricated from as-grown material was also tested under similar conditions with output power measurements taken every 24 hours (on average).

Fig. 24 shows how the normalised output powers of the two lasers vary as a function of time. It is obvious that the laser fabricated from disordered material exhibits more degradation than the laser fabricated from as-grown material, although this seems to be saturating slightly i.e. the output power level seems to be bottoming out. This effect is indicative of some transient degradation mechanisms and does not reflect the long term wear-out mode of the device. A typical way of removing this initial transient effect is to "burn-in" the laser by operating it at high temperature (~85°C), high drive current (~100 mA) for around 10 hours. This burn-in effectively purges the transient degradation modes from the laser, thereby ensuring that, when the laser is tested, the only degradation is caused by the long term wear-out mode.

It is obvious that this apparent degradation needs to be examined further as the sample size used is not large enough to give adequate confidence in the results. A more appropriate way of carrying out the experiment would be to burn-in a large number of devices and then test them at elevated temperature (to accelerate the degradation) and use constant output power to control the input current. This approach is more useful, since the most common criterion for measuring the lifetime of a laser is the time when the drive current has increased by 50% over the start of life condition. It is worth noting that the lifetime of a standard optoelectronic telecomms component is 25 years.

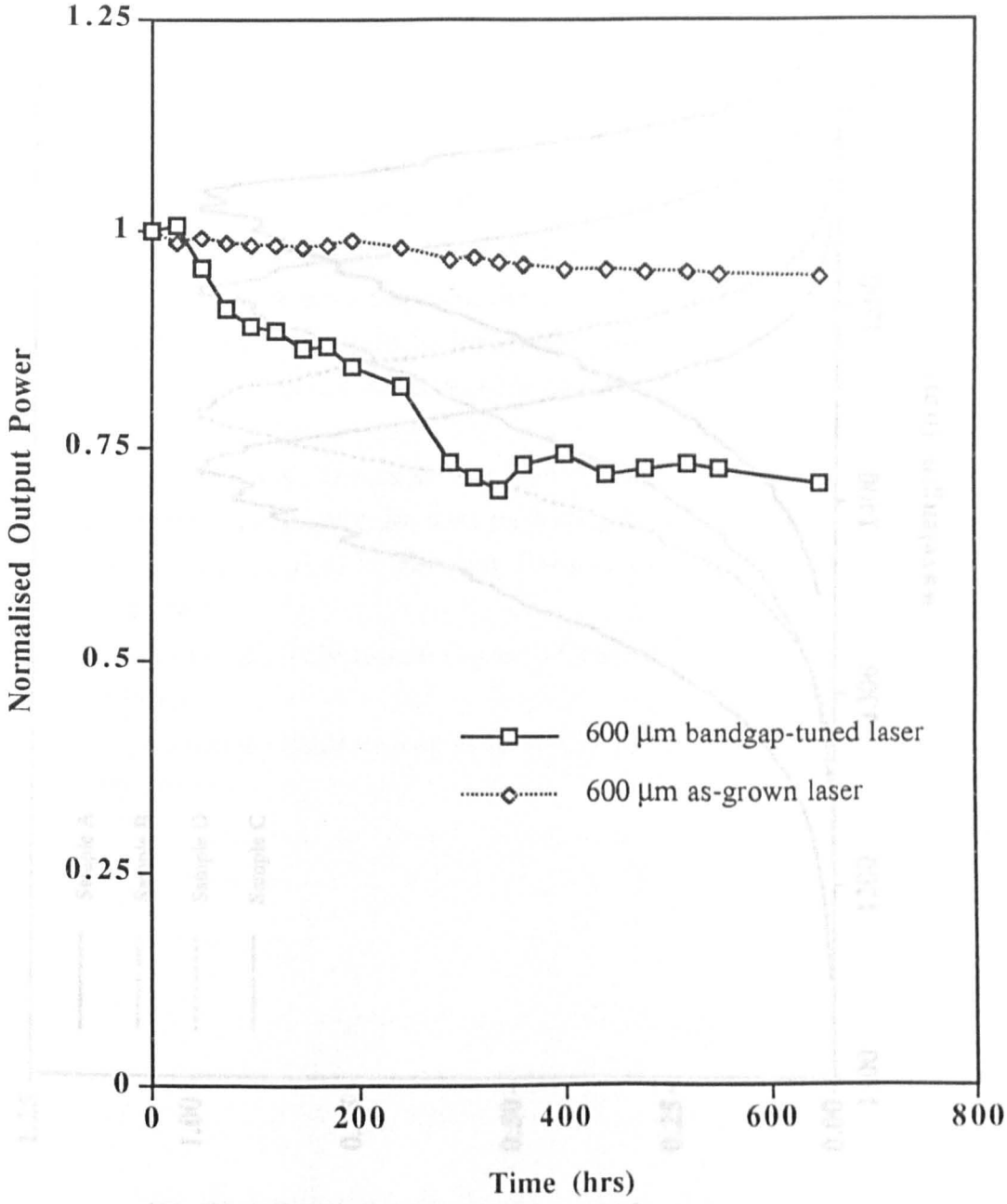

Fig. 24 Normalised output power as a function of time

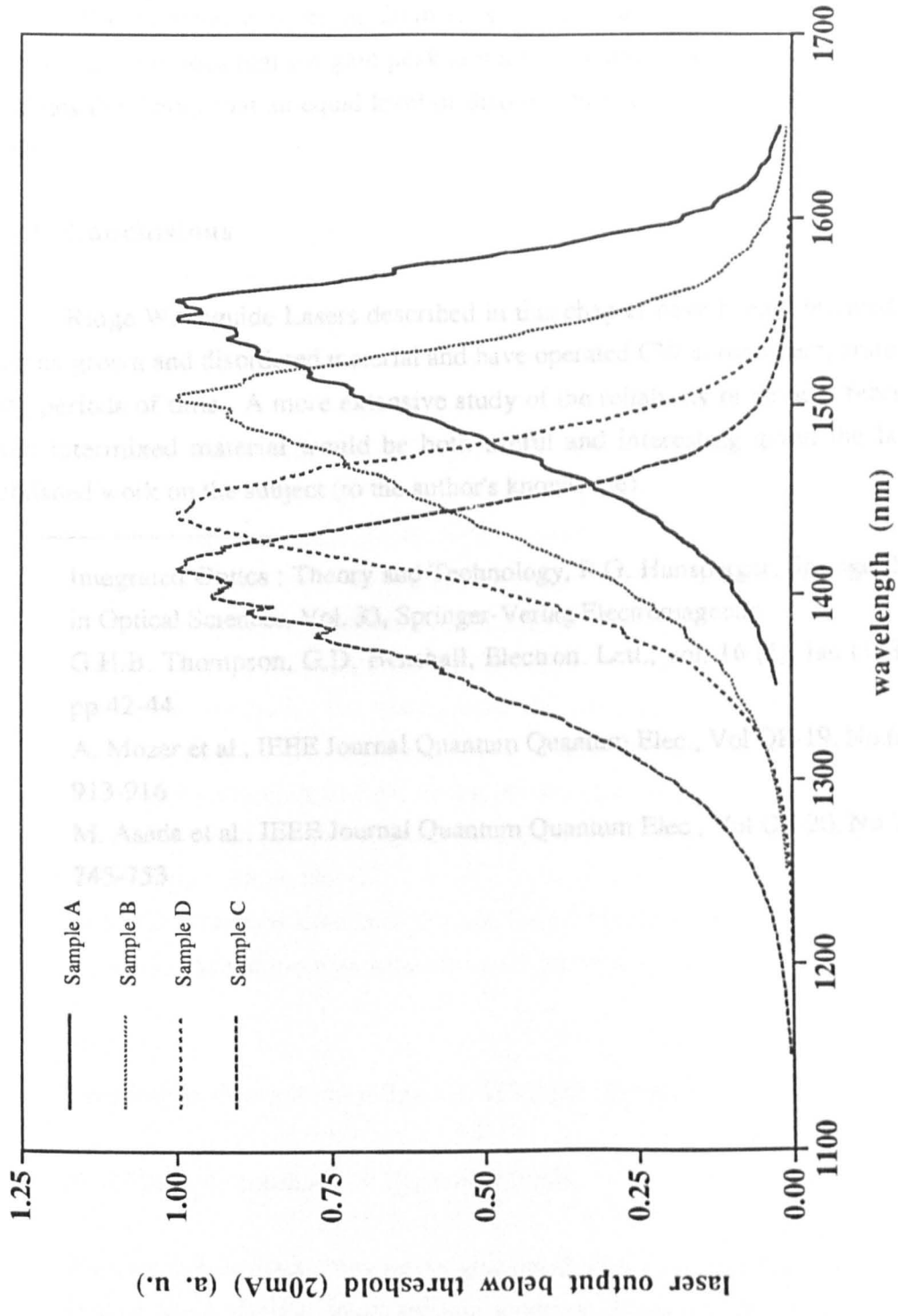

Fig. 25 Spontaneous emission spectra of 1000 μm long devices from samples A, B, C, and D.

7.9 Spontaneous Emission of Lasers

The spontaneous emission of the lasers is shown in Fig. 25 for 1000 μm long lasers. The injected current, at 20 mA, is approximately 50 % of the threshold current. It is obvious that the gain peak is not broadening to any great extent, which validates the theory that an equal level of disordering is occurring in all the quantum wells

7.10 Conclusions

Ridge Waveguide Lasers described in this chapter have been fabricated from both as-grown and disordered material and have operated CW at room temperature for long periods of time. A more extensive study of the reliability of devices fabricated from intermixed material would be both useful and interesting given the lack of published work on the subject (to the author's knowledge).

---

1 Integrated Optics : Theory and Technology, R.G. Hunsperger, Springer Series in Optical Sciences, Vol. 33, Springer-Verlag Electromagnetic

2 G.H.B. Thompson, G.D. Henshall, Electron. Lett., vol. **16** (1), Jan (1980), pp 42-44

3 A. Mozer et al., IEEE Journal Quantum Quantum Elec., Vol QE-19, No.6, pp 913-916

4 M. Asada et al., IEEE Journal Quantum Quantum Elec., Vol QE-20, No.7, pp 745-753

Chapter 8 Electroabsorption in InGaAs(P) MQW Structures

8.1 Introduction

Multiple Quantum Well (MQW) material has been shown to produce excellent modulators utilising the electroabsorption effect at wavelengths close to the bandgap[1].

The electroabsorption in MQW structures close to the bandgap is dominated by the Quantum Confined Stark Effect (QCSE) as discussed in Chapter 2. By applying a reverse bias voltage (and electric field) to material the electroabsorption characteristics can be determined by monitoring the photocurrent induced in the material.

8.2 Photocurrent Spectroscopy

Photocurrent measurements can be used very simply to gauge the modulation capabilities of disordered material at any wavelength without the need for fabricating any actual devices. They can also be used to determine what is the optimum bandgap shift required for an electroabsorption modulator to work at the original lasing wavelength of the material. The technique works by illuminating the material with monochromatic light to create free-carriers. These carriers are swept from the depletion region by the built in field of the *pin* structure and create a current in the bias circuit. By scanning monochromatic light over a range of wavelengths, the absorption spectrum can be found.

This technique was used to determine the electroabsorption properties of both as-grown and disordered multiple quantum well material.

8.3 Features in Photocurrent Spectra of MQW Structures

8.3.1 Forbidden Transitions In Quantum Wells

Photocurrent spectra show peaks associated with interband transitions which, for material in large electric fields, include some transitions which are forbidden for zero fields. This concept has already been discussed in chapter 2.

The appearance of forbidden transitions in the absorption spectrum of the matereial is accompanied by a corresponding reduction in the absorption of the zero-field transitions[2]. This is a direct result of the absorption sum rules[3] which states that

the net change in absorption in the material over the entire spectrum must be zero. Assuming that the hh and lh transitions are completely decoupled, the sum rule for heavy hole and light hole transitions operate independently.

8.3.2 Exciton Broadening

The exciton peaks measured by the photocurrent have an associated linewidth which is due to both homogeneous and inhomogeneous broadening.

The homogeneous broadening is mainly due to the lifetime of the exciton. Three possible mechanisms limiting the exciton lifetime are phonon interactions, carrier tunneling through the barrier, and electron hole recombination. At room temperature, phonon interactions dominate the lifetime and lead to an estimated exciton lifetime[4] of 300 fs. This lifetime leads to a spread of exciton energies through the Heisenberg uncertainty principle and therefore an associated linewidth ($\Delta\lambda$). In an electric field, the exciton lifetime is reduced since the electron and hole are spatially separated causing the linewidth to broaden further.

The exciton broadening is, however, dominated by inhomogeneous broadening. The two main mechanisms leading to this broadening are variations in the well widths and variations in the electric field strength across the *pin* structure[5]. Broadening through well width variations can occur in two ways. Firstly, there can be a variation in width from one well to another, giving the excitons in each well a different resonant energy[6]. The separation of these energies is small and leads to a broadening of the peak rather than different peaks for each well. Secondly, there can be a variation in the well width within a single well due to interface roughness. In the (Al)GaAs material system, the linewidth of excitons is narrower in high purity bulk GaAs[7] than for (Al)GaAs quantum wells[8] demonstrating that interface roughness is the main mechanism for exciton broadening[9].

The exciton broadening associated with variations in the electric field causes broadening of the peak which increases with field strength. The MQW structure experiences a non-uniform electric field strength due to residual doping in the intrinsic region, so each well experiences a different field strength and, since the resonant energy of the excitons is field dependent, there is a broadening in the absorption spectrum.

8.4 Device Fabrication

8.4.1 Material Structure

The material used was a standard laser structure (MR 193) as shown in Fig. 1. It was grown by metal organic vapour phase epitaxy (MOVPE) on an n+ doped (Si) InP substrate and consisted of five 85 Å InGaAs wells with 120 Å InGaAsP (λ_g = 1.26 μm) barriers. The active region was surrounded by a stepped graded index (GRIN) waveguide core consisting of InGaAsP confining layers. The thicknesses and compositions of these layers (working out from the QWs) were 500 Å of λ_g = 1.18 μm and 800 Å of λ_g = 1.05 μm. The structure, which was lattice matched to InP throughout, was completed with an InP upper cladding layer and a InGaAs contact layer. The first 0.2 μm of the upper cladding layer was doped with Zn to a concentration of 5 x 10^{17} cm^{-3} and the remaining 1.2 μm to 2 x 10^{18} cm^{-3}. The lower cladding layer was Si doped to a concentration of 1 x 10^{18} cm^{-3}. The waveguide core was undoped, so forming a *pin* structure with the intrinsic region restricted to the QWs and the GRIN region.

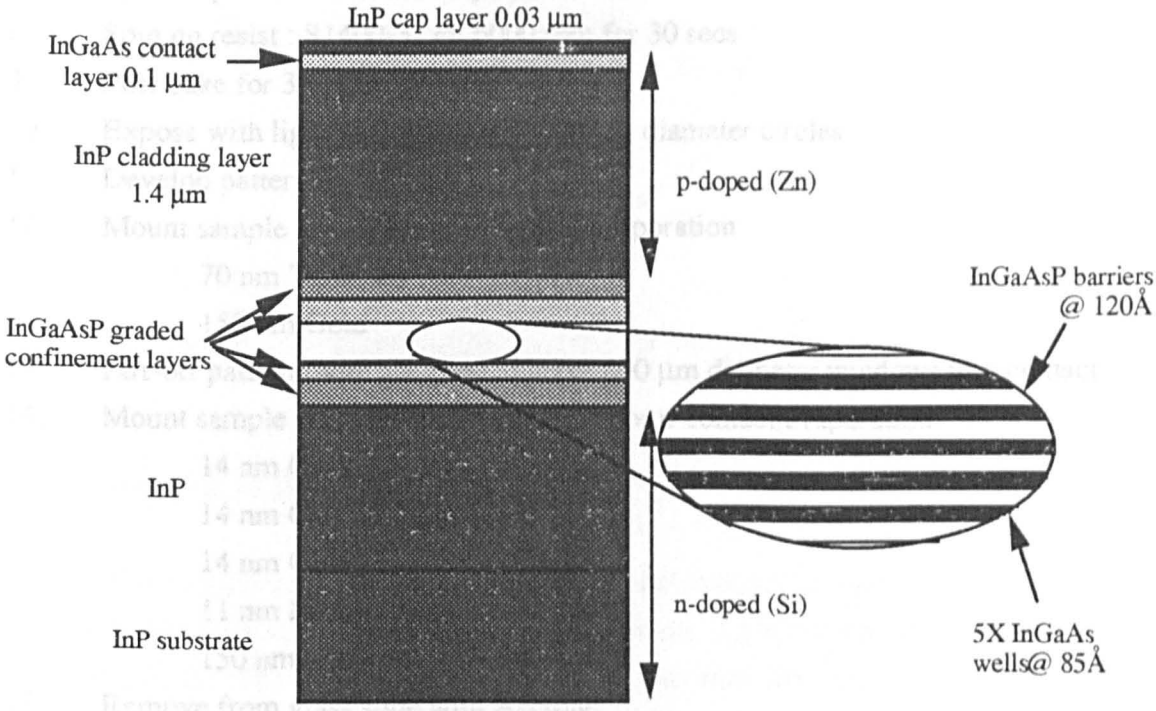

Fig. 1 Schematic of material structure used for photocurrent measurements

8.4.2 Fabrication

Samples were fabricated from both as-grown material and material which had been intermixed by varying amounts. The fabrication process is described in detail below

1. Scribe and cleave samples to 2 mm x 2 mm in size
2. Clean sample in ultrasonic bath: 3 mins. methanol,
   3 mins. acetone,
   rinse in RO water
3. Etch off InP cap layer with HCl : H_3PO_4 (in ratio 1:3) for 20 secs.
4. Plasma-Enhanced Chemical-Vapour-Deposition (PECVD) of 500 nm SiO_2
   Power = 10 watts
   Gas flow : SiH_4 = 9 sccm, N_2O = 710 sccm, N_2 = 171 sccm
   Temperature = 300°C
   Pressure = 1 torr
5. Disorder samples as described in Chapter 3
6. Remove 500 nm SiO_2 cap layer with buffered HF for 5 mins.
7. Spin on primer : dihexamethylsylane
8. Spin on resist : S1400-31 @ 6000 rpm for 30 secs
9. Post bake for 30 mins. @ 90°C
10. Expose with light-field pattern of 800 μm diameter circles
11. Develop pattern for 60 secs.
12. Mount sample in holder for p-contact evaporation
    70 nm Titanium
    150 nm Gold
13 Lift-off pattern (with acetone) to leave 800 μm diameter windows in p-contact
14. Mount sample on glass slide with resist for n-contact evaporation
    14 nm Gold
    14 nm Germanium
    14 nm Gold
    11 nm Nickel
    150 nm Gold
15. Remove from glass slide with Acetone
16. Anneal contacts in Rapid Thermal Annealer (RTA) at 360°C for 90 secs.

Fig. 2 shows a schematic representation of the devices used to measure photocurrent.

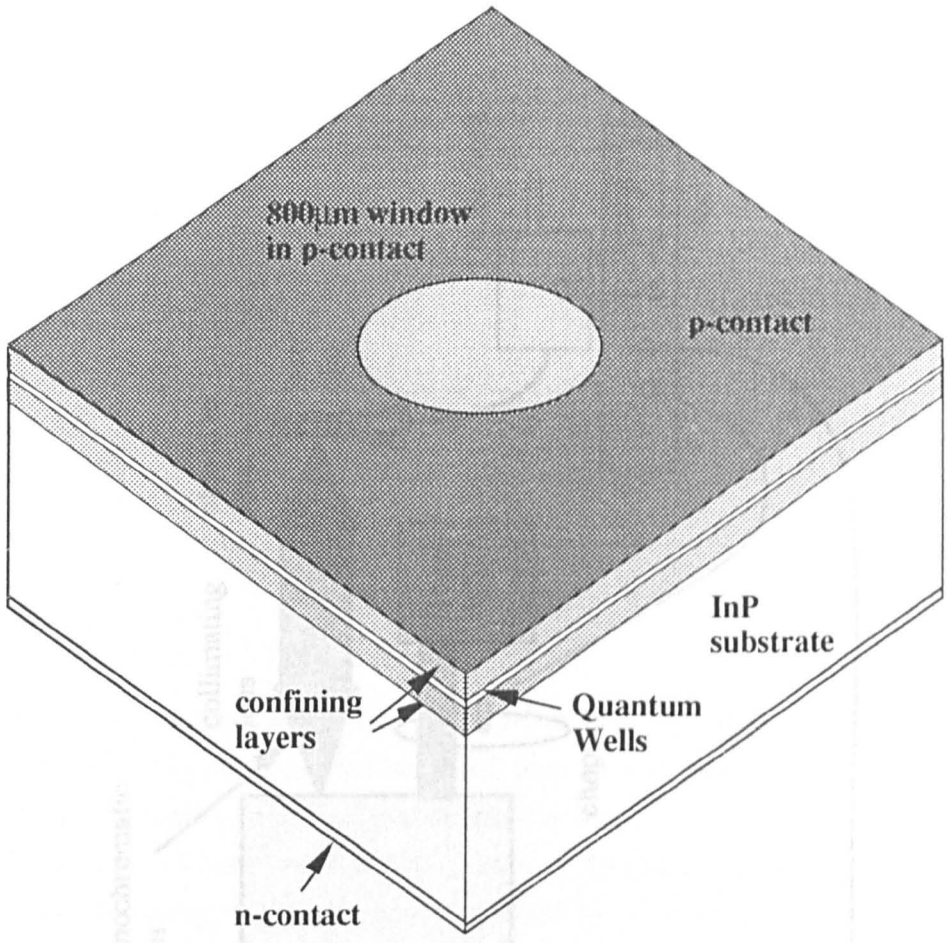

Fig. 2 Schematic diagram of device used for photocurrent measurements

8.5 Experimental Set-up

The experimental set-up for measuring photocurrent is shown in Fig. 3. The tuneable light source was derived from a white light source coupled into a monochromator. The output was collimated into an objective lens and focused onto the sample, which was held in a modified laser clip with a small aperture in it. The laser clip held the sample in place by means of a spring and provided electrical contacts to the sample from the bias circuit. The bias circuit is shown in Fig. 4 and allows the reverse bias voltage to the diode to be varied.

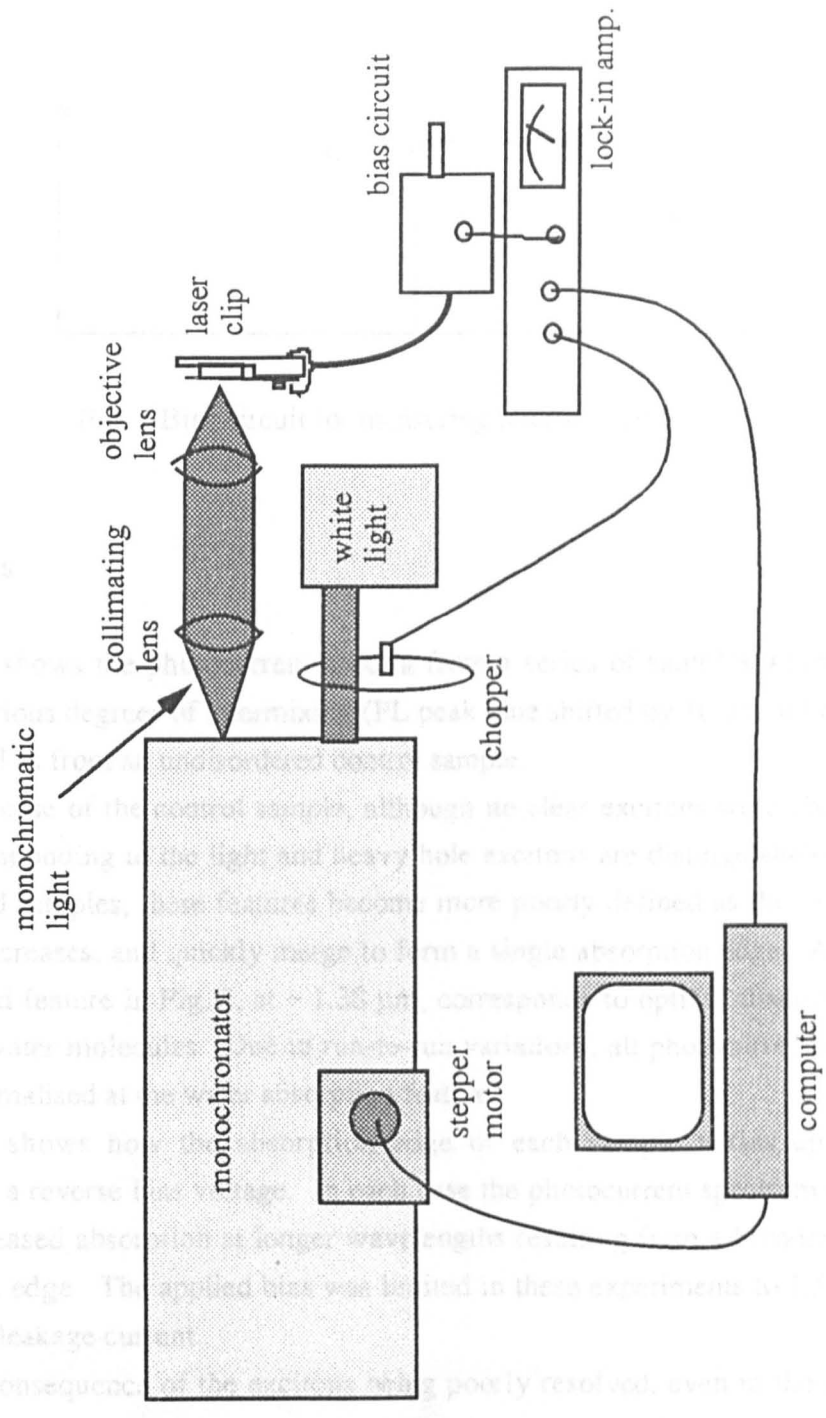

Fig. 3 Experimental set-up for measuring photocurrent

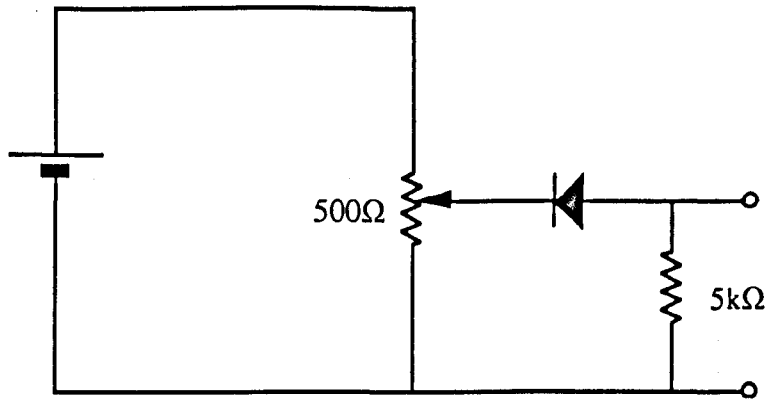

Fig. 4 Bias circuit for measuring photocurrent

8.6 Results

Fig. 5 shows the photocurrent spectra from a series of samples which have undergone various degrees of intermixing (PL peak blue shifted by 10 nm, 63 nm and 78 nm) as well as from an undisordered control sample.

In the case of the control sample, although no clear excitons were observed, features corresponding to the light and heavy hole excitons are distinguishable. For the intermixed samples, these features become more poorly defined as the extent of disordering increases, and quickly merge to form a single absorption edge. Another clearly defined feature in Fig. 5, at ~ 1.38 μm, corresponds to optical absorption by atmospheric water molecules. Due to run-to-run variations, all photocurrent spectra have been normalised at the water absorption feature.

Fig. 6 shows how the absorption edge of each sample varies upon the application of a reverse bias voltage. In each case the photocurrent spectrum clearly indicates increased absorption at longer wavelengths resulting from a broadening of the absorption edge. The applied bias was limited in these experiments to 1.5 V due to the reverse leakage current.

As a consequence of the excitons being poorly resolved, even in the control sample at zero bias, it is not clear whether or not there is any appreciable demonstration of the QCSE, however the broadening of the absorption edge shows there is a substantial FK effect.

The experiment was repeated with a different wafer (MR 378, with an identical structure to MR 193 described above) which had improved reverse-bias diode characteristics. Fig. 7 shows photocurrent spectra of the as-grown material with different reverse bias voltages applied. There is a clear excitonic feature visible at

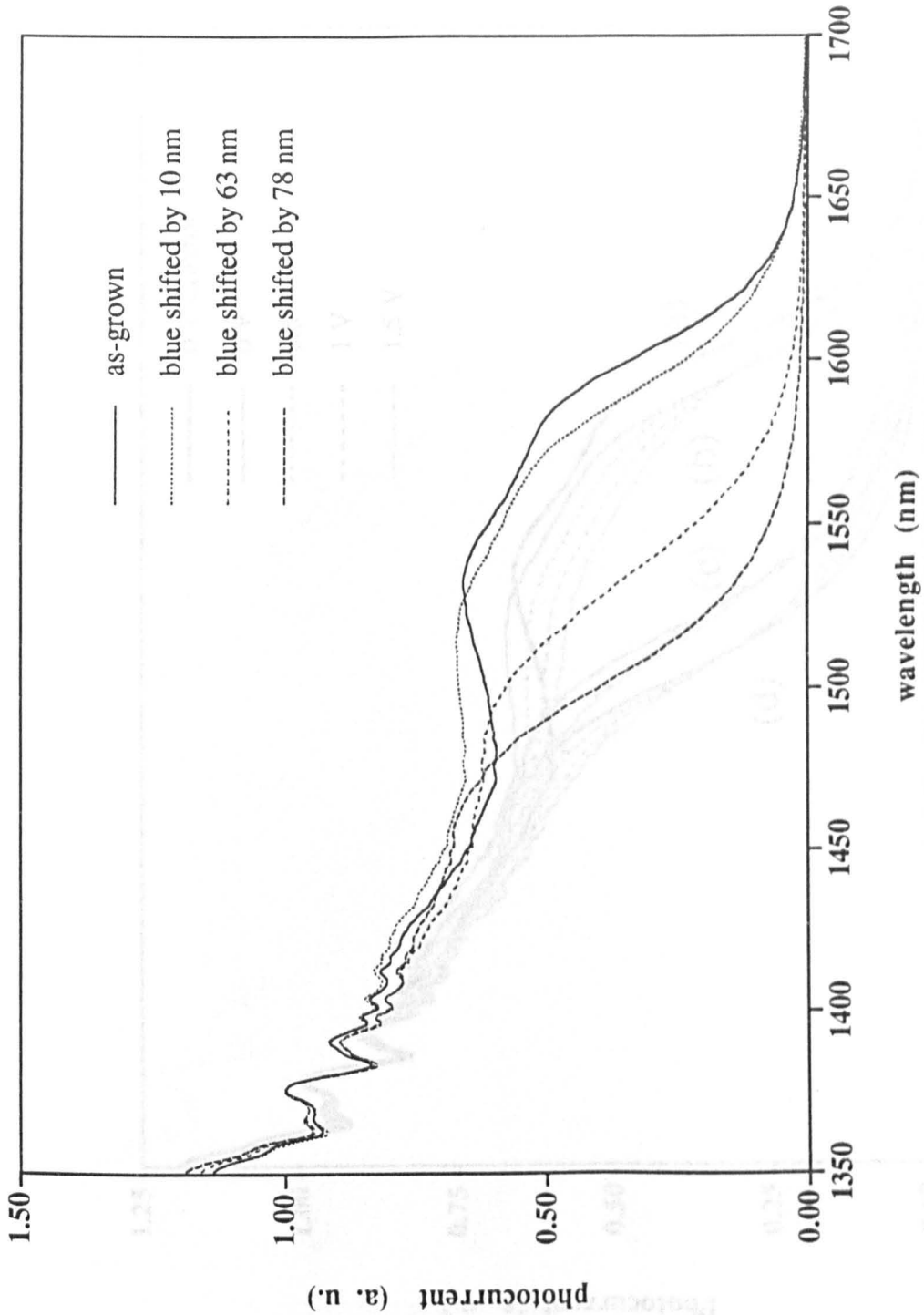

Fig. 5 Photocurrent spectra of samples intermixed by varying amounts

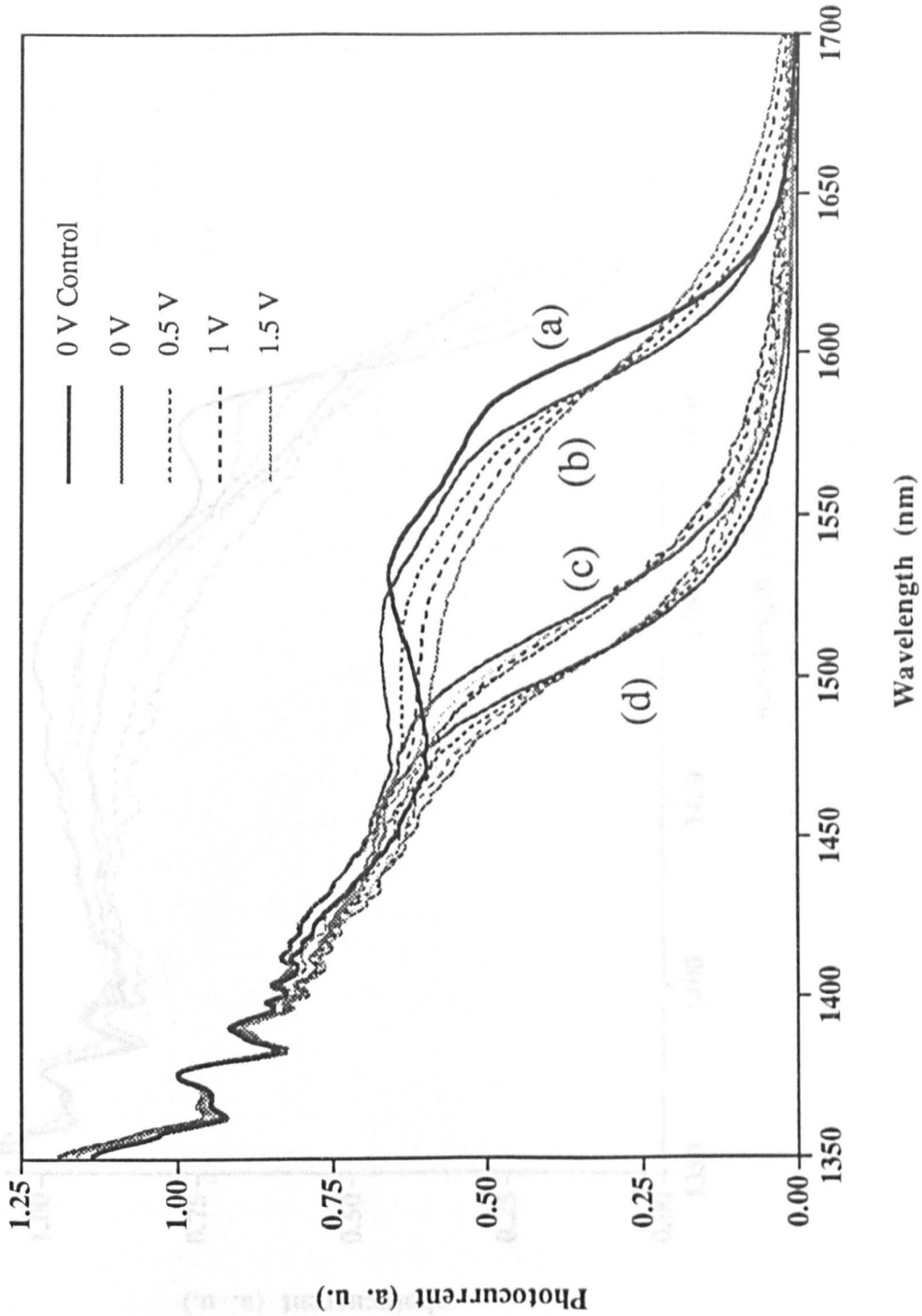

Fig. 6 Photocurrent spectra of samples under reverse bias, which have undergone intermixing of (a) 0 nm (control), (b) 10 nm, (c) 63 nm and (d) 78 nm.

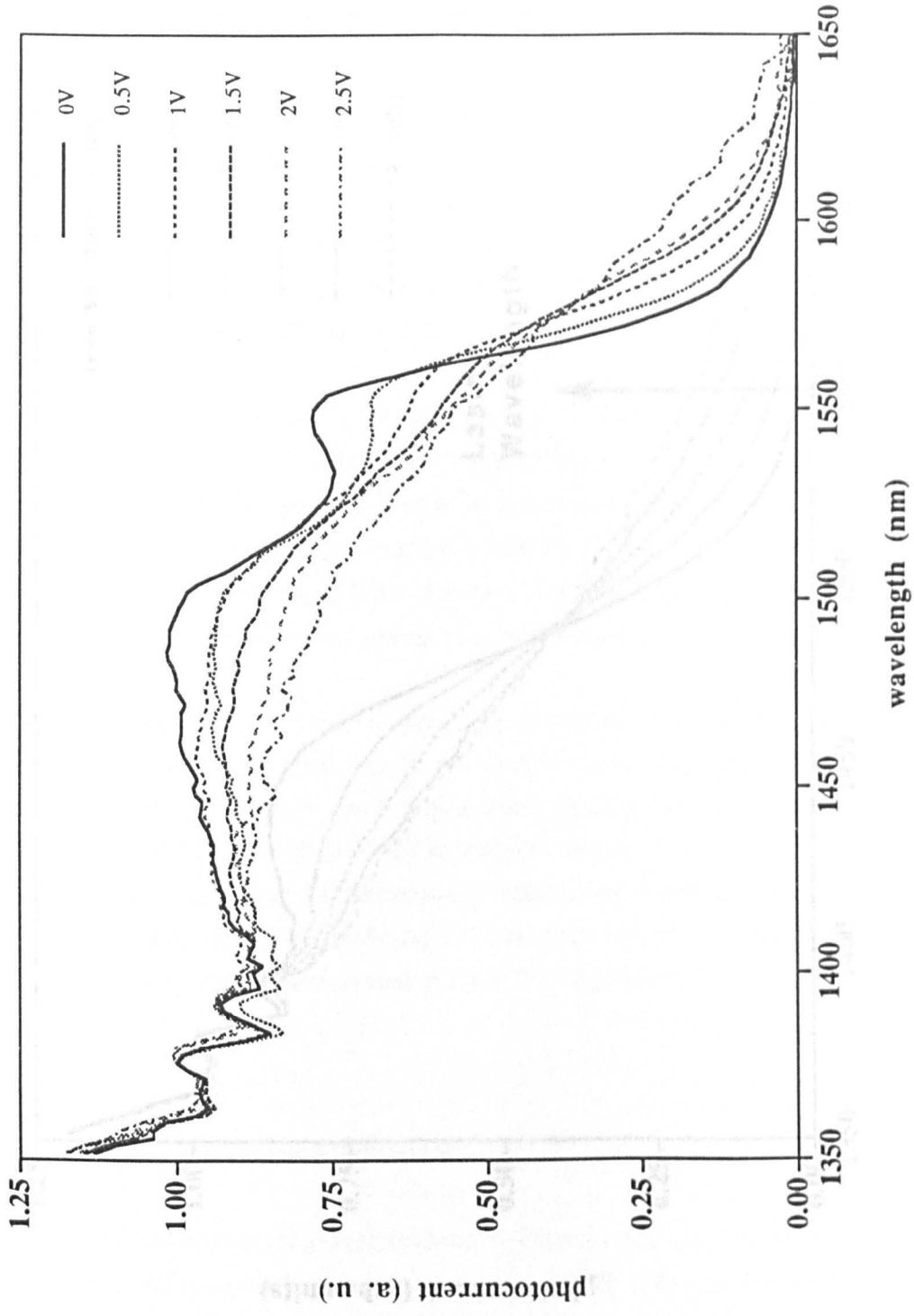

Fig. 7 Photocurrent spectra of as-grown material (MR378) under different reverse bias conditions

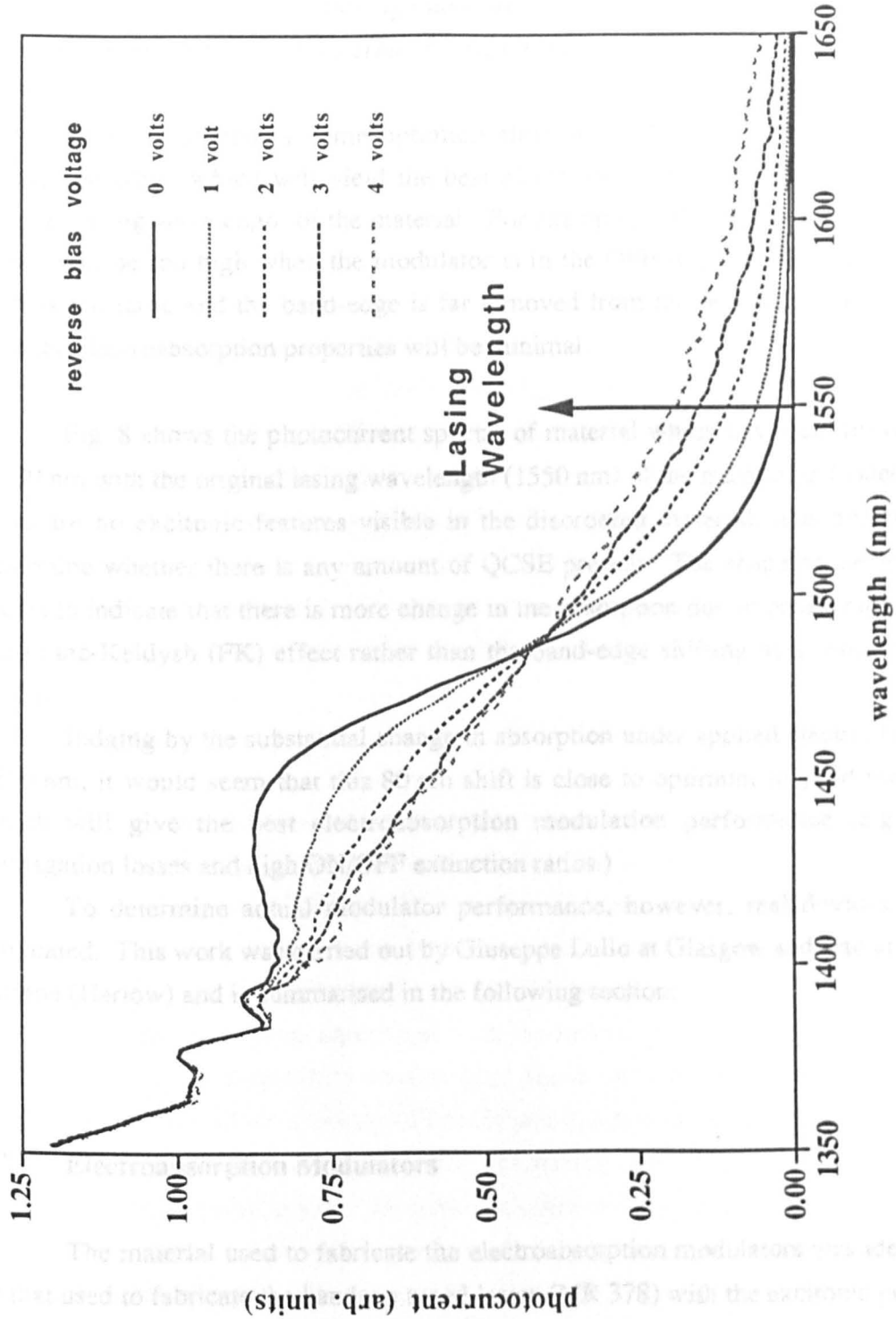

Fig. 8 Photocurrent spectra of disordered material (MR378) under different reverse bias conditions

1550 nm under zero bias conditions. As a voltage is applied and an electric field created, the feature is gradually shifted to longer wavelengths and washed out. This is clear evidence of the QCSE although also present is a broadening of the band-edge due to the Franz-Keldysh (FK) effect[10]. Again, the spectra have been normalised at ~ 1.38 μm.

There is obviously some optimum shift in the PL peak wavelength (and absorption edge) which will yield the best electroabsorption characteristics at the original lasing wavelength of the material. For example, if the shift is too small, the losses will be too high when the modulator is in the OFF regime. However, if the shift is too large and the band-edge is far removed from the operating wavelength, then the electroabsorption properties will be minimal.

Fig. 8 shows the photocurrent spectra of material which has been disordered by 80 nm with the original lasing wavelength (1550 nm) of the material indicated. As there are no excitonic features visible in the disordered material, it is difficult to determine whether there is any amount of QCSE present. The shape of the spectra seems to indicate that there is more change in the absorption due to broadening from the Franz-Keldysh (FK) effect rather than the band-edge shifting as a result of the QCSE.

Judging by the substantial change in absorption under applied electric field at 1550 nm, it would seem that this 80 nm shift is close to optimum to yield material which will give the best electroabsorption modulation performance (e.g. low propagation losses and high ON/OFF extinction ratios.)

To determine actual modulator performance, however, real devices were fabricated. This work was carried out by Giuseppe Lullo at Glasgow and also at BNR Europe (Harlow) and is summarised in the following section.

8.7 Electroabsorption Modulators

The material used to fabricate the electroabsorption modulators was identical to that used to fabricate the bandgap tuned lasers (MR 378) with the excitonic peak of the as-grown material, measured by photoluminescence at room temperature, occurring at approximately 1580 nm.

Room temperature photoluminescence and photocurrent measurements were carried out after disordering to determine the extent of bandgap shift in the samples. Depending on irradiation conditions, different amounts of shift were measured. The

maximum shift used for this group of devices was about 120 nm, although larger shifts can be realised in this structure.

The device structure of the modulators was identical to that of the ridge waveguide lasers and subsequently, the fabrication process was also identical (see section (7.2)). The only difference was that all devices were cleaved to a length of 500 μm.

8.8 Measurement Set-up

A semiconductor laser, tuneable in the wavelength range from 1480 nm to 1580 nm, was used to assess the device performance. Light was end-fire coupled into the sample through a tapered microlensed single-mode fibre. A fibre polarisation rotator ensured that only the TE-mode was excited in the waveguides. The output from the sample was collected by another fibre and detected by a germanium photodiode. Fig. 9 shows the experimental set-up. Transmission characteristics were investigated as a function of wavelength. Assuming a coupling loss of 6 dB at the sample facets, the estimated propagation loss of the modulators at the optimum operating wavelength with no applied bias was about 2 dB per 100 μm.

8.9 Results

Fig. 10 shows the modulation depth versus wavelength for three different degrees of disordering, corresponding to a shift in the bandgap edge, with respect to the as-grown material, of 80 nm, 95 nm and 120 nm. Measurements have been carried out with a voltage sweep between +0.5 V and -1 V. A decrease in the modulation depth is clearly noticeable in samples which have increased disordering. Such behaviour is in good agreement with theoretical expectation, as disordering causes a reduction in quantum confinement due to the smoothing of the potential barrier shape. This effect is worthy of further investigation because the use of shallow wells is suggested as a solution for increasing the saturation intensity in electroabsorption modulators[11]. Moreover, shallow wells would prevent hole pile-up in the active region, allowing a higher cut-off frequency at low bias voltages and an improvement in quantum efficiency.

The normalised transmitted power is plotted in Fig. 11 (for samples which have been disordered by 80 nm and 120 nm) which indicates that the transmitted power is strongly wavelength dependent for both samples. This is to be expected as these devices are working at wavelengths very close to the band-edge.

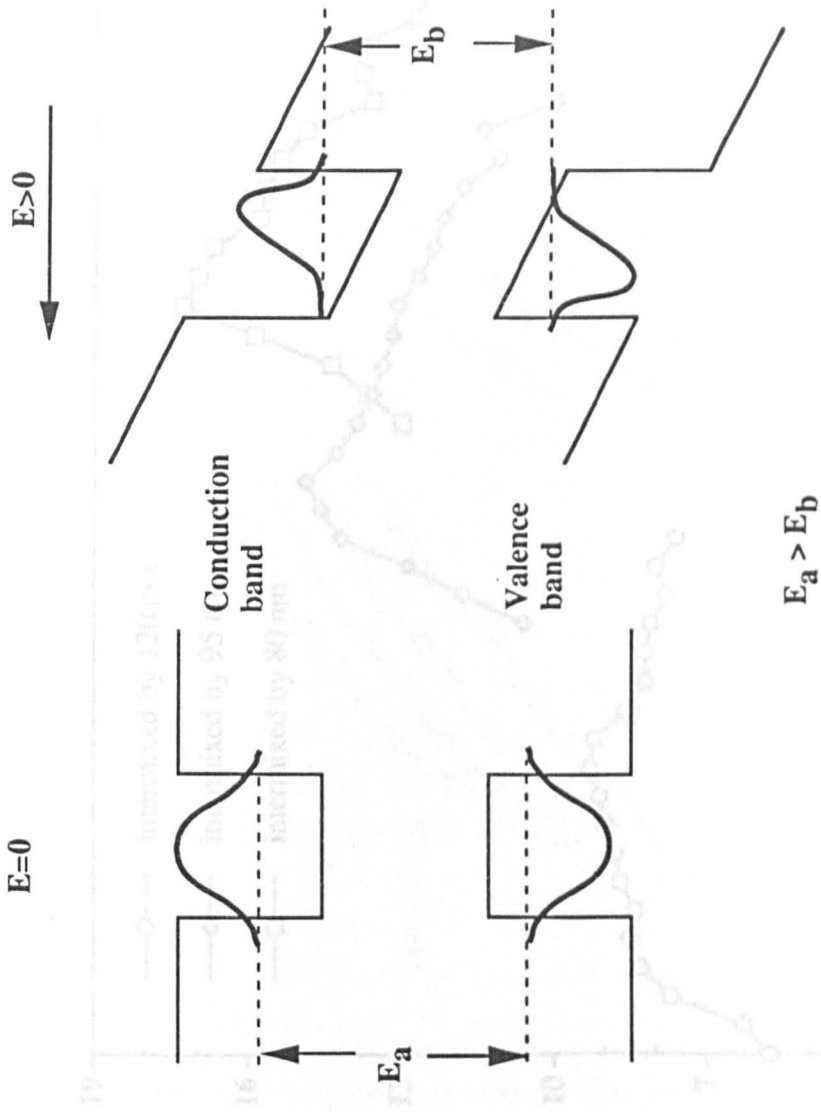

Fig. 9 Quantum Confined Stark Effect

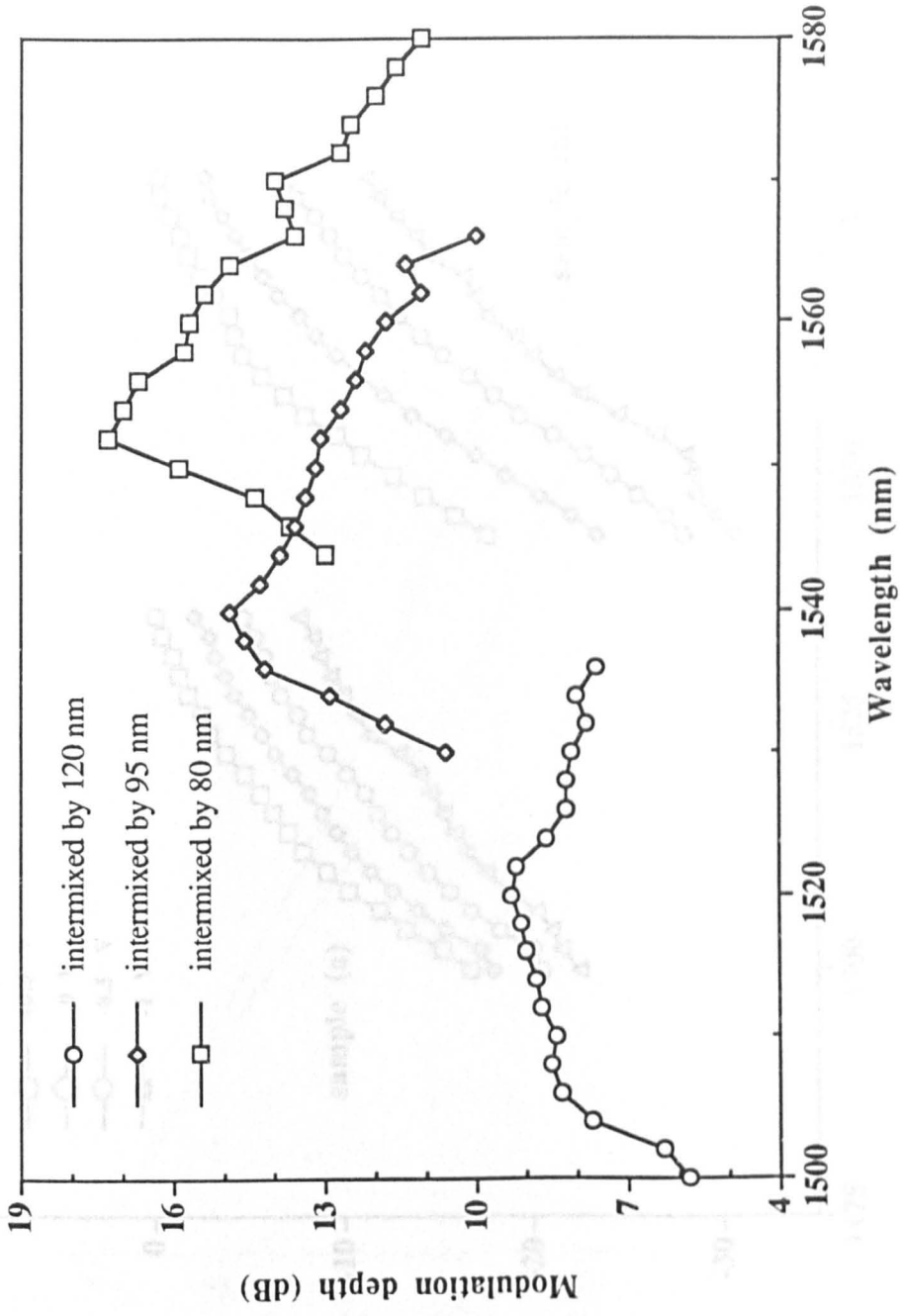

Fig. 10 Modulation depth as a function of wavelength
for three different degrees of intermixing

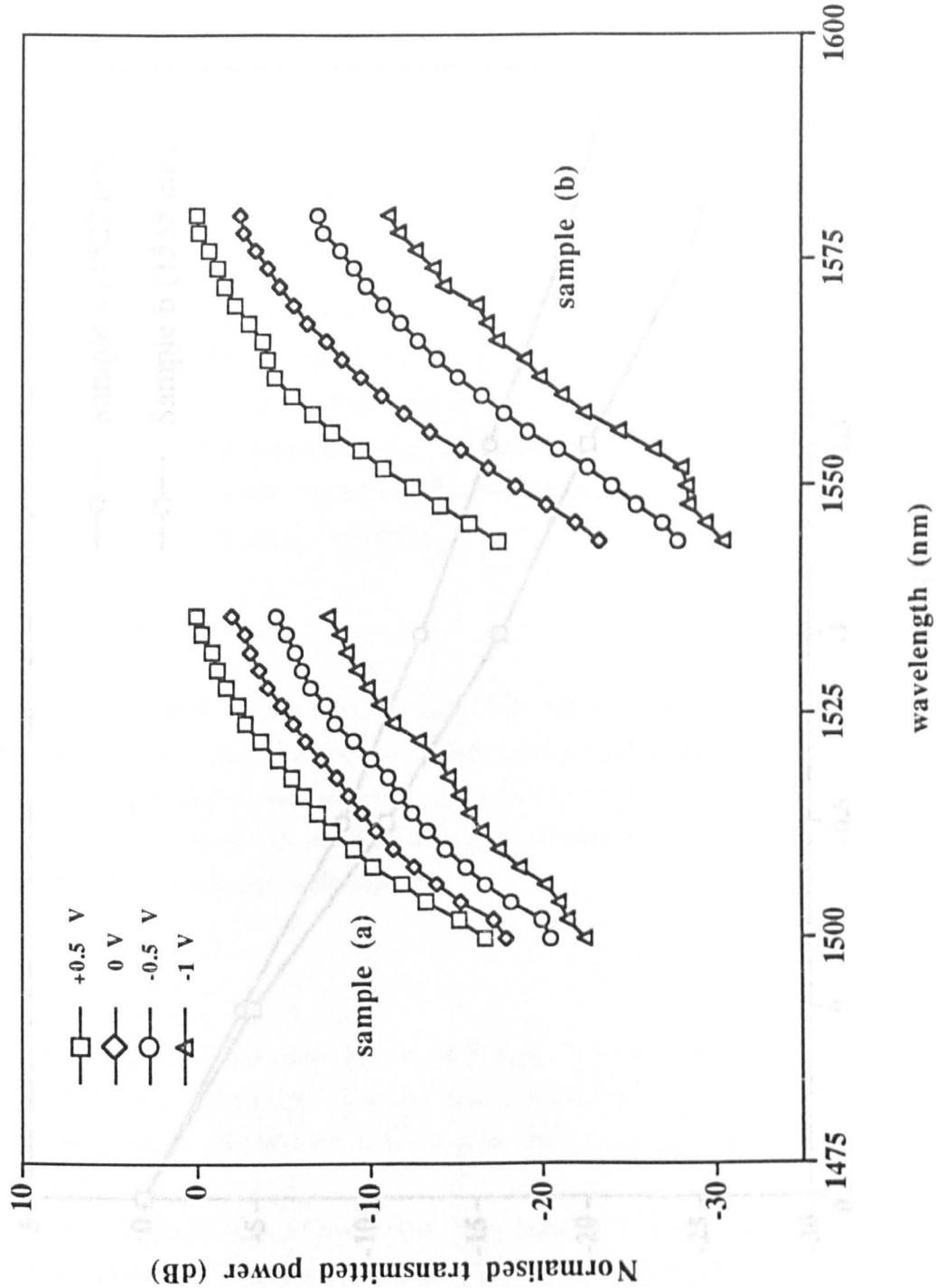

Fig. 11 Normalised transmitted power for sample (a) disordered by 120 nm and sample (b) disordered by 80 nm

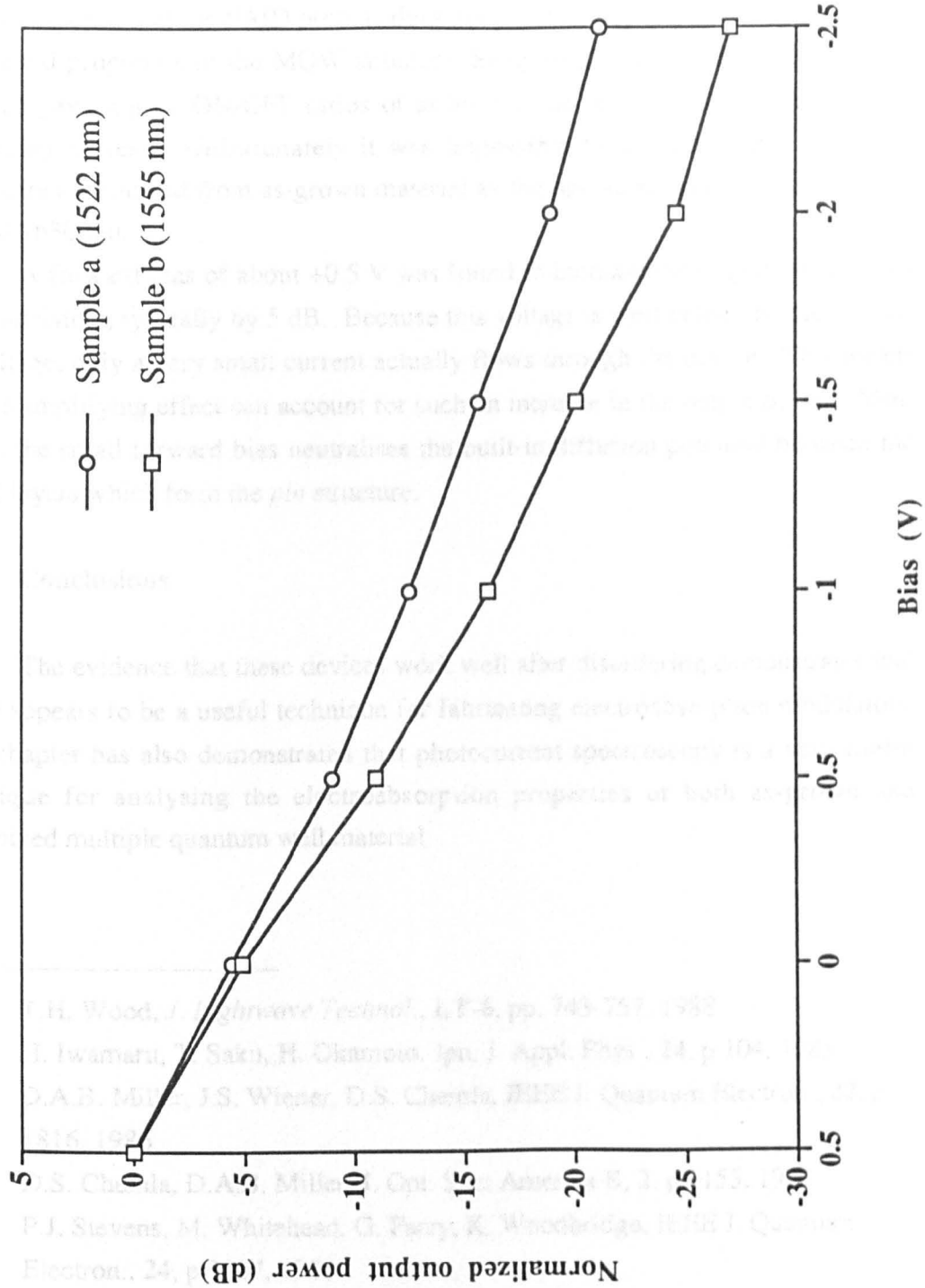

Fig. 12 Modulation depth as a function of reverse bias voltage at optimum operating wavelength

At the optimum modulation wavelength of 1522 nm for samples whose bandgap had been shifted as far as 120 nm, an ON/OFF ratio of over 20 dB (Fig. 12) was obtained when the bias voltage was varied between +0.5 V and -2.5 V. This is further evidence that the PAID process does not produce any dramatic degradation in the optical properties of the MQW structure. Samples disordered to a lesser degree (80 nm) gave higher ON/OFF ratios of at least 27 dB at 1555 nm, limited by the measuring system. Unfortunately it was impossible to compare these results to modulators fabricated from as-grown material as the operating wavelength would be around 1630 nm.

A forward bias of about +0.5 V was found to increase the output power from the modulators, typically by 5 dB. Because this voltage is well below the diode turn-on voltage, only a very small current actually flows through the device. This means that no amplifying effect can account for such an increase in the output power. Most likely, the small forward bias neutralises the built-in diffusion potential between the doped layers which form the *pin* structure.

8.10 Conclusions

The evidence that these devices work well after disordering demonstrates that PAID appears to be a useful technique for fabricating electroabsorption modulators. This chapter has also demonstrated that photocurrent spectroscopy is a very useful technique for analysing the electroabsorption properties of both as-grown and intermixed multiple quantum well material.

---

1 T.H. Wood, *J. Lightwave Technol.*, **LT-6**, pp. 743-757, 1988

2 H. Iwamaru, T. Saku, H. Okamoto, Jpn. J. Appl. Phys., **24**, p 104, 1985

3 D.A.B. Miller, J.S. Wiener, D.S. Chemla, IEEE J. Quantum Electron., **22**, p 1816, 1986

4 D.S. Chemla, D.A.B. Miller, J. Opt. Soc. America B, **2**, p 1155, 1985

5 P.J. Stevens, M. Whitehead, G. Parry, K. Woodbridge, IEEE J. Quantum Electron., **24**, p 2007, 1988

6 D.S. Chemla, D.A.B. Miller, P.W. Smith, A.C. Gossard, W. Wiegman, IEEE J. Quantum Electron., **20**, p 265, 1984

7 J.D. Dow, D. Renfield, Phys. Rev. Lett., **1**, p 3358, 1970

8 D.S. Chemla, D.A.B. Miller, J. Opt. Soc. America B, **2**, p 1155, 1985

9 F.Y. Juang, J. Singh, P.K. Bhattacharya, Appl. Phys. Lett., **48**, p 1246, 1986

10 L.V. Keldysh, Sov. Phys. Jept., **34**(9), p788-790, 1958

11 F. Devaux, E. Bigan, A. Ougazzaden, B. Pierre, F. Huet, M. Carre, and A. Carenco, IEEE Photonics Technol. Lett.,4 , pp 720-722, 1992

Chapter 9 Extended Cavity Broad Area Oxide Stripe Lasers

9.1 Introduction

An intermixing technique which allows discreet bandgap tuned devices to be fabricated could be useful for many applications. However, the real potential of intermixing processes lies in their ability to produce integrated optoelectronic circuits. One of the simplest forms of such a circuit is an extended cavity laser which contains a bandgap widened passive waveguide section.

A device such as this also has practical applications. For example, the use of external cavities to narrow the linewidth of semiconductor lasers is commonplace but they are bulky and require careful alignment with good stability. An internal cavity promises to be appreciably more stable and requires a cavity approximately four times[1] shorter than an equivalent air cavity.

Fabricating a laser with a built in waveguide section can be accomplished by using some form of intermixng process to create transparent waveguides at the lasing wavelength over selected areas of the wafer. The PAID process is particularly suited to this form of selective bandgap shifting as areas which are not required to be disordered can be effectively masked during the process. The extended cavity laser also allows loss measurements to be carried out on disordered waveguides, which can be compared with measurements obtained on passive ridge waveguide structures (as in Chapter 4).

9.2 Fabrication

The material used to fabricate the Extended Cavity Lasers (ECLs) was identical to that used in Chapter 8 except that the quantum wells were only 55 Å wide leading to a photoluminescence peak of a 1480 nm. Fig. 1 shows a schematic diagram of the ECLs. In the passive waveguide sections, the highly p-doped InGaAs contact layer has been etched off to prevent current spreading. The fabrication process is listed below:

1. Clean sample in ultrasonic bath: 3 mins. methanol,
   3 mins. acetone,
   rinse in RO water
2. Etch off InP cap layer with HCl : H_3PO_4 (in ratio 1:3) for 20 secs.

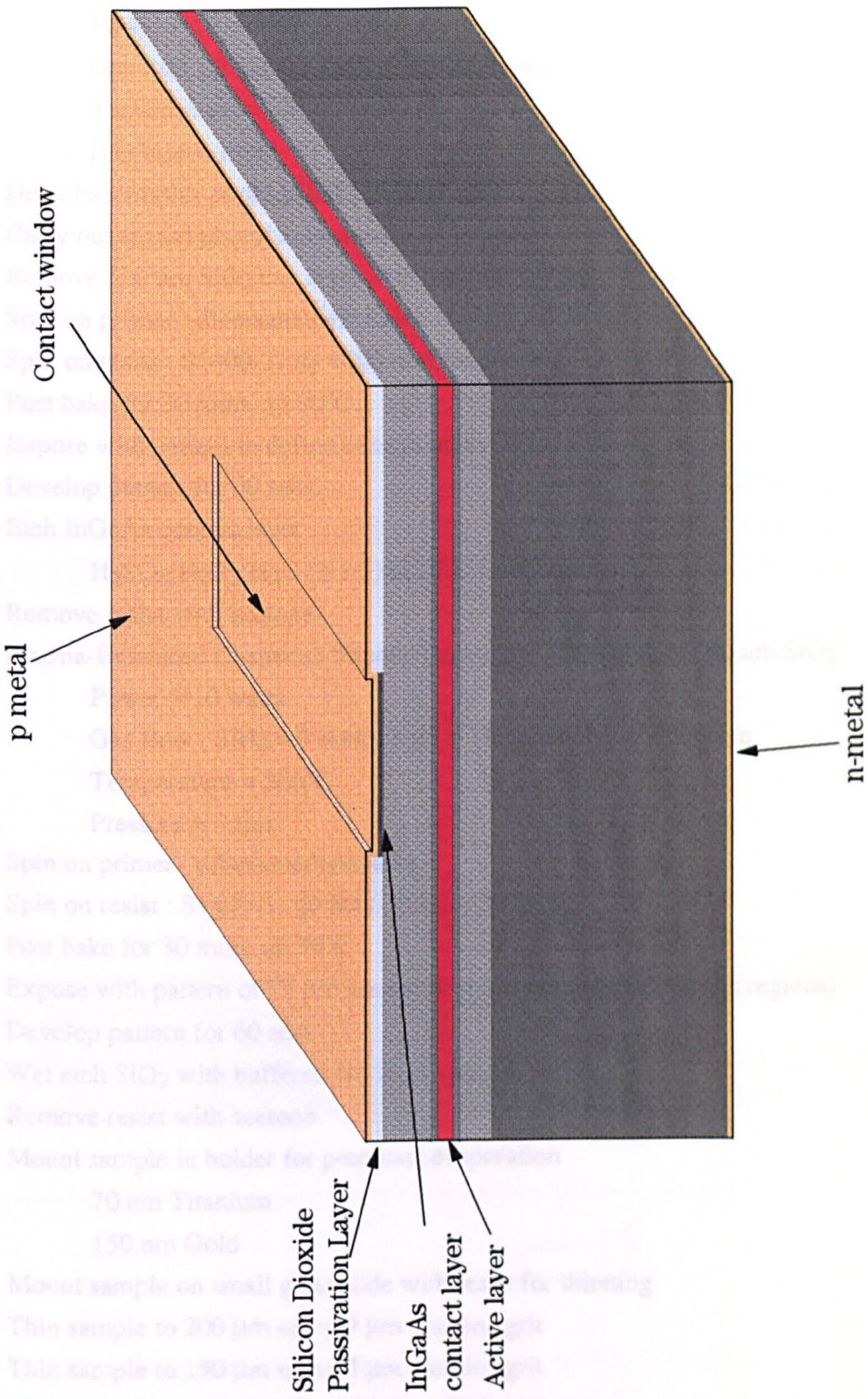

Fig. 1 Schematic Extended Cavity laser

3. Plasma-Enhanced Chemical-Vapour-Deposition (PECVD) of 500 nm SiO_2
   Power = 10 watts
   Gas flow : SiH_4 = 9 sccm, N_2O = 710 sccm, N_2 = 171 sccm
   Temperature = 300°C
   Pressure = 1 torr
4. Disorder samples as described in Chapter 3
5. Carry out spatial photoluminescence of sample
6. Remove 500 nm SiO_2 cap layer with buffered HF for 5 mins.
7. Spin on primer : dihexamethylsylane
8. Spin on resist : S1400-31 @ 6000 rpm for 30 secs
9. Post bake for 30 mins. @ 90°C
10. Expose with pattern to define contact regions
11. Develop pattern for 60 secs.
12. Etch InGaAs contact layer
    H_2SO_4:H_2O_2:H_2O (3:1:1) @20°C for 30 secs
13. Remove resist with acetone
14. Plasma-Enhanced Chemical-Vapour-Deposition (PECVD) of 200 nm SiO_2
    Power = 10 watts
    Gas flow : SiH_4 = 9 sccm, N_2O = 710 sccm, N_2 = 171 sccm
    Temperature = 300°C
    Pressure = 1 torr
15. Spin on primer : dihexamethylsylane
16. Spin on resist : S1400-31 @ 6000 rpm for 30 secs
17. Post bake for 30 mins. @ 90°C
18. Expose with pattern of 75 μm contact windows (on top of InGaAs regions)
19. Develop pattern for 60 secs
20. Wet etch SiO_2 with buffered HF for 12 seconds
21. Remove resist with acetone
22. Mount sample in holder for p-contact evaporation
    70 nm Titanium
    150 nm Gold
23. Mount sample on small glass slide with resist for thinning
24. Thin sample to 200 μm using 9 μm alumina grit
25. Thin sample to 150 μm using 3 μm alumina grit
26. Wet-etch with HCl : H_3PO_4 (in ratio 1:3) for 10 mins. to remove any damage
27. Remove from glass slide with acetone
28. Mount sample on glass slide with resist for n-contact evaporation
    14 nm Gold
    14 nm Germanium

14 nm Gold

11 nm Nickel

150 nm Gold

29. Demount from glass slide with acetone
30. Anneal contacts in Rapid Thermal Annealer at 360°C for 90 secs.
31. Scribe and cleave samples with active region lengths of 600 μm and a passive region length of 600 μm

The experimental set-up used to intermix the material is shown in Fig. 2. During the disordering process, half of the Gaussian profiled laser beam was shielded using a metal mask suspended approximately 200 μm above the material surface. This mask effectively stops any heat being generated within certain regions of the material, thereby generating an interface between disordered and undisordered regions. The beam size was approximately 2 mm (FWHM) and the material was disordered by moving the laser along the mask edge in steps of approximately 1.5 mm.

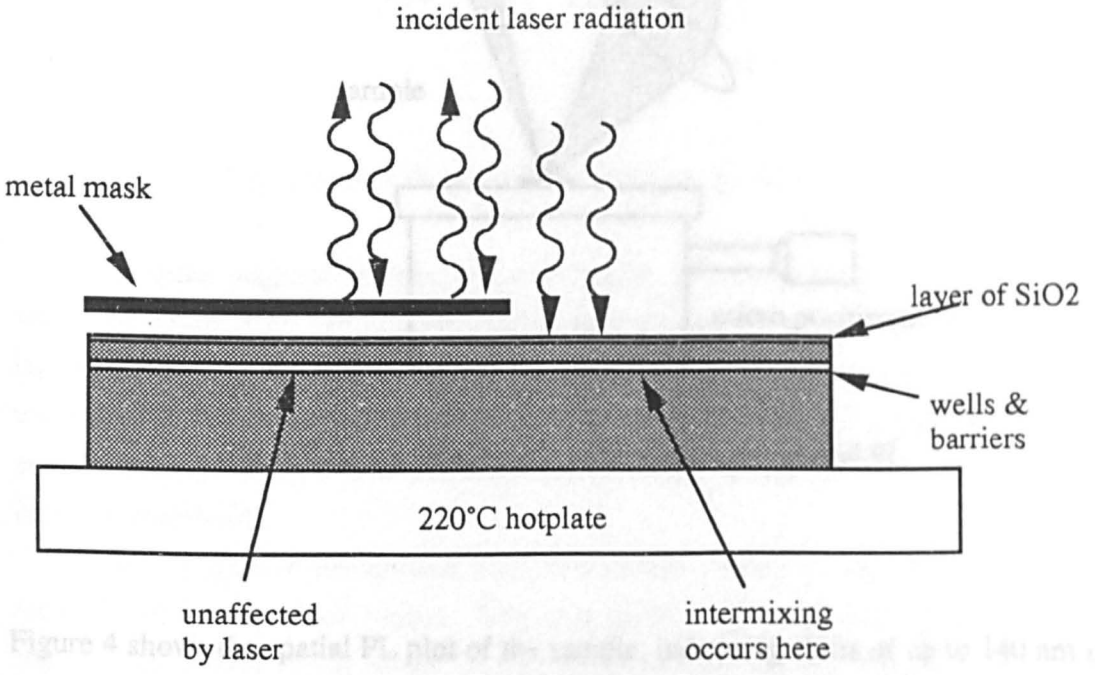

Fig.2 Experimental set-up used to intermix the ECL samples

The position of the metal mask does not determine the precise position of the interface because of the diffusion of heat away from the regions of high temperature i.e. the heat generated by the laser tends to diffuse under the mask. Chapter 10 deals

with analysis of this problem in more detail. In order to examine the spatial profile of the bandgap and determine where the active region and passive region of the ECL should be, photoluminescence measurements were carried out perpendicular to the mask edge in steps of 50 μm. Fig. 3 shows the experimental set-up used to carry out these measurements.

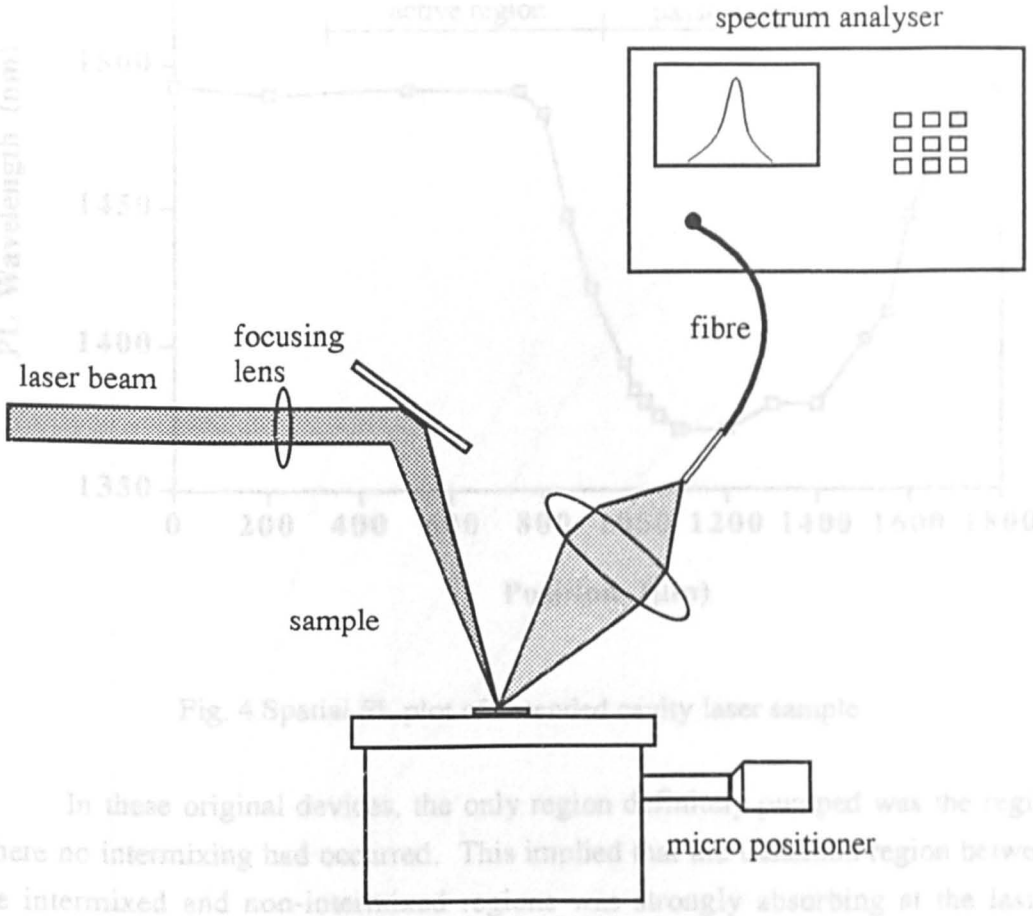

Fig. 3 Experimental set-up used to measure spatial PL

Figure 4 shows the spatial PL plot of the sample, indicating shifts of up to 140 nm in the disordered section, with a transition region width of around 200 μm. Also indicated on the graph is the position from which material for the fabricated devices was extracted. The interface between the active region and the passive region of the devices was chosen to be the mid-point between the zero intermixing and maximum intermixing regions. There were a number of reasons for this. Firstly, earlier devices fabricated by G. Lullo had a snap-on problem, as shown in Fig. 5. At threshold, these devices show a near vertical jump (snap-on) in the L-I characteristics but then a more

typical linear regime, with no kinks, takes over at higher currents. This sort of L-I relationship is typical of a Q-switched laser, which contains a saturable absorber in the cavity. This effect can also occur in broad area lasers with bad metal contacts, which cause inhomogeneous current injection, leading to gain switching[2].

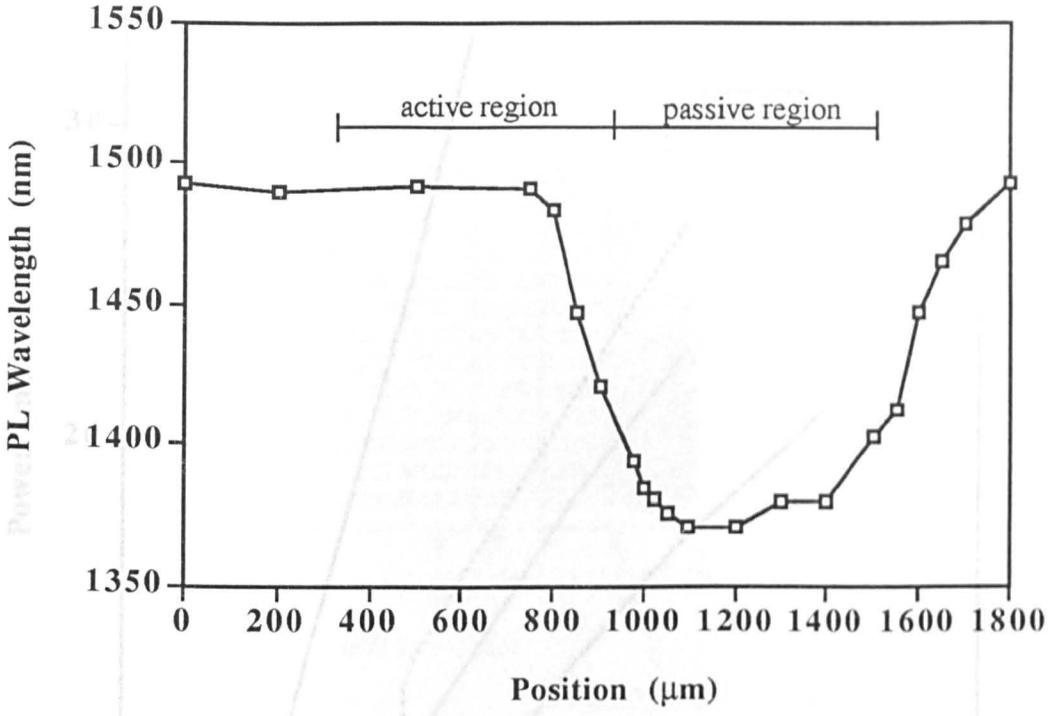

Fig. 4 Spatial PL plot of extended cavity laser sample

In these original devices, the only region definitely pumped was the region where no intermixing had occurred. This implied that the transition region between the intermixed and non-intermixed regions was strongly absorbing at the lasing wavelength. For the device to lase, this absorbing transition region must be bleached and, bleaching, being a non-linear effect, can explain the sudden burst in output power at threshold.

With regard to the devices fabricated in this chapter, it was decided to pump only half of the transition region. This was because the other half of the transition region would have much lower absorption losses, due to the wider bandgap, and similarly would contribute very little gain at the lasing wavelength.

9.3 Results

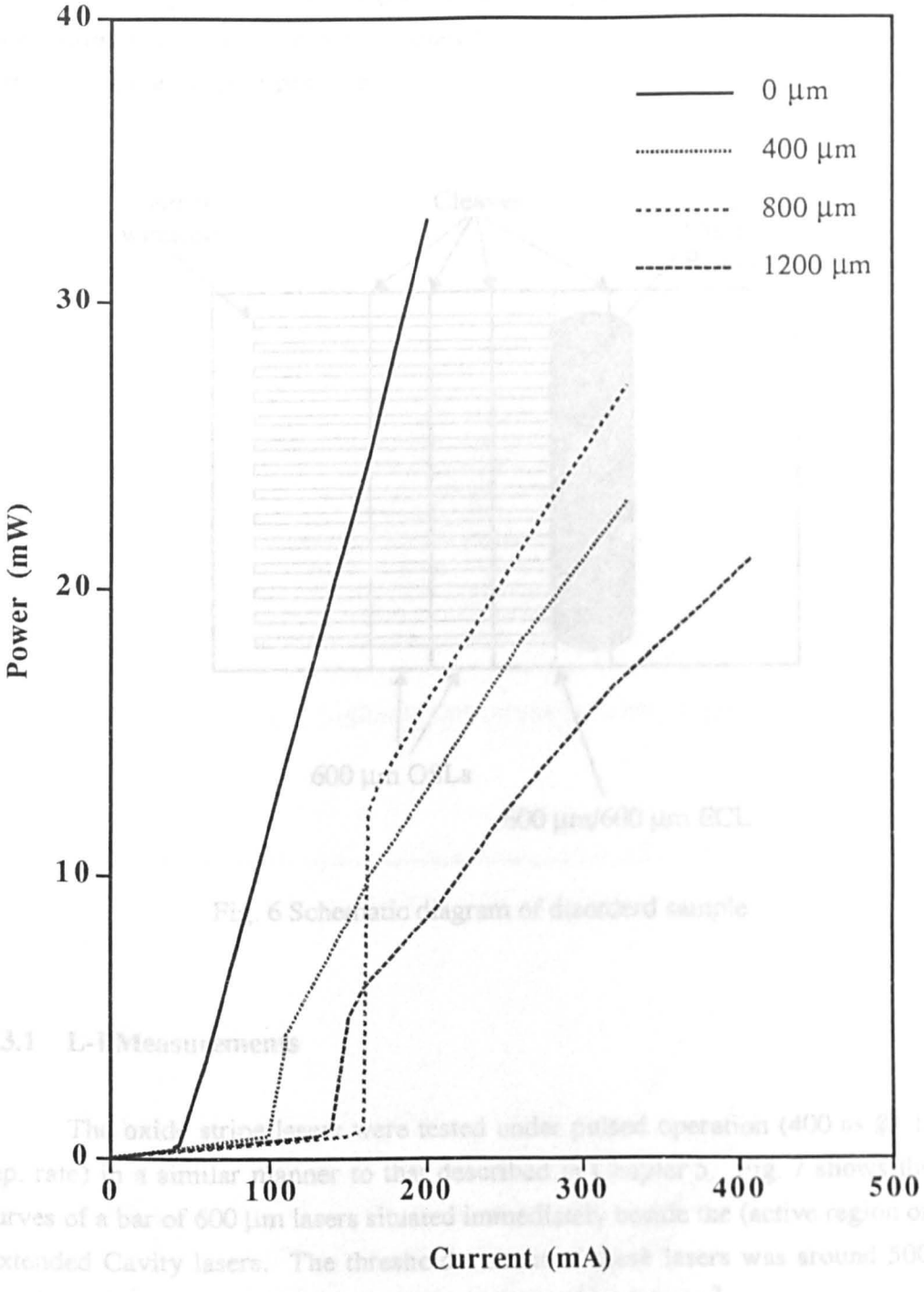

Fig. 5 Light-current curves for extended cavity lasers with passive sections of length 0 µm, 400 µm, 800 µm, and 1200 µm

The sample was cleaved (as shown in Fig. 6) in such a way as to produce broad area OSLs next to the extended cavity devices, making direct device performance comparison possible.

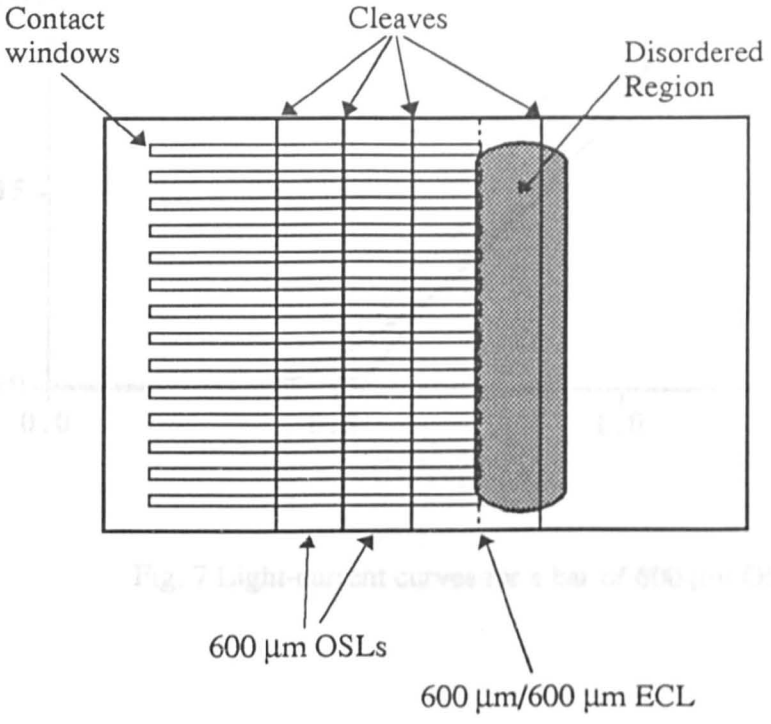

Fig. 6 Schematic diagram of disorderd sample

9.3.1 L-I Measurements

The oxide stripe lasers were tested under pulsed operation (400 ns @ 1 kHz rep. rate) in a similar manner to that described in Chapter 5. Fig. 7 shows the L-I curves of a bar of 600 μm lasers situated immediately beside the (active region of the) Extended Cavity lasers. The threshold current of these lasers was around 500 mA which corresponds to a threshold current density of 1.1 $kAcm^{-2}$.

Fig. 8 shows the L-I curves of the bar of EC lasers with 600 μm passive regions and 600 μm active regions. The best threshold current was around 1.2 A which is a factor of 2.4 greater than that of the 600 μm long oxide stripe lasers. The increase in threshold current is due to the absorption in the passive waveguide region, and the divergence of the light from the active region due to the lack of optical confinement in the waveguide region. It seems likely that the main loss is due to the lack of optical confinement in the transverse direction of the passive section, leading to poor coupling back into the active section.

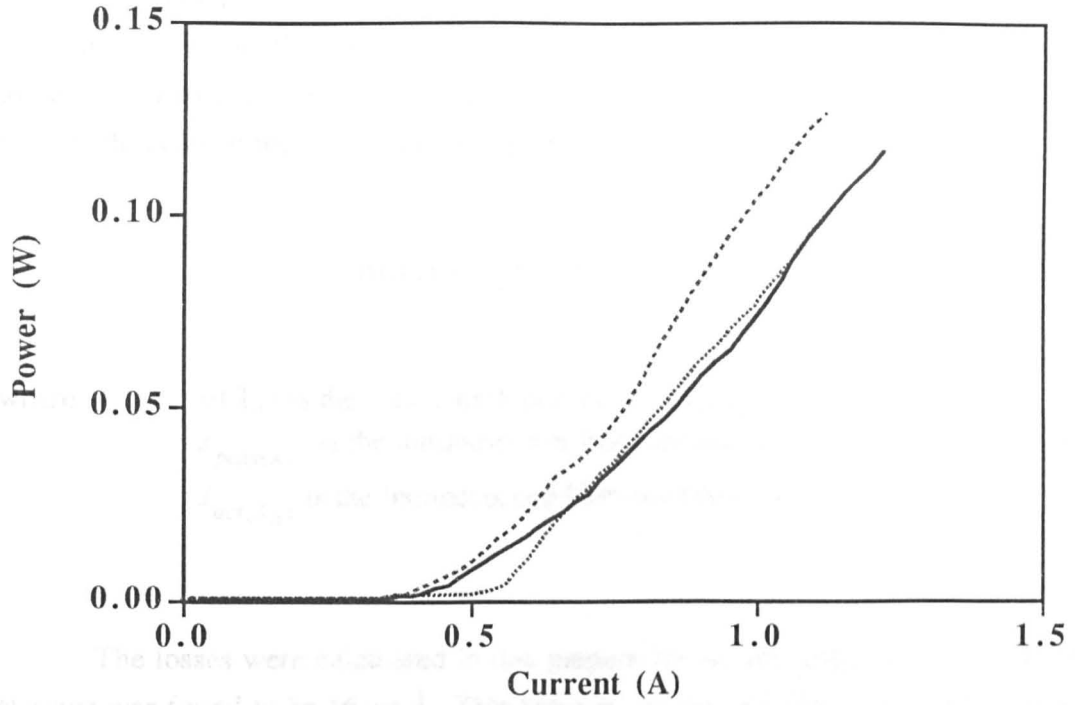

Fig. 7 Light-current curves for a bar of 600 μm OSLs

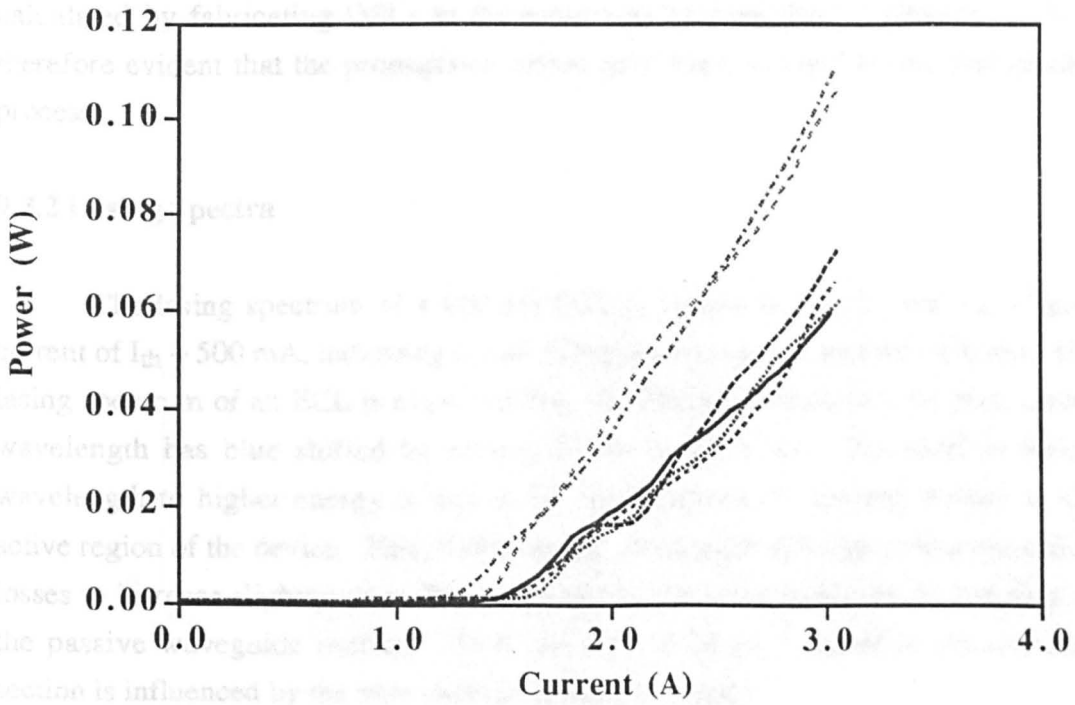

Fig. 8 Light-current curves for a bar of 600μm/600μm ECLs

It is not possible to determine the propagation losses from the change in threshold current as there is no transverse confinement in the passive section. The losses can, however, be determined by measuring the sub-threshold luminescence from both facets of the device and using the equation[3]:

$$\alpha(\lambda_o) = -\frac{1}{L_{pass}} \ln\left(\frac{J_{pass(\lambda_o)}}{J_{act(\lambda_o)}}\right) \tag{9.1}$$

where $\alpha(\lambda_o)$ is the wavelength dependent absorption (cm^{-1}),
$J_{pass(\lambda_o)}$ is the luminescence from the passive waveguide (mW), and
$J_{act(\lambda_o)}$ is the luminescence from the active laser side (mW).

The losses were calculated in this manner for all the lasers in the bar and the average was found to be 16 cm^{-1}. This value is the average loss of the entire passive waveguide section over the lasing wavelength range. It is expected that the losses are higher close to the interface (where the bandgap is narrower) and lower in regions away from the active section

The propagation loss of this particular laser wafer was found to be 28 cm^{-1} calculated by fabricating OSLs in the same way as described in Chapter 5. It is therefore evident that the propagation losses have been reduced by the intermixing process.

9.3.2 Lasing Spectra

The lasing spectrum of a 600 μm OSL is shown in Fig. 9, taken at a drive current of I_{th} + 500 mA, indicating a peak lasing wavelength of around 1500 nm. The lasing spectrum of an ECL is shown in Fig. 10, which indicates that the peak lasing wavelength has blue shifted by around 25 nm to 1475 nm. The shift in lasing wavelength to higher energy is due to the large increase in current density in the active region of the device. This shift in lasing wavelength will cause the propagation losses to increase slightly, since the energy of the photons is closer to the bandgap of the passive waveguide section. Thus, the loss of 16 cm^{-1} stated in the previous section is influenced by the blue shift in lasing wavelength.

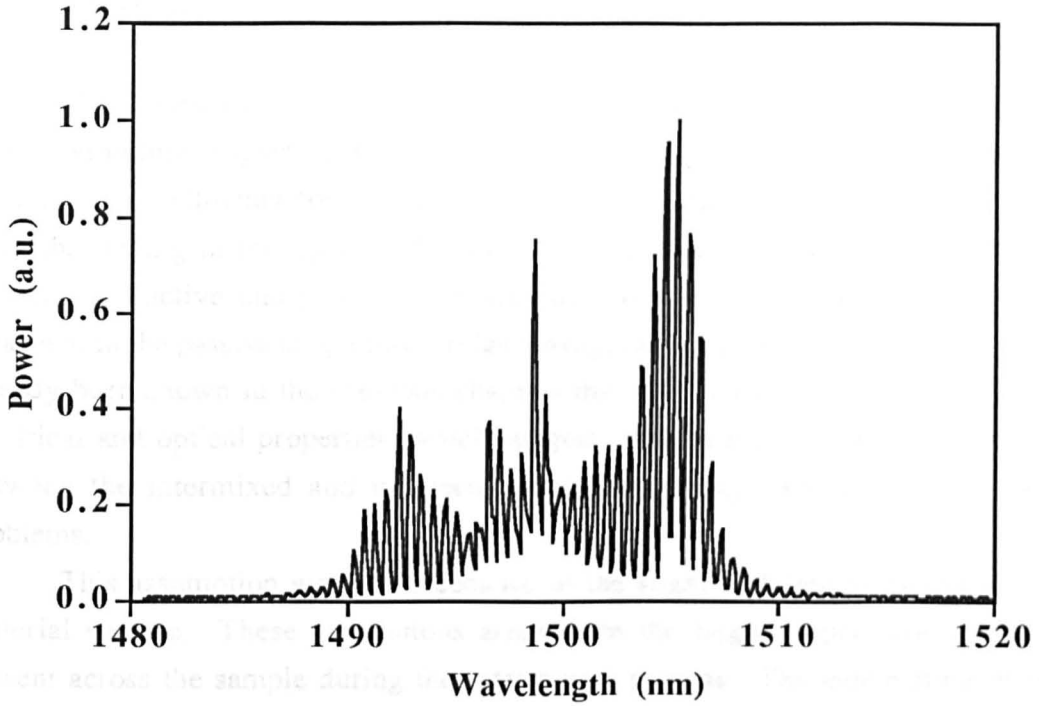

Fig. 9 Lasing spectrum for a 600 μm OSL

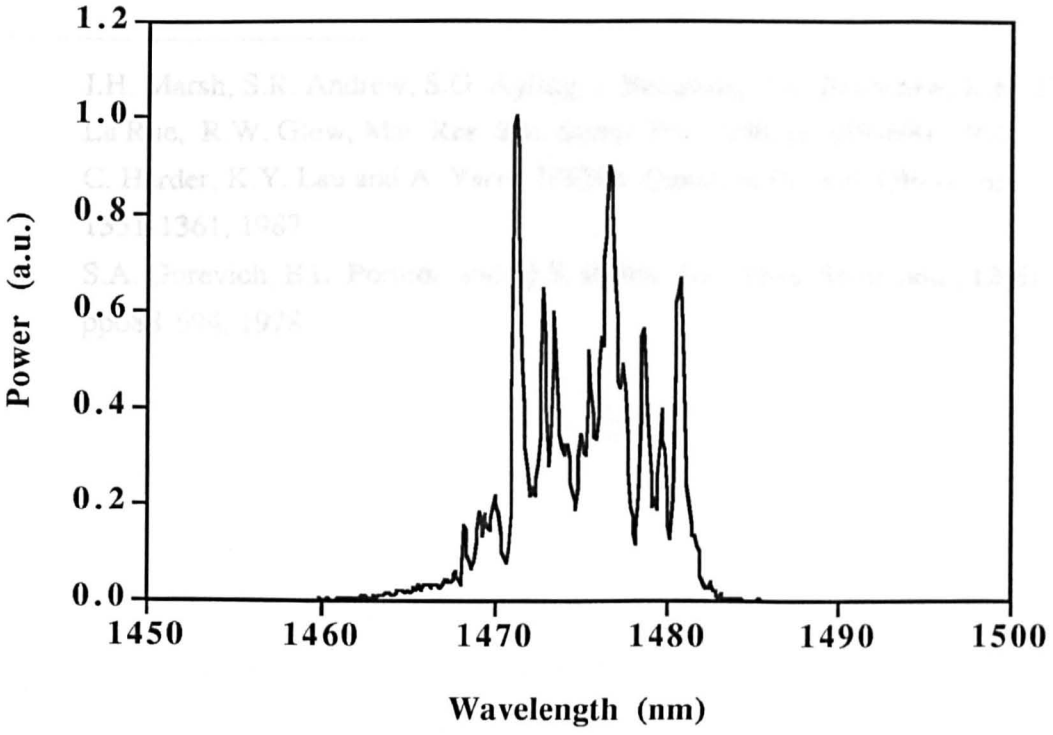

Fig. 10 Lasing spectrum for a 600μm/600μm ECL

9.4 Conclusions

The losses measured in the passive sections of Extended Cavity Lasers fabricated in this chapter are 16 cm^{-1} (70 $dBcm^{-1}$) compared to 28 cm^{-1} in the active regions. Even allowing for the extra losses incurred due to free-carrier absorption from the doping in the upper and lower cladding layers, and the coupling losses between the active and passive sections, the losses are much higher than those measured in the passive single-mode ridge waveguides fabricated in Chapter 4. It has already been shown in the previous chapters that intermixed material retains good electrical and optical properties, which suggests that perhaps the transition region between the intermixed and unintermixed material may have introduced some problems.

This assumption was made because of the slight undulations visible on the material surface. These undulations arose from the large temperature gradients present across the sample during the intermixing process. The temperature of the sample during the process varies from around 300°C (under the mask) to around 800°C in the areas exposed to the laser. This variation in temperature occurs in only about 150 μm, meaning that the strain placed on the material due to the varying amounts of thermal expansion probably causes it to warp in some way.

---

1 J.H. Marsh, S.R. Andrew, S.G. Ayling, J. Beauvais, S.A. Bradshaw, R.M. De La Rue, R.W. Glew, Mat. Res. Soc. Symp. Proc. **240**, pp 679-690, 1992

2 C. Harder, K.Y. Lau and A. Yariv, IEEE J. Quantum El., vol. QE-18, pp. 1351-1361, 1982.

3 S.A. Gurevich, E.L. Portnoi, and M.E. Raikh, Sov. Phys. Semicond., **12**(6), pp688-694, 1978

Chapter 10 Thermal modelling of the PAID process

10.1 Introduction

In this chapter, results will be presented on thermal modelling of PAID, giving an insight into the ultimate resolution capabilities of the process and the different factors such as laser spot size and heat sinking conditions which affect it.

Virtually all of the calculations carried out in this chapter are numerical in nature (i.e. they have been solved using a computer) because the model and therefore the calculations are complicated and the availability of a commercial software package allowed the problems to be solved with relative ease. It should be noted that the problems were solved with "relative ease" only after a rather complicated model and program had been created.

10.2 Equations of Heat Flow

In order to understand the model, it is useful to describe the basic equations of heat-flow and conduction.

10.2.1 1-D case

The simplest case of heat transfer by conduction is given by the Fourier rate equation[1] :

$$Q_x = -kA\frac{\partial T}{\partial x} \tag{10.1}$$

where Q_x is the rate of heat flow in the x direction (W),
k is the thermal conductivity of the material ($Wm^{-1}K^{-1}$)
A is the area of heat flow (m^2), and
T is the temperature (K).

The negative sign arises from the definition that positive heat flow is in the direction of negative temperature gradient. Eq. (10.1) is analogous to Ohms law which can be described by:

$$I = -\sigma A\frac{dV}{dx} \tag{10.2}$$

where I is the current (A),
σ is the electrical conductivity (Sm^{-1}),

A is the area (m^2), and

$\frac{dV}{dx}$ is the electric field (Vm^{-1}).

10.2.2 Differential Equation of Conduction in a Cartesian Co-ordinate System

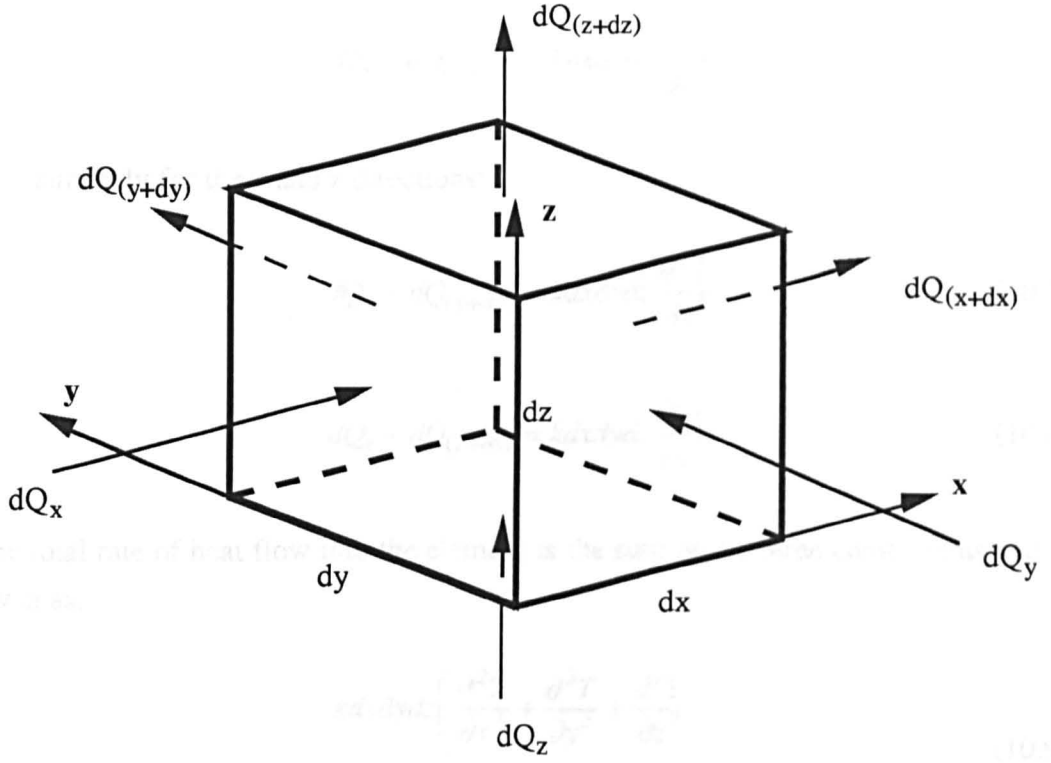

Fig. 1 Infinitesimal element of material

Consider an infinitesimal element of material of volume $dxdydz$ as shown in Fig. 1. The heat flowing into and out of the element can be resolved into x, y, and z components such that the rate of heat flowing into the element in the x direction is given by the Fourier Eq. as:

$$dQ_x = -kdydz\frac{\partial T}{\partial x} \tag{10.3}$$

since the area of heat flow is $dydz$. The rate of heat flowing out of the element in the x direction is given as:

$$dQ_{(x+dx)} = -kdydz\frac{\partial}{\partial x}\left(T + \frac{\partial T}{\partial x}dx\right) \tag{10.4}$$

$$= -kdydz\frac{\partial T}{\partial x} - kdxdydz\frac{\partial^2 T}{\partial x^2} \tag{10.5}$$

Therefore, the net rate of heat flowing into the element in the x direction is:

$$dQ_x - dQ_{(x+dx)} = kdxdydz\frac{\partial^2 T}{\partial x^2} \tag{10.6}$$

And similarly for the y and z directions:

$$dQ_y - dQ_{(y+dy)} = kdxdydz\frac{\partial^2 T}{\partial y^2} \tag{10.7}$$

$$dQ_z - dQ_{(z+dz)} = kdxdydz\frac{\partial^2 T}{\partial z^2} \tag{10.8}$$

The total rate of heat flow into the element is the sum of the three components and is given as:

$$kdxdydz\left(\frac{\partial^2 T}{\partial x^2} + \frac{\partial^2 T}{\partial y^2} + \frac{\partial^2 T}{\partial z^2}\right) \tag{10.9}$$

Heat may also be generated or stored within the element in addition to flowing into and out of it. If q' is the heat generated per unit volume, then the heat generated within the element is given by

$$q' dxdydz \tag{10.10}$$

The rate at which heat is stored within the element is given by:

$$dxdydz\rho c_P\frac{\partial T}{\partial t} \tag{10.11}$$

where ρ is the density of the material (Kgm^{-3}),

c_P is the specific heat capacity at constant pressure ($JKg^{-1}K^{-1}$), and

$\frac{\partial T}{\partial t}$ is the rate of change of temperature with time.

We can bring these 3 terms together, if we state that the rate at which heat is being stored in an element is the sum of the heat generated within the element and the net rate of heat flow into the element. This gives:

$$\rho c_P \frac{\partial T}{\partial t} = k\left(\frac{\partial^2 T}{\partial x^2} + \frac{\partial^2 T}{\partial y^2} + \frac{\partial^2 T}{\partial z^2}\right) + q' \tag{10.12}$$

$$\Rightarrow \frac{\partial T}{\partial t} = \alpha\left(\frac{\partial^2 T}{\partial x^2} + \frac{\partial^2 T}{\partial y^2} + \frac{\partial^2 T}{\partial z^2}\right) + \frac{q'}{\rho c_P} \tag{10.13}$$

where $\alpha = \dfrac{k}{\rho c_P}$ and is known as the thermal diffusivity of the material. Eq. (10.13) is the general differential equation of conduction in a Cartesian co-ordinate system and can be adapted to suit any application.

For example, the steady-state solution is when $\dfrac{\partial T}{\partial t}$ = 0 i.e. there is no variation in temperature with time. This simplifies Eq. (10.13) to:

$$0 = \alpha\left(\frac{\partial^2 T}{\partial x^2} + \frac{\partial^2 T}{\partial y^2} + \frac{\partial^2 T}{\partial z^2}\right) + \frac{q'}{\rho c_P}$$

$$\Rightarrow \frac{\partial^2 T}{\partial x^2} + \frac{\partial^2 T}{\partial y^2} + \frac{\partial^2 T}{\partial z^2} = -\frac{q'}{k} \tag{10.14}$$

10.2.3 Heat transfer by Convection

Heat will also be transferred from the edges of the solid object of interest due to thermal convection. Thermal convection can be either *free* or *forced* depending on whether there is any external pressure imposed on the fluid surrounding the solid body in which the body is immersed. In the present case, the motion of the fluid (which is air) is due solely to the action of buoyancy forces due to changes in density as the result of heating and therefore is said to be free convection.

The rate of heat transfer between the boundary surface and the fluid is given by:

$$q = hA(T_s - T_f) \tag{10.15}$$

where q is the rate of heat transfer (W),

h is the heat transfer coefficient in units of $Wm^{-2}K^{-1}$,

A is the surface area, m^2 and

T_s-T_f is the temperature difference between the surface and the fluid (K).

While this is a simple equation, h is a very complicated function due to the fluid flow and the geometrical configuration of the problem. Eq. (10.15) is in fact much simpler to solve numerically than analytically.

10.2.4 Heat transfer by Radiation

The effect of losing energy due to radiation has been discussed in section (3.5.2) when dealing with photons emitted from the material. It is worth pointing out that semiconductors are non-black bodies and therefore emit more strongly at specific optical wavelengths due to their band structure as described earlier.

10.3 Model of the PAID process

The simplest relevant way to model the PAID process is in 2 dimensions with the schematic diagram of the model used shown in Fig. 2. The laser beam is assumed to have a Gaussian profile (in 1-dimension) which can be described by the equation:

$$P = A\exp\left(-\frac{(x-a)^2}{w^2}\right) \tag{10.16}$$

where P is the power density (Wmm^{-2}),

A is the peak power at the centre of the beam,

a is the position of the beam centre, and

w is a measure of the width of the beam.

It is important to note here that in order to give the model physical dimensions, then it must have depth (in the z-direction). Therefore, all the power levels quoted in this chapter assume the laser beam is 5 mm deep in the z-direction which is the reason that some of the laser powers are quite large.

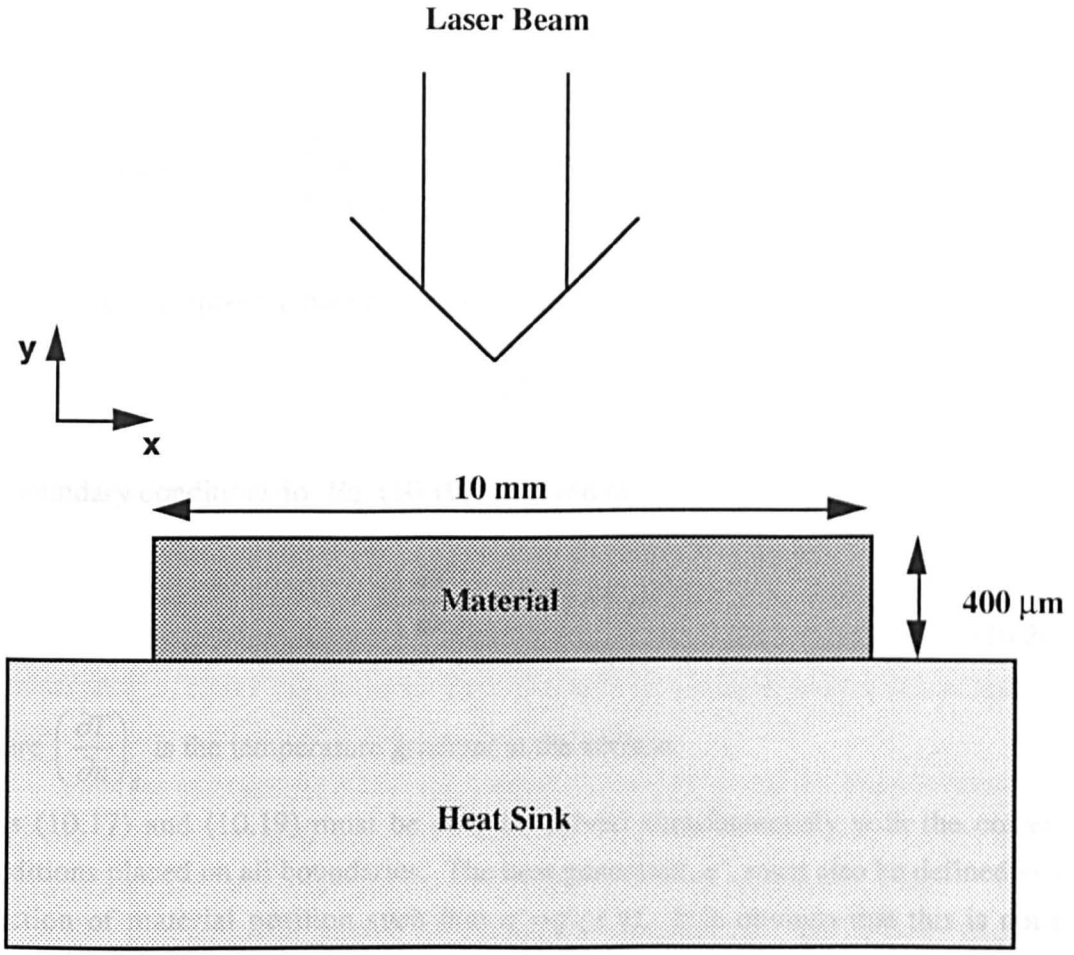

Fig. 2 Schematic diagram used to model the PAID process

The conduction equation for this problem can be simplified somewhat to:

$$\frac{\partial^2 T}{\partial x^2}+\frac{\partial^2 T}{\partial y^2}+\frac{\partial^2 T}{\partial z^2}=-\frac{q'}{k} \tag{10.17}$$

since we are interested in the steady state solution. The boundary condition for Eq. (10.17), assuming negligible thermal contact resistance, is given by:

$$k_1\frac{\partial T_1}{\partial y}=k_2\frac{\partial T_2}{\partial y} \tag{10.18}$$

where k_1 is the thermal conductivity of the heat sink,
k_2 is the thermal conductivity of the material, and
$\frac{\partial T_n}{\partial y}$ is the temperature gradient as a function of y.

In this model, it is assumed that $\frac{\partial T_1}{\partial y} = 0$ (i.e. the temperature within the heat sink is constant), and therefore $\left.\frac{\partial T_2}{\partial y}\right|_{y=0} = 0$.

The convection equation must also be solved and was given in Eq. (10.15) as:

$$q = hA(T_s - T_f) \tag{10.19}$$

Th boundary conditions for Eq. (10.19) are given as:

$$k\left(\frac{\partial T}{\partial n}\right)_s = h(T_s - T_f) \tag{10.20}$$

where $\left(\frac{\partial T}{\partial n}\right)_s$ is the temperature gradient at the surface.

Eq.s (10.17) and (10.19) must be now be solved simultaneously with the correct conditions placed on all boundaries. The heat generated, q', must also be defined as a function of material position such that $q'=q'(x,y)$. It is obvious that this is not a simple problem to solve especially as the thermal conductivity, k, is strongly dependent on temperature. Several papers[2,3,4,5] have attempted to solve these equations analytically and to provide general solutions. While these references have provided useful information, the equations presented tend to be too general to be of use, with the main problem being that they deal with the case of focused laser beams on a much smaller scale than those which are used here. This means that no account is taken of the equilibrium temperature of the material (controlled by the heat sink) and it is for these reasons that it was decided to use a numerical technique to solve the problem.

10.3.1 ABAQUS

The software used to run simulations of the model was a finite-element package called ABAQUS which has been tailored to solve complex non-linear problems. It is intended for a range of applied mechanics problems and can solve such things as stresses, displacements, mass diffusion, and a range of heat transfer problems (both transient and steady-state). In the case of heat transfer analysis, a Petrov-Galerkin[6] finite-element algorithm is used to solve the problem. References 7

and 8 give a detailed description of the formulas used within these algorithms and how they are applied to the models.

Appendix A is intended as a brief guide to ABAQUS and how problems can be solved using it. In particular it deals with how to generate a suitable mesh for the model, and how to define the correct initial and boundary conditions for the system. Also contained in App. A is some simple maths which is required to correctly calibrate the input power levels to the model.

10.3.2 Simplifications to the model

The model which has been described above makes several assumptions which may introduce very small errors. Firstly, it is assumed that the material is made purely of indium phosphide, which is not the case. There is an approximately 3 μm thick epitaxial structure containing layers of ternary and quaternary alloys of InGaAs and InGaAsP. These layers have different heat conduction properties to indium phosphide but are sufficiently thin as to be ignored.

Another assumption is that the base of the sample is at a fixed temperature i.e. that there is perfect heat-sinking between the sample and the hotplate. This will not always be the case but should not introduce large errors, as results will show.

The power levels quoted in the results are for absorbed power, and not necessarily the incident power from the laser. The ratio of incident power to absorbed power has been discussed in section (3.5.2) and allowances can be made for it.

No account is taken of the oxidation of the side walls of the model at the high temperatures used. Although no conduction takes place at these regions, the rate of heat lost by convection may be changed, although this is assumed to be small enough to ignore.

10.3.3 Results

The first set of simulations carried out was variation of the input power of the laser beam and monitoring of the subsequent temperature profile of the sample surface. The Full Width at Half Maximum (FWHM) was kept constant at 1.66 mm (w = 1 mm in Eq. (10.16)). Fig. 3 shows the temperature profiles on the sample surface with varying laser power. Fig. 4 shows the variation in peak temperature (which always occurs at the centre of the laser beam where the power density is maximum), and the FWHM of the temperature variation as a function of laser power. It is obvious that there is a non-linear relationship between the incident laser power density and the peak temperature on the sample surface, which is due to the strong temperature dependence of the thermal conductivity. Because the centre of the

sample tends to heat up to a greater extent, the temperature profile becomes non-Gaussian, which has the effect of reducing the FWHM of the temperature profile at higher input power levels.

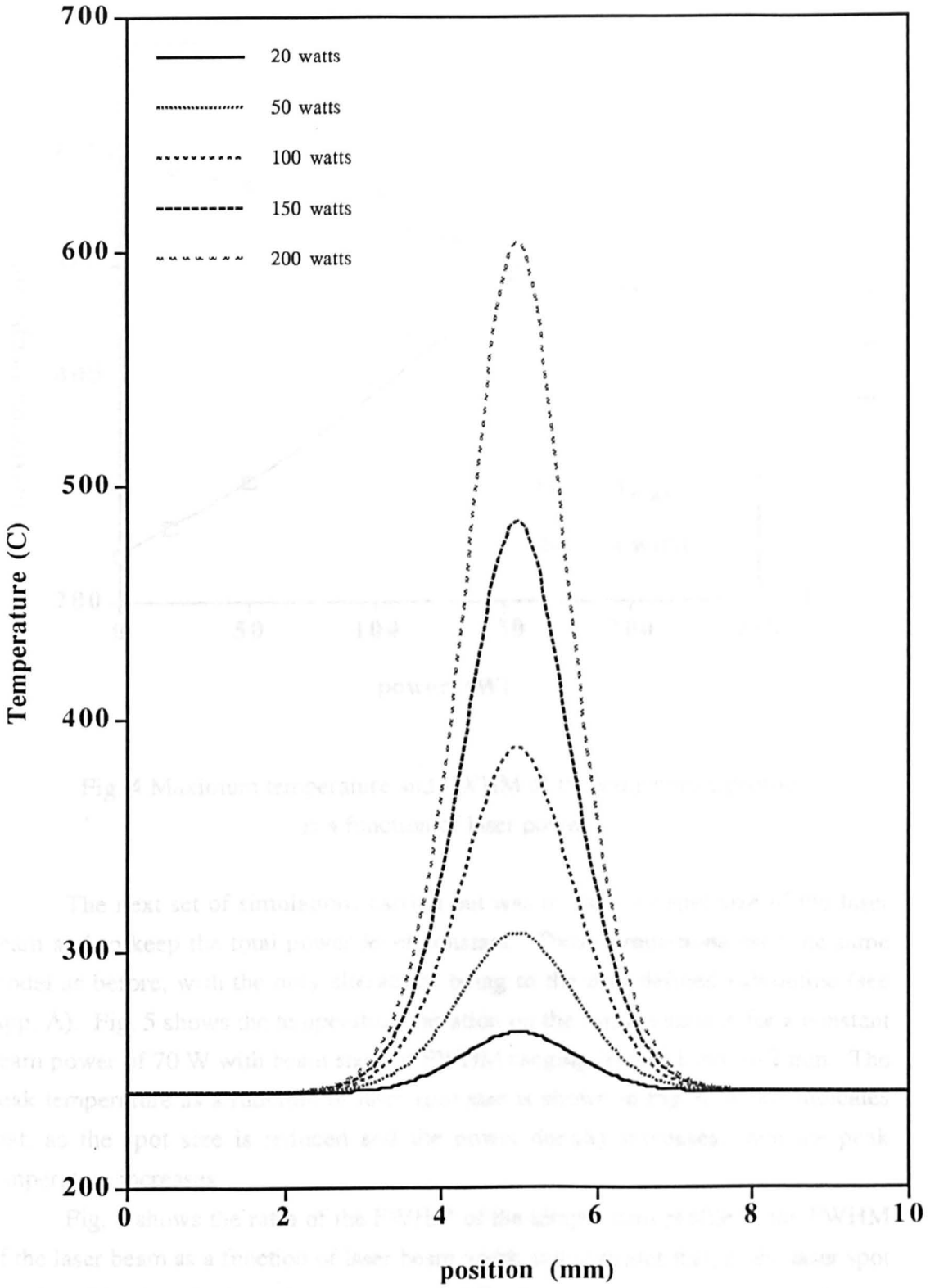

Fig. 3 Temperature rise induced by a Gaussian profiled laser beam

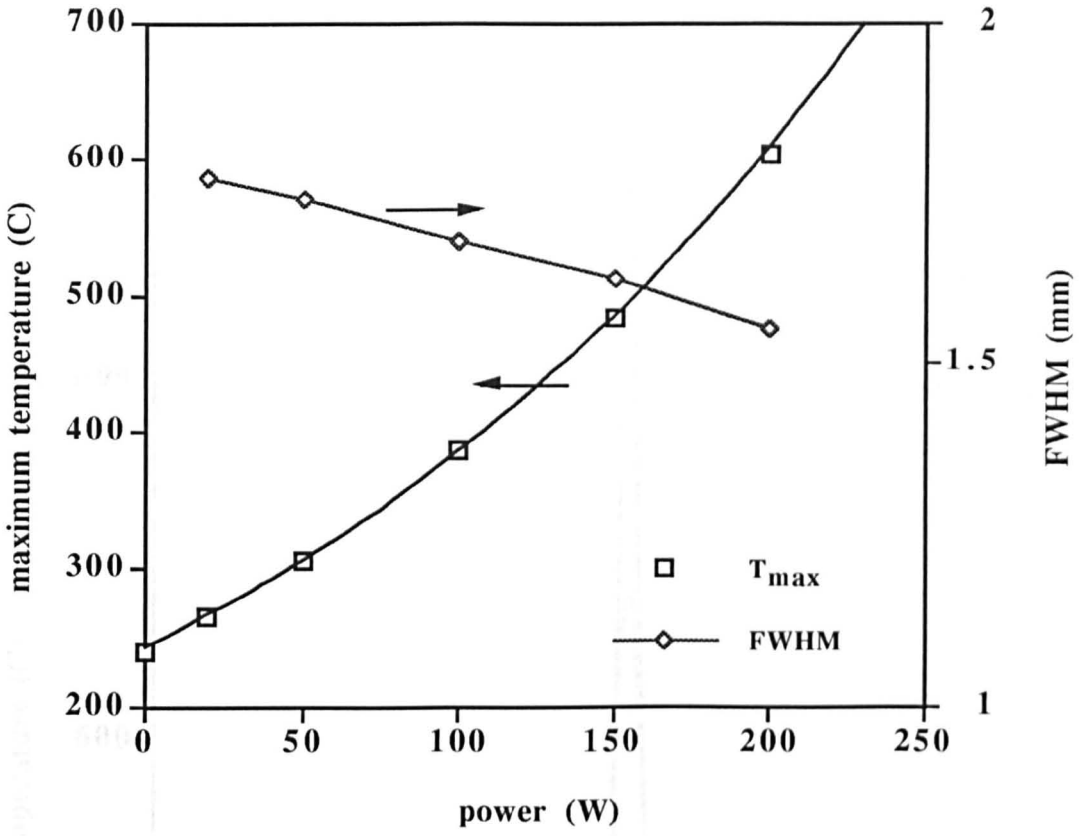

Fig. 4 Maximum temperature and FWHM of the temperature profile as a function of laser power

The next set of simulations carried out was to vary the spot size of the laser beam and to keep the total power level constant. These simulations used the same model as before, with the only alterations being to the user defined subroutine (see App. A). Fig. 5 shows the temperature variation on the sample surface for a constant beam power of 70 W with beam sizes of FWHM ranging from 0.1 mm to 2 mm. The peak temperature as a function of laser spot size is shown in Fig. 6, which indicates that, as the spot size is reduced and the power density increases, then the peak temperature increases.

Fig. 7 shows the ratio of the FWHM of the temperature profile to the FWHM of the laser beam as a function of laser beam width and indicates that, as the laser spot is reduced in size, the lateral temperature profile does not reduce by the same factor. This effect is to be expected because, as the laser spot size is reduced (and the power densities increase), the induced temperature gradients in the model become larger. Subsequently, according to Eq. (10.17), the diffusion of heat (from areas of high temperature to areas of low temperatures) will increase causing the temperature profile to broaden.

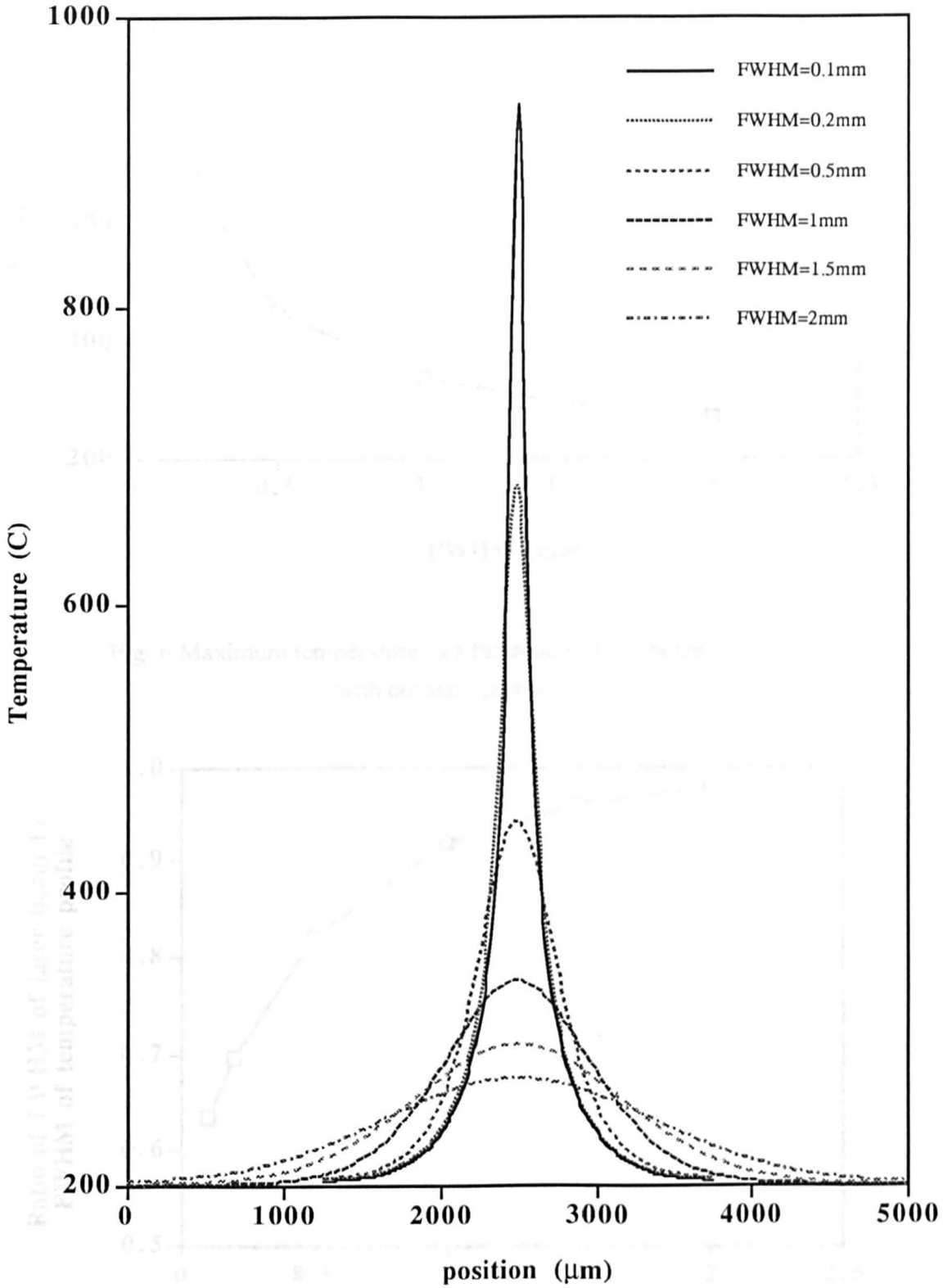

Fig. 5 Temperature profile produced by varying the laser beam width at constant power

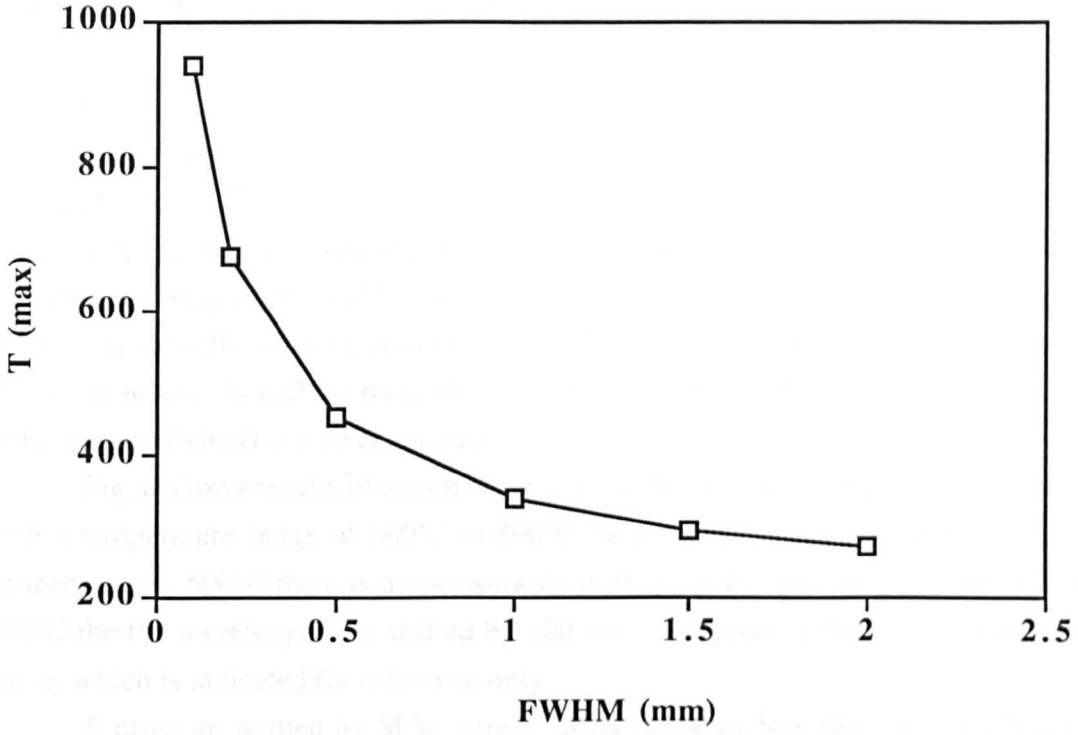

Fig. 6 Maximum temperature as a function of laser beam width with constant power

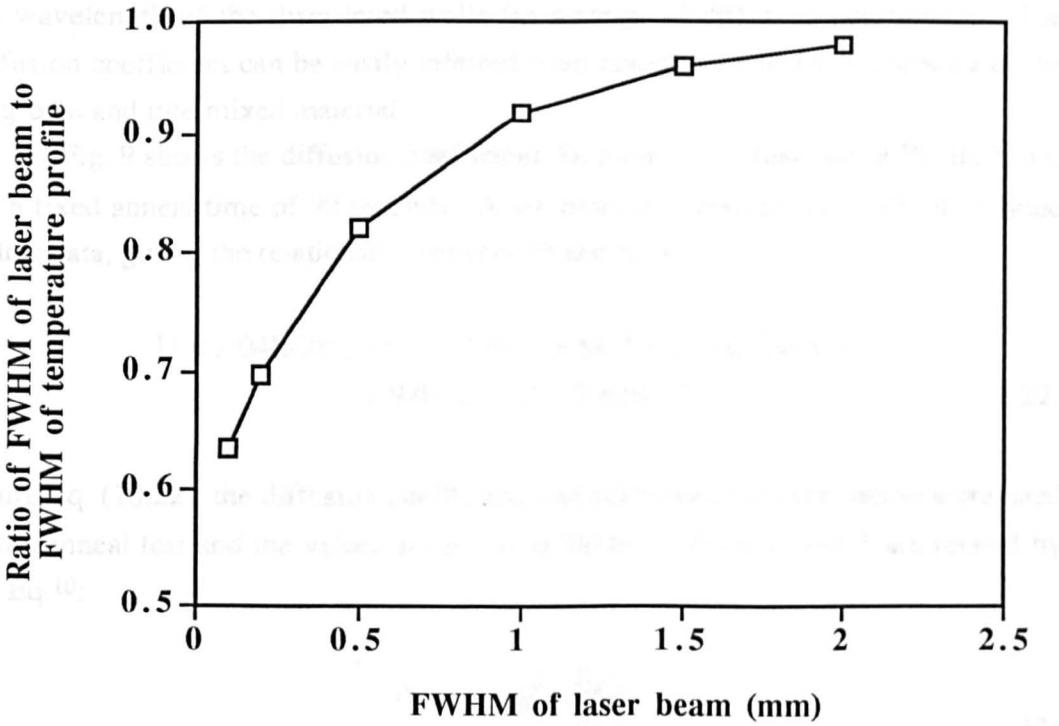

Fig. 7 Ratio of the FWHM of the temperature profile to the FWHM of the laser profile, as a function of laser beam width with constant power

10.4 Resolution of the PAID process

In order to determine the resolution of the PAID process, and how the different process parameters affect it, the temperature dependence of the intermixing rate must be quantified.

The easiest way to do this accurately is to anneal test multiple quantum well material in a Rapid Thermal Processor (RTP) and measure the photoluminescence (PL) shifts for different temperatures. Since the temperature and anneal time can be measured accurately and the material parameters are known, the diffusion length (and diffusion coefficient) can be calculated.

Fig. 8 shows results of an anneal test of MQW waveguide material carried out with a temperature range of 600°C to 800°C for a fixed time of 90 seconds. For a temperature of 600°C there is no measurable shift in the PL wavelength, whereas for 800°C the PL wavelength has shifted by 100 nm. The points follow quite a smooth curve, which is indicated for reference only.

A program written by M.W. Street (using the procedure described in Chapter 3) was used to fit diffusion coefficients to different PL wavelength shifts. The program models the interdiffusion of atoms between the wells and the barriers using an error function profile[9] and then uses a Schrödinger solver to calculate the energy levels in the disordered wells. For a specified anneal time, the program calculates the PL wavelength of the disordered wells for a range of diffusion coefficients. The diffusion coefficient can be easily inferred from comparison of the PL spectra of the as-grown and intermixed material.

Fig. 9 shows the diffusion coefficient, D, plotted as a function of PL shift, $\Delta\lambda$, for a fixed anneal time of 90 seconds. A 4th order polynomial curve was then fitted to this data, giving the relationship between D and $\Delta\lambda$ as:

$$D = 2.04\text{E-}28(\Delta\lambda)^4 - 2.43\text{E-}26(\Delta\lambda)^3 + 2.15\text{E-}24(\Delta\lambda)^2 + 2.97\text{E-}22(\Delta\lambda) + 2.60\text{E-}23 \qquad (10.22)$$

Using Eq. (10.22), the diffusion coefficient was calculated for each temperature used in the anneal test and the values are given in Table 1. Since D and T are related by the Eq.[10]:

$$D = D_0 \exp\left(-\frac{E_A}{kT}\right) \qquad (10.23)$$

D_0 and E_A can be found by plotting ln(D) as a function of 1/kT. This graph is shown in Fig. 10 and is known as an Arrhenius plot. The intercept of the line with the y axis

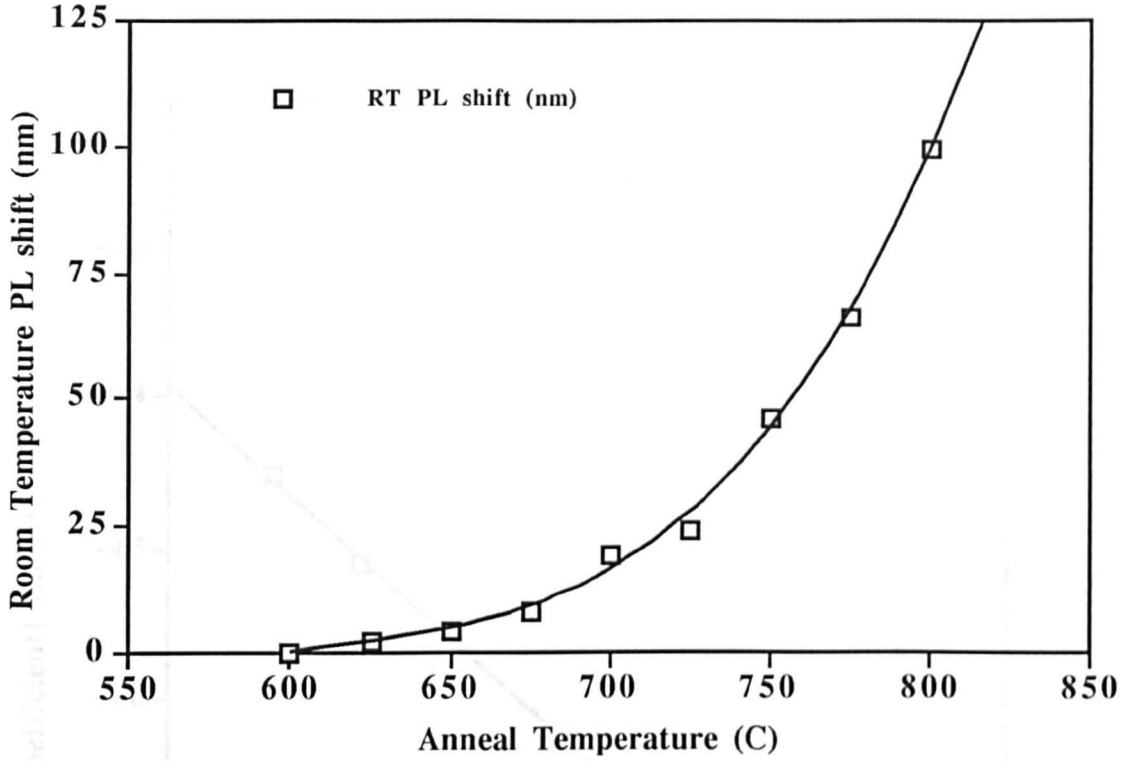

Fig. 8 PL shift as a function of anneal temperature

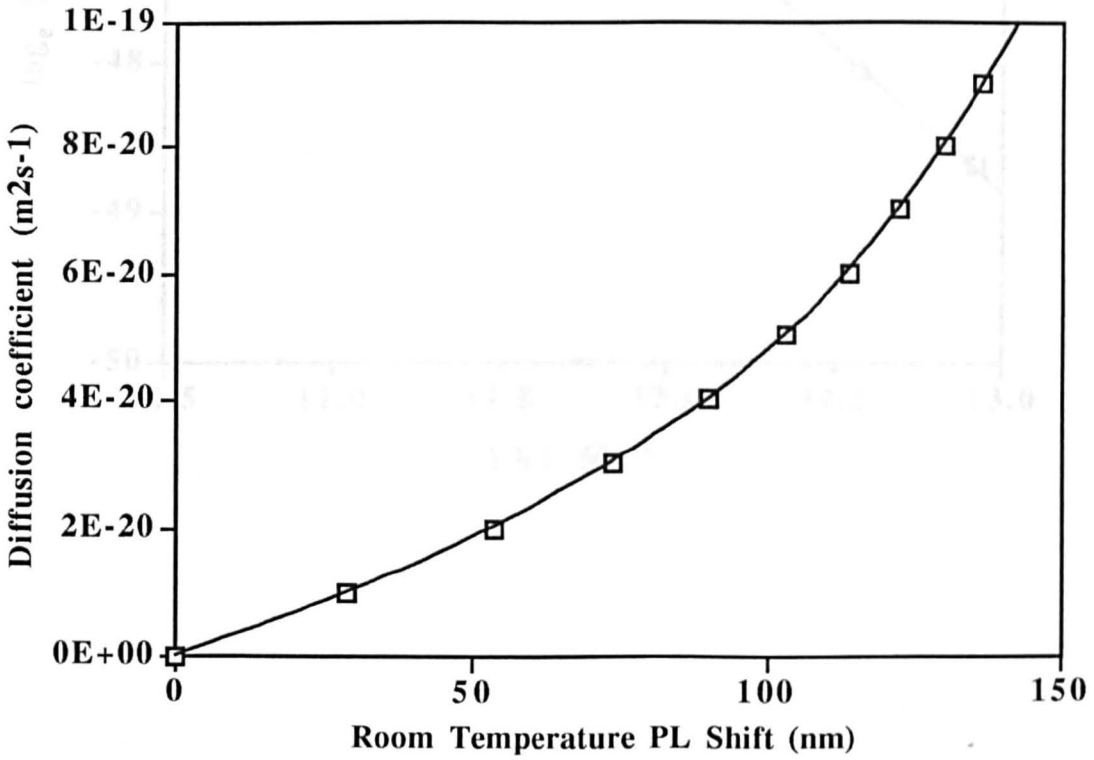

Fig. 9 Diffusion coefficient as a function of PL shift

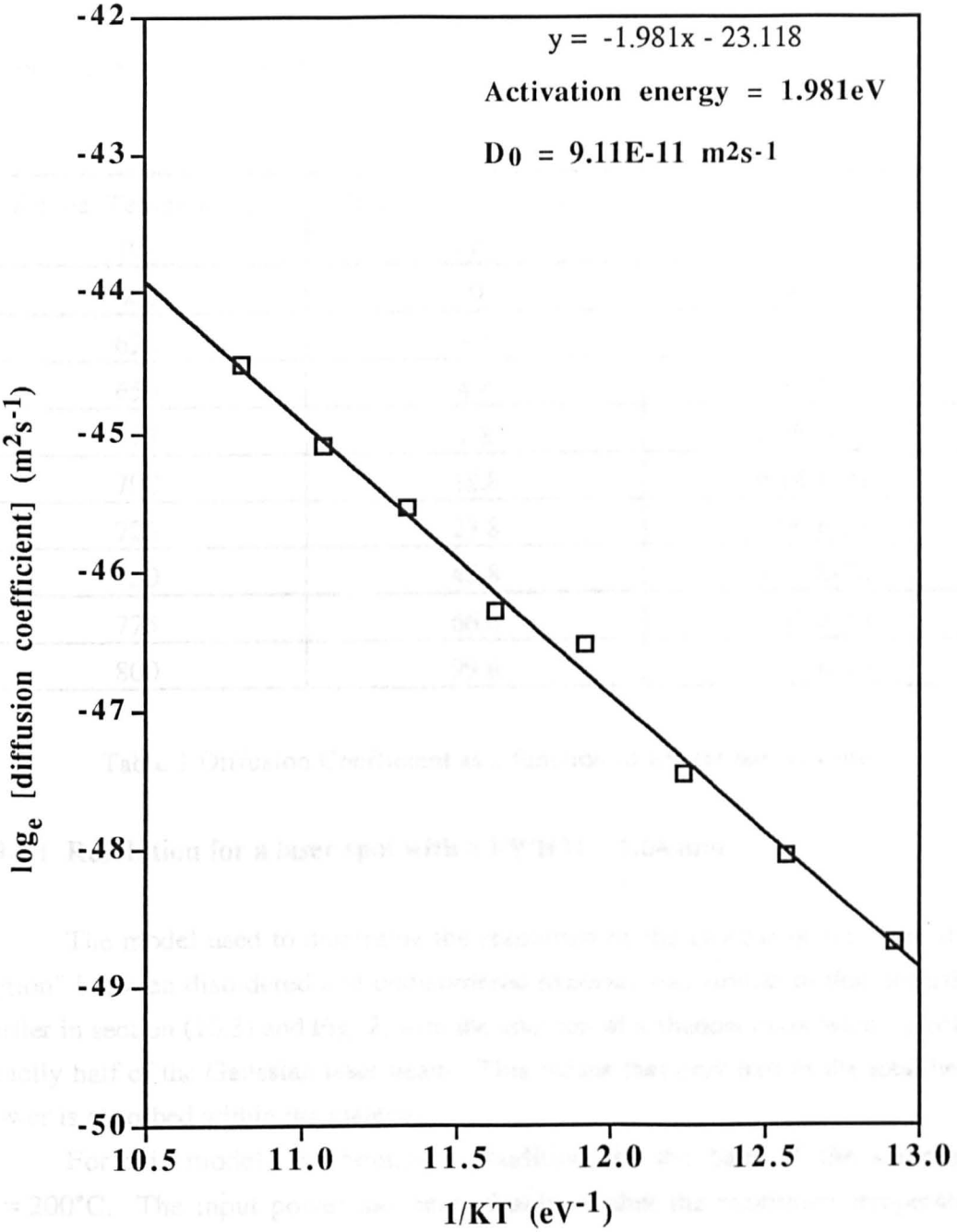

Fig. 10 Arrhenius plot of diffusion coefficient

is D_0, and is equal to 9.11E-11 m^2s^{-1} while the gradient of the graph is $-E_A$ and is equal to 1.981 eV which is the activation energy.

Since all the constants are known in Eq. (10.23), it is possible to calculate the PL peak shift of the material for any time and temperature using the same program.

Anneal Temperature (C)	Shift in PL wavelength (nm)	Diffusion Coefficient (m^2s^{-1})
600	0	2.60 E-23
625	2.3	7.21 E-22
650	4.4	1.37 E-21
675	7.8	2.46 E-21
700	18.8	6.24 E-21
725	23.8	8.06 E-21
750	45.8	1.67 E-20
775	66.6	2.62 E-20
800	99.6	4.70 E-20

Table 1 Diffusion Coefficient as a function of anneal temperature

10.4.1 Resolution for a laser spot with a FWHM = 1.66 mm

The model used to determine the resolution of the process or the "transition region" between disordered and undisordered material was similar to that described earlier in section (10.3) and Fig. 2, with the addition of a shadow mask which blocked exactly half of the Gaussian laser beam. This means that only half of the total beam power is absorbed within the material.

For this model, the boundary condition for the base of the sample is T = 200°C. The input power has been chosen so that the maximum temperature reached is 800°C, which requires a total power of 375.9 W (corresponding to a peak power density of 42.4 Wmm^{-2}) for a laser beam with a FWHM = 1.66 mm. The peak value of 800°C was chosen as it produced a PL shift of approximately 100 nm for a 90 second anneal time.

Fig. 11 shows the beam profile and the temperature rise induced by it. It is obvious that the peak temperature is at a different position from the peak power of the laser. This difference in position is due to the heat generated close to the mask diffusing away laterally underneath it, which means that the peak temperature occurs nearer to the centre of the incident power (i.e. where the laser beam is not blocked).

In the present case the peak temperature position is approximately 325 μm from the edge of the mask.

The temperature gradient under the mask is greater than the irradiated side which is to be expected due to the abrupt gradient of the incident power density.

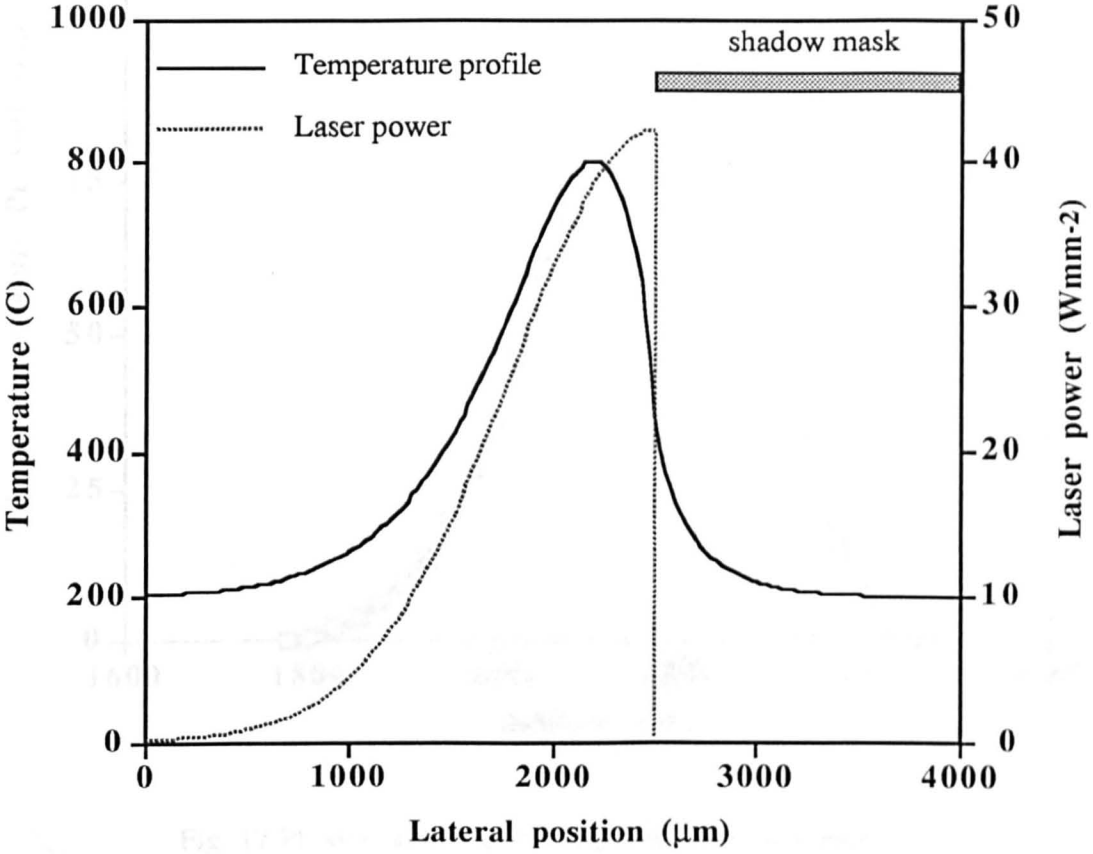

Fig. 11 Laser power profile and induced temperature profile of sample surface

Fig. 12 shows the PL peak shift across the sample. Although there is only a small area which is disordered by the maximum amount (100 nm), it is possible to achieve a much broader area of disordering which can be accomplished by either scanning the laser across the sample in a direction normal to the edge of the mask or by stepping the beam position. Both methods should ensure that the disordered region is broadly uniform over a larger area than a single exposure can achieve.

For this reason, the transition region will be considered only for the area under the mask.

The simulation was repeated under different heat sinking conditions. With T_{sink} = 350°C, the incident power required to produce a maximum temperature of 800°C was 233.5 W, while only 134 W was required when the base of the sample was

fixed at a temperature of 500°C. In all cases, the peak temperature of 800°C occurs at the same position of 325 μm away from the mask.

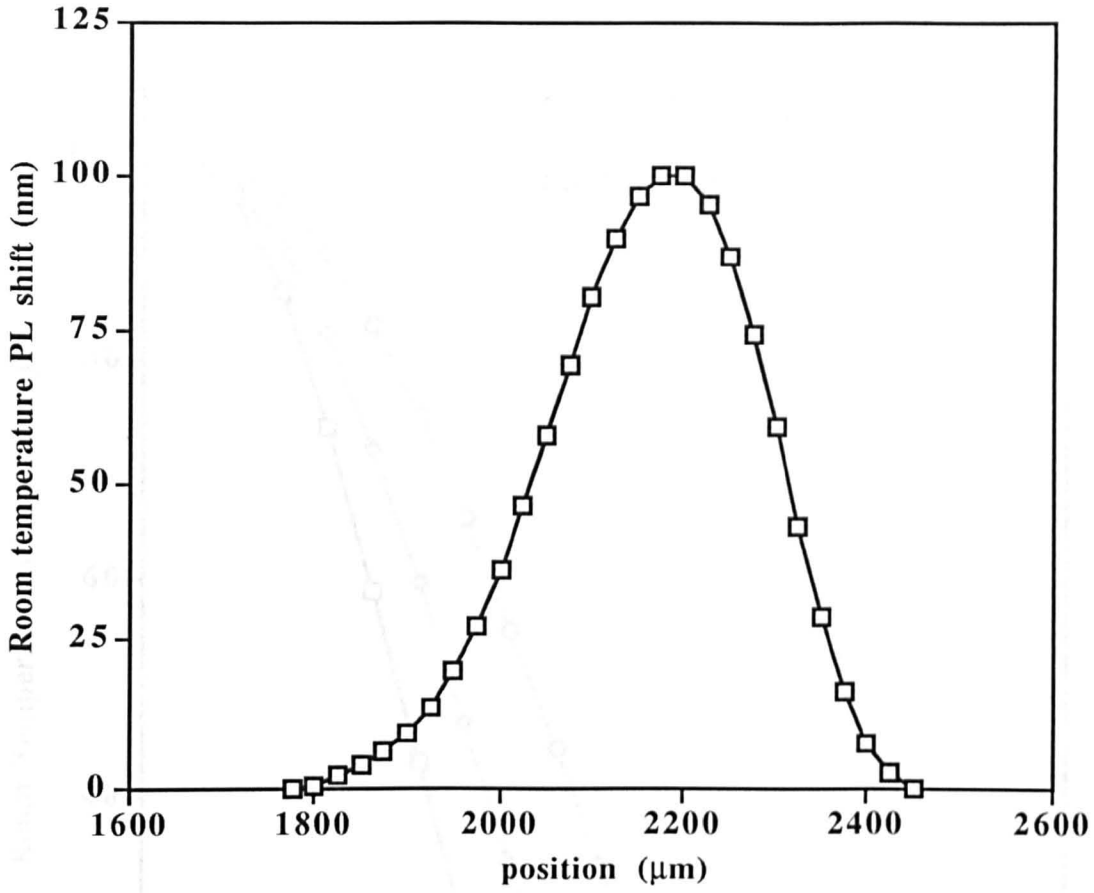

Fig. 12 PL shift as a function of position across sample

The transition regions produced for the three different heat sinking conditions are shown in Fig. 13. The resolution was considered to be the lateral distance between 10 % and 90 % of maximum disordering (i.e. from a PL shift of 10 nm to a PL shift of 90 nm). The size of the transition region for the three heat sinking conditions is given in Table 2 and indicates that the heat sinking plays an important role in determining the resolution of the process. It is interesting to note that for the heat sinking conditions T_{sink} = 200°C and T_{sink} = 350°C, there is essentially no intermixing at the edge of the mask (which can be regarded as being at a position of 325 μm on the graph). The reason that there is no intermixing, is that the temperature is 446°C and 556°C respectively for the two heat sinking conditions, i.e. below the temperature at which there is a measurable shift in the PL peak for a 90 second anneal.

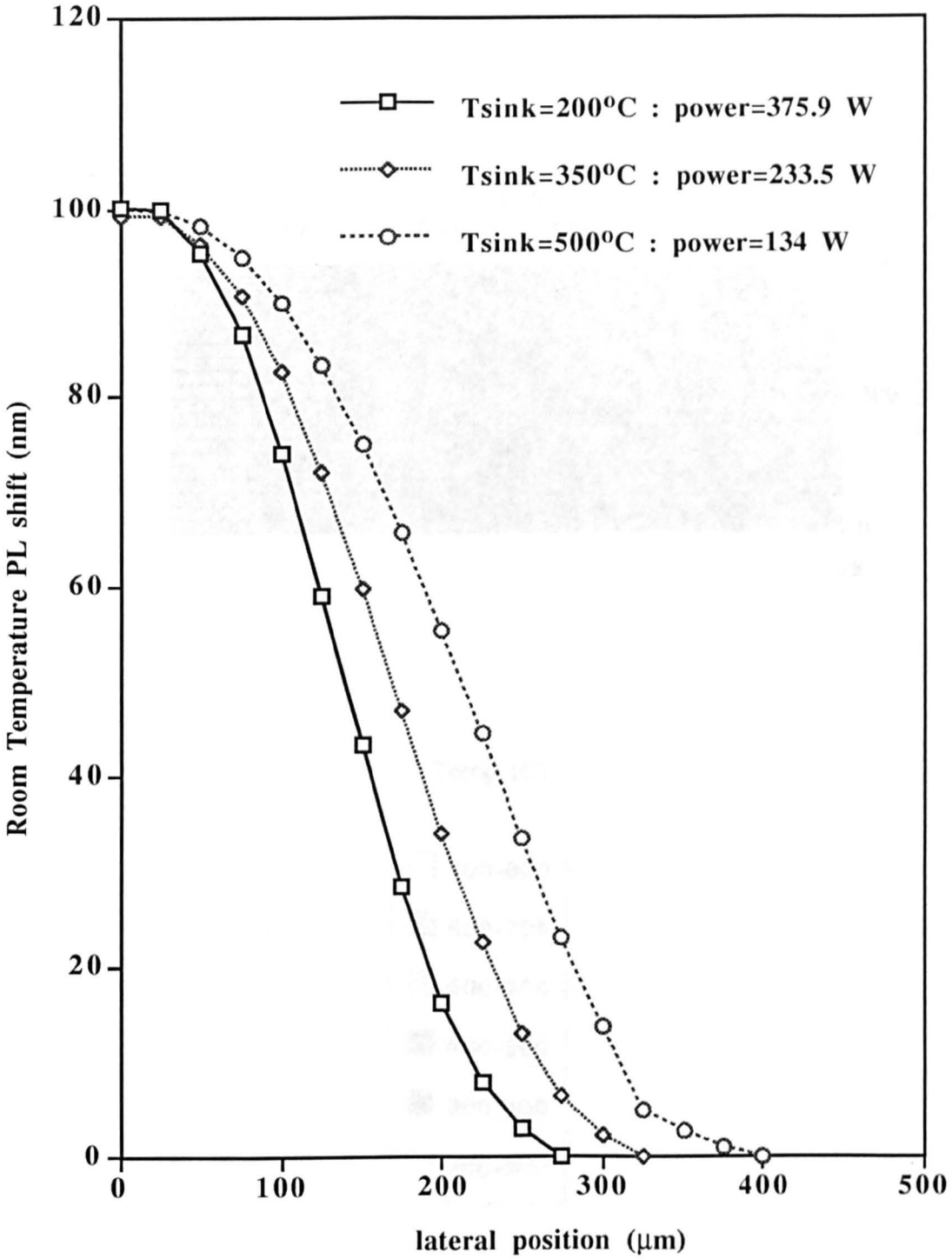

Fig. 13 Transition region profile for laser beam of FWHM = 1.66 mm

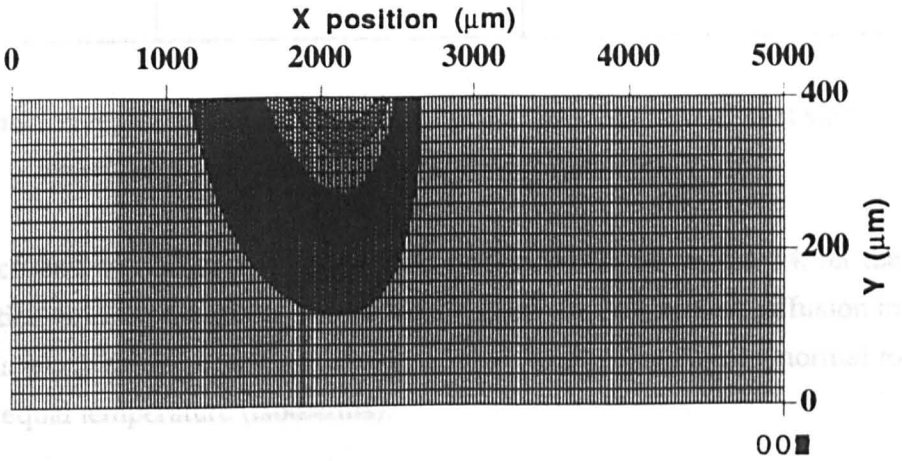

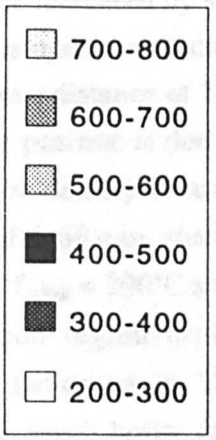

Fig. 14 Temperature profile of the cross section of the sample with a heat sink temperature of 200°C and a beam size of FWHM = 1.66 mm

Heat Sink Temperature (C)	Total Input Power (Watts)	Transition Region Width (μm)
200	375.9	150
350	233.5	183
500	134	211

Table 2 Transition region width and total input power as a function of heat sink temperature for a beam with FWHM of 1.66 mm

A contour plot of temperature as a function of x-y position is shown in Fig. 14, for the heat sink condition of 200°C, which gives an indication of the rate of heat diffusion in the sample. It is worth stating that the direction of heat flow will always be normal to the contours of equal temperature (isotherms).

10.4.2 Resolution for a laser spot with a FWHM = 0.83 mm

The simulation was repeated but with some alterations to the model. A reduced beam width of 0.83 mm was used, which required a finer mesh to achieve accurate analysis. To calibrate the power levels correctly, the peak amplitude, the factor A in Eq. (10.21), also had to be increased by a factor of 2.

In this simulation, the peak temperature occured at a position of 175 μm from the edge of the mask, compared with a distance of 325 μm for a FWHM of 1.66 mm. This change in the peak temperature position is due to the fact that the beam width is narrower and thus the average power density occurs much closer to the mask. In a similar fashion to a beam width of 1.66 mm, there is no intermixing at the mask interface for heat sink conditions of T_{sink} = 200°C and 350°C.

Fig. 15 shows the transition region profiles for different heat sinking conditions. The resolution (as indicated in Table 3) with a laser beam of FWHM = 0.83 mm is, as expected, much better due to the more localised heating caused by the smaller beam spot. For example, for a heat sink temperature of 200°C, the resolution has improved from 150 μm to 91 μm. This localised heating is also the reason that the input power levels required to reach a peak temperature of 800°C are much lower.

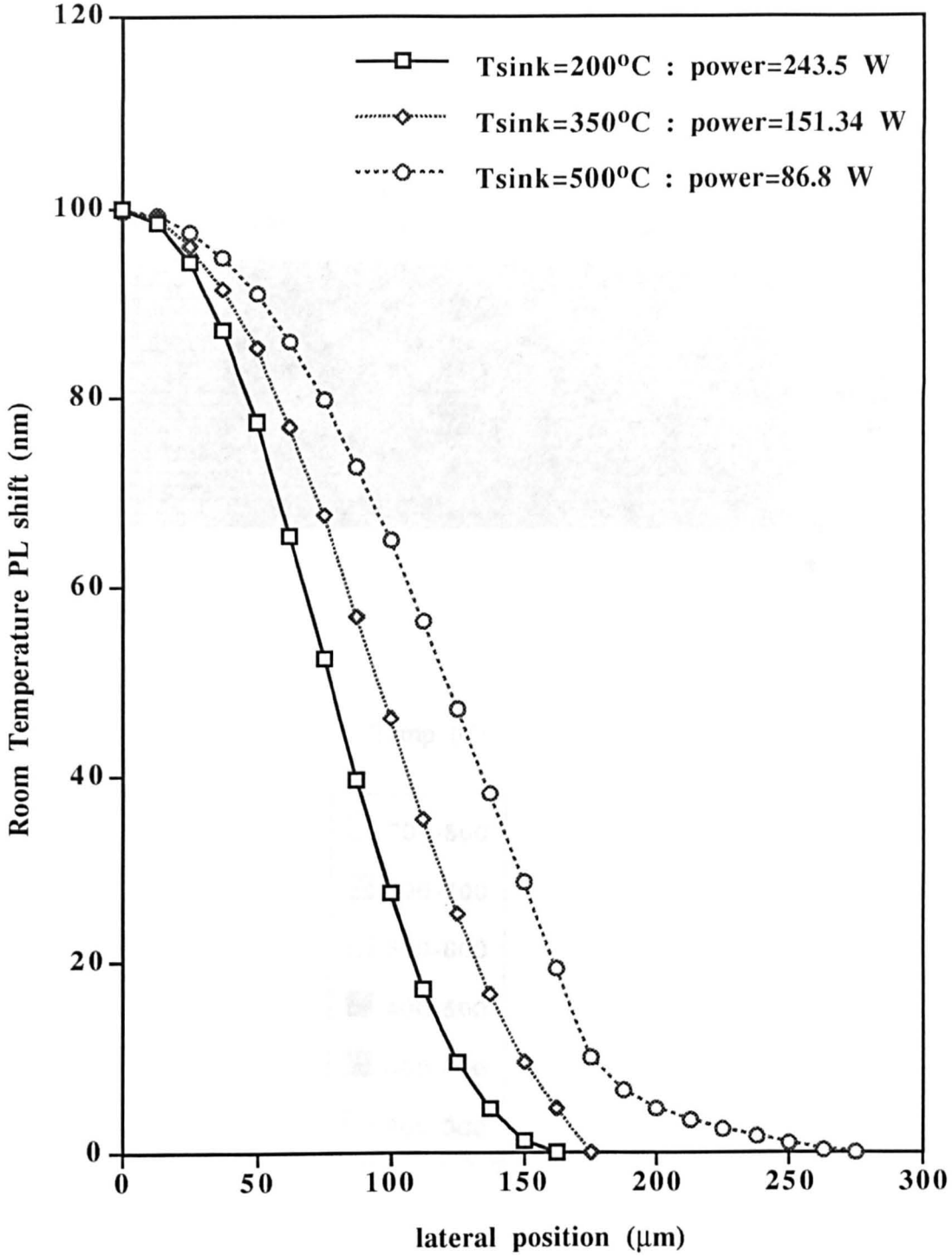

Fig. 15 Transition region profile for laser beam of FWHM = 0.83 mm

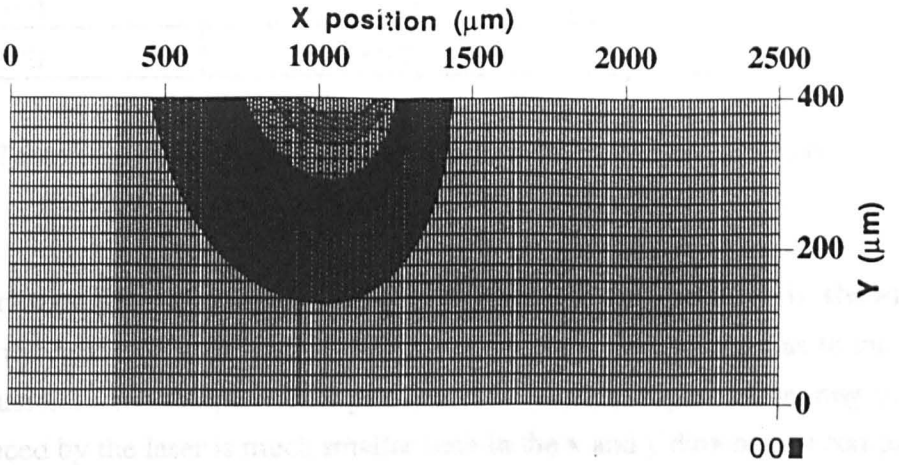

Temp. (C)

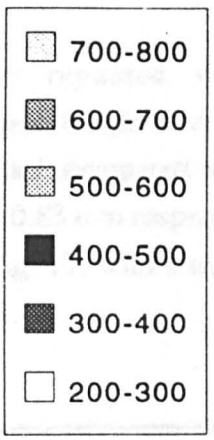

Fig. 16 Temperature profile of the cross section of the sample with a heat sink temperature of 200°C and a beam size of FWHM = 0.83 mm

Heat Sink Temperature (C)	Total Input Power (Watts)	Transition Region Width (μm)
200	243.5	91
350	151.3	109
500	86.8	123

Table 3 Transition region width and total input power as a function of heat sink temperature for a beam with FWHM of 0.83 mm

A contour plot of temperature as a function of x-y position is shown in Fig. 16, for the heat sink condition of 200°C, which gives an indication as to the rate of heat diffusion in the sample. This plot indicates that the region of heating in the sample induced by the laser is much smaller both in the x and y dimensions compared to the larger beam spot (of FWHM = 1.66 mm) used in the previous simulation.

10.4.3 Resolution for a laser spot with a FWHM = 0.415 mm

The simulation was repeated with a smaller laser beam spot (FWHM = 0.415 mm). The peak temperature in this case occurred at a distance of 90 μm from the edge of the mask compared to 325 μm and 175 μm for laser beams with a FWHM = 1.66 mm and 0.83 mm respectively. The transition region width has also decreased, as shown in Fig. 17, with a transition region width of 54.5 μm for a heat sink temperature of 200°C.

Heat Sink Temperature (C)	Total Input Power (Watts)	Transition Region Width (μm)
200	168.9	54.5
350	105	63
500	60.2	76

Table 4 Transition region width and total input power as a function of heat sink temperature for a beam with FWHM of 0.415 mm

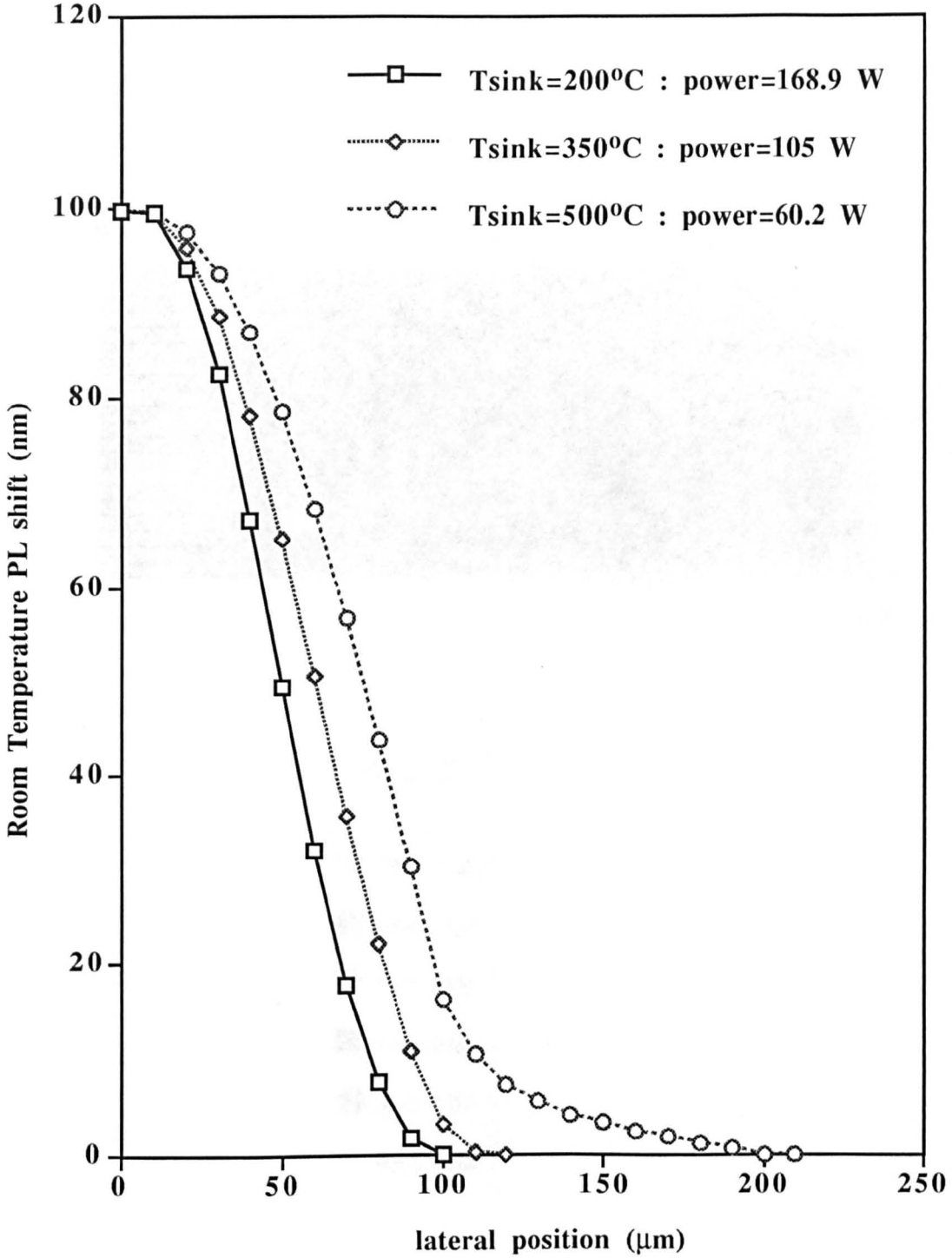

Fig. 17 Transition region profile for laser beam of FWHM = 0.415 mm

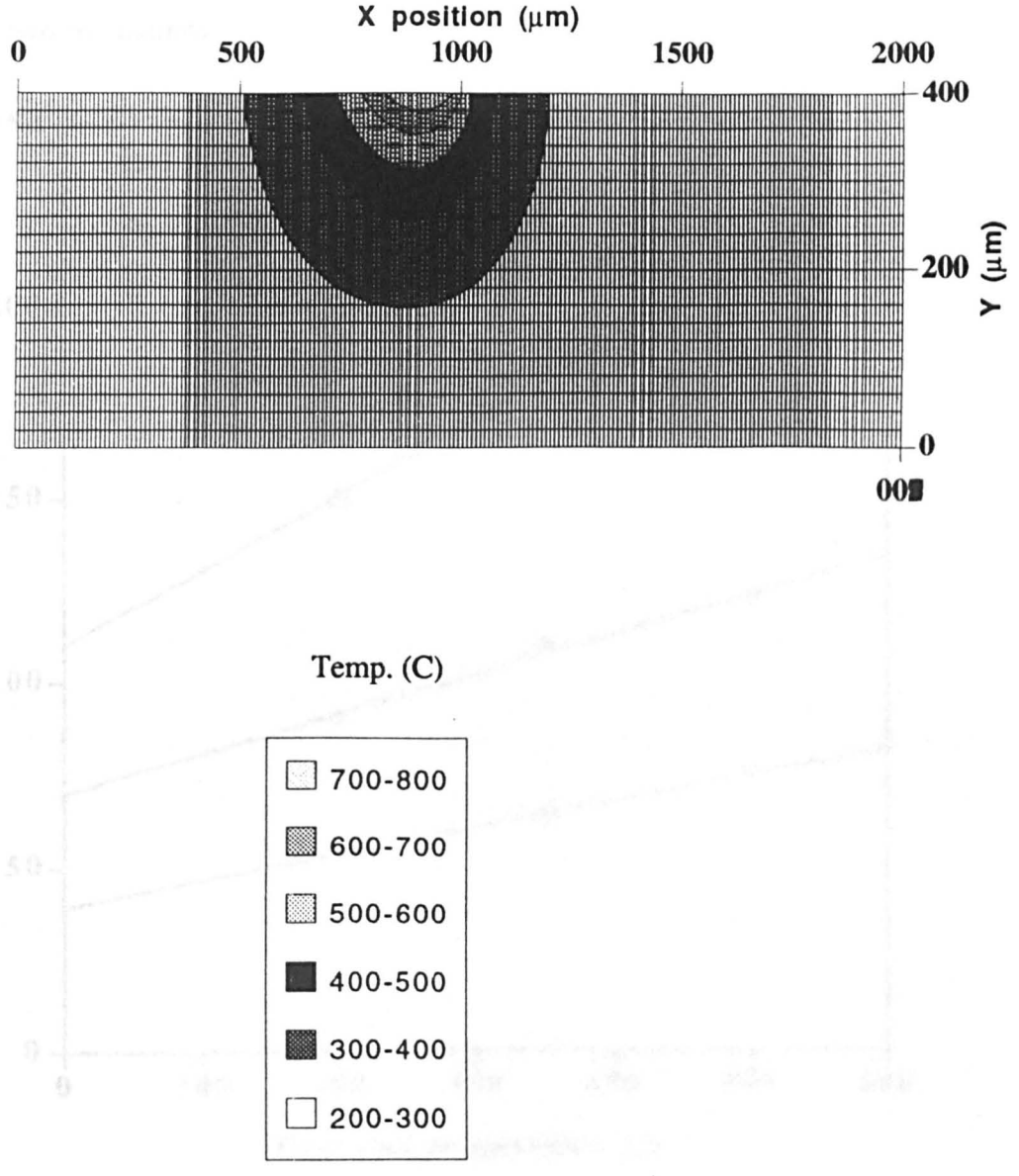

Fig. 18 Temperature profile of the cross section of the sample with a heat sink temperature of 200°C and a beam size of FWHM = 0.415 mm

A contour plot of temperature as a function of x-y position is shown in Fig. 18, for the heat sink condition of 200°C, which gives an indication as to the rate of heat diffusion in the sample. This plot indicates that the region of heating in the sample induced by the laser is again much smaller both in the x and y dimensions compared to the larger beam spots (with FWHM = 1.66 mm and 0.83 mm) used in the previous two simulations.

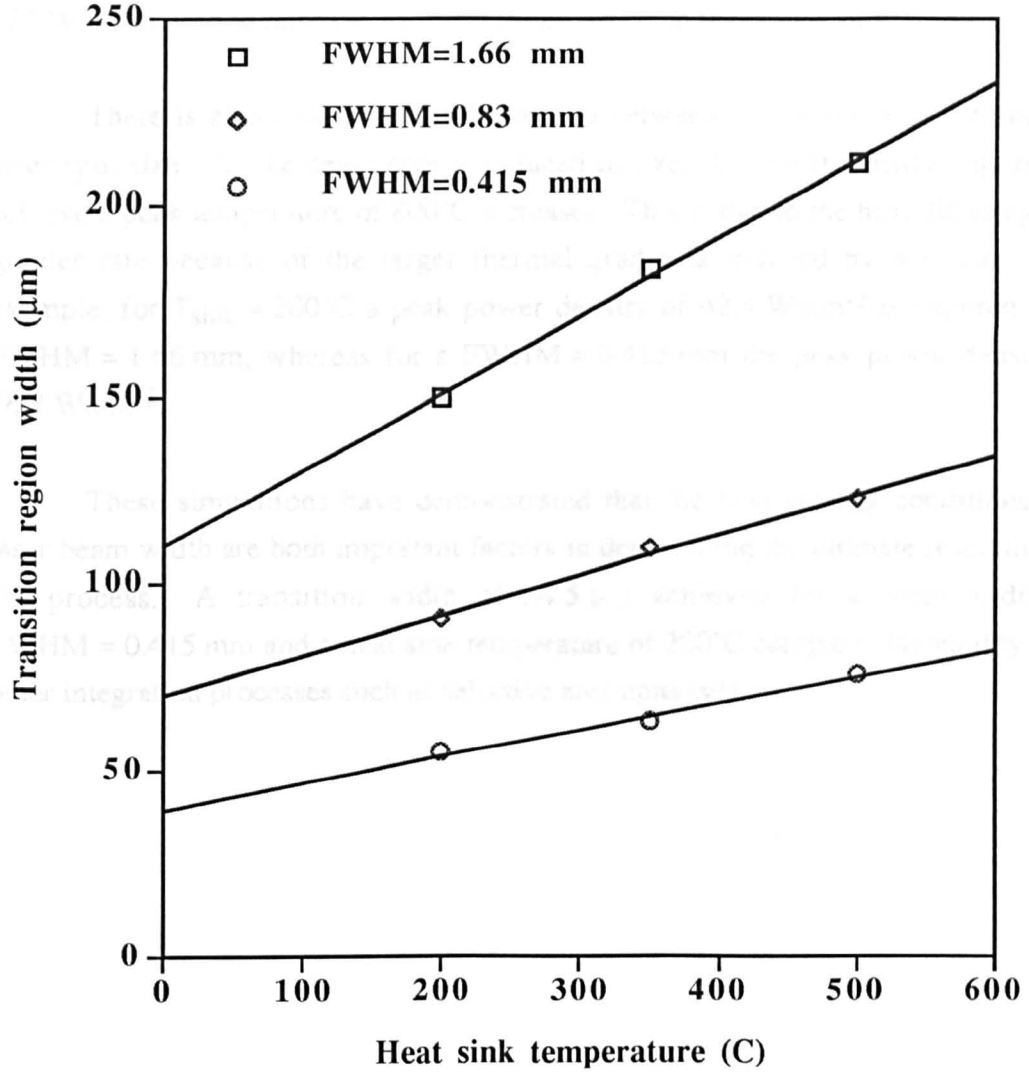

Fig. 19 Transition region width as a function of laser beam width and heat sink temp.

Fig. 19 shows the resolution as a function of laser beam width and heat sink temperature. As the laser width is reduced, the effect of the heat sink temperature becomes smaller. This reduction is simply due to the *effective depth* of the sample becoming larger as the lateral dimensions of the laser become smaller.

The total power required to achieve a peak temperature of 800°C is shown graphically in Fig. 20. It can be seen that, for a constant beam width, the power required becomes less as the heat sink temperature increases. The relationship is not linear however, because of the strong temperature dependence of the thermal conductivity. For example, with a heat sink temperature of 200°C (and a FWHM = 1.66 mm) it takes 375.9 W to raise the temperature by 600°C to 800°C (i.e. 0.6265 $W°C^{-1}$) whereas for a heat sink temperature of 500°C, a total power of of 134 W is required to raise the temperature by 300°C to 800°C, i.e. only 0.447 $W°C^{-1}$.

There is also a non-linear relationship between the power required and the laser spot size. As the beam spot is reduced in size, the power density required to achieve a peak temperature of 800°C increases. This is due to the heat diffusing at a greater rate because of the larger thermal gradients induced by the laser. For example, for T_{sink} = 200°C a peak power density of 42.4 Wmm^{-2} is required for a FWHM = 1.66 mm, whereas for a FWHM = 0.415 mm the peak power density is 76.2 Wmm^{-2}.

These simulations have demonstrated that the heat sinking conditions and laser beam width are both important factors in determining the ultimate resolution of the process. A transition width of 54.5 μm achieved for a beam width of FWHM = 0.415 mm and a heat sink temperature of 200°C compares favourably with other integration processes such as selective area epitaxy[11].

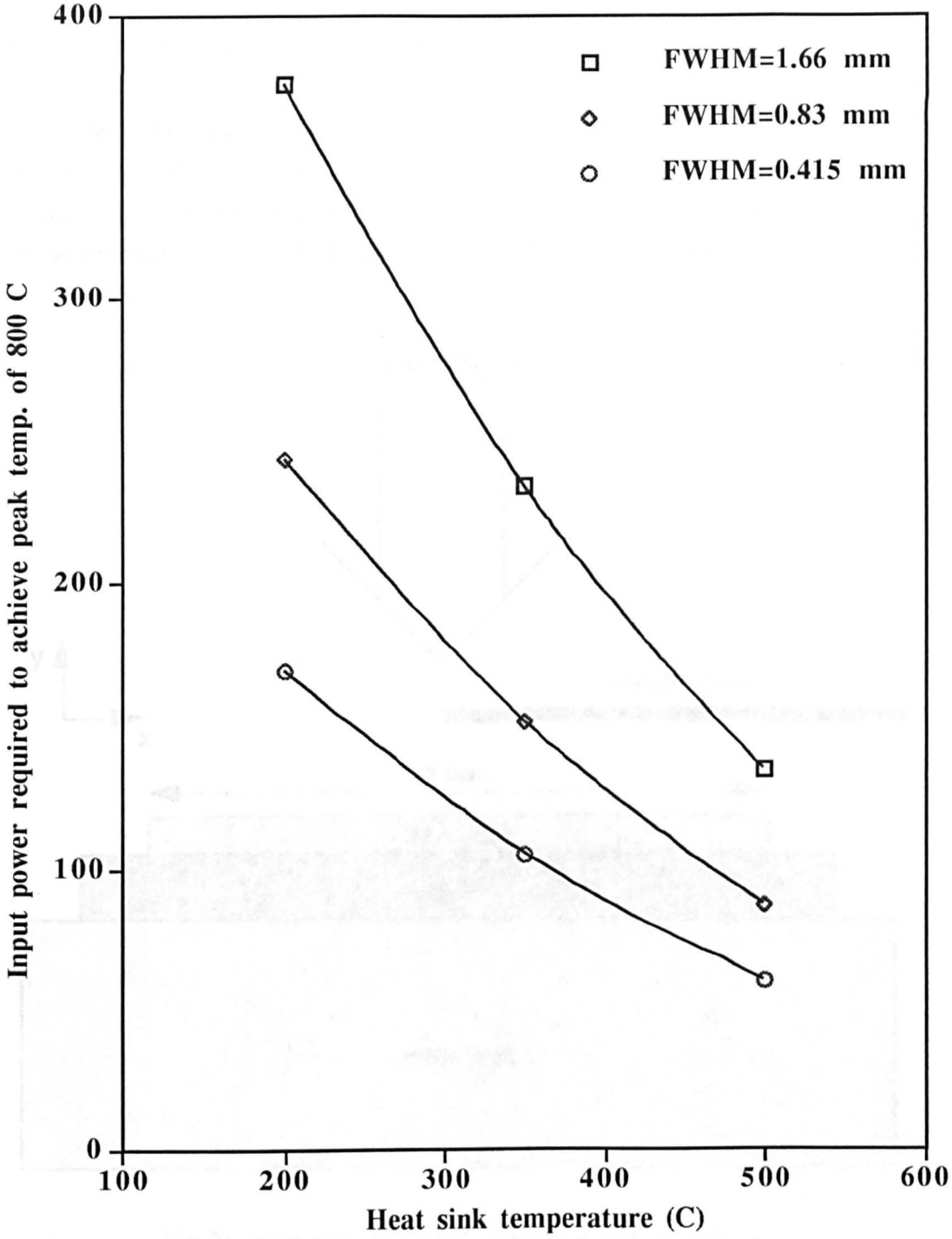

Fig. 20 Input power required to achieve peak temp. of 800°C as a function of laser beam width and and heat sink temperature

10.4.4 Resolution with a Ceramic Heat sink

The model was adapted to determine what effect introducing a layer of low conductivity material between the sample and the heat sink would have on the transition region width. A piece of ceramic with dimensions of 7 mm x 2 mm and a thermal conductivity of 0.015 $Wcm^{-1}K^{-1}$ was added to the model as shown in Fig. 21.

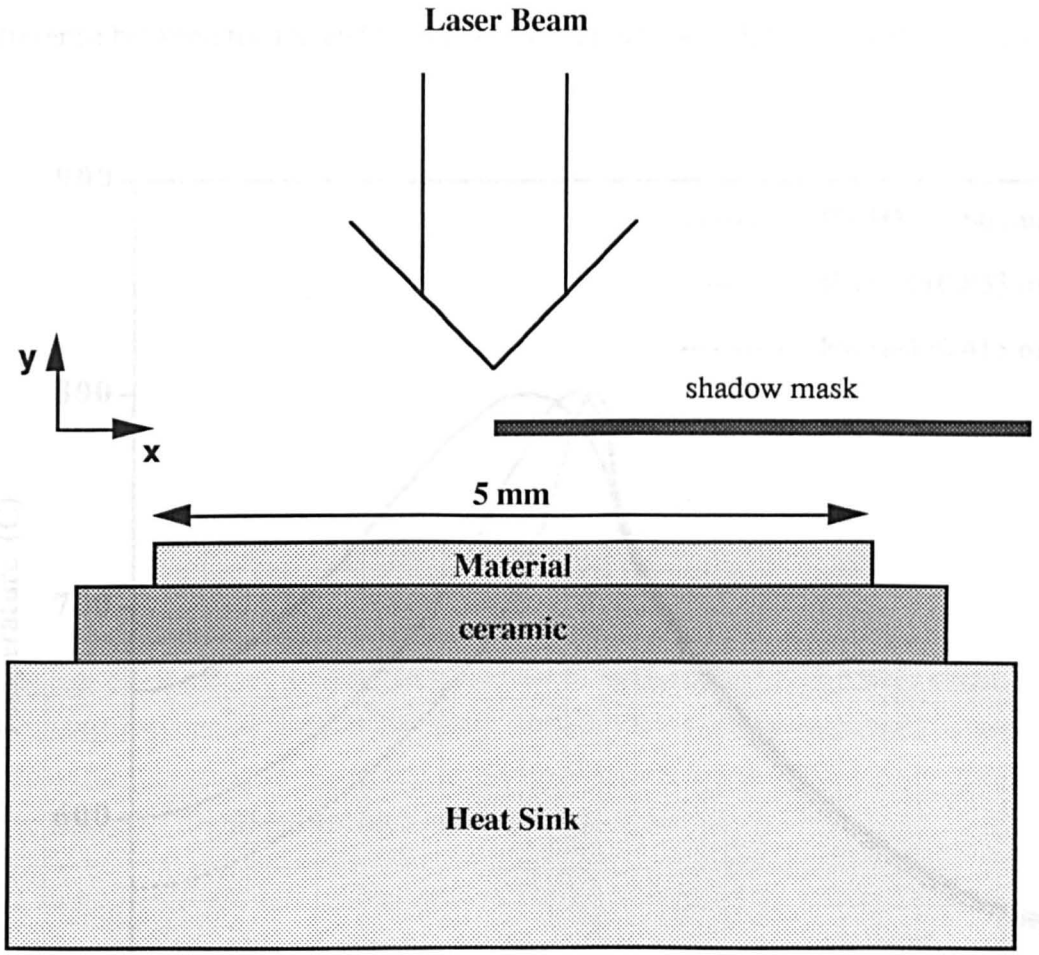

Fig.21 Schematic diagram of model including layer of low thermal conductivity ceramic

Simulations were carried out for three different laser beam widths with FWHM of 1.66 mm, 0.83 mm and 0.415 mm. In each case the heat sink temperature was kept constant at 200°C with a shadow mask extending from the centre of the material to the right hand edge (i.e. from 2.5 mm < x < 5 mm). Fig. 22 shows the temperature rises induced by the three different laser beam widths, calibrated so that the peak temperature was 800°C. The power levels required to achieve these

temperatures are given in Table 5 and indicate that there is only a small variation with beam size. This is because the ceramic plate is effectively trapping the heat within the material and therefore the heat tends to diffuse laterally to a much greater extent than in the previous simulations (without the ceramic plate). This also explains why the power levels are drastically reduced from the original model (e.g. for a FWHM = 1.66 mm the power required is 375.9 W without the ceramic plate, but only 20.7 W with the ceramic plate!). In fact, the temperature at the bottom of the sample is only 20°C to 50°C cooler than the top of the sample, when the ceramic plate is included. This result contrasts to the previous situation, where the temperature difference between the top and bottom of the sample was 600°C (i.e. 800°C - 200°C).

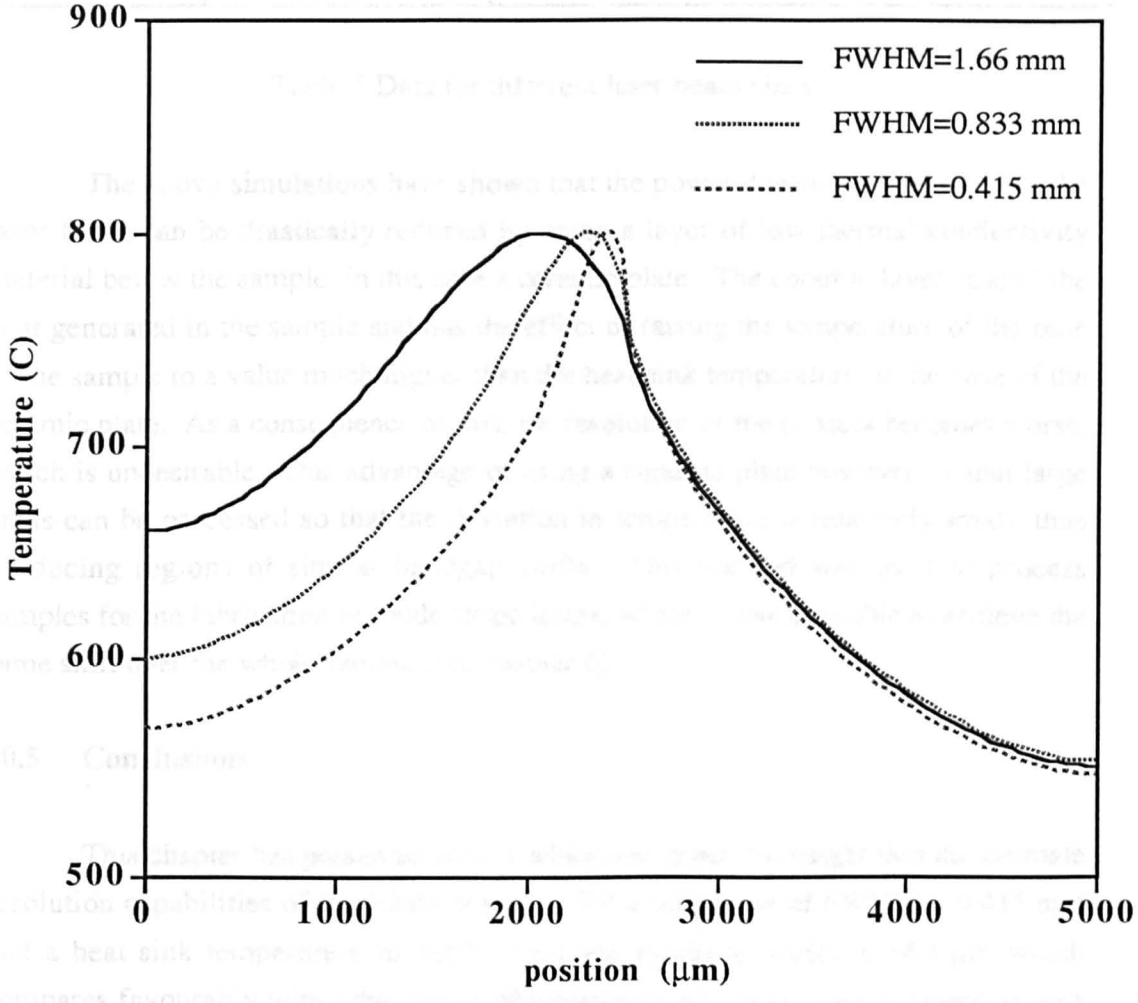

Fig. 22 Temperature rise induced with layer of ceramic and a heat sink temperature of 200 °C

Also shown in Table 5 is the distance from the edge of the mask to the position of peak temperature which shows similar trends to those of the previous model. The transition region width, however, does not show such a strong dependence on the beam width as seen in the previous model which is also a result of the increase in lateral diffusion of the heat within the sample.

FWHM (mm)	power required (Watts)	Distance of peak temp. from edge of mask (μm)	Transition region width (μm)
1.66	20.71	500	650
0.83	18.98	200	520
0.415	17.18	100	397

Table 5 Data for different laser beam sizes

The above simulations have shown that the power densities required from the laser beam can be drastically reduced by using a layer of low thermal conductivity material below the sample, in this case a ceramic plate. The ceramic layer "traps" the heat generated in the sample and has the effect of raising the temperature of the base of the sample to a value much higher than the heat sink temperature of the base of the ceramic plate. As a consequence of this, the resolution of the process becomes worse, which is undesirable. One advantage of using a ceramic plate however, is that large areas can be processed so that the deviation in temperature is relatively small, thus producing regions of similar bandgap shifts. This method was used to process samples for the fabrication of oxide stripe lasers, where it was desirable to achieve the same shift over the whole sample (see chapter 6).

10.5 Conclusions

This chapter has presented results which has given an insight into the ultimate resolution capabilities of the PAID process. For a beam size of FWHM = 0.415 mm and a heat sink temperature of 200°C then the transition width is 54.5 μm which compares favourably with other forms of integration processes such as selective area epitaxy.

---

1 J.B. Fourier, Théorie analytique de la chaleur, Paris, 1822. Translated by A. Freeman, Dover Publications, New York, 1955

2 M. Lax, Journal of Applied Physics, **48**, (1977), p 3919

3 M. Lax, Applied Physics Letters, **33** (18) October 1978, pp 786-788

4 M. Yamada,Japanese Journal Of Applied Physics, Vol.**30** (7), 1991, pp.1418-1427

5 W.B. Boyce, R.W. Dixon, Journal of Applied Physics, Vol. **46**, 1975, p855

6 Comp. Meth. Appl. Mech. Eng., **45** (1984)

7 C.C. Yu, J.C. Heinrich, International Journal for Numerical Methods in Engineering, Vol **23**, (1986), pp 883-901

8 D.W. Kelly, S. Nakazawa, O.C. Zienkiewicz, J.C. Heinrich, International Journal for Numerical Methods in Engineering, Vol **15**, (1980), pp 1705-1711

9 H. Peyre, F. Alsina, J. Camassel, J. Pascual, R.W. Glew, Journal of Applied Physics, **73** (8), April 1993 pp 3760-3768

10 J. Crank, The Mathematics of Diffusion, Oxford University Press, London, 1957

11 M. Gibbon, J.P. Stagg, C.G. Cureton, E.J. Thrush, C.J. Jones, R.E. Mallard, R.E. Pritchard, N. Collis, A. Chew, Semicond. Sci. Technol., **8**, pp 998-1010, 1993

Chapter 11 Conclusions and Future Work

11.1 Conclusions

A wide range of discrete optoelectronic devices have been reported in this thesis which have utilised Photoabsorption Induced Disordering (PAID) in some way to alter their bandgap. These devices included single-mode strip loaded waveguides, bandgap tuned lasers (both oxide stripe and ridge waveguide) and electroabsorption modulators.

Fabrication and testing of these devices has demonstrated that PAID is a very promising quantum well intermixing technique. For example, propagation losses of 5 $dBcm^{-1}$ at 1550 nm (with losses as low as 1.6 $dBcm^{-1}$ at 1570 nm) were measured in single-mode ridge waveguides which shows that PAID is an effective way of producing low loss interconnecting waveguides for use in photonic integrated circuits.

Broad area oxide stripe lasers of different lengths were fabricated from multiple quantum well laser material intermixed by varying amounts. It was shown that no significant degradation of the device properties (such as threshold current, ex-facet efficiency and propagation losses) occurred due to intermixing. The threshold current density of material intermixed by up to 140 nm was found to increase by only 20 % which was attributed to the alteration of the potential profile in the quantum wells leading to an increase in the current density required to achieve transparency.

There was further evidence that the multiple quantum well material retained good electrical and optical properties after intermixing with the fabrication of electroabsorption modulators. ON/OFF ratios were measured to be 20 dB in 500 μm long devices fabricated from material which has been bandgap shifted by 120 nm, while material shifted by only 80 nm yielded devices with extinction ratios as high as 27 dB. It was also demonstrated that photocurrent spectroscopy is a very useful technique for analysing the electroabsorption properties of both as-grown and intermixed multiple quantum well material.

In order to demonstrate that PAID is capable of selectively intermixing areas of a wafer and producing integrated devices, a simple extended cavity laser was fabricated. The device consisted of a broad area active lasing section and a passive waveguide section which had been bandgap widened by 140 nm using PAID. The losses measured in the passive sections of the lasers were 16 cm^{-1} (70 $dBcm^{-1}$)

compared to 28 cm^{-1} in the active regions. The main reasons that this loss was higher than the losses measured in the single-mode waveguides was due to the extra free-carrier absorption caused by the doping in the structure and the lack of optical confinement in the waveguide.

The process was modelled using a commercially available finite element package (ABAQUS) in order to determine the potential resolution of the PAID process. This modelling yielded useful results which gave an insight into how the physical parameters (such as spot size and heat sink temperature) affected it. It was found that a transition region width of only 54 μm was achievable with a laser beam size of FWHM = 0.415 mm assuming perfect heat sinking conditions of 200°C.

11.2 Future Work

Many of the results obtained in this thesis have assumed that the material remains lattice-matched as it is intermixed. This is particularly relevant in the section on modelling the band profiles of the intermixed quantum wells. More work is required on determining whether or not this is the case. For example, it would be useful to look at the polarisation of lasers fabricated from material intermixed by different amounts. This would give an indication if there was any strain present in the quantum wells induced by intermixing. It would also be useful to measure the x-ray rocking curves of material before and after intermixing to see if any satellites appear in intermixed material, indicative of strained layers present in the structure.

It is evident from the results presented in this thesis that more work is required in optimising the process for fabricating integrated devices. In particular, more understanding is needed of the transition region between intermixed and unintermixed material.

For a process such as PAID to be accepted, the reliability of devices fabricated using it must be proven. Although some testing was carried out in this thesis, a more comprehensive study would be required to ensure good device reliability. It would also be very interesting to see if any trends were observed from as-grown material to fully intermixed.

The process of PAID was initially investigated as it offered the possibility of processing large areas of a wafer quickly, unlike direct write laser processes. One potential application of the process could be in tuning the photoluminescence wavelength of epitaxial wafers. One major problem in fabricating lasers

commercially is the tight wavelength requirements. PAID, however, could be used to "fine tune" the PL wavelength of wafers in order that they would yield lasers in the required wavelength range. Obviously it would be restricted to wafers in which the PL wavelength was too long. PAID is particularly suited to this application as it would obviously not require high spatial resolution and it has been demonstrated in this thesis that the material still retains good electrical and optical properties after intermixing.

Appendix A

A.1 Introduction

ABAQUS is written in FORTRAN and runs on an IBM Scirroco computer. It has its own user language with programs written with lines of "data cards" of which there are three types. The first type is a line starting with ** which is ignored by ABAQUS and is used for comments. Lines starting with a * contain ABAQUS control parameters and are called keywords. Examples of these keywords are NODE, ELEMENT, PRINT, CONDUCTIVITY and BOUNDARY. All other lines contain data of some sort relating to the keywords which describe the model.

The program written by the user is split into two sections, the MODEL DEFINITION SECTION and the HISTORY DEFINITION SECTION. At the end of each section, output is usually requested such as the temperature at each node.

A.2 Model Definition Section

The model definition section of the input file contains a description of the model, made up of nodes, elements, material properties, initial conditions and fixed boundary conditions.

The simplest model to simulate is the 2-D case as shown in Fig. (10.2). The model must be split into a fine mesh of elements and nodes. In this case, the number of elements is 200 x 20 which means the element size is 50 μm x 20 μm. The program has internal mesh generating facilities which means that the user does not require to input the co-ordinates of every single node, but only the boundary ones. In this case, defining the four corner nodes is sufficient. These are defined as:

```
*NODE
1,0.0,0.0
201,0.01,0.0
8001,0.0,0.0004
8021,0.01,0.0004
```

where the keyword is NODE, and the relevant data cards are in the format: node number, x co-ordinate, y co-ordinate. The program must now be told to generate all the other nodes and calculate their co-ordinates:

```
*NGEN, NSET=BASE
```

```
1,201
*NGEN, NSET=SURFACE
8001,8021
*NFILL, NSET=CRSEC
BASE,SURFACE,20,400
```

The key word NGEN tells the computer to generate nodes (and their co-ordinates) at equal spacing between node 1 and node 201 in increments of 1. The keyword NSET assigns all these nodes to a set and calls it BASE. This can be useful especially when assigning boundary conditions to a large number of nodes. The keyword NFILL generates nodes (and their co-ordinates) in the mesh between the node sets BASE and SURFACE. The relevant data card for this keyword is in the format: node set 1, node set 2, number of nodes between each set, node increment between each set. All the nodes have now been defined with the mesh shown in Fig. A1.

After the nodes have been defined, it is necessary to assign the node numbers to the elements as shown in Fig. A.1. The convention is to number the element nodes in an anti-clockwise direction starting from bottom left such that element 1 is defined as:

```
*ELEMENT,TYPE=DC2D4
1,1,2,402,401
```

where the keyword ELEMENT defines the nodes of an element with the relevant data card in the format: element number, node1, node2, node3, node4. The keyword TYPE is necessary to define what type of analysis will be carried out in the simulation. In this case DC2D4 is a heat transfer element with Diffusive and Convective properties, 2D indicates that the problem is two dimensional and 4 indicates the number of nodes associated to each element. Again the program must generate all the other elements within the mesh and assign the nodes to them. Element 1 is regarded as the Master Element with the remainder generated by:

```
*ELGEN,ELSET=CRSECEL
1,200,1,1,20,400,200
```

The keyword ELGEN generates elements with the data card in the format: master element number, number of elements in first row (x direction), increment in node numbers along the row, increment in element numbers along the row, number of rows

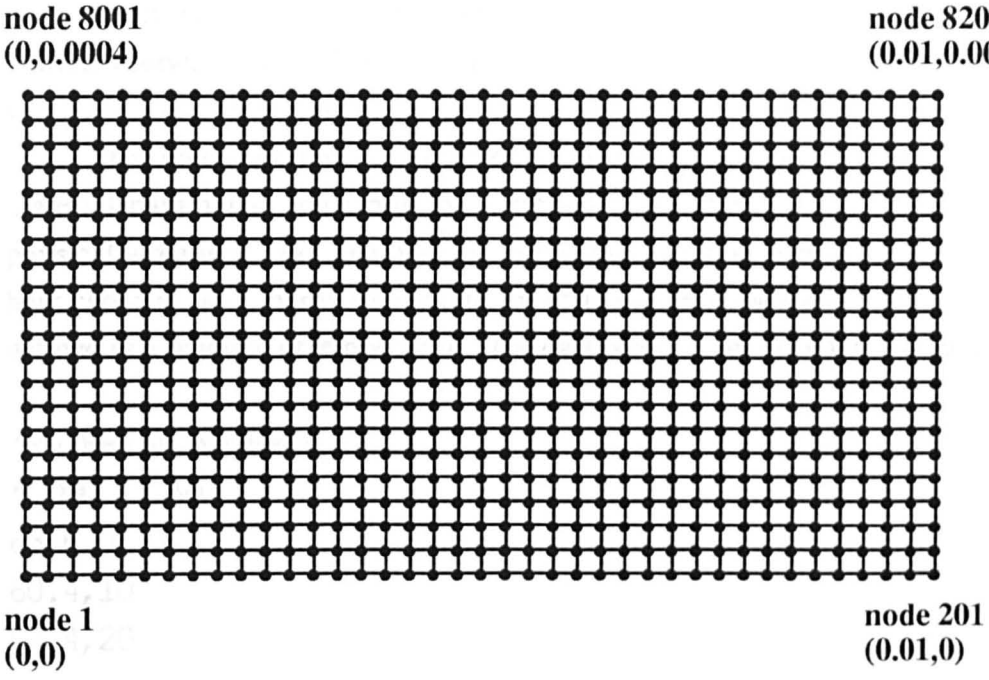

8001	8002	8003	.	.	.	.	.	8200	8201
7601	7602	7603	.	.	.	.	.	7800	7801
.	.	.	.	.	.	.	.	.	.
.	.	.	.	.	.	.	.	.	.
.	.	.	.	.	.	.	.	.	.
.	.	.	.	.	.	.	.	.	.
.	.	.	.	.	.	.	.	.	.
.	.	.	.	.	.	.	.	.	.
401	402	403	.	.	.	.	.	600	601
1	2	3	.	.	.	.	.	200	201

Fig.1 Node mesh layout with x-y coordinates

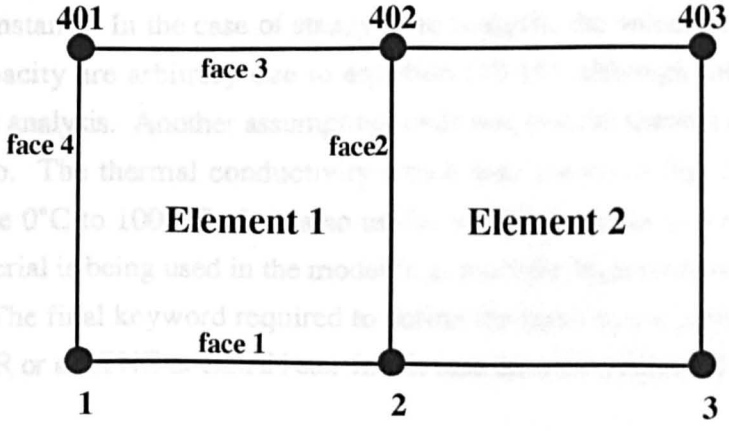

Fig. A1 Element Identification

(in y direction), increment in node numbers between rows, increment in element numbers between rows. The keyword ELSET assigns all the elements to a set called CRSECEL in a similar fashion to NSET.

The mesh has now been defined in terms of elements and node numbers. The material parameters must now be assigned to the mesh which makes the model physically realistic. For heat transfer simulations such as these, the density, specific heat capacity, and thermal conductivity of the material are all required and can be defined as a function of temperature. The data below is for doped indium phosphide

```
*MATERIAL,NAME=IN_P
*CONDUCTIVITY
63.6,0
60.4,10
57.4,20
.
.
.
7.0,980
6.9,990
6.8,1000
*SPECIFIC HEAT
350
*DENSITY
4790
```

All material parameters are in units of watts, metres, kilograms and seconds. Over the temperature range used in these simulations, the density and specific heat were assumed to be constant[1]. In the case of steady state analysis, the values of density and specific heat capacity are arbitrary due to equation (10.14), although this is not the case for transient analysis. Another assumption made was that the thermal expansion coefficient was zero. The thermal conductivity which was shown in Fig. 3.6 was defined over the range 0°C to 1000°C. It is also useful to assign names to a material if more than one material is being used in the model (e.g. multiple layer structures).

The final keyword required to define the mesh is the physical shape. This can be a BAR or a RING or BEAM etc. In this case the mesh is defined as:

```
*SOLID SECTION,ELSET=CRSECEL,MATERIAL=IN_P
0.005
```

The SOLID SECTION has been defined as consisting of the element set CRSECEL (i.e. all the elements in the model) and it being formed of IN_P (indium phosphide). The accompanying data card defines the depth of the SOLID SECTION and is necessary simply to calibrate input power levels in the simulations.

The final data required in the model section is the initial conditions of the mesh nodes which in this model are absolute temperatures.

```
*INITIAL CONDITIONS,TYPE=TEMPERATURE
CRSEC,240
```

The keyword TYPE simply indicates that the initial conditions defined for the nodes is temperature. The relevant data indicates that the nodes in CRSEC (i.e. all of the nodes) are initially at 240°C.

A.3 History Definition Section

The history section lists the step definitions, boundary conditions and requests for output data etc. In this case, the step definition is given by:

```
** Define step conditions
*STEP
*HEAT TRANSFER,END=SS,STEADY STATE
0.5,2,,,2
*DFLUX
CRSECEL,S3NU,
*BOUNDARY,OP=MOD
BASE,11,,240
*NODE PRINT,NSET=SURFACE,FREQ=1
NT11
*NODE FILE,FREQ=4
NT
*EL PRINT,FREQ=0
*END STEP
```

The keywords STEP and END STEP define the start and end of the step of which there may be any number in a simulation. The keyword HEAT TRANSFER tells ABAQUS the nature of the simulation with the associated keywords STEADY STATE and END=SS indicating that it is a steady state problem with the simulation (or STEP)

terminated when the steady state solution is found. The following data is in the format: time step, time period, minimum time increment, maximum time increment, rate of temperature change. These values of different analysis control parameters can be defined by the user, or left blank in which case default values are assumed by ABAQUS.

The keyword DFLUX is perhaps the most important in the program. It allows the user to define a heat flux (surface or volume) as a function of material position which means that the heat generated by the laser can be incorporated into the model very accurately. This flux is defined by writing a subroutine (in FORTRAN) and incorporating it into the listing. The accompanying data indicates that the flux is being generated in the element set CRSECEL and that it is a Non-Uniform Surface flux flowing through face 3 of the element (see Fig. A1). A typical example of this is given by:

```
*USER SUBROUTINES
                                        SUBROUTINE     DFLUX
(FLUX,TEMP,KSTEP,KINC,TIME,NOEL,NPT,COORDS,JLTYP)
C
      INCLUDE 'ABA_PARAM.INC'
C
      DIMENSION FLUX(2),TIME(1),COORDS(3)
            FLUX(2)=0.0
C       power in watts
            POWER=20
          IF (COORDS(2).GE.0.000395) THEN
            FLUX(1)=POWER*1.1284E+5*EXP((-(COORDS(1)-
0.005)**2)/1e-6)
          ELSE
            FLUX(1)=0.0
          END IF
      RETURN
      END
```

This subroutine defines the input power which is created in the uppermost row of elements (where the y co-ordinates of face 3 is > 3.95 mm). This surface flux is in units of Wm^{-2}. Fig. 10.11 shows how the heat generated varies across the sample with a Gaussian distribution.

It is important to calibrate the power levels correctly in the model and to do this, the total power in a Gaussian beam must be calculated. In this model, it is assumed that

the power is constant in the z direction which gives an expression for the total power, P as:

$$P = zA \int_{-\infty}^{\infty} \exp\left(-\frac{x^2}{w^2}\right) dx \tag{A.1}$$

where z is the "depth" of the model defined in the model definition section,
A is the peak power at the centre of the Gaussian beam, and
w is a measure of the beam width. Since

$$\int_{-\infty}^{\infty} \exp\left(-\frac{x^2}{w^2}\right) dx = w\sqrt{\pi} \tag{A.2}$$

the total power is given as:

$$P = zAw\sqrt{\pi} \tag{A.3}$$

$$\Rightarrow A = \frac{P}{zw\sqrt{\pi}} \tag{A.4}$$

This factor, A, has been used to ensure that the power levels are correct in all simulations carried out using a Gaussian laser beam.

The keyword BOUNDARY defines that a boundary condition is placed on the node set BASE, restricting its 11 th degree of freedom (which is the absolute temperature) to a value of 240°C. This keyword could also have been placed in the model definition section as it is constant throughout the simulation.

It is worth pointing out at this stage that boundary conditions do not need to be specified on the three other surfaces This is because ABAQUS assumes that free convection takes place on unspecified boundaries, which is the case in this model.

Other keywords in the STEP conditions are used to define the data required. For example, NODE PRINT sends a copy of the node conditions to the results file. The node set defined is SURFACE with the data sent at the end of every iteration. The relevant data NT11 indicates that only the absolute temperature of the node is required. The data card NT would send all temperature conditions of the node (i.e. $\frac{\partial T}{\partial x}$, $\frac{\partial^2 T}{\partial x^2}$, $\frac{\partial T}{\partial t}$ etc.) to a file. The keyword FREQ indicates the frequency at which the requested data is sent to a file, with FREQ=0 suppressing data transmission.

1 Properties of Indium Phosphide, INSPEC EMIS Datareviews Series No. 6